

STRATIGRAPHIC AND CO-FUNDED
DRILLING OF THE EUCLA BASEMENT
– THE PROTEROZOIC GEOLOGY
BENEATH THE NULLARBOR PLAIN

by
CV Spaggiari, RH Smithies, CL Kirkland,
MTD Wingate, RN England and Y Lu

EXPLORATION
INCENTIVE
SHEME





Government of **Western Australia**
Department of **Mines, Industry Regulation
and Safety**

REPORT 204

STRATIGRAPHIC AND CO-FUNDED DRILLING OF THE EUCLA BASEMENT – THE PROTEROZOIC GEOLOGY BENEATH THE NULLARBOR PLAIN

by

CV Spaggiari, RH Smithies, CL Kirkland¹, MTD Wingate, RN England² and Y Lu

- 1 Timescales of Mineral Systems Group, Centre for Exploration Targeting – Curtin Node, School of Earth and Planetary Sciences, Curtin University, Bentley WA 6102
- 2 Petrology Services, Duncraig WA 6023

PERTH 2020



**Geological Survey of
Western Australia**

MINISTER FOR MINES AND PETROLEUM
Hon Bill Johnston MLA

DIRECTOR GENERAL, DEPARTMENT OF MINES, INDUSTRY REGULATION AND SAFETY
David Smith

EXECUTIVE DIRECTOR, GEOSCIENCE AND RESOURCE STRATEGY
Jeff Haworth

REFERENCE

The recommended reference for this publication is:

Spaggiari, CV, Smithies, RH, Kirkland, CL, Wingate, MTD, England, RN and Lu, Y 2020, Stratigraphic and co-funded drilling of the Eucla basement – the Proterozoic geology beneath the Nullarbor Plain: Geological Survey of Western Australia, Report 204, 147p.

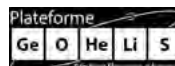
ISBN 978-1-74168-889-4

ISSN 1834-2280



A catalogue record for this book is available from the National Library of Australia

Grid references in this publication refer to the Geocentric Datum of Australia 1994 (GDA94). Locations mentioned in the text are referenced using Map Grid Australia (MGA) coordinates, Zones 51 and 52. All locations are quoted to at least the nearest 100 m.



About this publication

U–Pb measurements of Geological Survey of Western Australia (GSWA) samples were conducted using SHRIMP II ion microprobes in the John de Laeter Centre at Curtin University in Perth, Western Australia. These facilities receive financial support from AuScope and the Australian Research Council (ARC). Lu–Hf measurements were conducted using LA-MC-ICPMS at the ARC National Key Centre for Geochemical Evolution and Metallogeny of Continents (GEMOC), via the ARC Centre of Excellence in Core to Crust Fluid Systems (CCFS), based in the Department of Earth and Planetary Sciences at Macquarie University, Australia. Sm–Nd measurements were conducted by ID-TIMS at the GeOHeLiS analytical platform, based in the Geosciences Department at the University of Rennes, France, and at the Radiogenic Isotope Facility at the University of Queensland. Isotope analyses were funded in part by the Western Australian Government Exploration Incentive Scheme (EIS).

Disclaimer

This product was produced using information from various sources. The Department of Mines, Industry Regulation and Safety (DMIRS) and the State cannot guarantee the accuracy, currency or completeness of the information. Neither the department nor the State of Western Australia nor any employee or agent of the department shall be responsible or liable for any loss, damage or injury arising from the use of or reliance on any information, data or advice (including incomplete, out of date, incorrect, inaccurate or misleading information, data or advice) expressed or implied in, or coming from, this publication or incorporated into it by reference, by any person whatsoever.

Published 2020 by the Geological Survey of Western Australia

This Report is published in digital format (PDF) and is available online at <www.dmirs.wa.gov.au/GSWApublications>.



© State of Western Australia (Department of Mines, Industry Regulation and Safety) 2020

With the exception of the Western Australian Coat of Arms and other logos, and where otherwise noted, these data are provided under a Creative Commons Attribution 4.0 International Licence. (<http://creativecommons.org/licenses/by/4.0/legalcode>)

Further details of geoscience products are available from:

Information Centre
Department of Mines, Industry Regulation and Safety
100 Plain Street
EAST PERTH WA 6004
Telephone: +61 8 9222 3459 Email: publications@dmirs.wa.gov.au
www.dmirs.wa.gov.au/GSWApublications

Cover image: Bottle Corner, after which the Bottle Corner Shoshonite is named, northeast of Forrest on the Nullarbor Plain

Contents

Abstract	1
Introduction	1
Logistical information and drilling techniques	6
Drillsites	7
Drilling techniques	7
Rehabilitation	10
Geological overview of the region	11
Cover sequences	16
Lithological, petrographic and structural analysis of the stratigraphic drillcores	18
Madura Province drillcores	18
Stratigraphic drillcore MAD002	19
Stratigraphic drillcore MAD011	23
Stratigraphic drillcore MAD014	24
Coompana Province drillcores	24
Stratigraphic drillcore FOR004	24
Stratigraphic drillcore FOR008	32
Stratigraphic drillcore FOR010	38
Stratigraphic drillcore FOR011	44
Stratigraphic drillcore FOR012	47
Exploration drillcores	52
Connie Sue Formation	52
Sleeper Camp Formation	59
Structural features of the BKD01 and BKD02 drillcores	59
Haig Cave Supersuite	59
Loongana prospect	61
Serpent prospect	61
Haig prospect	63
Moodini Supersuite at the Moodini prospect	63
Malcolm Metamorphics	63
Geochronology	68
Madura Province	68
Sleeper Camp Formation (1536–1471 Ma)	68
Haig Cave Supersuite (1415–1389 Ma)	70
Moodini Supersuite (1182–1127 Ma)	72
Coompana Province	72
Toolgana Supersuite (1613–1604 Ma)	72
Undawidgi Supersuite (1499–1479 Ma)	72
Moodini Supersuite (1192–1140 Ma)	72
Whole-rock geochemistry	73
Whole-rock geochemistry of Madura Province rocks	73
Basalts and fine-grained mafic rocks	74
Ultramafic, mafic and intermediate (monzonitic) intrusive rocks	83
Sodic leucogranites	91
Potassic granites and associated mafic rocks of the Moodini Supersuite	94
Whole-rock Sm–Nd data for the Haig Cave and Moodini Supersuites	97
Whole-rock geochemistry of Coompana Province rocks	100
Geochemistry of the Toolgana Supersuite	100
Geochemistry of the Undawidgi Supersuite	107
Geochemistry of the Moodini Supersuite	108
Lu–Hf isotope geology	111
Analytical methods	111
Lu–Hf isotope results	111
Madura Province	111
Coompana Province	114
Discussion	118
Formation of the lithological units of the Madura Province	118
Pinto Basalt and Haig Cave Supersuite adakite	118
Haig Cave Supersuite — Loongana oceanic arc	119
Sleeper Camp Formation and the Malcolm Metamorphics	122
Narilya Bore Basalt	122
Formation of the lithological units of the Coompana Province	123
Toolgana Supersuite	123
Undawidgi Supersuite	123
Moodini Supersuite high-KFe mafic to felsic intrusions	124
Madura Province	124
Coompana Province	127
Moodini Supersuite high-KMg series	127
Comparisons of magmatic evolution between the Madura and Coompana Provinces	129
Hf isotope evolution of the Madura and Coompana Provinces	129

Structural evolution and crustal architecture.....	130
Structural interpretation of the Madura Province	130
Structural interpretation of the Coompana Province.....	133
The Mundrabilla Shear Zone	135
Regional implications and tectonic models.....	137
The Madura vs Coompana Province and the role of the Mundrabilla Shear Zone.....	137
Linking the Albany–Fraser Orogen.....	139
Conclusions	142
References.....	143

Figures

1. Major crustal elements of Australia and adjoining portion of Antarctica	2
2. False-colour Shuttle Radar Topography Mission image showing the extent of the Eucla Basin.....	3
3. Simplified structures and drillsite locations plotted on a drape image of gravity and aeromagnetic data	4
4. Map of the Nullarbor Plain showing rainfall isohyets and major caves, dolines and paleochannels.....	6
5. Topographic maps of the drillsites showing pastoral leases, Crown land and DBCA managed lands	8, 9
6. Photo of a typical track on the Nullarbor Plain	10
7. Photos showing the rehabilitation of stratigraphic drillsites	11
8. Time–space diagram showing basin evolution, mineralization and major events.....	12
9. Aeromagnetic image of the region covered by the 13GA-EG1 seismic line	13
10. Interpreted seismic profile from the 13GA-EG1 seismic section.....	14, 15
11. Stratigraphic chart of the cover rocks in the region.....	16
12. Photos of drillcores from the cover rocks	17
13. Schematic diagram showing the main lithologies of the cover successions	17
14. Surface elevation map of crystalline basement and basal clastic sediments of the Madura Shelf	18
15. End-Cretaceous sediment surface and thickness map of the Madura Shelf	19
16. Aeromagnetic image showing interpreted structures in the vicinity of the MAD002 drillhole	20
17. Interpreted bedrock geology in the vicinity of the Rodona Shear Zone and the MAD002 drillhole.....	21
18. Photos of the drillcore MAD002	22
19. Photos of the drillcore MAD002	23
20. Stereonets showing structural data from drillcore MAD002.....	24
21. Geophysical imagery over the MAD011 and MAD014 drillsites, showing structural interpretation.....	25, 26
22. Photos of the MAD011 drillcore	27
23. Photos of the MAD014 drillcore.....	28
24. Aeromagnetic image over part of the Western Australian section of the Coompana Province.....	29
25. First vertical derivative aeromagnetic image of the area in the vicinity of the FOR004 drillsite.....	30
26. Bouguer gravity image of part of the Coompana Province and far eastern part of the Madura Province.....	31
27. Photos of the FOR004 drillcore.....	33
28. Schematic cross-section of the measured foliations and folds in drillcore FOR004.....	34
29. Aeromagnetic image over drillholes FOR008, FOR010 and FOR011, Coompana Province	35
30. Gravity and aeromagnetic data showing structural interpretation and drillsite locations in the Coompana Province	36
31. Photos of the FOR008 drillcore.....	37
32. Stereonets showing structural data from drillcore FOR008	38
33. Examples of structural features in drillcore FOR008.....	38
34. Photos of igneous and meta-igneous lithologies from drillcore FOR010	40
35. Photos of alteration in drillcore FOR010	41
36. Stereonets showing structural data from drillcore FOR010	42
37. Photos of drillcore FOR011.....	44
38. Stereonets showing structural data from drillcore FOR011	46
39. Geophysical images of drillsite FOR012 showing interpreted major structures.....	48, 49, 50
40. Photos of drillcore FOR012.....	51
41. Stereonets showing structural data from drillcore FOR012	53
42. Interpreted bedrock geology and structures in the northern part of the eastern Nornalup Zone.....	56
43. Photos of the Connie Sue Formation in drillcore NDDH002.....	57
44. Gravity and aeromagnetic image showing structural interpretation and drillsite locations of the Loongana, Haig and Serpent prospects	58
45. Photos of the Sleeper Camp Formation.....	60
46. Photos of drillcores containing the Haig Cave Supersuite	62
47. Aeromagnetic image showing strongly magnetic intrusions of the Booanya Suite	64
48. Photos of Moodini prospect drillcores	65
49. Aeromagnetic image and interpreted bedrock geology of the region including exposures of the Malcolm Metamorphics.....	66
50. Photos of the Malcolm Metamorphics	67
51. Summary of geochronology results from drillcore samples from the Madura and Coompana Provinces.....	70
52. Photos of dated rocks from the Madura Province	71
53. Trends in various elements or metabasaltic rocks of the Madura Province	75
54. Variation in major element concentrations with Mg# for metabasaltic rocks of the Madura Province	76
55. Variation in selected trace elements with Mg# for metabasaltic rocks of the Madura Province.....	77
56. Primitive mantle-normalized trace element spider diagrams for metabasaltic rocks from the Madura Province.....	80

57. Logarithmic Th/Yb vs Nb/Yb diagram for mafic rocks of the Madura Province	81
58. Geochemical groups of the Narilya Bore Basalt associated with depth intervals within drillcore MAD011....	82
59. Variation in Mg#, Zr, Th and Th/Yb with Zr/Zr* for metabasaltic rocks of the Madura Province.....	82
60. Variation of MgO and Rb with depth from drillcore LNGD001 from the Loongana prospect.....	83
61. Compositional variation diagrams for mafic and intermediate intrusive rocks from the Madura Province.....	84
62. Primitive mantle-normalized trace element spider diagrams for mafic and intermediate intrusive rocks from the Madura Province	86
63. Primitive mantle-normalized trace element spider diagrams for mafic and intermediate intrusive rocks from the Madura Province with trace elements affected by cumulate processes.....	87
64. Comparison of V/Ti ratios for Haig Cave Supersuite mafic and ultramafic intrusions	88
65. Primitive mantle-normalized trace element spider diagrams for the Kestrel Cavern Gabbro and Hannah monzodiorite	88
66. Variation in selected trace elements and ratios against SiO ₂ for mafic and intermediate intrusive rocks from the Madura Province.....	89
67. Plots of selected elements and La/Sm ratios with depth of the sampled portion of the Kestrel Cavern Gabbro in the drillcore MAD011	90
68. Variation in TiO ₂ , total Fe (FeO ^T) and P ₂ O ₅ with both SiO ₂ and MgO for the Kestrel Cavern Gabbro and Narilya Bore Basalt.....	91
69. N-MORB normalized trace element spider diagram for the Hannah monzonite, shoshonite from Loongana prospect drillcore LNGD001, and the Kestrel Cavern Gabbro	92
70. Variation in selected major elements and element ratios with SiO ₂ for metagranitic rocks of the Haig Cave Supersuite and Sleeper Camp Formation	92
71. Variation in selected major and trace elements with SiO ₂ for metagranitic rocks of the Haig Cave Supersuite and Sleeper Camp Formation	93
72. Variation in selected trace elements with SiO ₂ for metagranitic rocks of the Haig Cave Supersuite and Sleeper Camp Formation	94
73. N-MORB normalized trace element spider diagrams for the Haig Cave Supersuite and Pinto Basalt.....	95
74. Variation in Sr/Y with Dy/Yb for metagranitic rocks of the Haig Cave Supersuite	95
75. Compositional variation diagrams for Moodini Supersuite rocks of the Madura Province compared to intrusive rocks of similar age	96
76. Trace element variation diagrams for Moodini Supersuite rocks of the Madura Province compared to intrusive rocks of similar age	98
77. Geochemical comparisons of metagranitic rocks of the Madura Province with rocks interpreted to be subduction-related from the Coompana and Musgrave Provinces	99
78. Sm–Nd data for gabbros of the Haig Cave Supersuite, Serpent and Loongana prospects.....	100
79. Sm–Nd data for granites of the Haig Cave and Moodini Supersuites, Madura Province	100
80. Variation in K ₂ O, Fe* and MALI with SiO ₂ for felsic rocks of the Coompana Province	101
81. Variation in selected major elements and ratios with SiO ₂ for felsic rocks of the Coompana Province	103
82. Variation in selected trace elements with SiO ₂ for felsic rocks of the Coompana Province	104
83. Primitive mantle-normalized trace element spider diagrams for the Toolgana Supersuite	105
84. Variations with SiO ₂ of ε _{Nd} for the Toolgana Supersuite, younger anatectic granites, the Undawidgi Supersuite and Bottle Corner Shoshonite.....	105
85. Primitive mantle-normalized trace element spider diagrams for primitive rocks of the Toolgana Supersuite, including samples from drillcore FOR011	106
86. Variation in selected trace element ratios with SiO ₂ for felsic rocks of the Coompana Province.....	107
87. Variation in ε _{Nd} at 1500 Ma for felsic rocks of the Coompana Province.....	108
88. Variation in selected trace elements with Fe*, comparing rocks of the Toolgana and Undawidgi Supersuites with rocks of the Musgrave Province	109
89. Variation in ε _{Nd} at 1200 Ma for felsic rocks of the Coompana Province.....	110
90. Hf evolution diagram for samples from the Coompana and Madura Provinces	112
91. Zircon Lu–Hf data for granite vein sample GSWA 182485 (Sleeper Camp Formation).....	113
92. Hf isotope signature of zircons from the Haig Cave Supersuite	114
93. Hf isotope signature of zircons from the Moodini Supersuite in the Madura Province	115
94. Hf evolution diagram for zircons of the Moodini Supersuite, Madura Province	115
95. Hf isotope signature of zircons from the Toolgana Supersuite.....	116
96. Plot of ¹⁷⁶ Lu/ ¹⁷⁷ Hf vs measured ¹⁷⁶ Hf/ ¹⁷⁷ Hf for Toolgana Supersuite sample GSWA 213822.....	116
97. Hf isotope signature of zircons from the Undawidgi Supersuite.....	117
98. Hf isotopic signature of zircons from the Moodini Supersuite in the Coompana Province.....	117
99. Variation in Zr/Zr* with Mg# for mafic and ultramafic rocks of the Madura Province.....	120
100. Variation in Zr/Zr* with ε _{Nd(t)} for mafic and ultramafic rocks of the Madura Province.....	121
101. Variation in selected major and trace elements and Mg# with ε _{Nd(t)} for rocks of the Haig Cave Supersuite....	121
102. Variation in ε _{Nd(1400 Ma)} with K ₂ O for Loongana sodic granites.....	123
103. Comparison of V/Ti ratios for mafic and ultramafic intrusions and basaltic rocks of the Madura Province ...	124
104. Section of modelled magnetotelluric data overlain with interpreted linework from merged seismic lines 12GA-AF3 and 13GA-EG1	125
105. N-MORB normalized trace element spider diagram for adakite and plagiogranites of the Haig Cave Supersuite and granites of the Moodini Supersuite from the Madura Province	125
106. Variation in Ti/V vs Th/U for high-KFe granites and plagiogranites of the Madura Province	126
107. Nd isotope diagram for the Madura Province	127
108. Nd isotope diagram for the Coompana Province.....	128
109. Primitive mantle-normalized trace element spider diagrams comparing shoshonites of the Coompana Province with rare shoshonite from the Madura Province	128
110. Hf evolution diagram for the Madura and Coompana Provinces compared to the Albany–Fraser Orogen, Musgrave Province and adjacent sedimentary basins.....	130
111. Schematic tectonic models showing the evolution and accretion of the Arubiddy Ophiolite Complex onto the West Australian Craton margin	132

112. Interpreted migrated section of seismic line 13GA-EG1 showing the Mundrabilla Shear Zone.....	134
113. Interpreted migrated section of seismic line 13GA-EG1 in the vicinity of Forrest	135
114. Gravity image showing the possible trace of the Lasseter Shear Zone	138
115. Schematic tectonic models showing Stage I of the Albany–Fraser Orogeny	140

Tables

1. Location and collar information of the eight stratigraphic drillholes.....	5
2. Structural and metamorphic synthesis of drillcore FOR010	43
3. Drillhole information for exploration drillcores from the Eucla basement	54
4. Summary of lithological and structural characteristics of metavolcanic and metasedimentary rocks of the Connie Sue Formation, Sleeper Camp Formation and coastal exposures of the Malcolm Metamorphics ...	55
5. U–Pb zircon geochronology results and sample information.....	69
6. Whole-rock Sm–Nd data and sample information from the Madura Province.....	78, 79
7. Whole-rock Sm–Nd data and sample information from the Coompana Province	102
8. Summary statistical description of Hf isotope signature (ϵ_{Hf}) of the Madura and Coompana Provinces	112
9. Summary of interpreted structures in the stratigraphic drillcores in the Coompana Province.....	136

Appendices

Available with the PDF online as an accompanying digital resource

1A and 1B.

- Gyro orientation surveys of the 2013 and 2014 drillholes
- Logs of the stratigraphic drillcores, including structural data and sample information
- Wireline survey data and report of drillhole FOR010 provided by GAA Wireline
- Photographs of the stratigraphic drillcores taken on site
- Petrographic report of the stratigraphic drillcores
- Magnetic susceptibility measurements of the stratigraphic drillcores
- Whole-rock geochemistry data, assay data and sample information
- Petrographic and sample information on the Burkin prospect drillcores
- Zircon Hf isotope data

Stratigraphic and co-funded drilling of the Eucla basement — the Proterozoic geology beneath the Nullarbor Plain

by

CV Spaggiari, RH Smithies, CL Kirkland¹, MTD Wingate, RN England² and Y Lu

Abstract

The Eucla basement stratigraphic drilling program, funded through the Exploration Incentive Scheme (EIS), was established to investigate the greenfields Madura and Coompana basement provinces. In Western Australia, these basement provinces are completely overlain by up to 500 m of cover rocks belonging to the Cretaceous and Cenozoic, Bight and Eucla Basins. Stratigraphic drillsites were chosen by identifying geophysical domains in aeromagnetic and gravity data to maximize the potential for a broad array of lithologies and units, and to inform geophysical data interpretation and aid mapping under cover. Detailed analysis of the 1560 m of stratigraphic basement drillcore obtained from eight diversely located sites within the Nullarbor region has provided the means to establish a stratigraphic and crustal evolution framework for the covered Proterozoic basement, and to broadly assess its prospectivity. The drillsites intersected a variety of metabasaltic rocks, felsic metavolcanic rocks and related schists, gabbroic rocks, and dominantly metamorphosed granitic rocks including shoshonite, adakite, and granites with syenogranitic to dioritic compositions. Combined with work on existing EIS co-funded and donated company drillcores, the new drillcores confirm the presence of a suture zone between the hyperextended continental crust of the Albany–Fraser Orogen and the dominantly oceanic and oceanic-arc crust of the Madura Province. Analysis of the drillcores farther east, shows that the Coompana Province is similarly dominated by oceanic to oceanic-arc crust but records different components of the tectonic history. The oceanic crust in both provinces is interpreted to have initially developed at c. 1950 Ma, with various oceanic-arc assemblages and additional juvenile oceanic crust formed between c. 1610 and 1389 Ma. The Madura and Coompana Provinces, and the southeastern region of the Albany–Fraser Orogen, have been affected by voluminous mainly high-KFe magmatism, deformation and metamorphism related to the 1225–1125 Ma Maralinga Event, which stabilized the crust in this region.

KEYWORDS: geochemistry, geochronology, prospectivity, stratigraphic drilling, tectonics

Introduction

The basement to the Nullarbor Plain has remained one of the most significant, and to some extent forgotten, regions of Proterozoic Australia, yet this region is fundamental to understanding the assembly of the West and South Australian Cratons (the WAC and SAC; Myers et al., 1996). Buried beneath the cover are the Madura and Coompana Provinces and the northeastern part of the Albany–Fraser Orogen, which together define the Eucla basement (Figs 1, 2). The Eucla basement stratigraphic drilling program, funded through the Exploration Incentive Scheme (EIS), was established to investigate these hidden basement greenfields regions, which in Western Australia are completely overlain by up to 500 m of cover rocks belonging to the Cretaceous and Cenozoic Bight and Eucla Basins, and to the north by the Officer Basin (Lowry, 1970; Reynolds, 2016; O’Connell, 2011). This cover extends into South Australia, where it includes the Denman Basin.

Drillcores provide the only means of obtaining basement or basement-associated cover rocks for analysis. Combined with work on existing EIS co-funded and donated company drillcores, the stratigraphic drillcores have revolutionized our knowledge of the hidden basement provinces that are missing links in understanding Proterozoic Australian geology and provided critical information regarding the geodynamics and prospectivity of this vast region. The main objectives of the Eucla basement stratigraphic drilling program were to:

- obtain high-quality, oriented drillcores from diverse lithologies interpreted from geophysically distinctive units for detailed logging, structural analysis, petrography, geochronology, geochemistry and isotope analysis

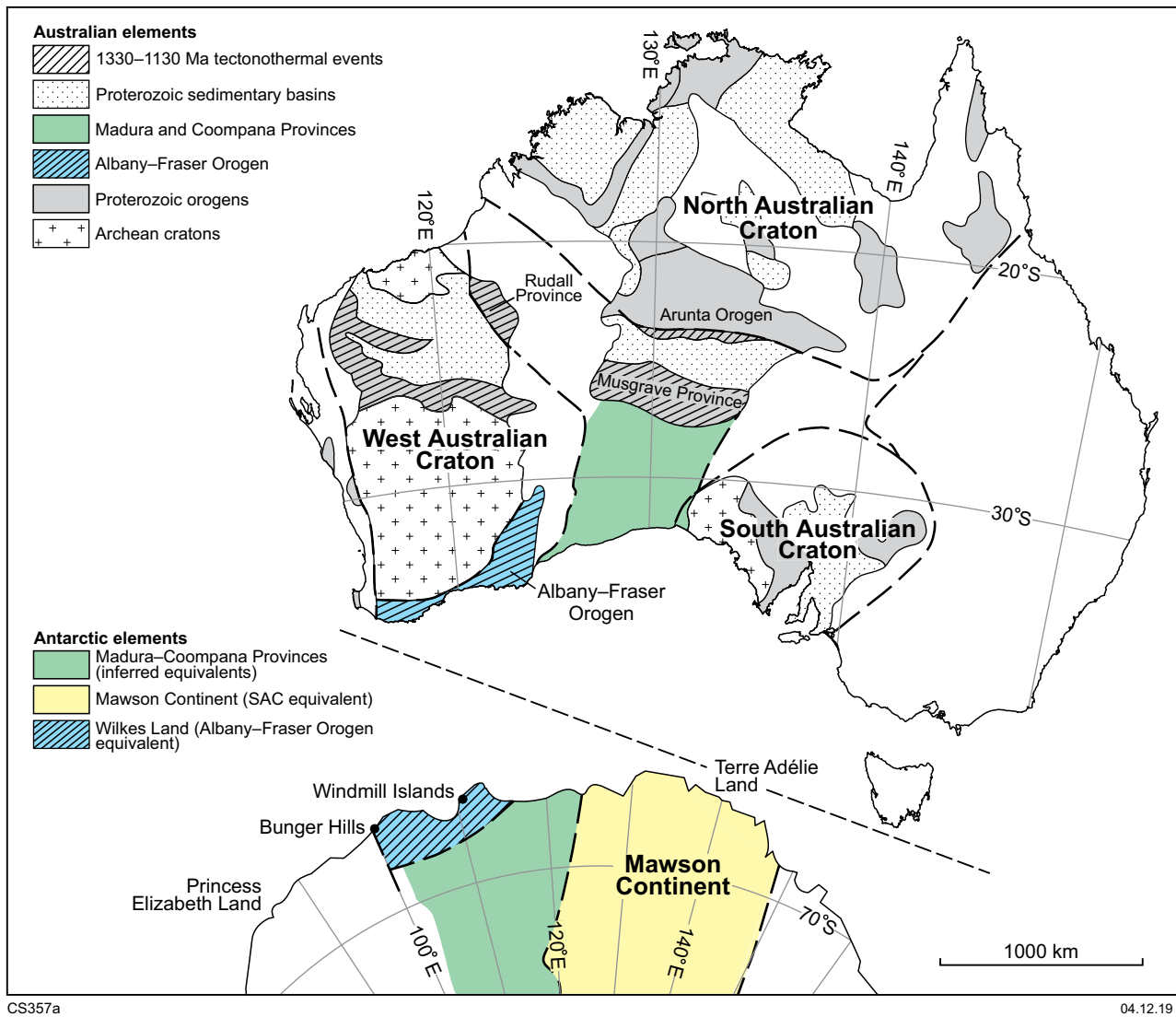
- understand the geological evolution of the basement provinces beneath the Bight and Eucla Basins (regional mapping under cover)
- understand the links between the Albany–Fraser Orogen, the Musgrave Province and the Gawler Craton
- assist mineral systems studies and provide insight into prospectivity
- provide the exploration industry with geological knowledge, rather than just geophysical targets.

The results of these objectives are covered in this Report. During 2013 and 2014, eight basement diamond holes were successfully drilled, providing 1560 m of high-quality, oriented HQ basement core (Figs 2, 3, Table 1). A diverse array of lithologies was encountered, including metabasaltic rocks, felsic metavolcanic rocks and related schists, gabbroic rocks, and mostly deformed and metamorphosed granitic rocks including shoshonite, adakite, and granites with syenogranitic to dioritic compositions. In some holes, basin cover rocks were also sampled (Table 1) and these drillcores and chips have been the subject of collaborative work between Curtin University’s School of Earth and Planetary Sciences and the Basins and Energy Geoscience project area of the Geological Survey of Western Australia (GSWA; Barham et al., 2015; Mounsher, 2016; Reynolds, 2016).

Prior to the Eucla basement stratigraphic drilling program, the first two diamond drillcores from the Madura Province were LNGD001 and LNGD002, drilled by Helix Resources Limited (Bunting and McIntyre, 2003) at the Loongana prospect northwest of Loongana siding (Figs 2, 3).

¹ Timescales of Mineral Systems Group, Centre for Exploration Targeting – Curtin Node, School of Earth and Planetary Sciences, Curtin University, Bentley WA 6102

² Petrology Services, Duncraig WA 6023



CS357a

04.12.19

Figure 1. Major crustal elements of Australia and adjoining portion of Antarctica. Modified from Fitzsimons (2003), Spaggiari et al. (2011), Aitken et al. (2016), Morrissey et al. (2017). Abbreviation: AFO, Albany–Fraser Orogen

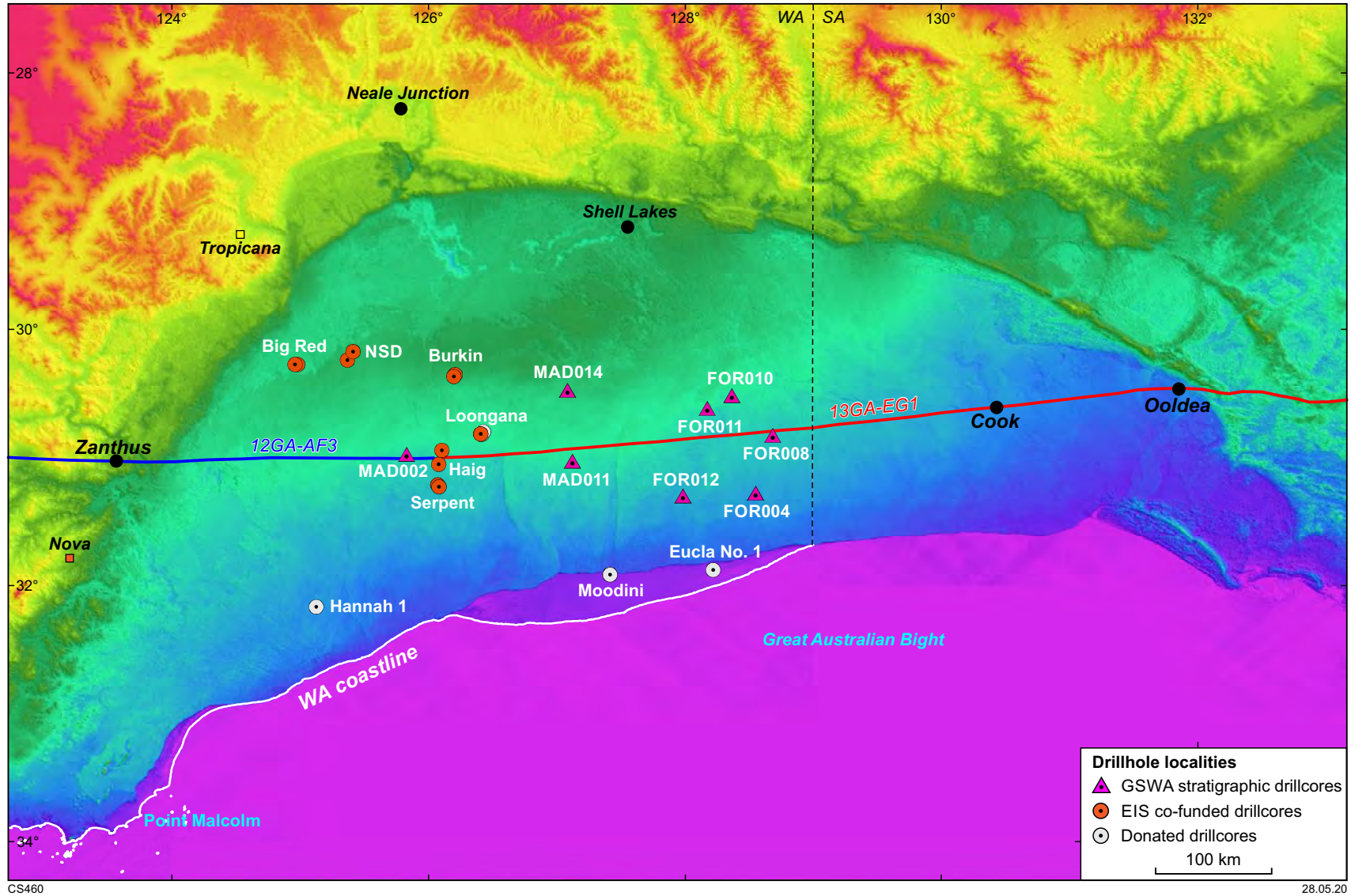


Figure 2. False-colour Shuttle Radar Topography Mission (SRTM) image showing drainage patterns and the extent of the Eucla Basin. The locations of drillholes, deep crustal seismic lines, mines and localities are plotted on the image

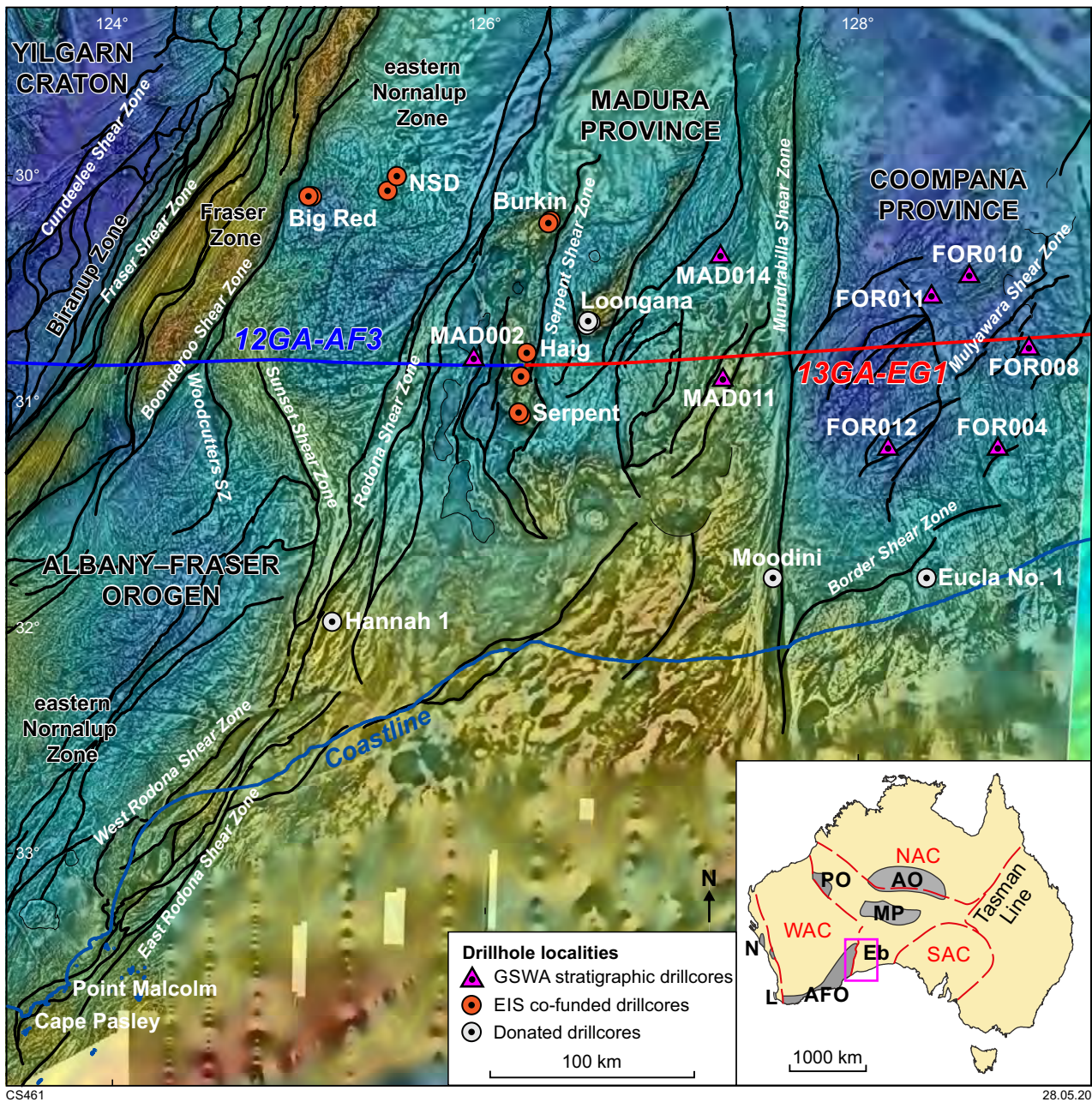


Figure 3. Simplified structures and drillsite locations plotted on a drape image of gravity (colour) and reduced-to-pole, first vertical derivative aeromagnetic data (greyscale). Warm colours represent a strong gravity response, cool colours represent a low response. The locations of deep crustal seismic lines, mines and localities are plotted on the image. Abbreviations on inset: AFO, Albany-Fraser Orogen; AO, Arunta Orogen; Eb, Eucla basement; L, Leeuwin Complex; MP, Musgrave Province; N, Northampton Complex; PO, Paterson Orogen

Table 1. Location and collar information of the eight stratigraphic drillholes. Abbreviations: MR, mud rotary; RC, reverse circulation

<i>2013 Hole ID</i>	<i>Location</i>	<i>Latitude/ longitude</i>	<i>Zone</i>	<i>Easting/ northing</i>	<i>Azimuth (°)</i>	<i>Inclination (°)</i>	<i>Drilled depth to basement (m)</i>	<i>Collar (m)</i>	<i>PQ basin cover core (m)</i>	<i>HQ basin cover core (m)</i>	<i>HQ basement core (m)</i>	<i>Total depth of hole (m)</i>
FOR004	Northwest of Eucla	-31.280080°S 128.553960°E	52	457543E 6539272N	70	-80	389.90	137.7 (RC)	229.00	17.50	180.50	570.40
FOR011	North-northeast of Forrest	-30.617160° S 128.175830° E	52	421006E 6612536N	10	-80	284.87	88.6 (RC)	196.50	None	215.00	500.10
FOR010	Northeast of Forrest	-30.518600°S 128.366040° E	52	439176E 6623576N	140	-80	357.60	227 (RC)	None	130.60	170.20	527.80
MAD014	North of Loongana	-30.478610° S 127.085710° E	52	316247E 6626622N	340	-80	250.00	270 (RC)	None	None	189.40	459.50
MAD002	Near Gunnadorrah homestead	-30.975750° S 125.831450° E	51	770428E 6569645N	290	-80	389.10	389.1 (MR)	None	None	202.50	591.60
<i>2014 Hole ID</i>												
MAD011	Southeast of Loongana	-31.029953° S 127.123210° E	52	320871E 6565566N	140	-75	440.40	440.4 (MR)	None	None	200.75	641.15
FOR012	Forrest–Mundrabilla Track	-31.300655° S 127.985770° E	52	403478E 6536633N	150	-75	310.10	310.1 (MR)	None	None	200.50	510.60
FOR008	East of Reid	-30.829034° S 128.686140° E	52	469984E 6589303N	105	-75	383.75	383.75 (MR)	None	None	201.70	585.45

These intersected interlayered granitic and gabbroic rocks that crystallized at c. 1410 Ma (Wingate et al., 2015a, and references therein). These ages did not correlate with any dates in the Albany–Fraser Orogen, were extremely rare in the context of the Proterozoic evolution of Australia, and pointed to a different history preserved in the region beneath the Nullarbor Plain. Following the release of government regional aeromagnetic (200 m line-spacing) and gravity data (nominal 2.5 km station spacing), Teck Australia Pty Ltd drilled four diamond drillholes (Haig and Serpent prospects), Gunson Resources Limited drilled two diamond drillholes (Burkin prospect) and Venus Metals Corporation Ltd drilled two diamond drillholes into the Mundrabilla Shear Zone (Moodini prospect) (Figs 2, 3). These drillcores, stored at the Perth Core Library, have provided valuable background information to the three stratigraphic holes subsequently drilled into the Madura Province.

In contrast, no diamond drillcores existed in the Western Australian part of the Coompana Province and the five stratigraphic drillcores provided the first information about the nature of that basement. Very few of the older petroleum wells in the Nullarbor region intersected basement, and in most cases only minor amounts of small chips were recovered. In addition to the geological knowledge gained, the Eucla basement stratigraphic drilling program has also provided valuable experience and technical insight into the drilling conditions in the Nullarbor region, and the challenges of drilling through the variable cover sequences to basement.

The Eucla basement stratigraphic drilling program, and the techniques it employed, is a proven example of a successful under cover mapping program. The results show that both high-quality geophysical data, of as much variety as is feasible, and quality diamond drillcores are required to provide robust information about basement evolution. Geophysical and structural data provide information about crustal architecture, whereas carefully selected drillcore samples, based on detailed logging including structural analysis, provide information about crustal evolution through metamorphic studies, geochronology, whole-rock geochemistry and isotope data. These datasets and their integrated interpretations provide the necessary context for the evaluation of mineralization prospectivity and mineral systems analysis.

Logistical information and drilling techniques

Although not as remote as some of Australia's desert regions, the semi-arid to arid Nullarbor Plain has unique conditions that require careful planning for drilling projects. It is one of the largest karst plains in the world, covering about 200 000 km² and sloping gently seawards with minimal internal relief (Fig. 4; Webb and James, 2006). Abundant small blowholes or subcircular vents (typically tens of centimetres to about 2 m in diameter) are widely scattered throughout, and much less abundant, larger caves mostly occur towards the coast from about 75 km inland (Burnett et al., 2013).

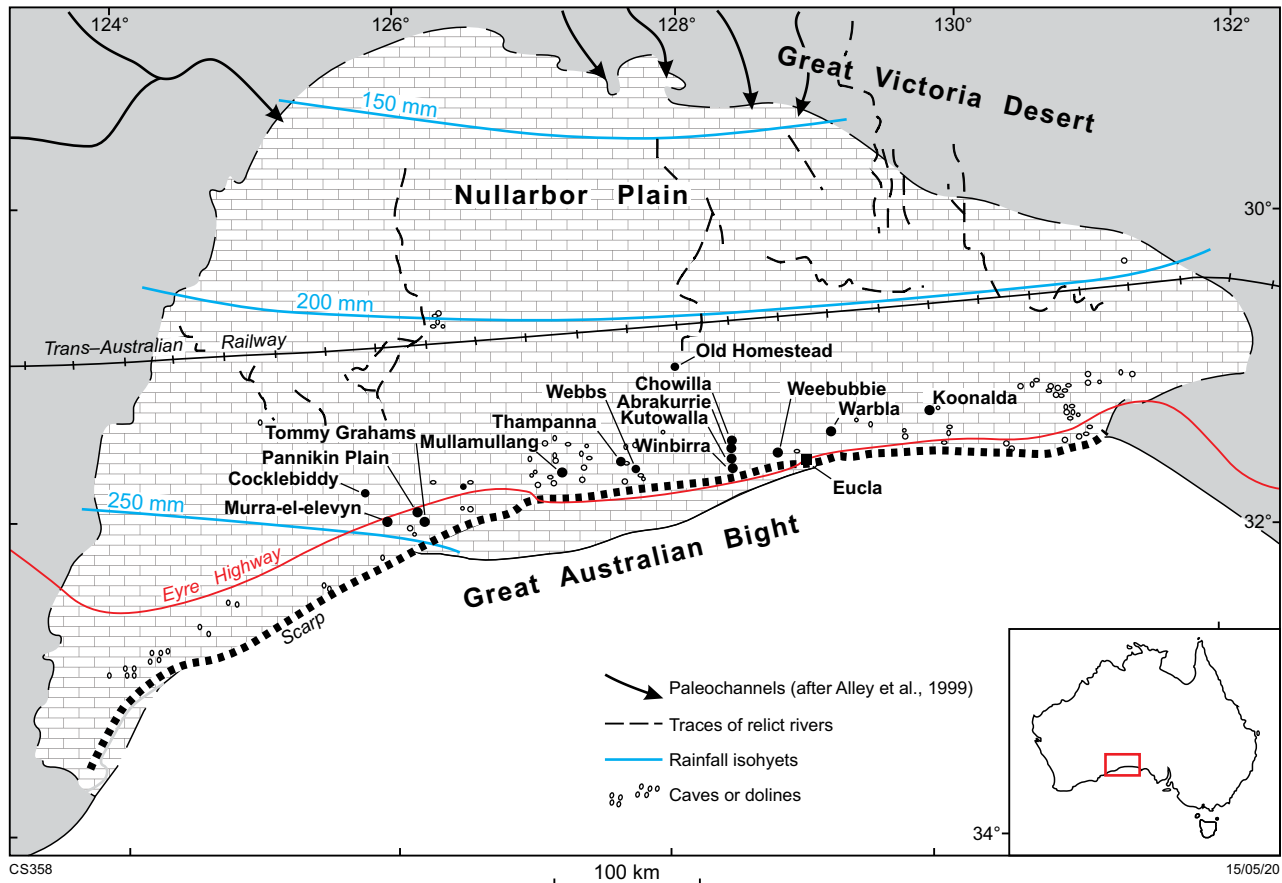


Figure 4. Map of the Nullarbor Plain showing rainfall isohyets (contours of equal rainfall) and locations of major caves, dolines and paleochannels. After Webb and James (2006)

In Western Australia, the Nullarbor Plain is divided into a mix of pastoral leases (in the western portion), unallocated Crown land (mostly in the east and up to the State border), and nature reserve (along the coast; Fig. 5). Pre-existing tracks are reasonably numerous, but travel is slow due to the bouldery limestone surface that cannot be graded (Fig. 6; average speed 40 km hr on most tracks with a 4WD light vehicle). The relatively flat, open limestone plain provides no shelter, and strong winds are common. Fine dust from weathering limestone is problematic for machinery and camping, especially during summer and where frequent travel has created bull dust.

East–west access is possible along the Eyre Highway near the coast, and the Trans-Australian Railway about 100–150 km inland. A graded access track follows the railway line from Kalgoorlie, but east of Haig it becomes an ungraded private track, and a permit from the Australian Rail Track Corporation Ltd (ARTC) is required. There are several small towns or roadhouses along the Eyre Highway, but none along the Trans-Australian Railway. There, the railway siding and locality with the most infrastructure is Forrest, which has a sealed aerodrome and several small houses for accommodation. Fuel and water are available at Forrest with prior arrangement.

Drillsites

To maximize return on geological knowledge, drillhole locations were chosen to investigate and map distinct geophysical domains interpreted in magnetic and gravity data, rather than as specific geophysical targets. They were also chosen to investigate potential host rocks to known mafic intrusions in the Madura Province (i.e. at the Loongana, Haig and Serpent prospects). The eight drillholes cover an area of about 35 000 km² of Crown land, and one pastoral lease (Gunnadorrah). The drillsites were located on flat, open, grassy plain, close to pre-existing tracks. No land clearing was required and an Aboriginal heritage survey was conducted for all sites, as well as for selected backup sites. A Program of Works (POW) was submitted to the then Department of Mines and Petroleum, now the Department of Mines, Industry Regulation and Safety (DMIRS).

Collar and drillcore information are provided in Table 1. Drillcores were oriented during drilling using a Reflex orientation kit and the orientations of each hole were surveyed using a north-seeking gyro. This work was done by Gyro Australia in 2013 once drilling was complete and the holes had been cased with 50 mm PVC. The only hole they were able to fully penetrate was FOR010, as it appeared that the casing in the other drillholes had been crushed by collapse within the Madura Formation. The orientation surveys are provided in Appendix 1. In light of the potential for hole collapse, all holes drilled in 2014 were surveyed by the driller using a Reflex gyro prior to removing the drill rods, both downwards and upwards to test that the data matched each way. These surveys showed some deviation of the hole, particularly within the Madura Formation (Appendix 1B). Orientation lines were drawn on the drillcores where they could be matched along three complete, 3 m rod lengths. The gyro results were applied to structural measurements taken during logging (Appendix 2). In 2013, a wireline

survey of borehole imaging with an acoustic televiewer and collection of natural gamma ray data was conducted by GAA Wireline at the FOR010 drillsite, funded by AuScope (Appendix 3). The acoustic televiewer data analysis, predominantly fracture analysis, is presented in a report within Appendix 3. In addition, each tray of drillcore from all of the eight localities was photographed on-site (Appendix 4).

Drilling techniques

Drilling in the Nullarbor region presents significant challenges, including remote access, weather conditions, availability of water and maintaining supply, and maintaining hole stability while drilling through cover to basement. The cover comprises limestone formations (Eucla Basin) underlain by shale and siltstone, and locally sandstone and conglomerate (Bight Basin), some of which is unconsolidated. Both reverse circulation (RC) and mud-rotary techniques were trialled and assessed to reach basement, or the desired depth within the cover. Although RC drilling is faster, the required depth is not always achievable, and this is particularly important in this region as the basement depth varies greatly, is often unknown, and difficult to estimate using currently available geophysical methods. As with other techniques, RC drilling is also prone to bogging. Mud-rotary became the preferred method, and although it consumed large quantities of water it proved more reliable, provided drilling was continuous once commenced (i.e. double shifts are recommended).

The following is from Mander (2015):

Using mud rotary techniques, hole advancement and stability were achieved allowing successful casing of the hole into basement. From there, the target zones for the hole could be accurately drilled in competent rock using diamond drilling techniques. Choosing a mud drilling system with flexibility to change to the nature of the ground conditions as the holes progressed was paramount to success. Generally using a saltwater tolerant Gel and PAC based system enabled production whilst reducing hole degradation of the poorly consolidated sandstones, siltstones and shale formations of the Madura Formation. Inhibition of the shales was extremely important in maintaining rotation and reducing drilling torque. Constant adjustment of the fluids makeup was necessary due to the changing ground conditions.

Continuous 12-hour shifts are required with crews changing over on the rig. To avoid the risk of compromising the hole, consistent fluid pressure is needed to aid stability, so wherever possible the drilling process should not be stopped until case off. Lost circulation through the early stages of the hole within the limestones poses an additional challenge as the crew work hard to maintain a water supply for drilling and then to prepare the drilling fluid to acceptable strengths and yields before pumping down the hole. Several other additives are required to try and maintain as much fluid circulation as possible.

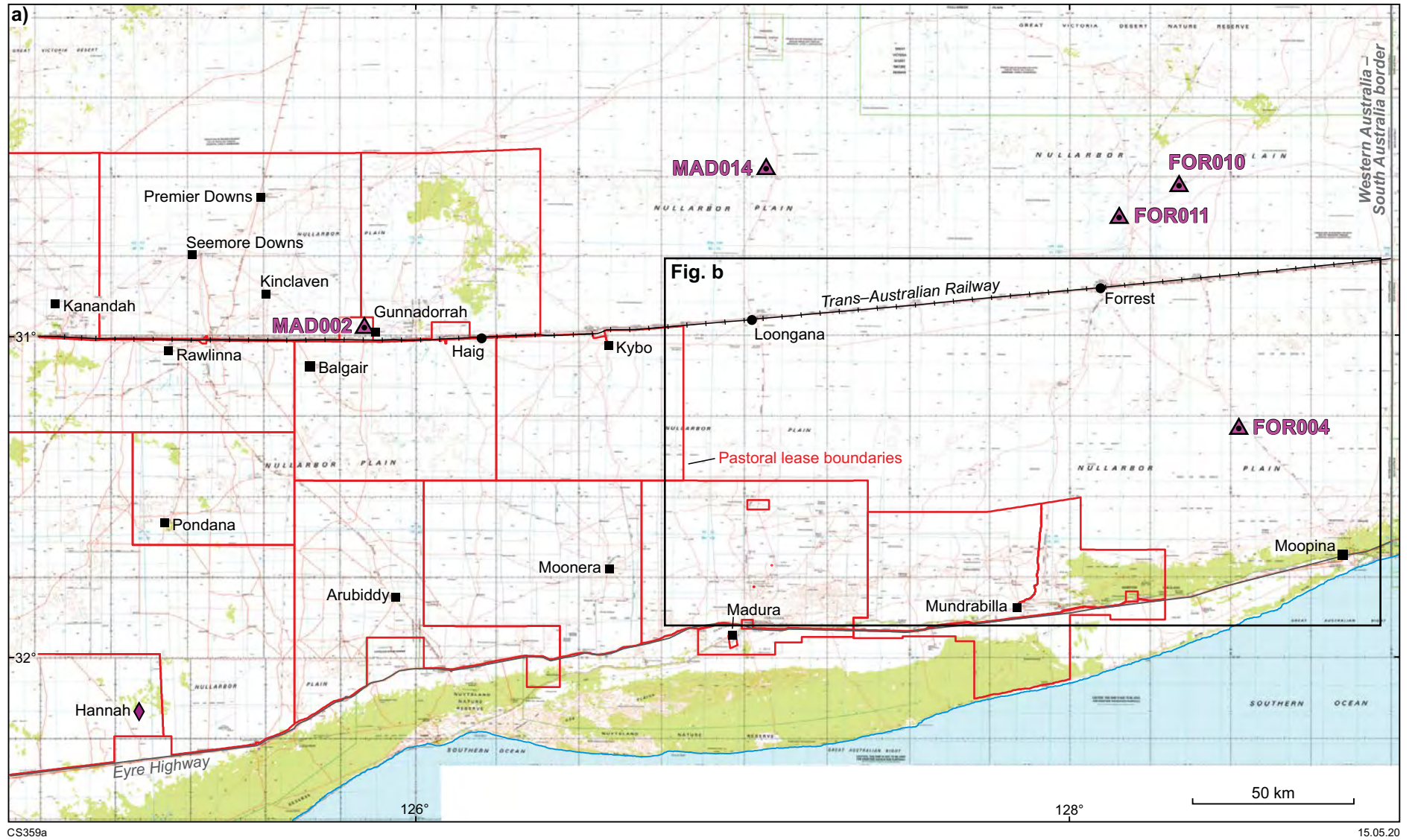
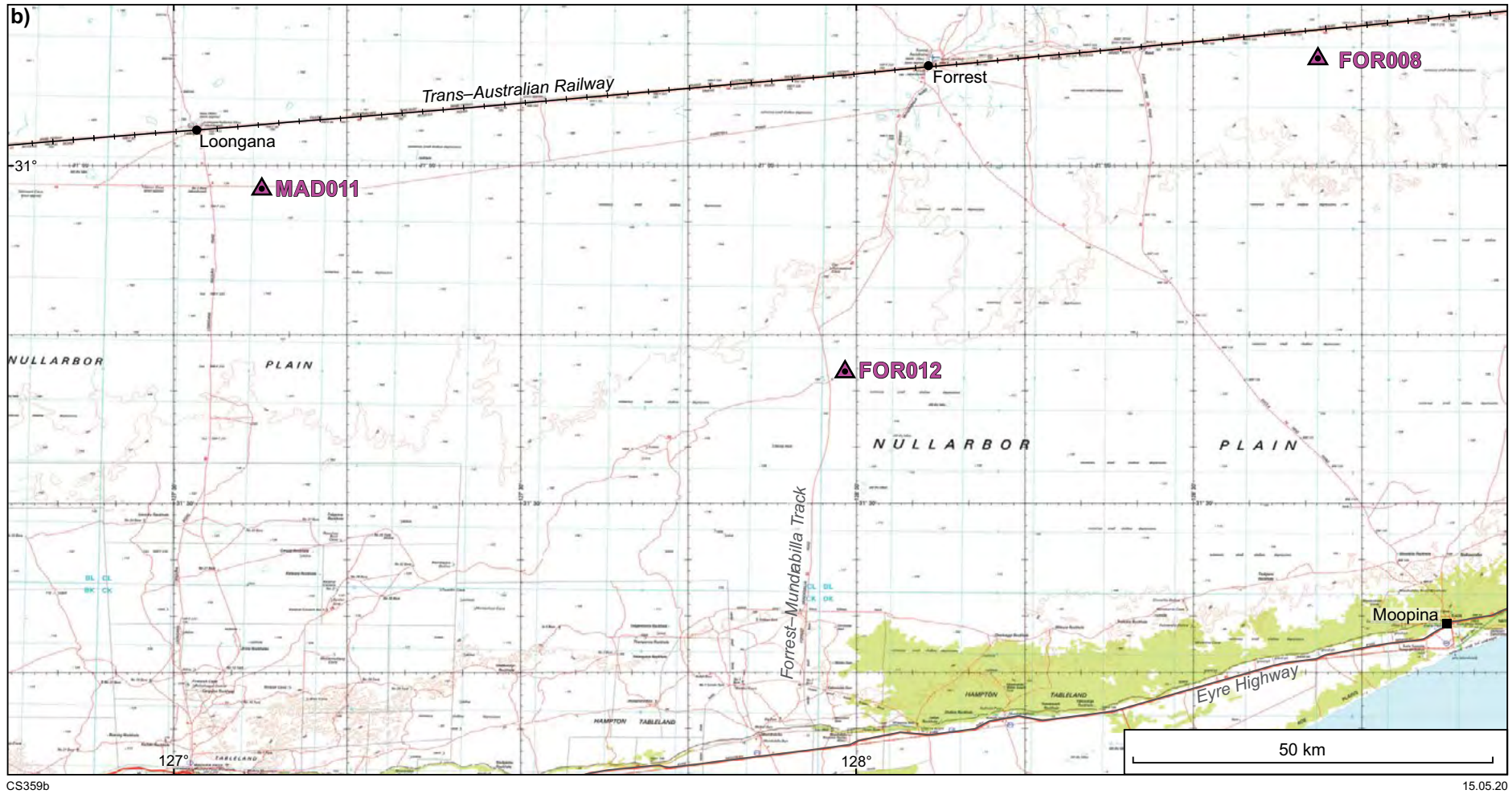


Figure 5. Topographic maps of the drillsites showing pastoral leases, Crown land, DBCA managed lands, and main roads and tracks: a) map of the 2013 drillsites



CS359b

15.05.20

Figure 5. Continued: b) map of the 2014 drillsites



CS441

19.08.19

Figure 6. Typical track on the Nullarbor Plain. Photograph taken north of Loongana siding

A Solids Removal Unit (SRU) was employed on site to assist with recirculation of fluids when achievable. The most beneficial use of this equipment was during the diamond drilling phase as circulation at the top of the hole was rarely achieved even after attempts at cementing through the voids. An added advantage of the SRU is that it keeps the site clean and dry and makes rehabilitation much simpler. Every hole drilled was a success in reaching basement and continuing through to end of hole depth, a significant achievement given that no prior drilling had taken place in the vicinity.

The drillholes were capped immediately following drilling. The steel casing was left in place and the top of the hole was fitted with a steel cap secured with a padlock. This was necessary to reduce the risk posed to native fauna by uncapped drillholes, and to prevent access to the holes. Because the program was for scientific research purposes, the standard practice of plugging the holes after six months was not observed because of potential future downhole studies, and the possibility of re-entry in future drilling programs.

Rehabilitation

One of the advantages of working in the Nullarbor region is that minimal rehabilitation is required, especially when using an SRU, as was the case for this project. Due to the nature of the flat and open grassy surface,

the impact of drilling was minimal. Only light scarification was required in order to promote seed recruitment, to reduce erosion through water run-off and to alleviate soil compression caused by vehicles and rigs. Potential gullying of scarification zones was not a concern as there are no slopes or contours over the area. A survey of all eight drilled sites in October 2014 confirmed that the most crucial factor for soil and native vegetation recovery is rainfall, once sites are left undisturbed (Fig. 7). Sites that had received higher rainfall (e.g. FOR004, FOR012) showed the most regrowth.

Any topsoil that was cleared was stockpiled and re-spread during rehabilitation. Access tracks used were already established public routes prior to drilling. So as not to interfere with these main access routes, the drill pads were placed a short distance off the access tracks. Thus, the only sites that required scarification were sections of the non-established short access tracks, campsites and drill pads. Due to the high amount of *Maireana sedifolia* (common name pearl bluebush) in many areas, scarifying other areas would only serve to remove these slow-growing native flora. No gridlines were used.

Concrete pads were not constructed, and no buried infrastructure was in place due to the minimal nature of this drilling project. All camping was temporary with no structures erected. The campsites were lightly scarified and left to revegetate (Fig. 7c).

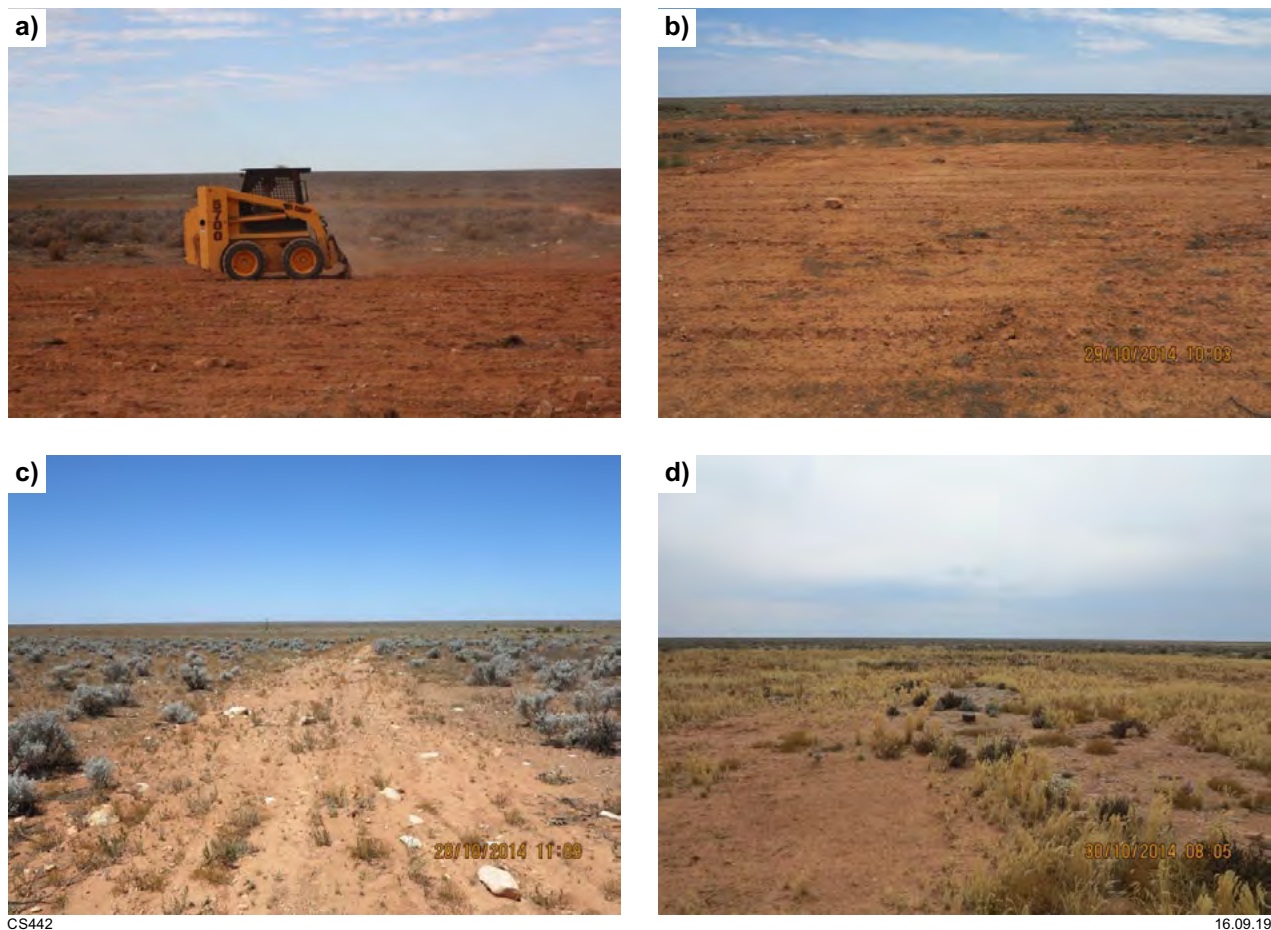


Figure 7. Photos showing the rehabilitation of stratigraphic drillsites: a) bobcat with front tines scarifying FOR010 drill pad in 2013; b) lightly scarified drill pad at site FOR008; c) lightly scarified campsite with good regrowth at site FOR010; d) capped hole at drillsite FOR004, surrounded by regrowth

Geological overview of the region

The Eucla basement is defined as the region completely hidden beneath the Eucla and Bight Basins, which, for the most part, comprises the Madura and Coompana Provinces, but also includes the northeastern part of the Paleoproterozoic to Mesoproterozoic Albany–Fraser Orogen (Figs 1–3). A time–space diagram of the tectonic evolution of these units is shown in Figure 8, which highlights the major differences between them, defined and discussed in this Report. Figure 8 also shows the main stratigraphic units of the Albany–Fraser Orogen and the Madura and Coompana Provinces.

The western boundary of the Madura Province is the Rodona Shear Zone, which is a broad, northeast-trending and southeast-dipping network of shear zones visible in aeromagnetic and seismic data (Figs 3, 9, 10a; Spaggiari et al., 2014, 2017a; Holzschuh, 2019). This shear zone system is interpreted as a suture zone separating the Madura Province from reworked Archean continental crust of the Albany–Fraser Orogen (Kirkland et al., 2011a, 2015; Smithies et al., 2015b; Spaggiari et al., 2015a, 2017a). Kinematic indicators interpreted from aeromagnetic data indicate craton-vergent thrusting, followed by sinistral strike-slip movement. To the east, the Madura Province is truncated by the Mundrabilla Shear Zone,

which is a wide, northerly trending and distinctly linear subvertical shear zone that separates the Madura Province from the Coompana Province (Figs 3, 9, 10a). Sinistral displacement has been estimated at up to 300 km based on matching magnetic and gravity features either side of the shear zone (the Mundrabilla–Frost Shear Zone, Aitken et al., 2016). Although the amount of displacement is not well constrained, the sinistral drag on the shear zone is clearly visible in aeromagnetic images, as are differences in the magnetic, gravity and seismic responses of the two provinces that the shear zone separates. Displacement of at least 100 km would be necessary to account for this, based on the length imaged (Fig. 3). Maximum ages of 1132 ± 9 and 1127 ± 7 Ma for this movement are provided by crystallization ages of metamonzogranite from drillcores that intersect high-intensity magnetic anomalies within the Mundrabilla Shear Zone (Wingate et al., 2015b,c). A minimum age is provided by the 1090–1040 Ma Giles Event in the Musgrave Province, where the interpreted northwards continuation of the Mundrabilla Shear Zone is stitched by voluminous intrusive and volcanic rocks of that age (Howard et al., 2015; Smithies et al., 2015a).

East of the Mundrabilla Shear Zone, the Coompana Province lies between the Madura Province and the Gawler Craton in South Australia (Figs 3, 9, 10). The boundary with the Gawler Craton is tentatively defined as the westerly dipping Jindarnga Shear Zone,

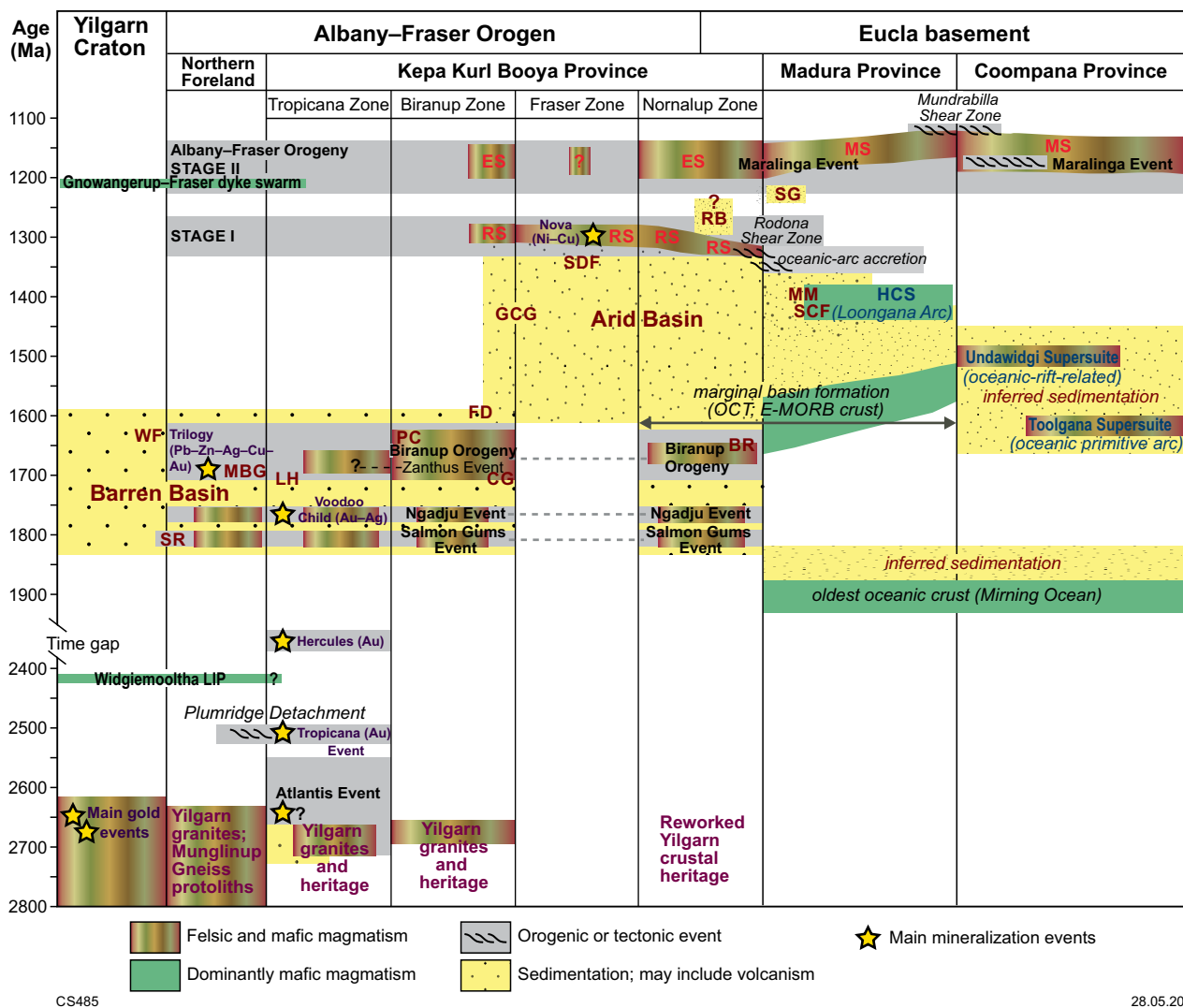


Figure 8. Time–space diagram showing sedimentation, basin evolution and major tectonothermal and mineralization events. The diagram is organized from approximately west to east and shows the stratigraphic hierarchy of the tectonic units. Abbreviations: BR, Big Red paragneiss; CG, Coramup Gneiss; ES, Esperance Supersuite; FD, Fly Dam Formation; GCG, Gwynne Creek Gneiss; HCS, Haig Cave Supersuite; LH, Lindsay Hill Formation; LIP, Large Igneous Province; MBG, Mount Barren Group; MM, Malcolm Metamorphics; MS, Moodini Supersuite; OCT, ocean–continent transition; PC, Ponton Creek paragneiss; RB, Ragged Basin; RS, Recherche Supersuite; SCF, Sleeper Camp Formation; SDF, Snowys Dam Formation; SG, Salisbury Gneiss; SR, Stirling Range Formation; WF, Woodline Formation (modified from Spaggiari et al., 2015a, 2017b)

although the extent of the western Gawler Craton is poorly understood (Dutch et al., 2015, 2016). The Coompana Province — also described by some as the Coompana Block — was previously divided into various domains (Shaw et al., 1996), and more recently the western part was tentatively defined as the Forrest Zone (Korsch et al., 2014; Spaggiari and Smithies, 2015). However, based on the new information from the stratigraphic drilling program, and the interpretation of the Eucla–Gawler seismic line 13GA-EG1, that subdivision has been abandoned. The Coompana Province is now divided into the eastern and western Coompana Province, based on major structures and differences in tectonic history (Fig. 8; Dutch et al., 2016; Spaggiari et al., 2017a). These are defined and discussed below.

Both the Madura and Coompana Provinces were extensively intruded by ferrogabbroic to granitic rocks of the 1192–1125 Ma Moodini Supersuite, during

the Maralinga Event (Fig. 8; Spaggiari and Smithies, 2015; Spaggiari et al., 2016). Igneous rocks in this supersuite are similar in composition and age to the Pitjantjatjara Supersuite of the Musgrave Province (Howard et al., 2015) and the Esperance Supersuite of the Albany–Fraser Orogen, with the latter supersuite additionally preserving an isotopic and geochemical heritage of reworked Archean crust of the Yilgarn Craton (Kirkland et al., 2015, 2017; Smithies et al., 2015b). In the southeastern part of the Coompana Province, the Moodini Supersuite is interpreted as a series of northeast-trending, mainly subcircular granitic plutons of high magnetic intensity, intersected by the Eucla No.1 petroleum well and dated at 1140 ± 8 Ma (Figs 3, 9; Kirkland et al., 2011c; Spaggiari et al., 2012).

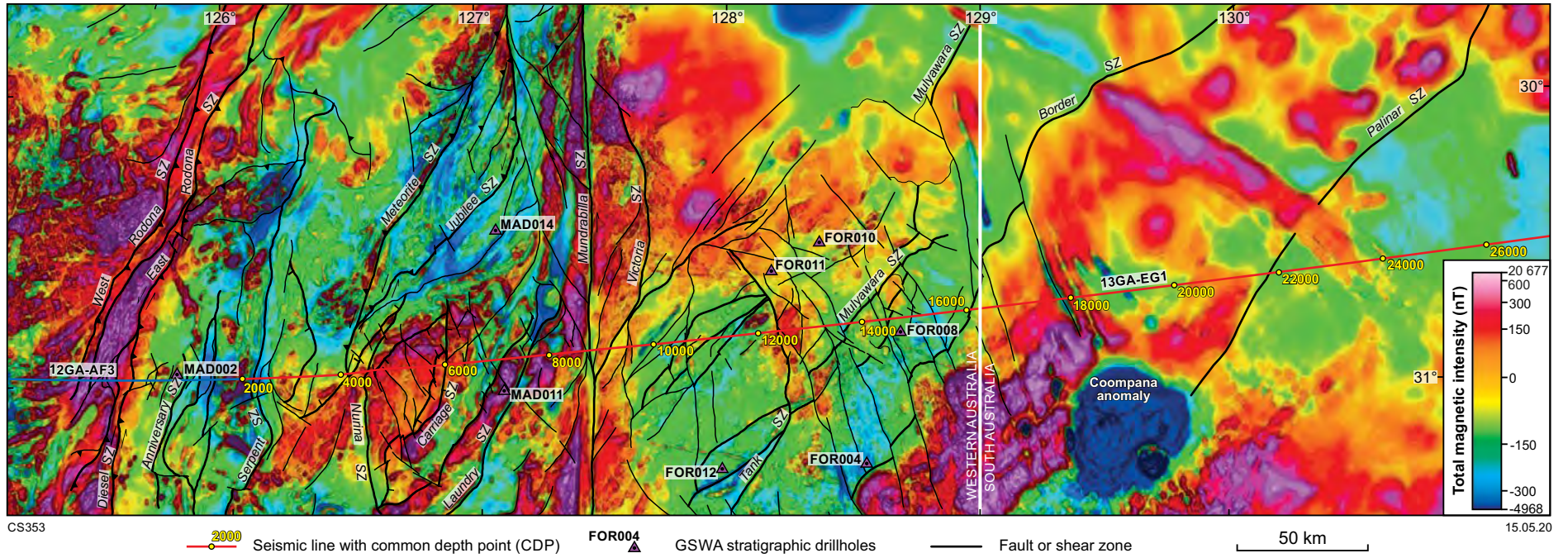


Figure 9. Aeromagnetic image of the region covered by the 13GA-EG1 seismic line, showing major structures and the locations of nearby drillholes

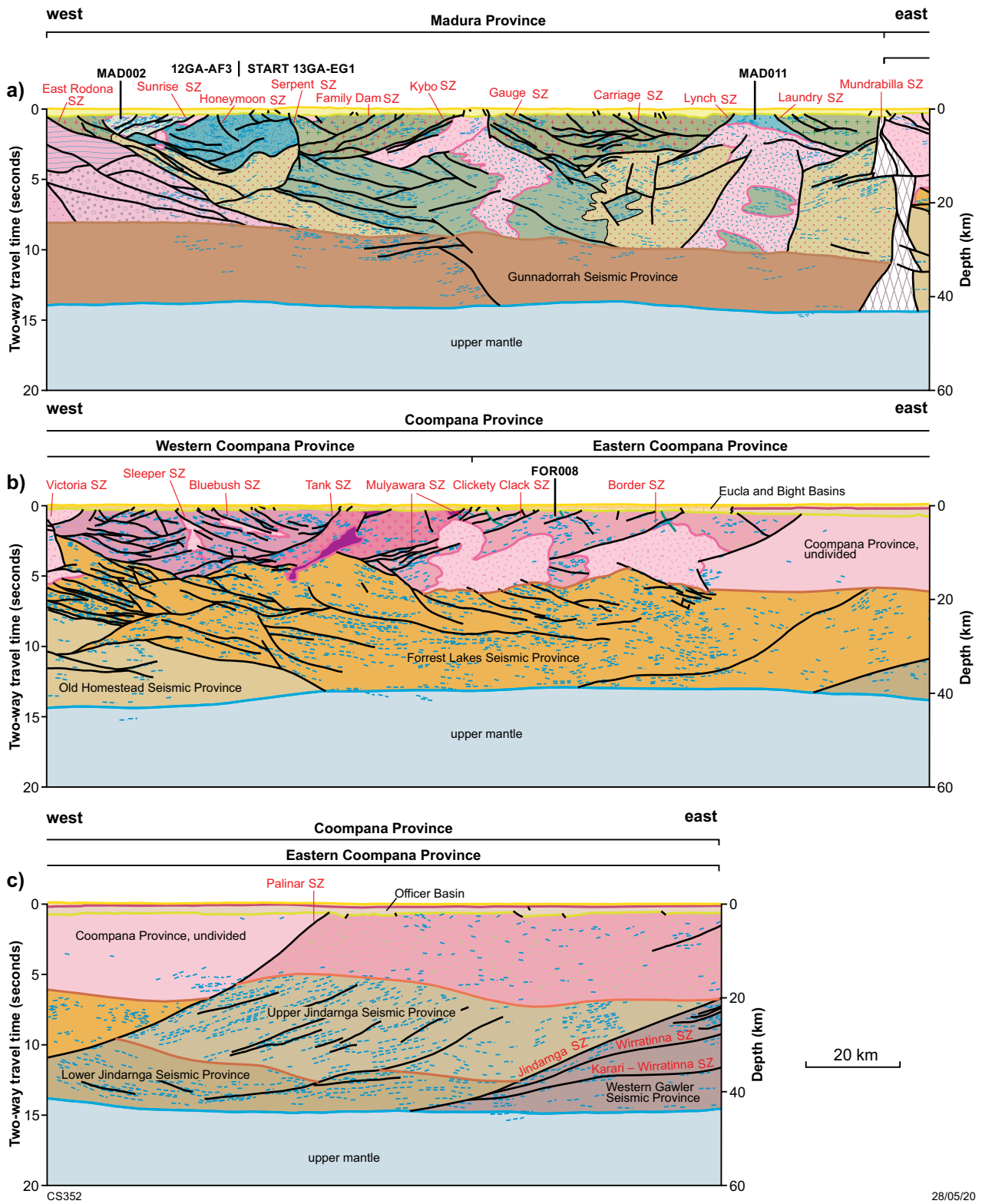


Figure 10. Interpreted seismic profile from the 13GA-EG1 seismic section (from Spaggiari et al., 2017a): a) Madura Province section; b) Western Coompana Province; c) Eastern Coompana Province

d)

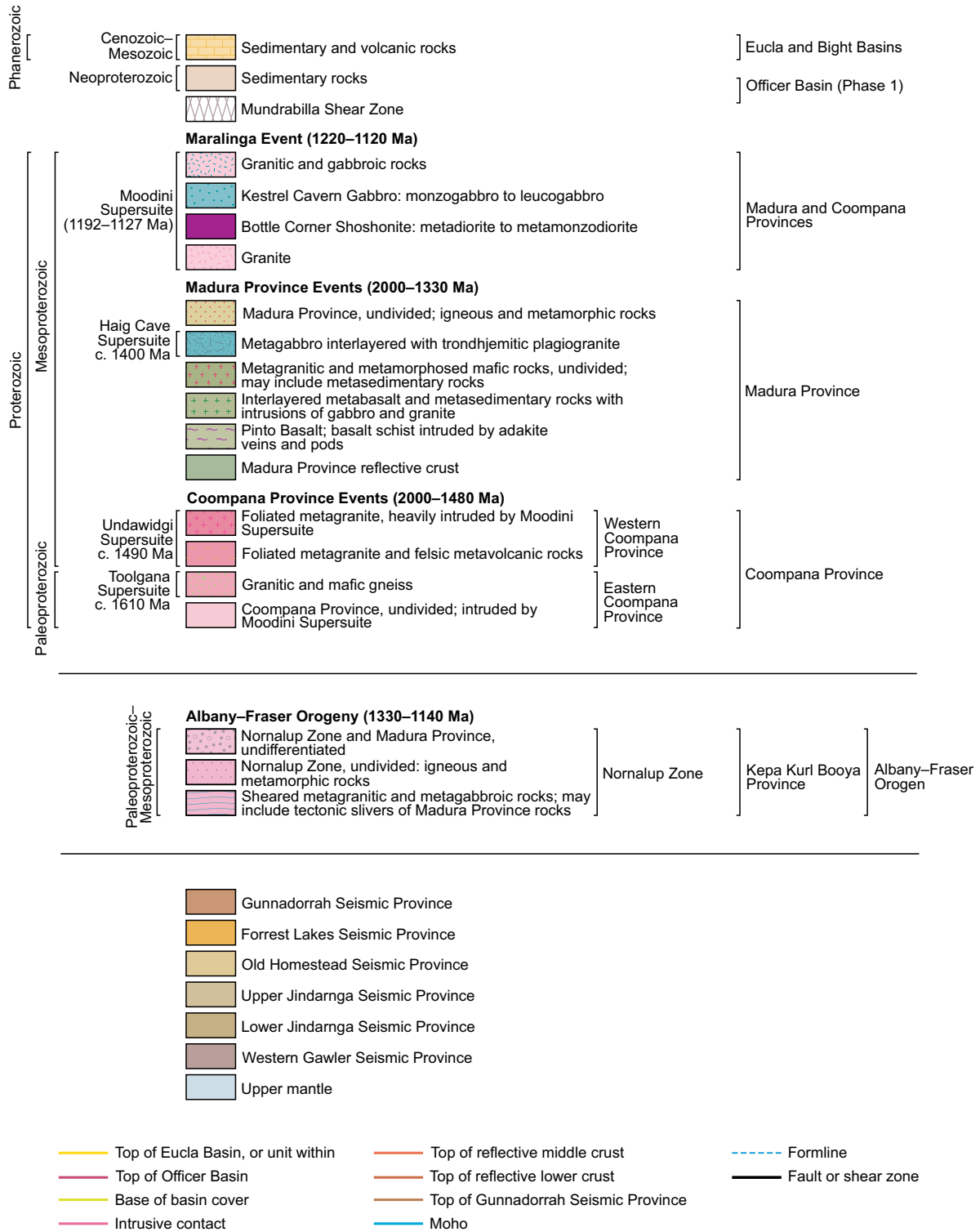


Figure 10. Continued: d) reference for interpreted sections

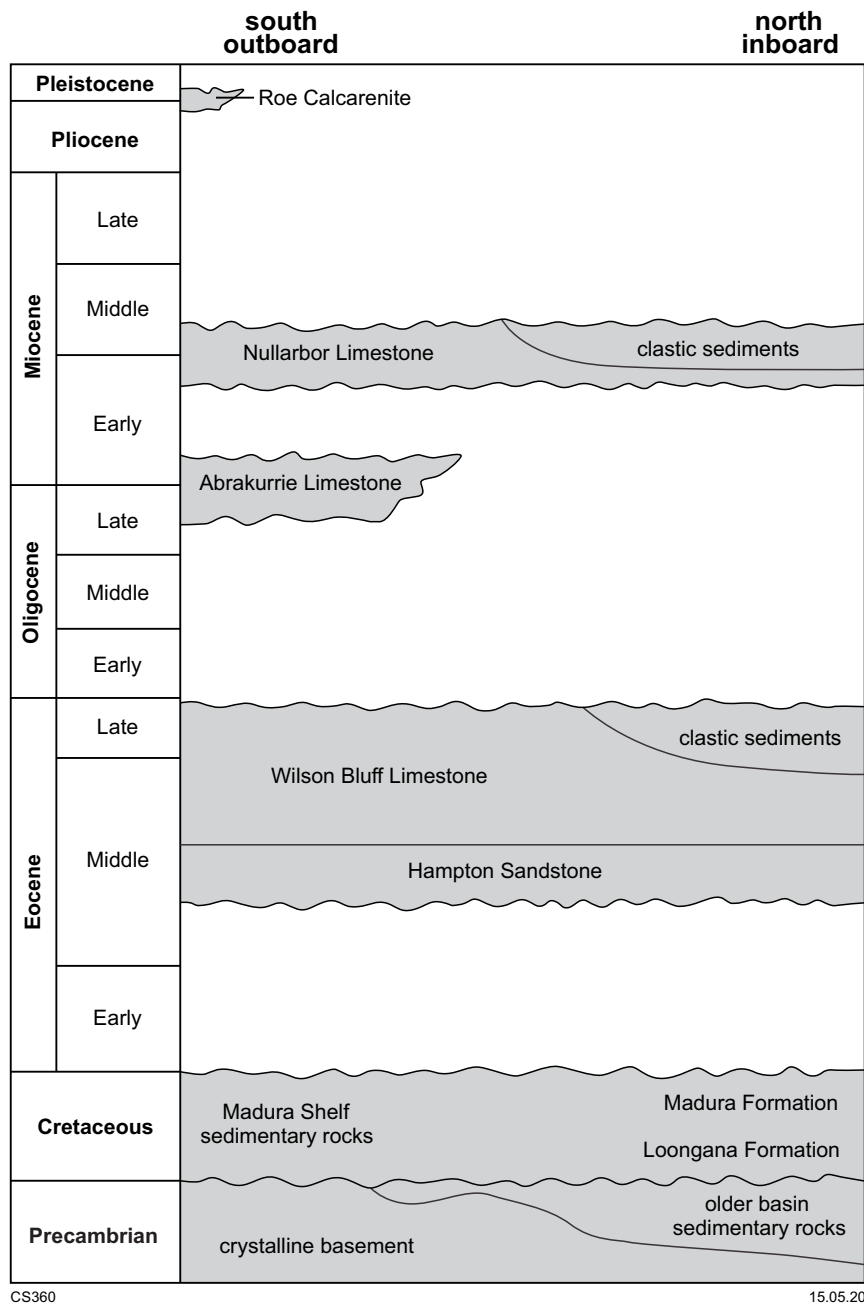


Figure 11. Stratigraphic chart of the cover rocks in the region, with emphasis on the Eucla Basin sedimentary successions (Eocene to Miocene carbonate units). After Mounsher (2016) modified from O’Connell et al. (2012)

Cover sequences

This section provides a brief overview of the cover rocks. In Western Australia, the onshore basin cover is up to 500 m deep and comprises a Cretaceous succession dominated by dark carbonaceous shale, siltstone and minor sandstone (Madura and Loongana Formations, Bight Basin), overlain by a succession of Eocene limestones (Wilson Bluff and Nullarbor Limestones, Eucla Basin; Figs 11–13; Lowry, 1970; Barham et al., 2015; Reynolds, 2016). To the north, in drillhole FOR010, a previously unknown sandstone unit was intersected below the Loongana Formation and named the Decoration Sandstone (Reynolds, 2016). Another new unit, Shanes Dam Conglomerate, was discovered in drillcore HDDH001

from the Haig prospect (Fig. 3; Reynolds, 2016). Both units disconformably underlie the Cretaceous sequence and attest to the complexity of the basement–cover interface. The base of the Madura Formation is marked by local anomalism, of which the Loongana Formation and Shanes Dam Conglomerate are representative, and their deposition may have been controlled by fault growth associated with Cretaceous rifting during the separation of Australia and Antarctica. These faults likely correlate with faults interpreted in present-day offshore seismic profiles (Barham et al., 2015).

The upper age limit of Shanes Dam Conglomerate is constrained by the overlying Early Cretaceous Madura Formation. A maximum depositional age is provided by the major detrital zircon age component in Shanes Dam

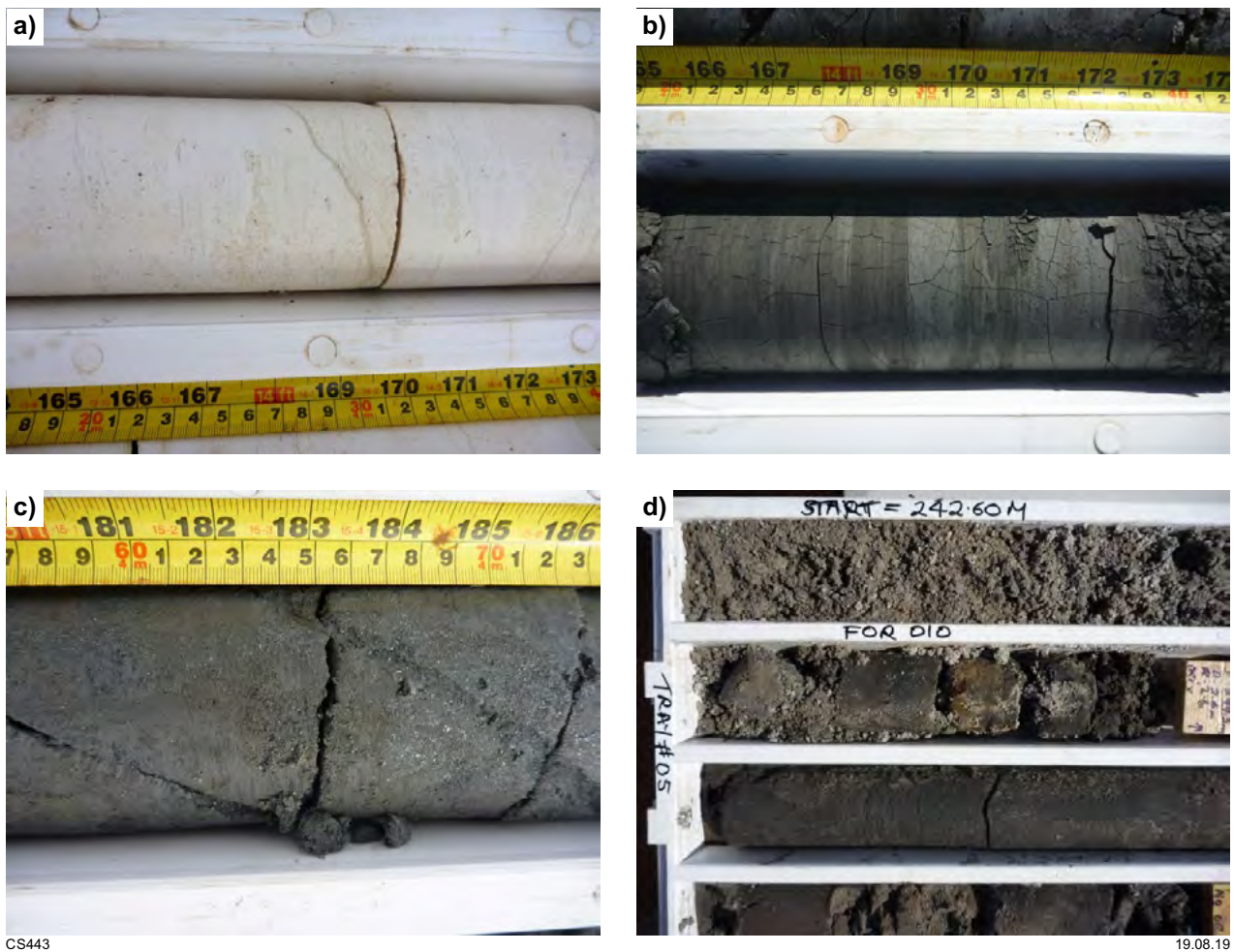


Figure 12. Photos of drillcores from the cover rocks (PQ core width 85 mm): a) typical example of Wilson Bluff limestone, drillcore FOR004; b) typical dark carbonaceous shale of the Madura Formation, drillcore FOR004; c) typical micaceous siltstone of the Madura Formation, drillcore FOR004; d) unconsolidated sand interlayered with dark siltstone, Loongana Formation, drillcore FOR010

Conglomerate at c. 1400 Ma (GSWA 199456; Reynolds, 2016), which matches the age of the underlying Haig Cave Supersuite basement rocks in the same drillcore (HDDH001, including metatonalite veins dated at 1400 ± 11 Ma [GSWA 192560] and 1397 ± 9 Ma [GSWA 192561]; Wingate et al., 2018a,b). The age of the Decoration Sandstone is also constrained by the overlying Early Cretaceous strata, in this case the Loongana Formation, and dating of detrital zircons in the Decoration Sandstone yielded two major age components of 1600–1700 Ma and 1100–1200 Ma (Reynolds, 2016). Although no fossils are present in the drillcore, the presence of bioturbation indicates a Paleozoic age. The Decoration Sandstone is assigned to the Officer Basin (Phase 2).

In the vicinity of the stratigraphic drillholes, the cover sequence typically comprises limestone between about 150 and 200 m thick, with a hard, chalky layer at the top that is about 10–20 m thick. A thin layer of sandstone (up to about 20 m) locally occurs at the base of the limestone sequence (Fig. 13). This is underlain by dark shale and laminated siltstone and, locally, carbonaceous sandstone of the Madura Formation, typically between 150 and 200 m thick. Below the Madura Formation is a 10–50 m-thick sandstone succession that is locally conglomeratic (Loongana Formation). Weathered

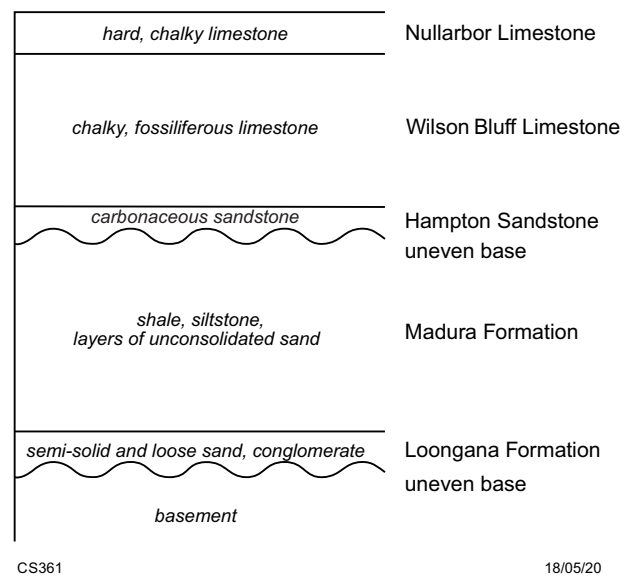


Figure 13. Schematic diagram showing the main lithologies of the cover successions encountered during the stratigraphic drilling program

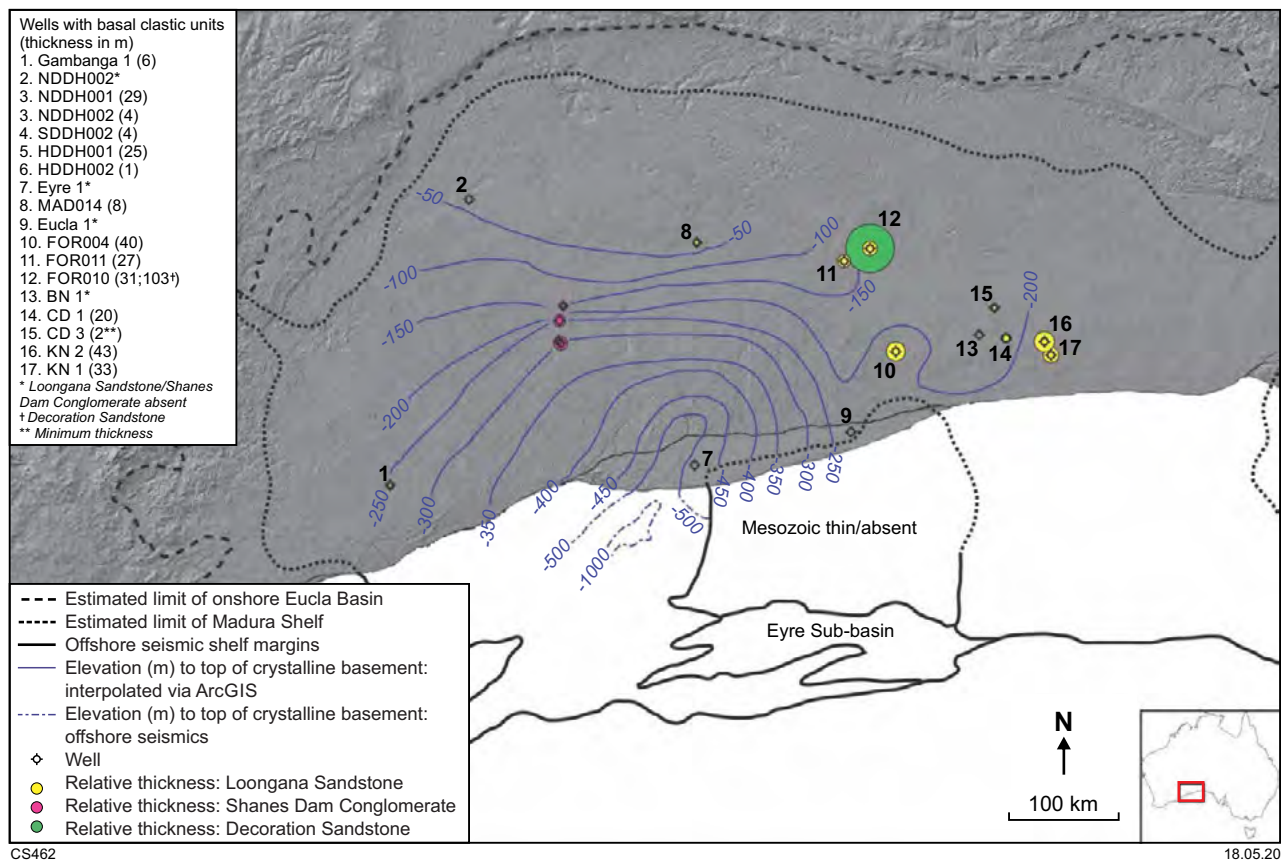


Figure 14. Surface elevation map of crystalline basement and basal clastic sediments of the Madura Shelf. Dots represent the relative total sediment thickness above basement derived from the available borehole data. Contours represent the crystalline basement surface and are plotted in metres relative to the Australian Height Datum. Modified from Barham et al. (2015)

basement occurs below this and in the past would have formed an uneven surface topography on which the basin sediments were deposited. Fresh crystalline basement rock occurs below a few metres of the weathered horizon. Estimated depth to basement at a regional scale and thicknesses of the overlying clastic units are shown in Figure 14; estimated thicknesses for the Madura Formation are shown in Figure 15.

Lithological, petrographic and structural analysis of the stratigraphic drillcores

This section provides detailed information from the basement components of each of the eight stratigraphic drillcores and is divided into drillcores from the Madura Province, followed by drillcores from the Coompana Province. The stratigraphic units were determined on the basis of results from geochronology and whole-rock geochemistry, as well as observations of contacts and crosscutting relationships. Detailed logs and structural data are provided in Appendix 2, and a petrographic report is provided in Appendix 5. It is worth noting that not all thin sections were cut perpendicular to the foliation, so do not necessarily show microstructural information well. This particularly relates to geochemistry and geochronology samples and some of the samples to investigate sulfides. In addition, the petrographic report was written without

the benefit of the petrographer being able to observe the drillcores or hand samples due to time constraints. Magnetic susceptibility measurements were collected during initial logging on site and are provided in Appendix 6.

The eight stratigraphic drillcores were oriented during drilling using a Reflex orientation kit. Orientation lines and metre marks were completed at the Perth Core Library by ensuring continuity of the drillcore and orientation marks between three drill rods was achievable. Each rod was 3 m long. Where this was not possible, no orientation line was marked and this is noted in the logs in Appendix 2. The drillcores were laid out on sections of angle iron so the orientation lines could be drawn accurately. Structural measurements were taken from the oriented drillcores (Appendix 2) by re-orienting chosen lengths of drillcore in a sandbox to their drilled position, taking note of the results of the gyro surveys (see section Drillsites and Appendix 1). Structural features were measured with a geological compass, similar to taking measurements from outcrops in the field. This method has the benefit of permitting structural analysis and visualization during logging (Holcombe, 2016).

Madura Province drillcores

The three GSWA stratigraphic drillcores in the Madura Province were located to sample distinct geophysical domains, away from existing exploration drillholes so as to maximize the sampling of completely unknown units (Fig. 3).

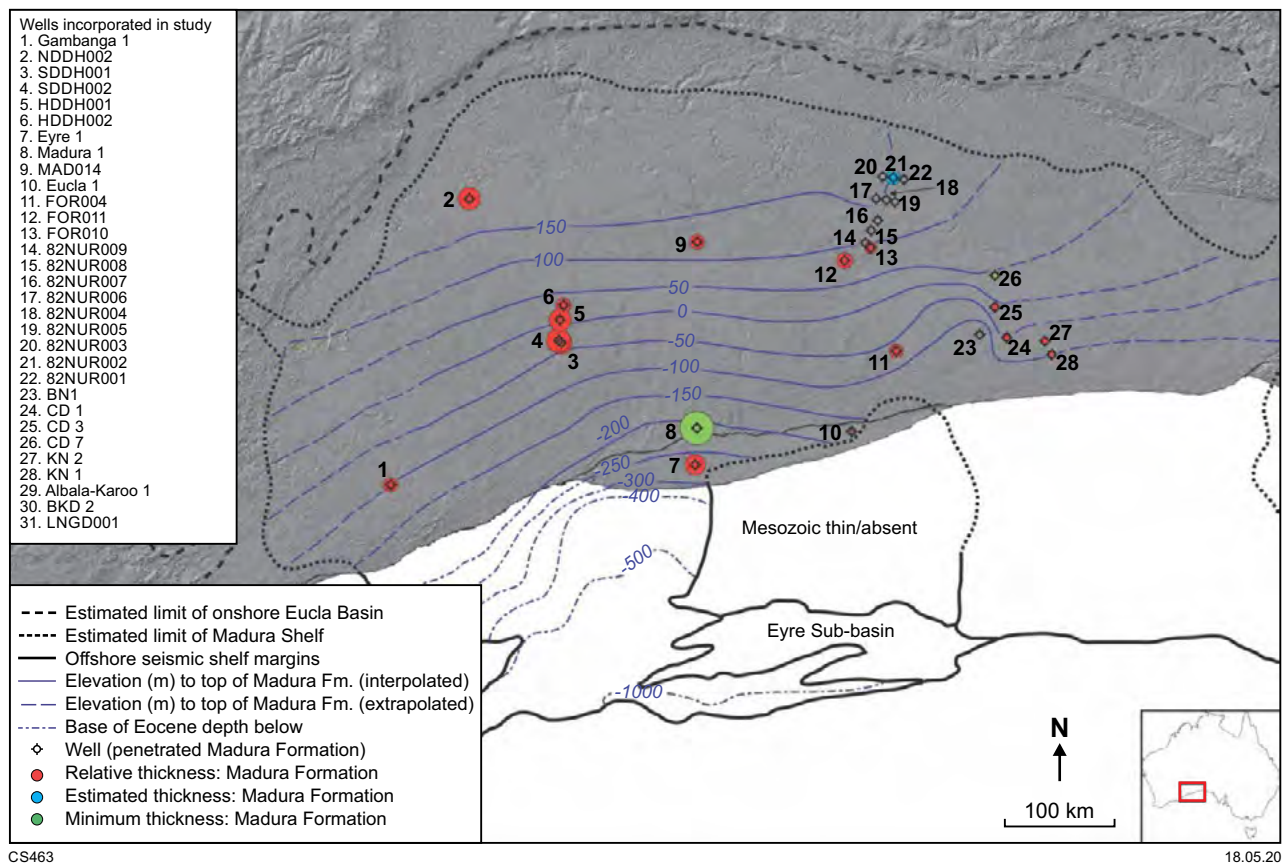


Figure 15. End-Cretaceous sediment surface and thickness map of the Madura Shelf. Dots show the relative thickness of the Madura Formation. Contours represent the top of the Madura Formation, which is the top of the known Cretaceous sediments on the Madura Shelf, and are plotted in metres relative to the Australian Height Datum. Modified from Barham et al. (2015)

Stratigraphic drillcore MAD002

Drillhole MAD002 was located to intersect an area of moderate gravity response and a curving, generally north-to northeast-trending, locally folded, striated magnetic fabric (Figs 16, 17). These rocks are imaged in the merged seismic lines 12GA-AF3 and 13GA-EG1 as a west-dipping package within the hangingwall of the Rodona Shear Zone, lying structurally above the main occurrences of the Haig Cave Supersuite represented at the Haig, Serpent and Loongana prospects (Figs 3, 10; Spaggiari et al., 2014, 2017a). The MAD002 drillcore comprises two main lithologies: 1) fine-grained (average 1–2 mm), variably coloured, distinctly laminated to layered, foliated mafic amphibolite schist; 2) medium-grained, generally pale grey to white, thin leucogranite veins. The leucogranite is part of the Haig Cave Supersuite and intrudes the fine-grained amphibolite, the Pinto Basalt.

Pinto Basalt

The mafic amphibolite schist has distinct millimetre-scale laminations to centimetre-scale layering (Fig. 18a,b). It comprises assemblages of blue-green hornblende–plagioclase–titanite (locally replacing ilmenite), typically with variable proportions of epidote, biotite and quartz, and locally with ilmenite, rutile and magnetite (Fig. 18c,d). Sulfide minerals are described in a separate section below. The assemblage blue-green hornblende–epidote–oligoclase–quartz–biotite–ilmenite–magnetite is likely to record a lower amphibolite facies metamorphic peak, with

very minor indications of retrogression. The amphibolite is interpreted to have a basalt protolith based on its fine grain size and distinct laminated to layered texture.

Although speculative, the metabasalt could further be interpreted as a tuff of mafic composition, with the fine-grained, differentiated layering and laminations formed as an ash-fall sequence, possibly in a shallow-marine setting (see Appendix 5).

Haig Cave Supersuite

The leucogranite is composed of plagioclase–quartz–biotite, locally with hornblende and magnetite, and minor chlorite, and has the geochemical composition of adakite (see section Whole-rock geochemistry of Madura Province rocks). It occurs as intrusive veins that are generally parallel to the main fabric in the metabasalt, but also locally crosscut the folded layering (Figs 18b, 19a).

Sulfides and alteration

Sulfides are present in minor amounts throughout much of the core and in both metabasalt and leucogranite. They occur as disseminated grains (Fig. 19b), in stringers and veins with similar minerals to the host rocks, and along fracture fillings. The veins are generally millimetre scale and cut the fabrics in both units (Fig. 19c). Some veins include calcite and chlorite and may be younger, lower temperature veins. Thin veins are locally associated with small brittle faults, with offsets of a few millimetres to a few centimetres.

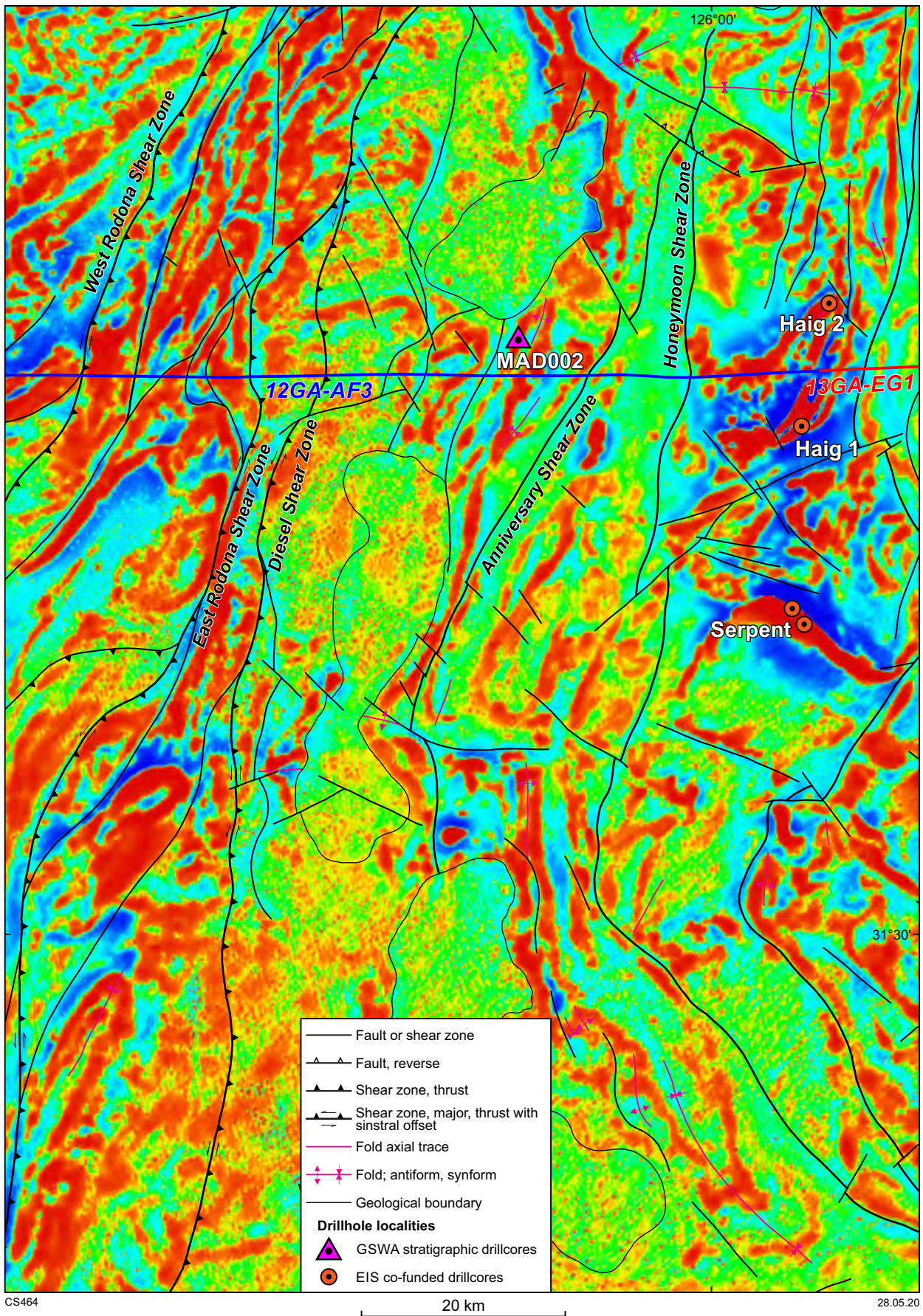


Figure 16. Aeromagnetic image showing the striated features in the vicinity of the MAD002 drillhole, and interpreted structures as shown in Figure 17. The locations of the deep crustal seismic reflection lines are also shown

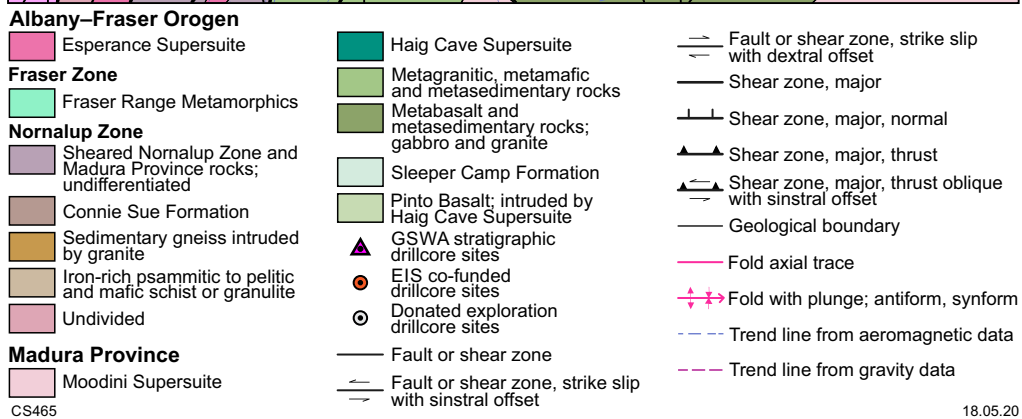
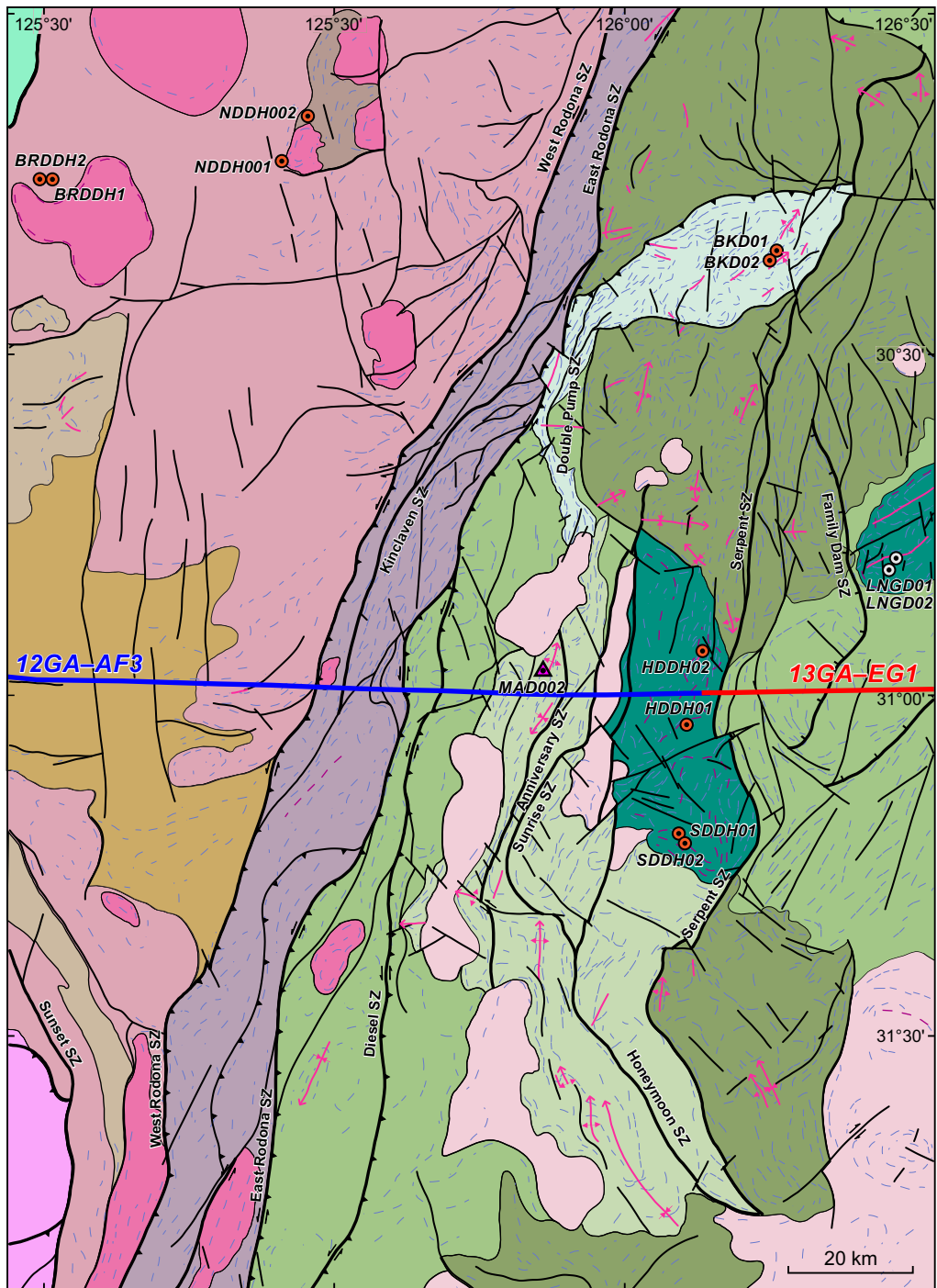
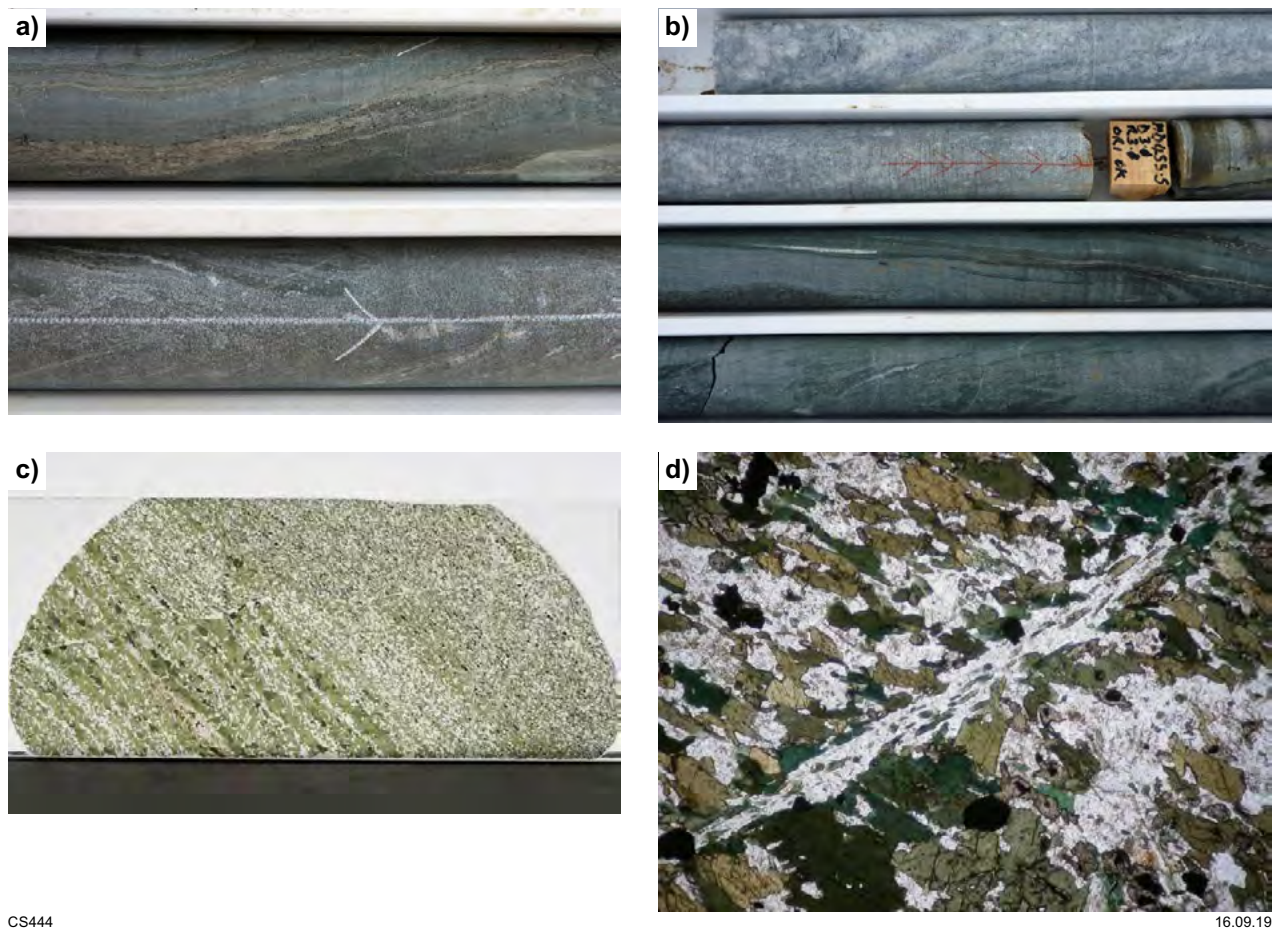


Figure 17. Interpreted bedrock geology and structures in the vicinity of the Rodona Shear Zone and the MAD002 drillhole, including the area shown in Figure 16 (modified from Spaggiari, 2016). The locations of the deep crustal seismic reflection lines are also shown. Abbreviation: SZ, shear zone



CS444

16.09.19

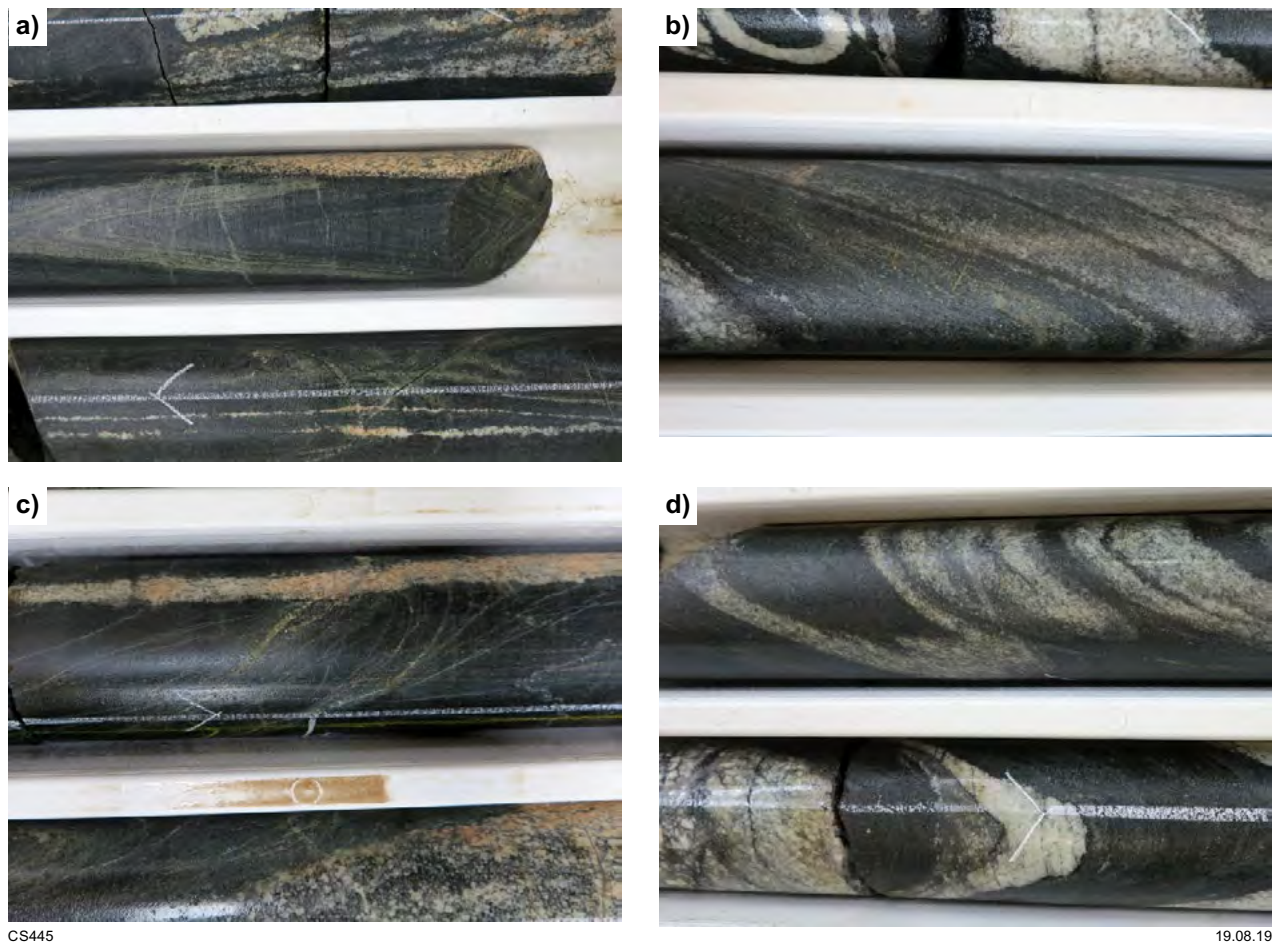
Figure 18. Photos of the drillcore MAD002 (HQ core width 63.5 mm): a) typical variably coloured fine layering in the metabasalt, photographed dry; b) layered, chlorite-rich metabasalt and leucogranite veins, photographed wet; c) entire thin section of faulted, layered amphibolite (GSWA 216208). Hornblende is pleochroic from olive-brown to deep green. One layer contains abundant dark tan biotite. The colourless mineral is plagioclase, with subordinate quartz. A fault with a 10 mm displacement cuts the layering obliquely. Height of slide is 26 mm; d) plane-polarized light photomicrograph from near the top right in c). The fault that displaces the layering contains plagioclase and green hornblende similar to the layered host rock, indicating that it was present at the metamorphic peak. The roughly octahedral opaque grains are magnetite, and the tiny opaque grains included in titanite are ilmenite of probable igneous origin. Field width 3.5 mm

Some of the veins contain similar minerals to the host metabasalt, suggesting they formed at similar metamorphic conditions.

The disseminated sulfides comprise anhedral pyrite (probably retrogressed pyrrhotite), variably pyritized pyrrhotite, and chalcopyrite. Stringers comprise pyrite, hornblende, titanite and minor anhedral chalcopyrite. One example of veinlets in the metabasalt (GSWA 206767, 435.48 – 435.59 m) comprises plagioclase–biotite–pyrite–chalcopyrite–titanite–magnetite, interpreted to have been present at the metamorphic peak. Another example (GSWA 206769, 457.73 – 457.88 m; 15 cm, ½ HQ core, 1147 ppm Cu) comprises sericitized plagioclase, blue-green hornblende and tan biotite concentrated along the vein walls, and minor chlorite. Anhedral <1.5 mm pyrite, forming about 3% of the vein, is commonly rimmed with or partly surrounded by <0.1 mm granular magnetite and anhedral chalcopyrite. Chalcopyrite also forms a veinlet in a coarse, unaltered hornblende crystal with no associated retrogression. GSWA 206769 is similar to metabasalt GSWA 206770 (458.29 – 458.46 m; 17 cm, ½ HQ core, 2146 ppm Cu), which comprises sericitized plagioclase-rich veins and quite strong pyrite–chalcopyrite mineralization.

Structural analysis of the MAD002 drillcore

The metabasalt layering and thin leucogranite veins are folded into steeply northeast to vertically plunging, tight chevron and typically Z- or S-folds (F_2 ; Fig. 19a) that in the metabasalt have a hornblende-bearing, axially planar foliation (S_2). Together, the foliation and the layering define the main fabric in the metabasalt (S_1), which has a predominant, steep northwest or southeast dip (Appendix 2). Small-scale refolded folds imply an older phase of (F_1) folding (Fig. 19d). Stereonet analysis of a best-fit great circle, calculated from poles to planes of the main fabric, yields a calculated fold axis of 86° towards 356° (Fig. 20). Fitting an axial plane to the poles gives an orientation of 86° towards 029° (dip, dip direction), and the interlimb angles indicate an open fold. The calculated open fold is inconsistent with the tightness of observed F_2 folds, so the stereonet analysis could indicate that the F_2 folds were refolded into an open, west-northwesterly trending, larger scale (F_3) fold. Alternatively, the spread of the poles may simply be due to the anastomosing fabric, and the S- and Z-geometry of the F_2 folds. However, large-scale, west-northwesterly trending open folds interpreted in aeromagnetic data support the interpretation of F_3 folds in the stereonet data (Figs 16, 17).



CS445

19.08.19

Figure 19. Photos of the drillcore MAD002 (photographed wet, HQ core width 63.5 mm): a) leucogranite vein crosscutting epidote-rich folded layering; b) disseminated pyrite, pyrrhotite, and chalcopyrite in metabasalt with leucogranite veins; c) pyrite and chalcopyrite stringers in metabasalt; d) refolded folds within leucogranite veins and metabasalt layering

Although the folds are observed in both the metabasalt layering and the leucogranite veins, thin leucogranite veins also locally crosscut the fabric and F_2 folds (Fig. 19a). This suggests the leucogranite veins intruded either pre- or syn-folding. The preferred interpretation is that the veins intruded during the same event as the folding, with late injections or remobilization of felsic material as the folds formed. This would also likely be during peak metamorphism and formation of the hornblende-bearing, axially planar S_2 foliation.

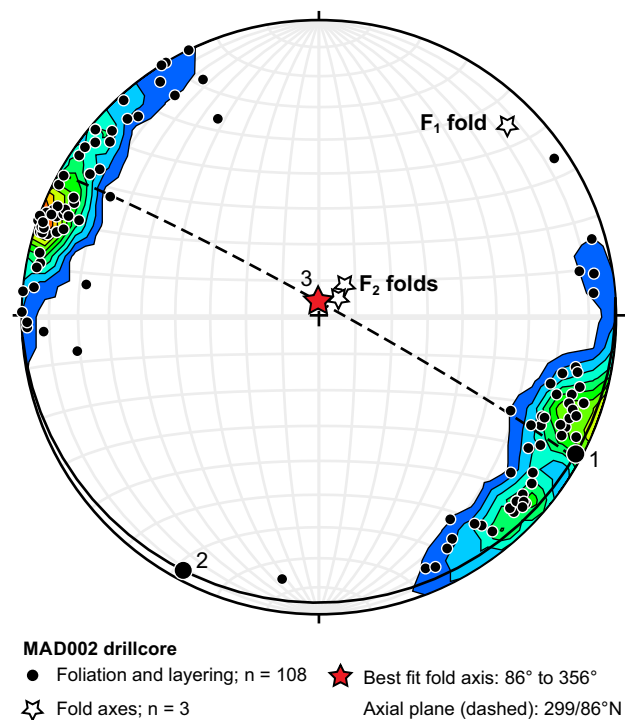
Stratigraphic drillcore MAD011

Drillhole MAD011 was located to intersect a large, triangular-shaped area of strong magnetic intensity and high gravity response that is drawn into the Mundrabilla Shear Zone with sinistral shear sense (Fig. 3). The drillsite was located just south of a northwest-trending fault that is visible in magnetic data (Fig. 21). The location is situated close to the Trans-Australian Railway and seismic line 13GA-EG1. The interpretation of the seismic profile indicates that the strong magnetic and gravity anomaly intersected by the MAD011 drillhole has an apparent antiformal geometry that is cut by the Lynch and Laundry Shear Zones, which are interpreted as extensional structures (Fig. 10a; Spaggiari et al., 2017a). The MAD011 drillcore comprises two main lithologies: 1) medium- to coarse-grained (average 3–10 mm) ferro-monzogabbro, which grades to a very coarse-

grained (average 10–15 mm), plagioclase-rich pegmatitic leucogabbro; 2) fine-grained (average 1–2 mm), layered to laminated, locally foliated mafic rock (Fig. 22). The fine-grained mafic rock is the Narilya Bore Basalt, which occurs as inclusions within the intrusive monzogabbro, the Kestrel Cavern Gabbro.

Narilya Bore Basalt

The Narilya Bore Basalt occurs as inclusions that are centimetre- to metre-scale, with the thickest occurrences below about 585 m in the drillcore. Their texture is highly variable, ranging from massive to layered, or laminated. The layering is typically anastomosing and is locally openly folded. The metabasalt contains orthopyroxene, clinopyroxene, plagioclase, hornblende and biotite with accessory ilmenite and magnetite, and locally disseminated pyrite and chalcopyrite. In thin section, the texture is typically granoblastic, although a weak foliation is locally defined by brown hornblende and red-brown biotite. Plagioclase is calcic with an optically estimated composition between An_{63} and An_{70} . The layering is typically defined by variation in pyroxene type and abundance. The metabasalt could be a mafic hornfels (i.e. a hornfelsed basalt), possibly up to granulite facies, with metamorphism due to the intrusion of the Kestrel Cavern Gabbro. Where present, the foliation is variably orientated, interpreted to reflect the occurrence of the metabasalt as rafts or inclusions within the monzogabbro.



CS362

18/05/20

Figure 20. Equal area stereonet analysis of structural measurements from oriented drillcore MAD002, showing poles to foliation and their contours, calculated fold axis and axial plane, and measured fold axes

Kestrel Cavern Gabbro (Moodini Supersuite)

The Kestrel Cavern Gabbro is an undeformed, medium- to coarse-grained quartz monzogabbro that locally grades into very coarse, blocky, pegmatitic gabbro. The quartz monzogabbro typically has a cumulate texture, with subhedral to euhedral plagioclase that is dark and greenish, or pale grey to white. Locally, white plagioclase is more abundant in gradational subhorizontal layers up to about 15 cm thick (Fig. 22b).

The quartz monzogabbro contains clinopyroxene (locally retrogressed to green hornblende), orthopyroxene (locally retrogressed to cummingtonite), plagioclase, biotite and quartz, with accessory magnetite, ilmenite, titanite and locally abundant prismatic apatite. Plagioclase composition is optically estimated to be An_{43-52} . Myrmekite and microcline occur locally. Magnetite and ilmenite are rimmed with titanite, which has locally completely replaced them. Minor, thin leucogabbro veins locally contain pyrite and chalcopyrite (Fig. 22e). The very coarse, blocky, pegmatitic gabbro is dominated by euhedral, variably coloured plagioclase up to 15 mm in size, together with quartz and mafic clots (Fig. 22a).

Stratigraphic drillcore MAD014

Drillhole MAD014 is located in the centre of an elongate, northeasterly trending area of low gravity response and low- to moderate-response magnetic fabric, cut by splays off the Mundrabilla Shear Zone (Fig. 21). This

location was, in part, chosen to test whether basement rocks intruded by Haig Cave Supersuite gabbroic and granitic rocks of the Loongana prospect were present; however, this was not achieved as only younger rocks were encountered.

The MAD014 drillcore comprises unfoliated, mesocratic, medium- to coarse-grained, equigranular biotite-hornblende granodiorite to monzogranite (Fig. 23). The typical assemblage is plagioclase, microcline, quartz, biotite, titanite and possibly allanite and locally, hornblende and fluorite. This is intruded by fine- to medium-grained, equigranular, biotite monzogranite to syenogranite, commonly with 1–10 cm-thick pegmatite margins and similar assemblages to the coarse-grained host. The granites are cut by minor quartz or quartz-epidote veins, locally containing sulfide minerals (Fig. 23c,d). Both granites are assigned to the Moodini Supersuite. These granites appear to be undeformed, even though they occur within the regional, northeasterly trending magnetic fabric. It is feasible that the margins of the elongate magnetic zone are deformed but the centre is not.

Coompana Province drillcores

The five GSWA stratigraphic drillcores represent the first diamond drillholes to reach basement in the Western Australian part of the Coompana Province (Fig. 3). This basement was previously completely unknown, although magnetic and gravity data, acquired through the EIS, clearly showed its complexity and variability. As in the Madura Province, the drillholes were located to intersect specific geophysical regions, which are described with the drillcores below.

Stratigraphic drillcore FOR004

Drillhole FOR004 is located on an area of subtly northwesterly trending magnetic fabric of low to moderate response, and within an area of moderate gravity response (Figs 24–26). The FOR004 site is about 10 km east of a north-northwesterly trending fault, interpreted as part of a series of steeply dipping, dominantly sinistral strike-slip faults. The Eucla No. 1 petroleum well lies to the south of the FOR004 drillsite, and overlies an ovoid feature with high magnetic intensity, interpreted to be part of a distinct, northeasterly trending belt of granite intrusions truncated by, and dragged into, the Mundrabilla Shear Zone (Fig. 24). The magnetic signature is similar to intrusions with high magnetic response belonging to the Booanya Suite of the 1200–1140 Ma Esperance Supersuite in the Albany–Fraser Orogen (Smithies et al., 2015b). Cuttings of granite sampled from the base of the Eucla No. 1 petroleum well yielded a date of 1140 ± 8 Ma (GSWA 194773, Kirkland et al., 2011c), and the granite is assigned to the Moodini Supersuite.

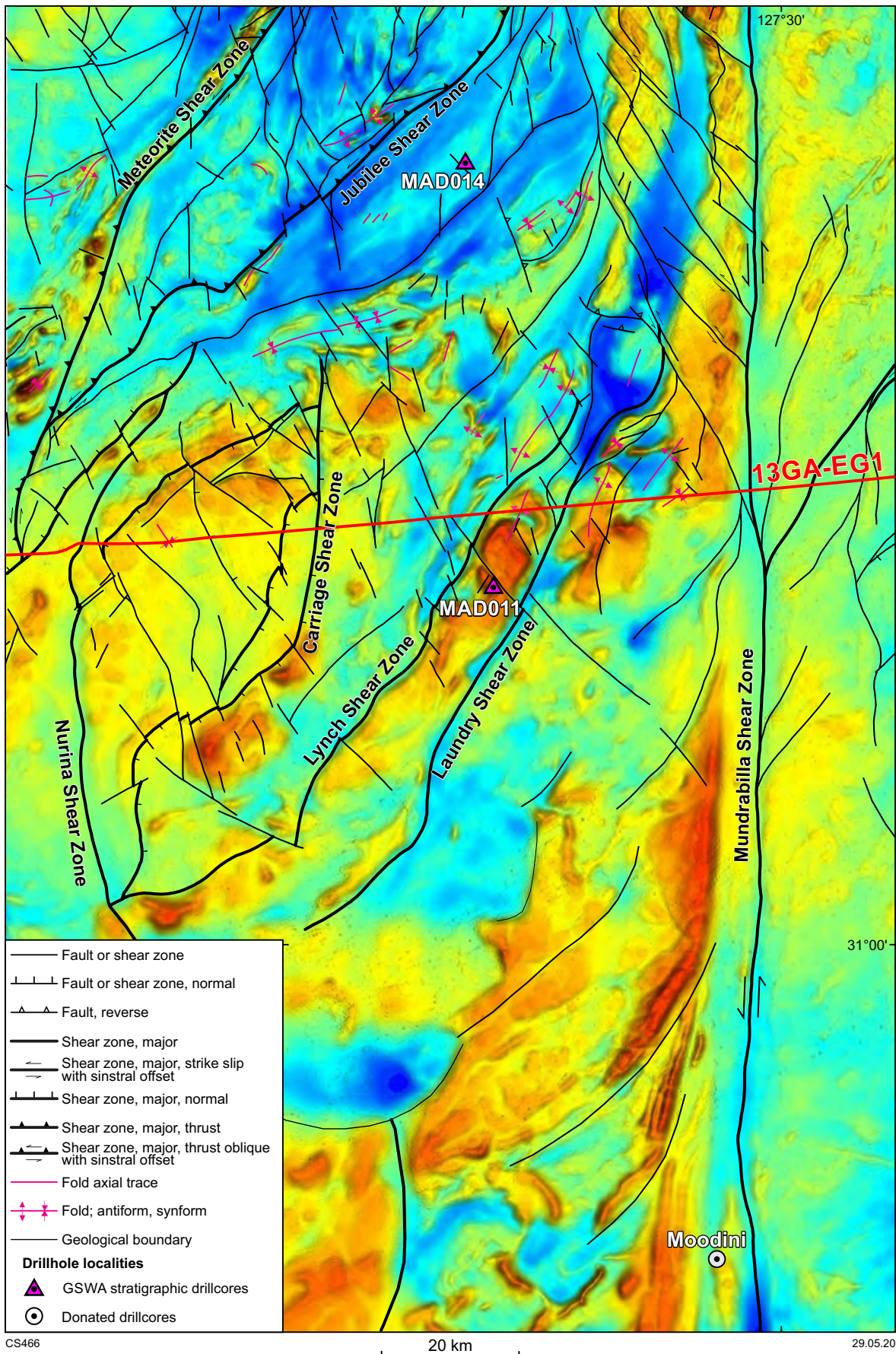


Figure 21. Pseudocolour geophysical imagery over the MAD011 and MAD014 drillsites, showing structural interpretation. Warm colours represent high intensity, cool colours low intensity: a) aeromagnetic image, with sun shading overhead

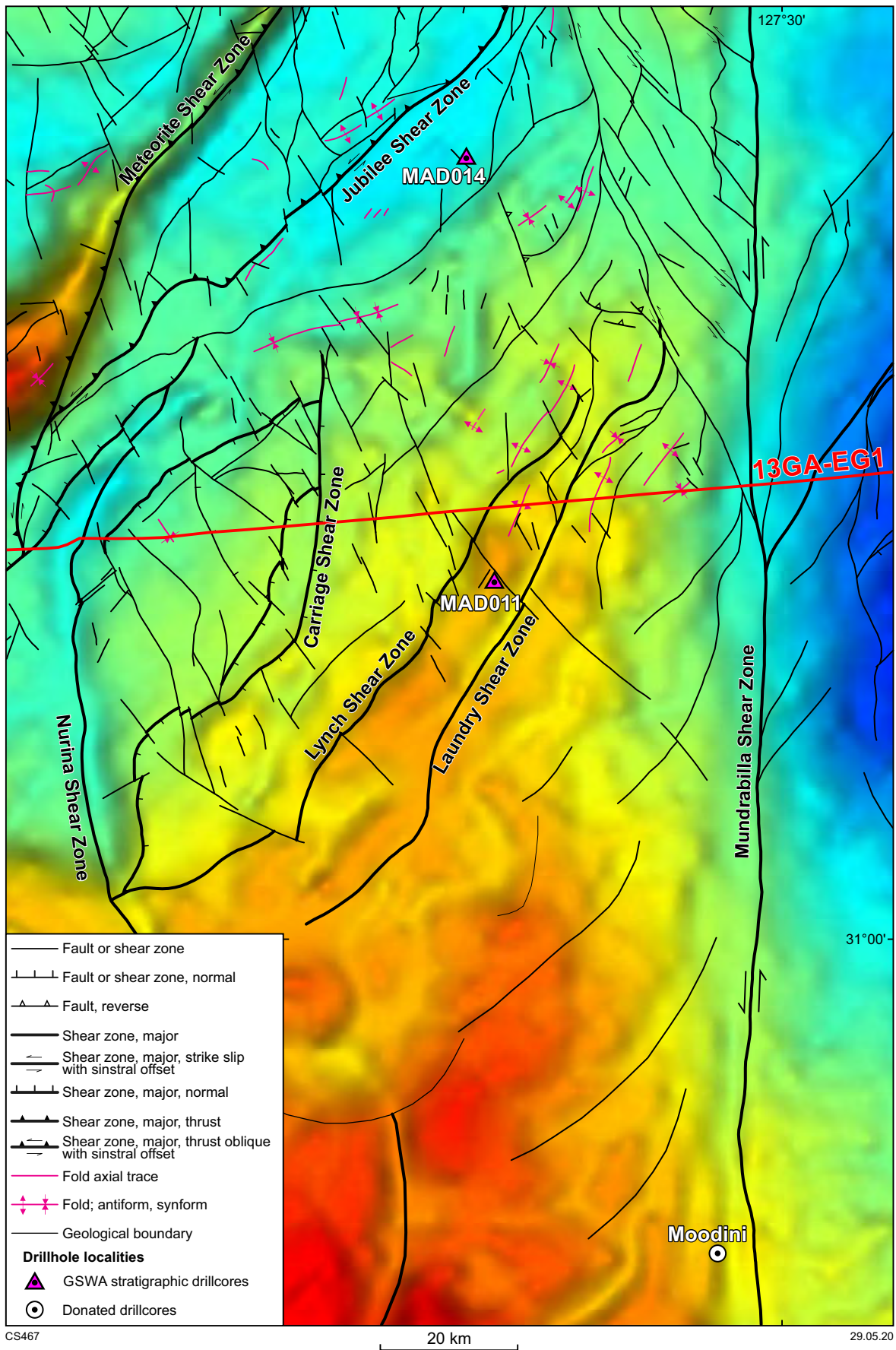
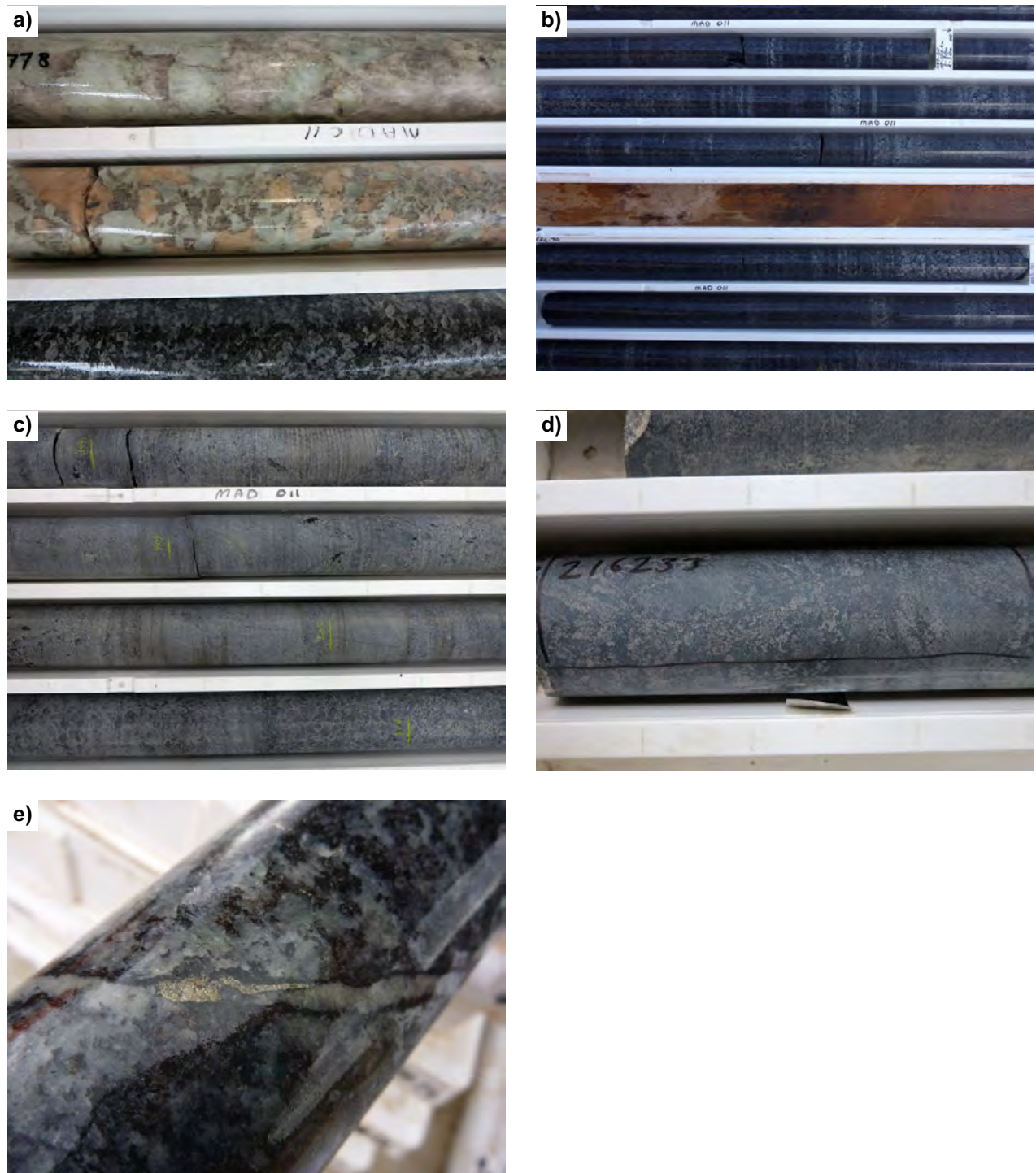


Figure 21. Continued: b) Bouguer gravity image



CS446

26.08.19

Figure 22. Photos of the MAD011 drillcore (HQ core width 63.5 mm): a) monzogabbro grading to very coarse pegmatitic gabbro, which was sampled for geochronology (GSWA 206778); Kestrel Cavern Gabbro; b) subhorizontal layering defined by white plagioclase; Kestrel Cavern Gabbro; c) Kestrel Cavern Gabbro with inclusions of variably textured metabasalt; Narilya Bore Basalt; d) metabasalt geochemistry sample GSWA 216233 showing contorted and locally disaggregated layering; e) leucogabbro vein with sulfides (pyrite and chalcopyrite) in Kestrel Cavern Gabbro

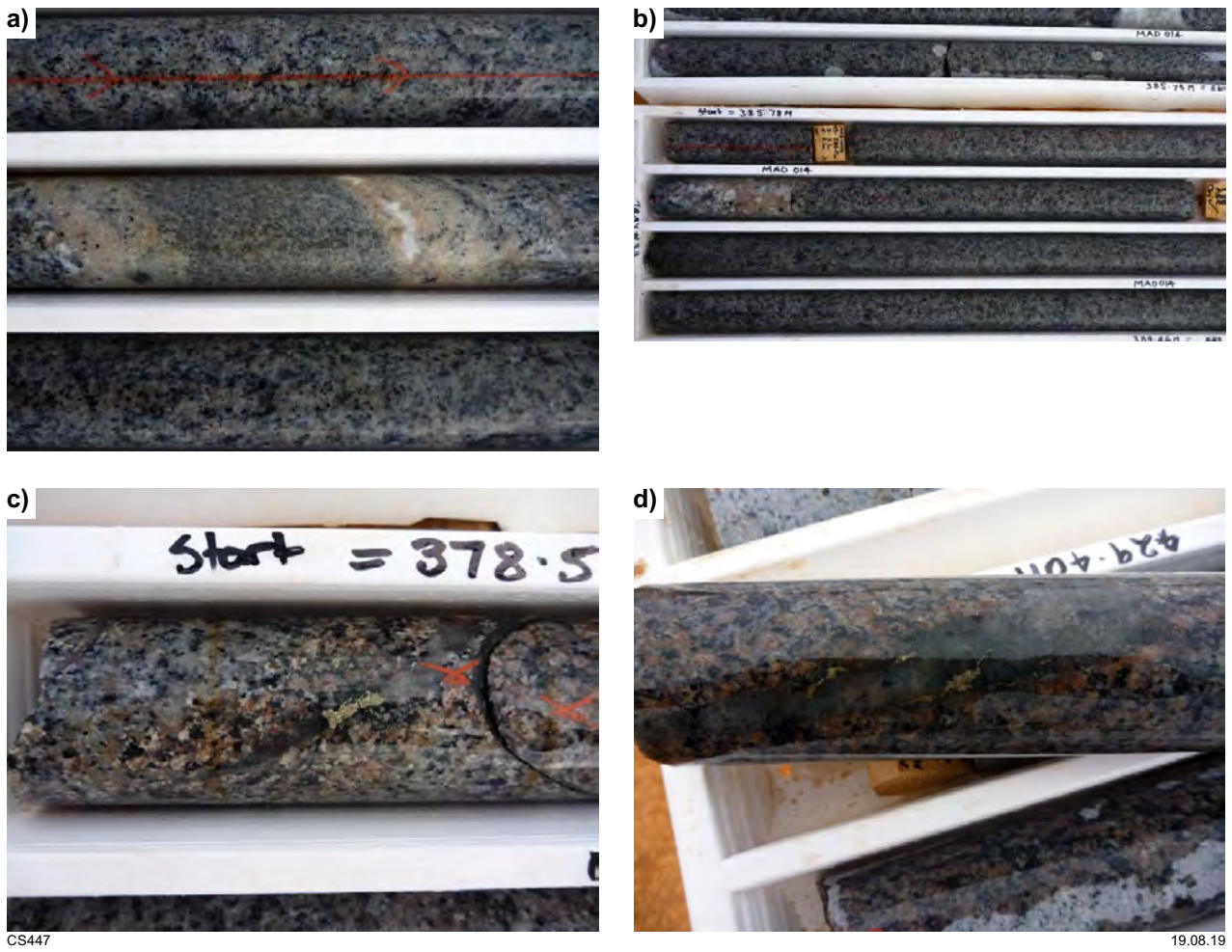


Figure 23. Photos of the MAD014 drillcore (HQ core width 63.5 mm): a) Moodini Supersuite granodiorite intruded by finer grained monzogranite vein with pegmatitic margins; b) Moodini Supersuite granodiorite to monzogranite, which makes up the bulk of this drillcore, with a pegmatitic vein; c) and d) quartz veins with sulfides

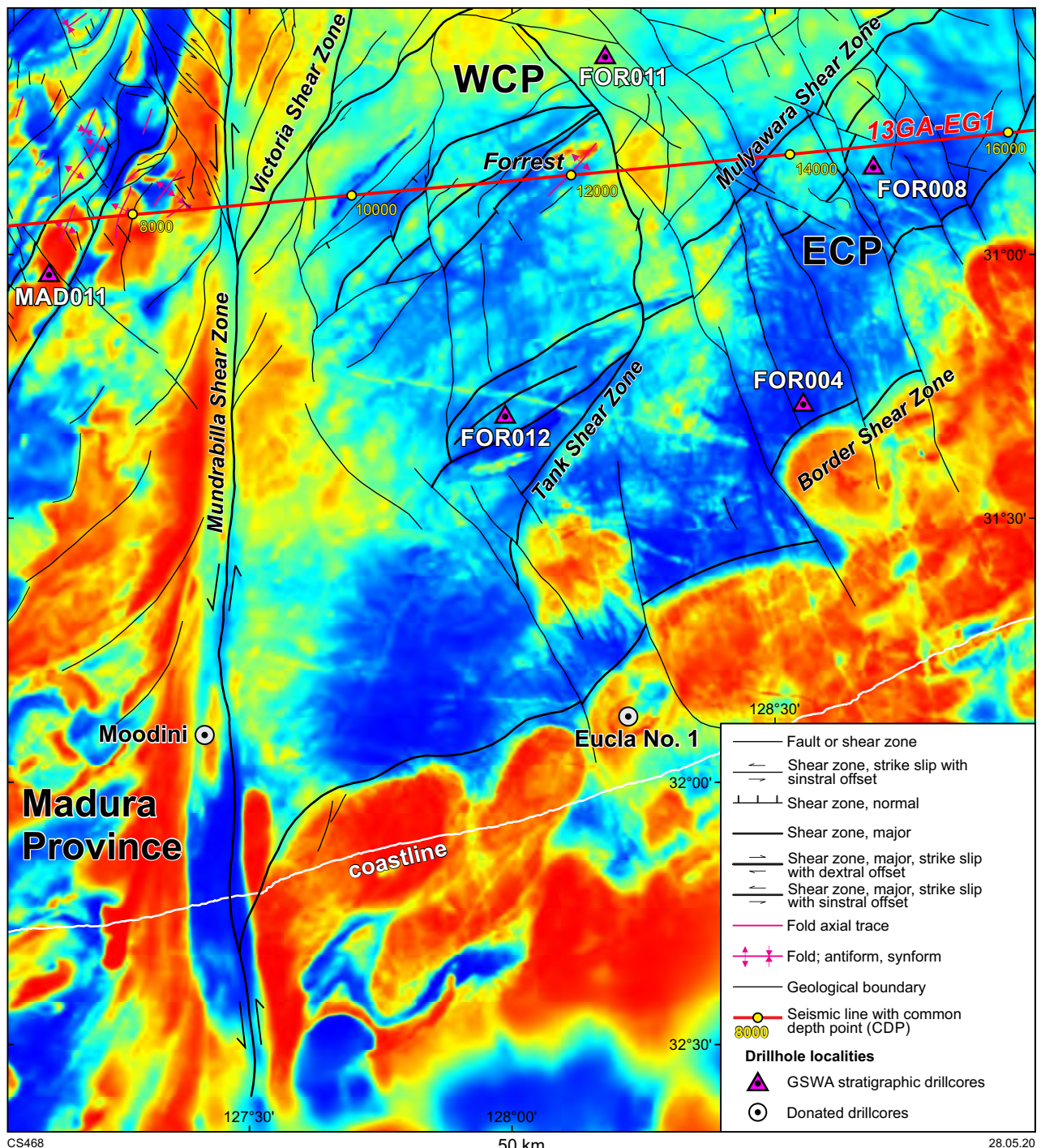


Figure 24. Reduced-to-pole aeromagnetic image over part of the Western Australian section of the Coompana Province, showing structural interpretation, drillhole locations and the position of the 13GA-EG1 seismic line. Common depth points along the seismic line are shown in yellow (see Spaggiari et al., 2017a). Warm colours represent high magnetic intensities, cool colours low intensity

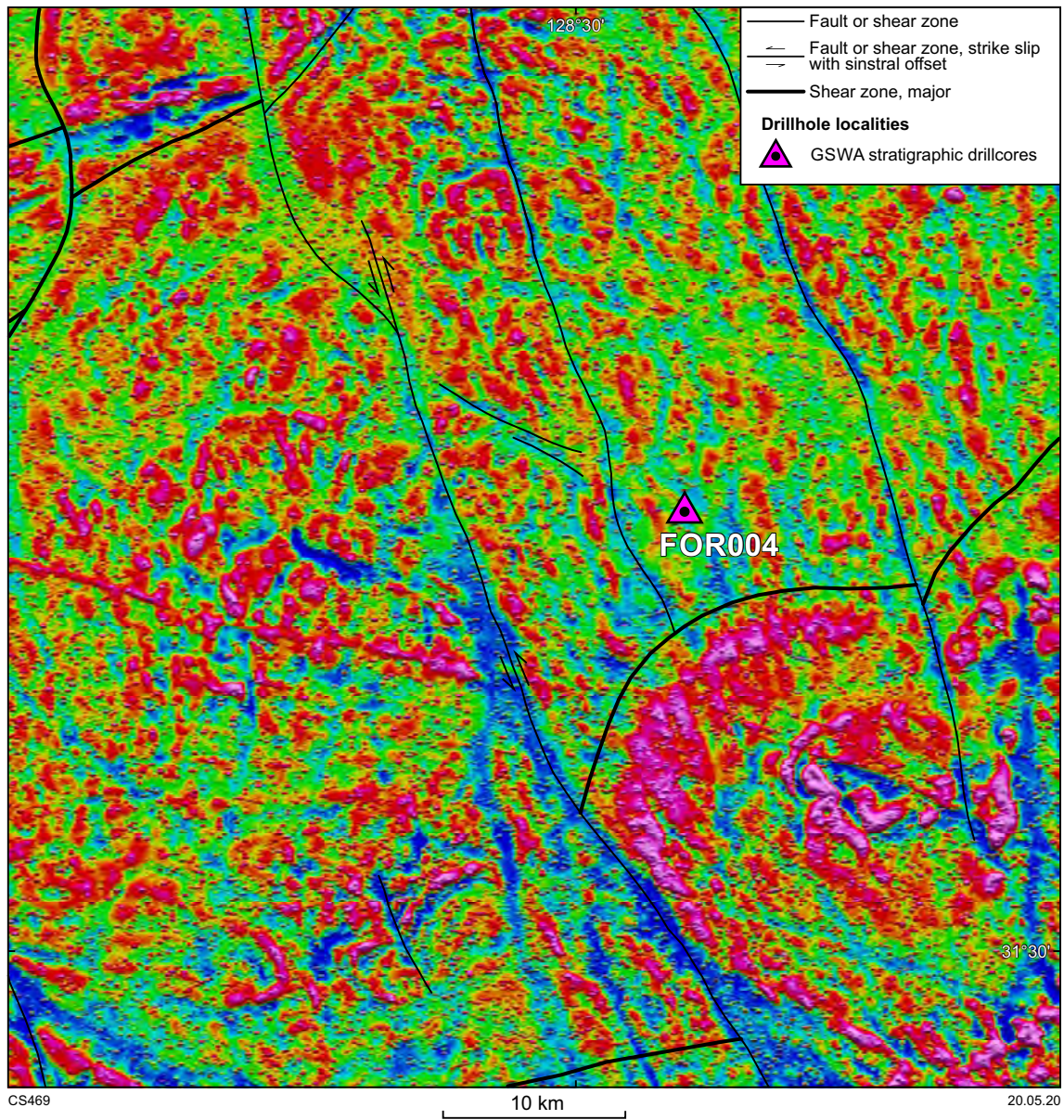


Figure 25. Reduced-to-pole, first vertical derivative aeromagnetic image of the area in the vicinity of the FOR004 drillsite showing the dominant north-northwesterly trending fabric, and major structures. Warm colours represent high magnetic intensity, cool colours represent low intensity

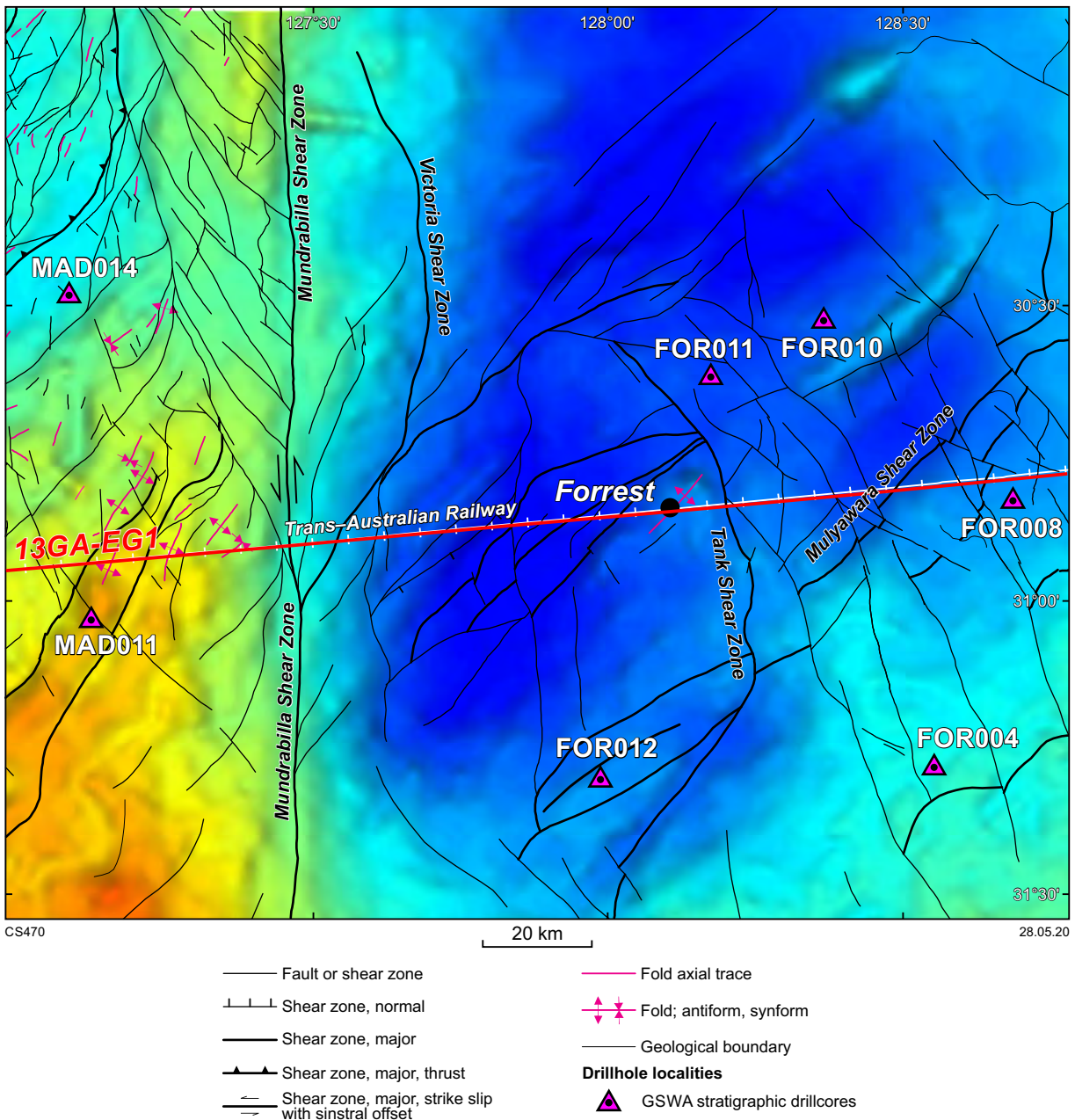


Figure 26. Bouguer gravity image of over part of the Western Australian section of the Coompana Province and far eastern part of the Madura Province, showing structural interpretation, stratigraphic drillhole locations and the position of the 13GA-EG1 seismic line. Warm colours represent strong gravity response, cool colours represent a weak response

The FOR004 drillcore comprises three main lithologies: 1) medium-grained (average 2–4 mm), mesocratic, layered granodiorite to monzogranite gneiss; 2) fine- to medium-grained (average 2–3 mm), equigranular to seriate-textured, foliated biotite-leucogranite; 3) fine- to medium-grained dioritic or mafic gneiss typically with centimetre-scale layering (Fig. 27). These rocks are assigned to the Toolgana Supersuite.

Toolgana Supersuite

Granodiorite to monzogranite gneiss dominates the FOR004 drillcore. It is distinctly layered at the centimetre scale, and has a well-developed, anastomosing and folded gneissosity. The granodiorite to monzogranite protolith is mostly equigranular, although locally porphyritic, with pink K-feldspar phenocrysts up to 2 cm long. A typical assemblage is anhedral to subhedral blocky plagioclase (An_{30-33}), anhedral orthoclase inverted to microcline, interstitial quartz, anhedral dark olive-green hornblende, anhedral to roughly tabular dark-brown biotite, and subordinate anhedral to subhedral titanite, which occurs locally with biotite in clots, locally with ilmenite cores. Minor magnetite, locally up to 4 mm, is locally interstitial to feldspar. Zircon and apatite are common accessory minerals.

The granodiorite gneiss is intruded by fine- to medium-grained, biotite-leucogranite. The leucogranite is typically pink, equigranular and moderately foliated, and includes clots, wisps or schlieren of the granodiorite gneiss host, resulting in a variably layered texture. The layering is, in part, due to metamorphism and fabric formation during deformation. The contacts between the granodiorite gneiss and pink leucogranite are mostly gradational or cusped, suggesting they were coeval, although whole-rock geochemistry indicates the leucogranite is likely an anatectic melt of the host granodiorite (see below). In the lower part of the drillcore, a fine- to medium-grained, grey, equigranular, foliated biotite-rich metagranite is likely a less layered variant of the granodiorite, as it also contains layers of the pink equigranular leucogranite. A typical assemblage of the pink leucogranite is plagioclase (oligoclase), orthoclase (or microcline), quartz, biotite, minor magnetite, titanite and sparse ilmenite.

Moderately to strongly foliated amphibolite to diorite gneiss occurs as centimetre scale to up to 1 m scale layers, and is interpreted as remnants of the host protolith intruded by the granitic rocks (Fig. 27b). These gneisses are fine to medium grained and contain plagioclase (about An_{35}), green hornblende, dark-tan biotite, minor quartz and titanite. Their assemblage and typical granoblastic texture indicate the middle to upper amphibolite facies.

Sulfides and alteration

The rocks in drillcore FOR004 locally show retrograde alteration with biotite altered to chlorite and locally sericite, and plagioclase overgrown by sericite. Muscovite flakes up to 0.2 mm occur locally with sericite. Patchy sericite and probable epidote alteration occur locally. Where present, the alteration gives the granitic rocks a pink to red speckled appearance (Fig. 27c). Hydrothermal

quartz, calcite and rare, anhedral to subhedral pale buff-pink garnets, up to 0.5 mm in diameter, are less common alteration products. The most abundant veins are thin chlorite–quartz veins that cut the foliation.

The drillcore contains only minor sulfides. A sample of granodiorite gneiss (GSWA 213829; 548.16 – 548.38 m) contains clustered chalcopyrite and sparse bornite. A second sample of granodiorite gneiss (GSWA 213834; 569.84 – 570.00 m) contains partly chloritized, anhedral biotite up to 2 mm in size, coarse magnetite, and a 1 mm anhedral grain or aggregate of chalcopyrite with biotite and plagioclase.

Structural analysis of the FOR004 drillcore

The rocks in drillcore FOR004 typically have a gneissic foliation that has a predominant, gentle to moderate, west to southwesterly dip. Stereonet analysis of a best-fit great circle from poles to foliation planes in all units gives a calculated fold axis of 1° towards 349° (Fig. 28). Small-scale, tight folds of the gneissic layering have gentle plunges, mostly around 15° to 20° to the west-northwest or northwest, and gently to moderately dipping axial planes. At around 525 m drilled depth, the layering and gneissosity of the granodiorite gneiss are folded into small-scale refolded folds, with early (F_1) folds plunging gently to the southwest, and second-generation (F_2) folds plunging to the west-northwest or northwest (Fig. 28; Appendix 2). These F_2 folds are cut by the veins and alteration.

A schematic, northwest-facing cross-section of the gneissosity measurements indicates that the drillhole, which was oriented 80° towards 070° and deviated to 093° (Appendix 1), intersected a series of stacked, predominantly gently west- to northwest-plunging folds with moderately, generally southwest-dipping axial planes (Fig. 28). These are likely the F_2 folds, which fit reasonably well with the measured fold axes, but less so with the calculated fold axis in the stereonet. This may be because the gneissosity measurements are not a complete spread of fold data from both limbs due to the restricted area intersected by the drillcore, and hence are not fully recording the fold profile. Overall, the data indicate a series of south-southwesterly inclined to recumbent, second-generation folds, potentially indicative of tectonic transport to the east-northeast above a décollement.

The presence of folds in the drillcore suggests larger scale, shallowly plunging folds are likely to be present in the area. The first vertical derivative aeromagnetic image shows both north-northwesterly trending anomalies and northwesterly trending anomalies, the latter coinciding with the FOR004 drillsite (Fig. 25) and the orientation of the measured F_2 fold axes. The north-northwesterly trending anomalies could be related to the north-northwesterly trending faults that are numerous in the region and truncate the northwesterly trending anomalies.

Stratigraphic drillcore FOR008

Drillhole FOR008 is located within an area of subtly northwesterly trending magnetic fabric of moderate response, but within a broad area of moderate,



Figure 27. Photographs of the FOR004 drillcore (HQ core width 63.5 mm): a) typical example of granodiorite and diorite gneiss intruded by and interlayered with pink leucogranite; b) example of amphibolite to diorite gneiss interpreted as the oldest (host) phase within the granodiorite gneiss (middle right). A porphyritic example of the granodiorite gneiss is shown on the left-hand side of the photograph; c) pink equigranular leucogranite with schlieric layers of granodiorite (middle row); d) folded section of granodiorite gneiss at 488 m, shown here reoriented to its original drilled position in a sandbox for measuring; e) red to pink speckled alteration of pink equigranular leucogranite, with a crosscutting chlorite vein and patchy chlorite–epidote alteration, especially around a mafic inclusion

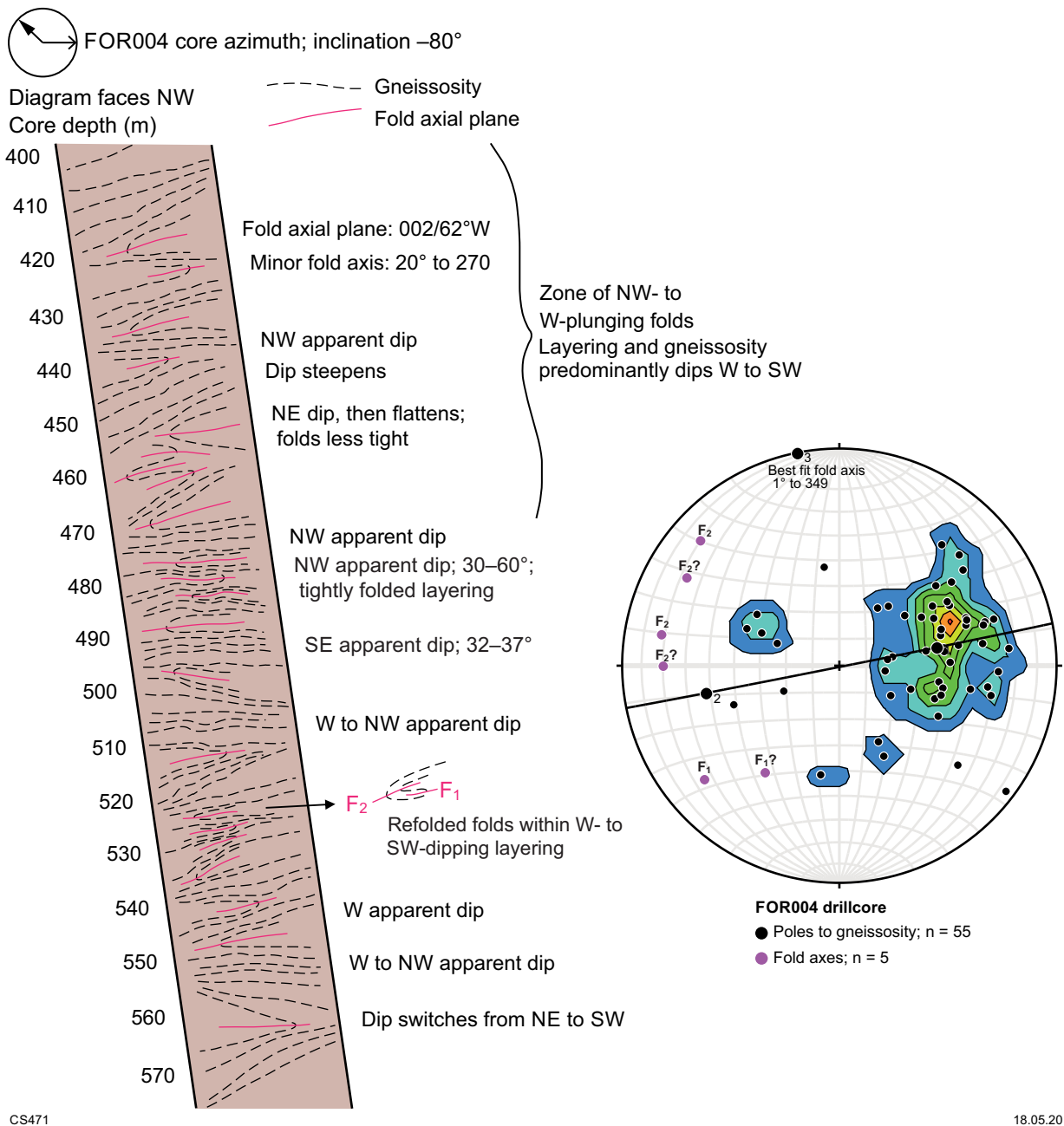


Figure 28. Schematic cross-section facing northwest of the measured foliations and folds in oriented drillcore FOR004, and interpreted folds. Apparent dips are taken into account. The poles to the gneissosity and their contours, measured fold data and calculated fold axis are shown in the equal area stereonet

northeasterly trending gravity response (Figs 26, 29, 30). A northeasterly trending gravity low lies to the northwest of the drillsite, and a series of northeasterly trending, northwest-dipping shear zones lie to its northwest, bounded by the Mulyawara Shear Zone (Fig. 10b). The Mulyawara Shear Zone is a major structure separating the western and eastern components of the Coompana Province, and these two elements lie above the middle to lower crustal Forrest Lakes Seismic Province (Fig. 10b,d). The Forrest Lakes Seismic Province is dominated by seismic reflectors and inferred shear zones with apparent easterly dips.

The FOR008 drillcore comprises three main lithologies: 1) medium-grained (2–4 mm) to locally coarse-grained (3–5 mm), seriate-textured to porphyritic, granodiorite to monzogranite gneiss; 2) fine-grained (1–3 mm),

equigranular to locally porphyritic monzogranite gneiss; 3) fine- to medium-grained (1–4 mm), biotite-rich and hornblende-bearing monzodiorite gneiss (Fig. 31). These rocks are assigned to the Toolgana Supersuite.

Toolgana Supersuite

As was the case for the FOR004 drillcore, granodiorite to monzogranite gneiss dominates the FOR008 drillcore. The granodiorite to monzogranite gneiss is red to grey, seriate textured to porphyritic (porphyroclasts up to 4 cm), migmatitic, biotite rich and locally hornblende bearing (Fig. 31a). It is locally interlayered with a pale grey, equigranular to locally porphyritic, monzogranite gneiss with distinct thin layering that has a finer grained

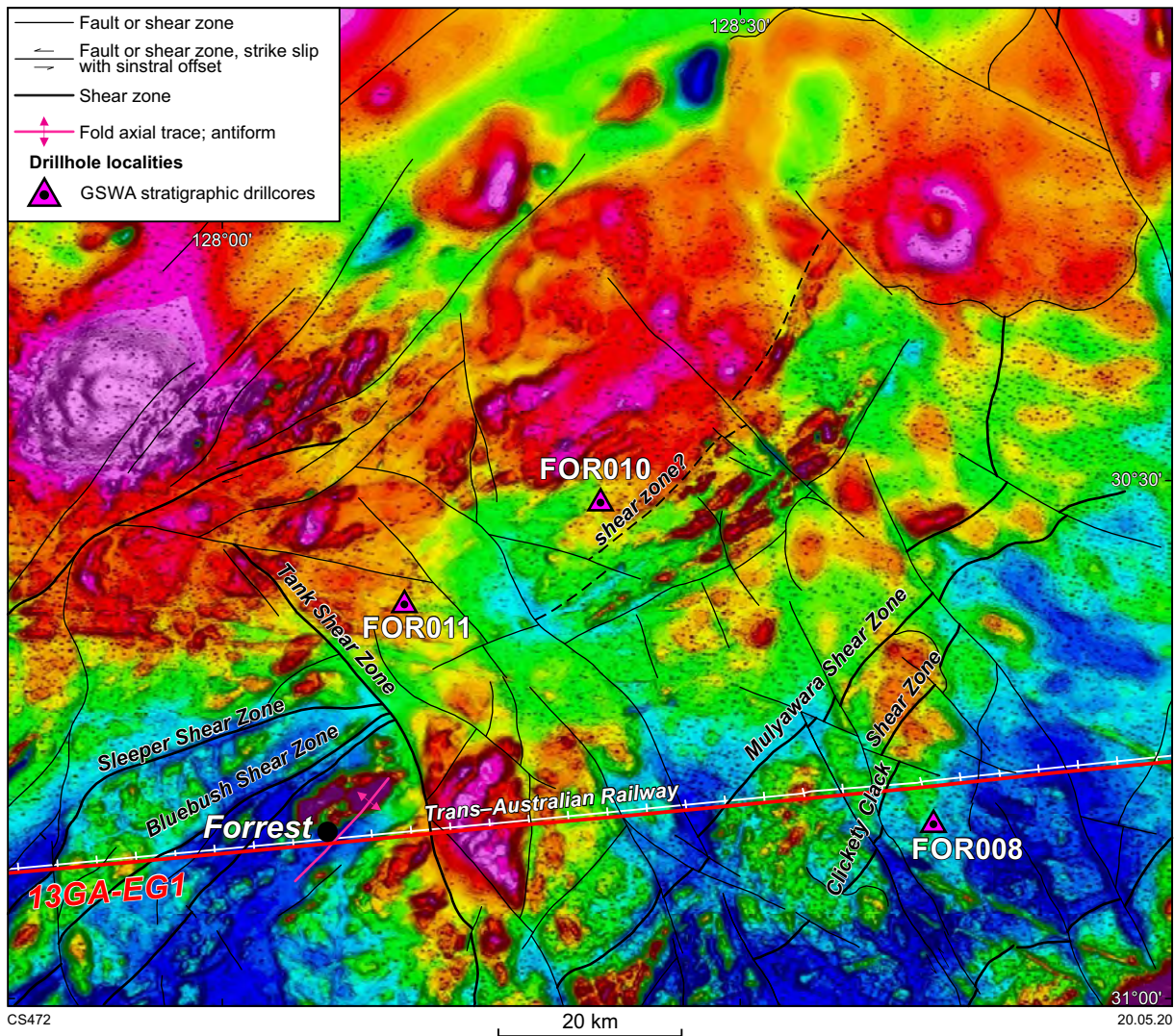


Figure 29. Reduced-to-pole aeromagnetic image over the Coompana Province in the vicinity of drillholes FOR008, FOR010, and FOR011, showing the structural interpretation, drillsite locations and position of the 13GA-EG1 seismic line. Warm colours represent high magnetic intensity, cool colours represent low intensity

groundmass and is more leucocratic. These two phases may be variants of the same intrusion. A fine- to medium-grained monzodiorite gneiss is locally interlayered with the coarser grained, biotite-rich granodiorite to monzogranite gneiss (Fig. 31b). All have a well-developed, moderate to strong, anastomosing gneissosity that is locally folded. The gneissosity and folds are cut by felsic migmatitic layers or diatexite patches. These locally have biotite-rich selvages.

The granodiorite to monzogranite gneiss typically comprises anhedral to blocky subhedral plagioclase (locally antiperthite or myrmekite), anhedral orthoclase (in various stages of strain-inversion to microcline), anhedral olive-green hornblende (typically poikilitic and up to 10 mm), anhedral quartz and weakly tabular biotite, locally in clots up to several millimetres. Porphyroclasts of microcline up to 10 mm locally enclose euhedral blocky microcline grains up to 4 mm in size in other orientations. Anhedral to blocky subhedral plagioclase (albite-oligoclase) is as common as microcline in the groundmass. Accessory minerals include anhedral to roughly octahedral magnetite that is mainly altered to coarse hematite, anhedral titanite (some with

cores of ilmenite and some rimming magnetite), zircon and rare chlorite-epidote-altered possible allanite. The accessory minerals are unevenly distributed and all are associated with hornblende and biotite. Foliation-parallel, centimetre- to metre-scale quartzofeldspathic layers are generally coarser grained, locally have biotite-rich selvages, and are interpreted as partial melt patches and veins. These are also folded but locally transgress the gneissic foliation. The presence of metamorphic biotite and hornblende suggests amphibolite facies, and the partial melt patches and veins suggest upper amphibolite or possibly granulite facies.

The monzodiorite gneiss is similar to the granodiorite to monzogranite gneiss but is much richer in hornblende and biotite. It also contains anhedral to blocky subhedral plagioclase and anhedral orthoclase. The hornblende is fresh and green and mainly interstitial to plagioclase. Accessory minerals include octahedral magnetite and stubby prismatic apatite. These more mesocratic layers appear to be less migmatized than the more leucocratic layers, which were most likely more susceptible to anatexis during metamorphism.

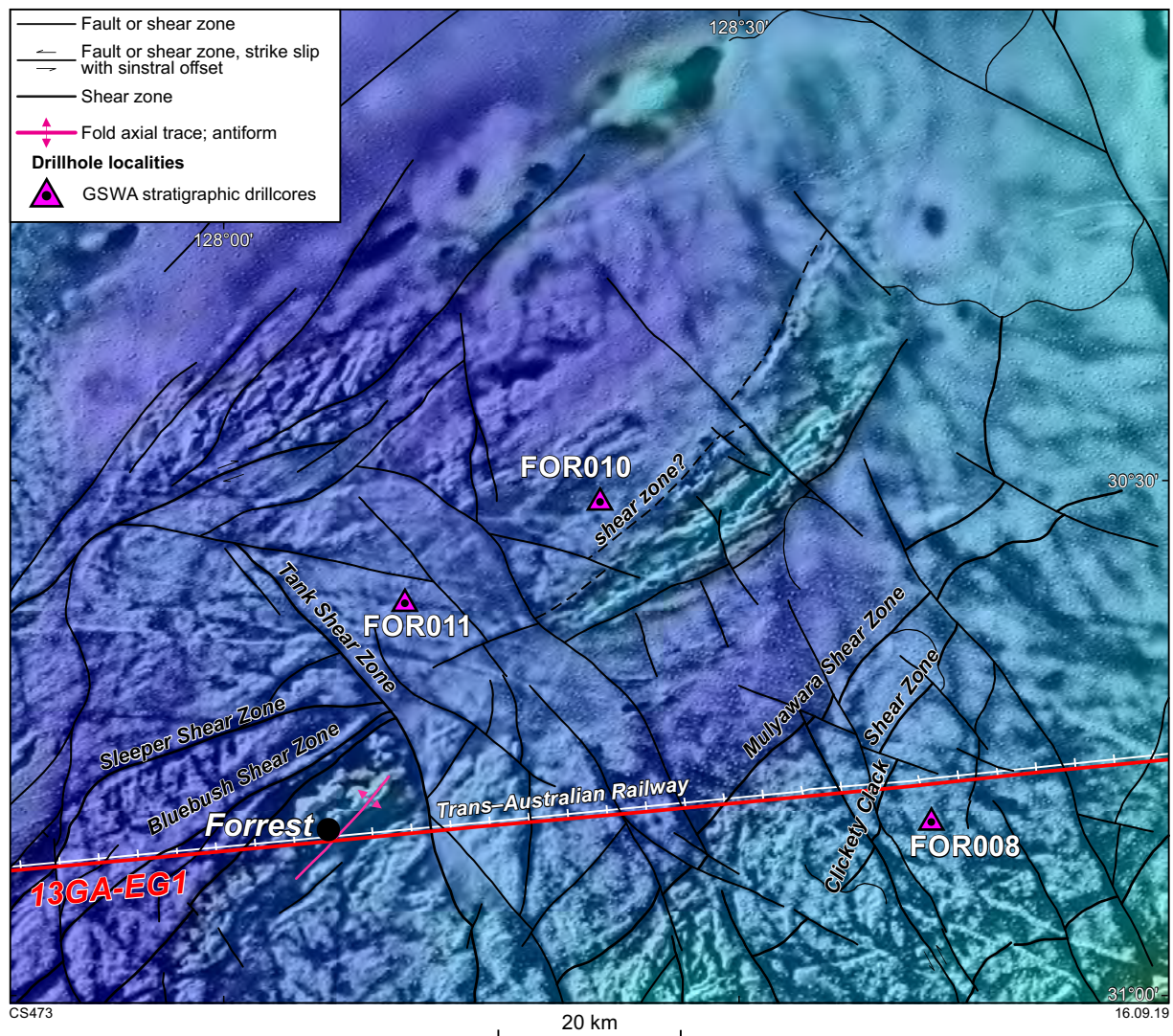


Figure 30. Structural interpretation and drillsite locations plotted on a drupe image of gravity (colour) and reduced-to-pole, first vertical derivative aeromagnetic data (greyscale) over the Coompana Province in the vicinity of drillholes FOR008, FOR010 and FOR011. Warm colours represent a strong gravity response, cool colours represent a low response

Sulfides and alteration

The assemblage in the granodiorite to monzogranite gneiss shows local retrogression to low greenschist facies. Plagioclase is moderately altered to sericite, biotite to chlorite and epidote, and hornblende to chlorite and sericite.

Sulfides are sparse in this core, but do occur locally and assays indicate the presence of Cu (Appendix 7). Granite gneiss GSWA 219009 (448.16 – 448.36 m; ½ HQ core, 101 ppm Cu, 10 ppb Pd) contains a millimetre-scale stockwork consisting of <0.1 mm-thick veinlets of chalcopyrite. The stockwork is close to a stringer a couple of millimetres wide dominated by dark-brown, Fe-rich biotite with abundant subordinate anhedral magnetite up to 2 mm in size that has been completely altered to hematite. Hematite alteration is a common feature in this core and some sections are distinctly reddish. Coarse-grained porphyritic granite gneiss sample GSWA 219012 (565.60 – 565.81 m; ½ HQ core) contains 1154 ppm Cu, although no sulfide minerals were identified in thin section (Fig. 31c). The section of core shows patchy chlorite (from biotite) and sericite (from plagioclase) alteration, and hematite staining. This is just above a zone of increased

chlorite–epidote alteration and centimetre-scale calcite veins with white, zoned, euhedral 5–8 mm crystals. GSWA 219013 (570.45 – 570.65 m, ½ HQ core) is similar to GSWA 219012 and contains 166 ppm Cu.

Structural analysis of the FOR008 drillcore

All rock types in this core have a well-developed, moderate to strong gneissosity that has a variable, dominantly shallow dip (Fig. 32). The gneissosity is locally folded into flat-lying, small-scale Z-folds and curvilinear folds (Fig. 31d). These are locally cut by migmatitic patches and veins, indicating the folding took place prior to, or during, high-temperature metamorphism. A weak to moderate intensity mineral lineation is subhorizontal, and is probably anastomosing in a similar fashion to the gneissosity (measured at plunging 6–10° towards 096° or towards 196°; Fig. 32). Stereonet analysis of a best-fit great circle from poles to gneissosity planes gives a calculated fold axis of 5° towards 070°, similar to measured fold axes and the mineral lineation. The subhorizontal fold axes and flat-lying axial planes, which are subparallel to the gneissosity, are suggestive of recumbent folding.

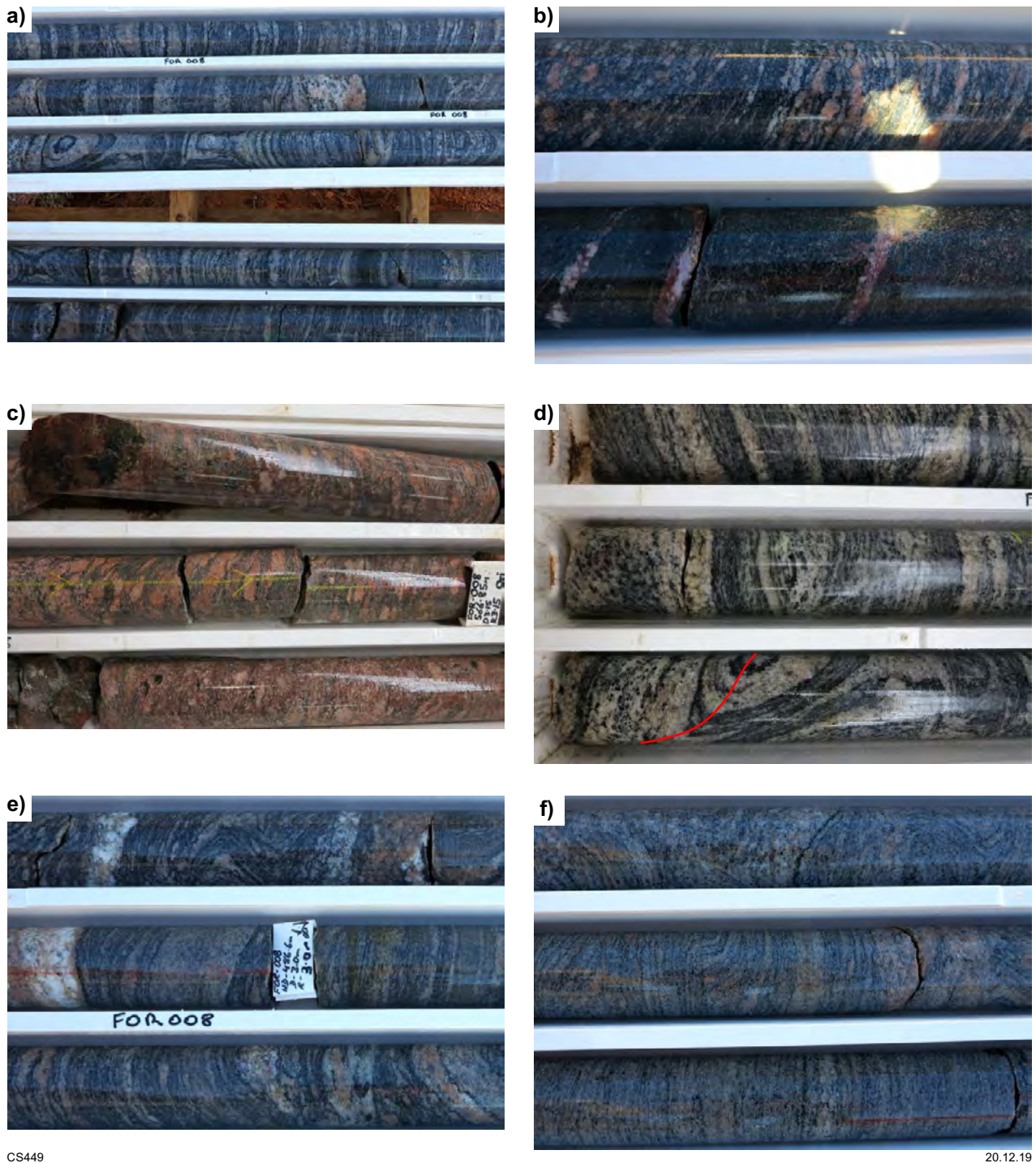


Figure 31. Photographs of the FOR008 drillcore (HQ core width 63.5 mm): a) typical medium-grained, biotite-rich, migmatitic granodiorite to monzogranite gneiss; trays 31 and 32; b) interlayered fine-grained monzodiorite gneiss with hornblende phenocrysts and felsic migmatite patches; tray 33; c) coarse-grained porphyritic granite gneiss with patchy chlorite (from biotite) and sericite (from plagioclase) alteration, and hematite staining. The top part of the core in the photograph contains 1154 ppm Cu (GSWA 219012, 565.60 – 565.81 m, ½ HQ core); d) example of a curvilinear fold truncated by melt in granodiorite gneiss. Fold axial trace denoted by the red line. Axial plane envelope: 049/28°NW, fold axis 17° to 216°, tray 31; e) small-scale folds containing K-feldspar porphyroclasts (top row) in granodiorite gneiss; tray 29; f) small-scale asymmetric kink folds of the gneissosity; tray 22

CS449

20.12.19

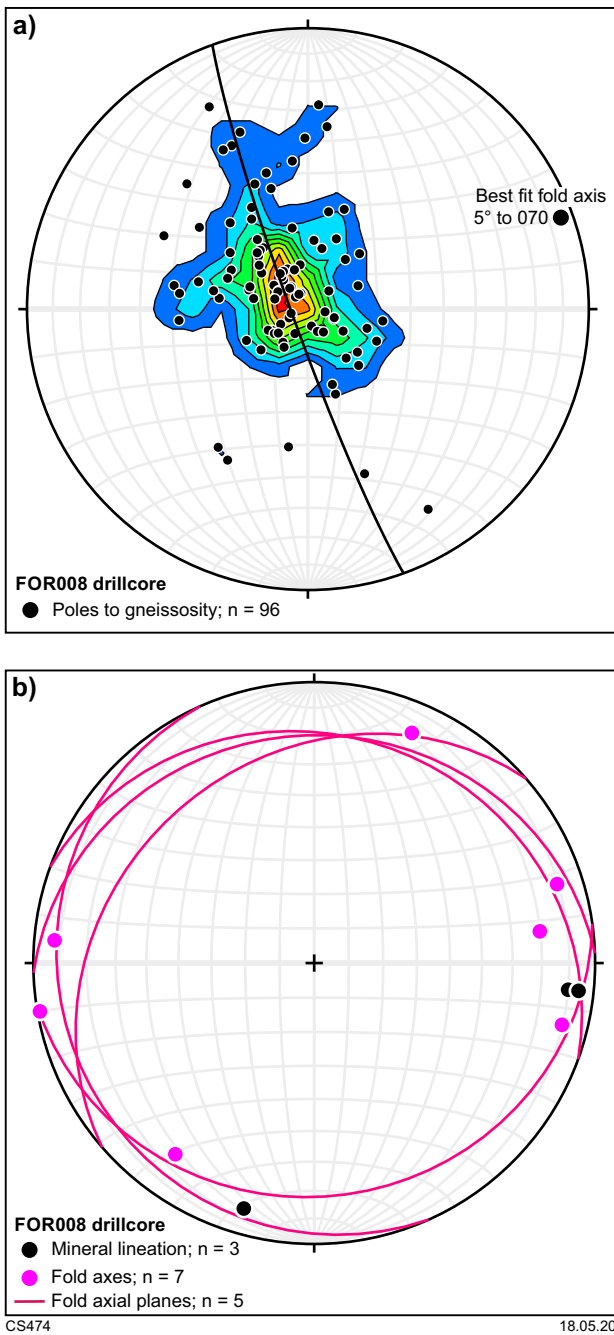
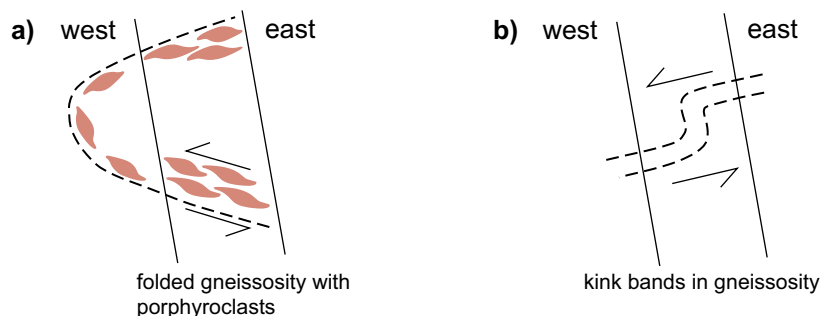


Figure 32. Equal area stereonet showing structural data from oriented drillcore FOR008: a) poles to the gneissosity and their contours and calculated fold axis; b) mineral lineations, fold axes and axial planes

Figure 33. Examples of structural features in drillcore FOR008. The parallel lines denote the core: a) K-feldspar porphyroclasts with top to the northwest asymmetry, folded with the gneissosity; b) asymmetric kink bands of gneissosity within high-strain zones indicating top to the west or southwest shear sense



CS475

27.08.19

Throughout much of the core, the asymmetry of feldspar porphyroclasts indicates top to the northwest shear sense. The porphyroclasts occur within the gneissosity, which is folded (Figs 31e, 33a). Localized high-strain zones contain small, flat-lying kink bands that indicate top to the west or southwest transport (Figs 31f, 33b). A small shear zone at 484 m dips 50° towards 104° (dip, dip direction) and offsets the layering and a coarse-grained leucosome vein with top to the northwest thrust displacement. The relationships indicate a history of top to the west or northwest transport (prior to or during migmatization), recumbent or strongly inclined folding, closely followed by partial melting. High-strain zones and asymmetric kink bands may have developed as folding progressed, whereas the small shear zone at 484 m indicates a younger phase of thrusting.

Stratigraphic drillcore FOR010

Drillhole FOR010 is located within an area of northeasterly trending, linear magnetic fabric of moderate intensity, and within a large area of generally low-gravity response (Figs 26, 29, 30). The drillsite lies about 10 km northwest of a northeasterly trending ridge of moderate gravity response, coincident with a stronger magnetic fabric in the same orientation. This ridge is inferred to include mafic to intermediate rocks described in this drillcore and in drillcore FOR011.

The FOR010 drillcore is one of the more complex stratigraphic drillcores and comprises five lithological units belonging to two supersuites. In order of relative ages determined by crosscutting relationships in the drillcore these are, from oldest to youngest: 1) porphyritic monzogranite gneiss; 2) foliated metatonalite; 3) mafic to intermediate, variably foliated to unfoliated, hornblende-bearing metadiorite to metamonzodiorite (shoshonite); 4) unfoliated porphyritic syenogranite (evolved Si-rich shoshonite); 5) unfoliated equigranular syenogranite (evolved Si-rich shoshonite). The porphyritic monzogranite gneiss is interlayered with the metatonalite and it is unknown which phase is the oldest because the contacts are parallel to the foliation. These rocks are assigned to the Undawidgi Supersuite. In contrast, the hornblende metadiorite to metamonzodiorite clearly intrudes both the monzogranite gneiss and the metatonalite, and the unfoliated porphyritic and equigranular syenogranites intrude all of the above. The equigranular syenogranite intrudes the porphyritic syenogranite and is therefore the youngest phase. These three phases are assigned to

the Bottle Corner Shoshonite of the Moodini Supersuite. Alteration and associated veins affect all lithologies, and are therefore late.

Undawidgi Supersuite: monzogranite gneiss and metatonalite

The porphyritic monzogranite gneiss is medium to coarse grained (average 3–5 mm), greyish brown to red, biotite rich, and has a moderate to strong gneissic foliation within which the recrystallized feldspars form elongate aggregates or porphyroclasts up to 2 cm long (Fig. 34a). The porphyroclasts are either microcline or aggregates of anhedral K-feldspar (orthoclase in various stages of strain-inversion to microcline) with subordinate quartz, granular oligoclase and, locally, small flakes of biotite. The porphyroclasts occur in a finer grained, more mafic matrix dominated by plagioclase (typically An₂₀) and biotite, minor quartz and interstitial K-feldspar and, locally, anhedral green hornblende. Fine-grained anhedral titanite, equant euhedral zircon, and anhedral magnetite locally rimmed with titanite, are common. The feldspars are locally stained with hematite, contributing to the red colour of the monzogranite.

The metatonalite is grey, fine to medium grained (average 2–4 mm) and moderately to strongly foliated with 1–2 cm long porphyroclasts (Fig. 34b–d). These porphyroclasts comprise anhedral plagioclase (typically An₂₀) distinctly flattened into a foliation defined by the preferred orientation of dark, Fe-rich biotite, subhedral prismatic to anhedral dark green hornblende, and anhedral quartz. Both the biotite and hornblende are concentrated into streaky lenses parallel to the foliation. Biotite in the lenses tends to be coarse and anhedral, but locally there is less common, finer, tabular biotite outside the lenses that has a distinct preferred orientation at a high angle to the lenses and main foliation. Anhedral magnetite is mostly altered to hematite.

The mineral assemblage suggests lower amphibolite facies metamorphic conditions. The metatonalite is particularly strongly deformed and altered near the top of the drillcore (387.5 – 400.3 m and 429.2 – 430.2 m) where it is more finely grained, thinly layered and dark greenish grey due to modification into a chloritized biotite–epidote schist. The presence of biotite and the calcic composition of the plagioclase suggests this deformation and alteration took place at low amphibolite facies metamorphic conditions.

Bottle Corner Shoshonite; Moodini Supersuite

The hornblende metadiorite to metamonzodiorite and the two phases of syenogranite veins are assigned to the Bottle Corner Shoshonite of the Moodini Supersuite, based on their geochemical affinities (Kirkland et al., 2017; see also Whole-rock geochemistry). The suite is divided into two groups based on SiO₂ content: mafic shoshonite (hornblende metadiorite to metamonzodiorite) and evolved Si-rich shoshonite (syenogranite).

The hornblende metadiorite to metamonzodiorite is fine to medium grained (average 1–2 mm), mesocratic and variably foliated (Fig. 34b–f). It typically contains

3–4 mm (locally up to 15 mm) aligned mafic lenses comprising columnar prismatic dark green hornblende commonly wrapped in biotite, which in the unfoliated examples occur as mafic phenocrysts in the protolith (Fig. 34d,f). These occur in a fine-grained groundmass of hornblende, biotite, K-feldspar, plagioclase and titanite, typically with abundant prismatic apatite. Fine-grained quartz occurs locally with (metamorphic) hornblende reaction rims. One example (GSWA 213868) is slightly altered and contains subhedral, stubby prismatic 0.3 – 2 mm pale green actinolitic hornblende, chloritized similar-sized biotite, 2 mm subhedral blocky K-feldspar, and anhedral plagioclase up to 2 mm (about An₂₅) that is locally albitized. The assemblages indicate metamorphism in the low amphibolite or upper greenschist facies, and GSWA 213868 indicates the hornblende metadiorite to metamonzodiorite was locally retrogressively altered (chloritizing biotite) at low or very low greenschist facies.

Unfoliated medium- to coarse-grained, red porphyritic syenogranite occurs as veins of variable thickness throughout the core (Fig. 34b,f). It typically has an assemblage of subhedral <8 mm orthoclase phenocrysts (commonly inverted to microcline), euhedral oligoclase phenocrysts and anhedral quartz in a groundmass of subhedral plagioclase, interstitial quartz, partly chloritized dark (Fe-rich) biotite, minor microcline, titanite, magnetite, and rare subhedral dark olive hornblende. Although for the most part this unit is clearly undeformed, it does locally contain a weak foliation defined by biotite and titanite (e.g. GSWA 206745, Appendix 5).

The youngest unit is an unfoliated, fine-grained, pink to red equigranular syenogranite that also occurs as veins of variable thickness throughout the core (Fig. 34a,d,e). It typically has an assemblage of partly chloritized plagioclase, microcline, biotite and quartz. Biotite is dark (Fe rich) and partly chloritized. Accessory minerals include granular and prismatic apatite, subrounded sphenoidal titanite, and mainly interstitial magnetite that is largely altered to hematite.

Sulfides and alteration

Thin quartz–epidote and locally chlorite veins cut most lithologies, including the younger syenogranite veins. The upper part of the drillcore contains a section that is strongly altered to a laminated chlorite–epidote schist with centimetre-scale quartz or carbonate veins (Fig. 35a,b). The protoliths were likely the hornblende metadiorite to metamonzodiorite and the metatonalite. The schistose foliation is cut by the equigranular syenogranite. Although patchy chlorite and epidote occur locally elsewhere throughout the drillcore, the most prevalent alteration is the strong red colouration, for the most part due to hematite dusting on feldspars (Fig. 35c).

Sulfides occur in minor amounts in the monzogranite gneiss and both types of syenogranite veins, and along the contacts of the phases the veins intrude. Minor, disseminated pyrite and chalcopyrite occur in the monzogranite gneiss. In GSWA 213862 (447.94 – 448.20 m), disseminated subhedral <0.6 mm pyrite (0.5%) is weakly associated with very



CS450

16.09.19

Figure 34. Photographs of drillcore FOR010 (HQ core width 63.5 mm): a) porphyritic monzogranite gneiss with biotite-rich clots and foliation, and flattened feldspar aggregates. The centre-left shows a fine-grained, equigranular syenogranite vein crosscutting the foliation; tray 61; b) strongly foliated metatonalite (centre top) interlayered with monzogranite gneiss. Foliated hornblende metamazonzodiorite (centre-right) intruded by undeformed porphyritic syenogranite (centre-left); tray 61; c) strong foliation in metatonalite cut by weakly foliated hornblende metamazonzodiorite; tray 39; d) strongly foliated metatonalite intruded by undeformed equigranular syenogranite (top). Unfoliated hornblende metamazonzodiorite (bottom); e) strongly foliated hornblende metamazonzodiorite cut by a fine-grained, undeformed syenogranite vein (bottom); tray 47; f) monzogranite gneiss cut by unfoliated hornblende metamazonzodiorite (top), which is intruded by the porphyritic syenogranite (bottom); tray 76

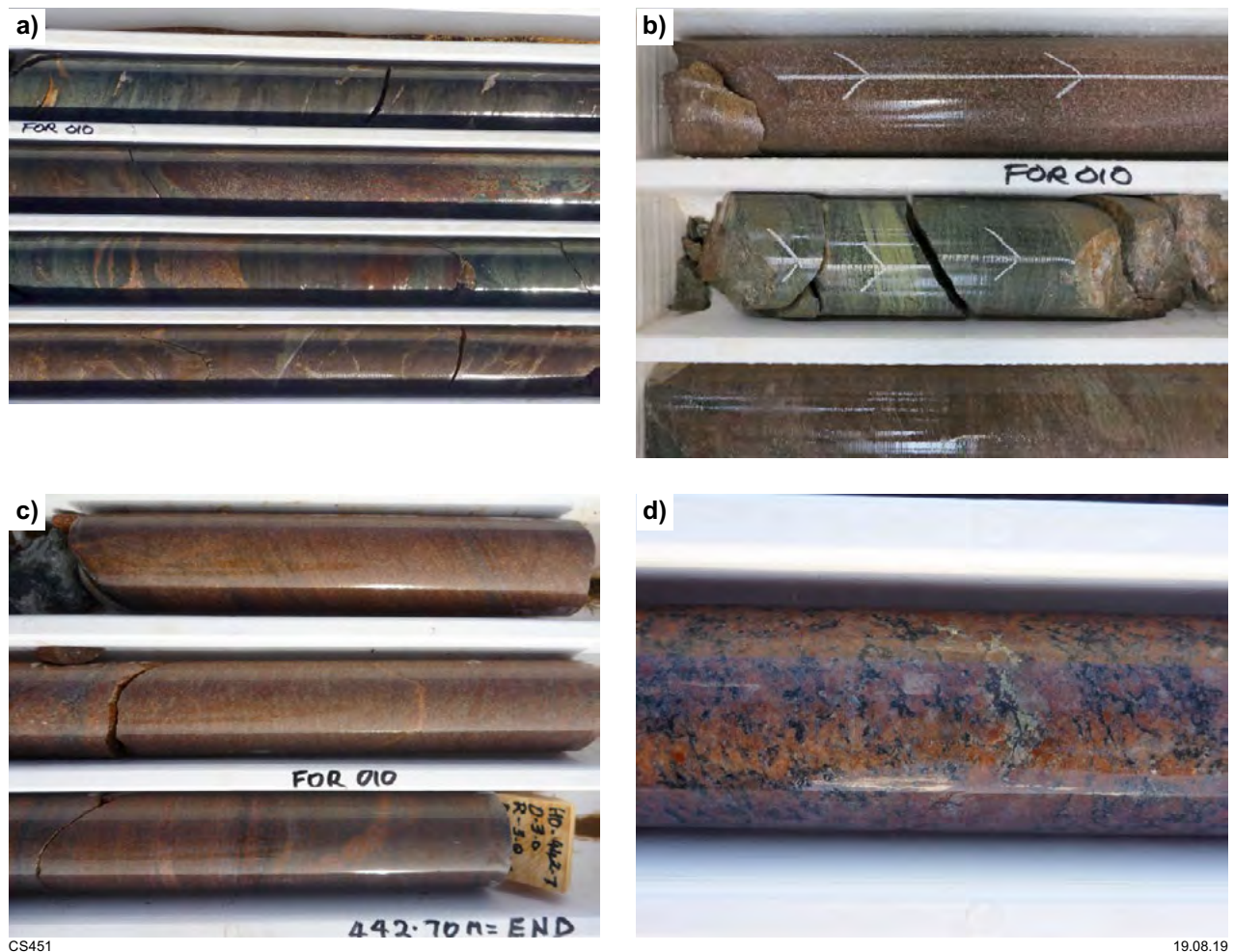


Figure 35. Photos of alteration in drillcore FOR010 (HQ core width 63.5 mm): a) intense chlorite–epidote alteration, quartz–carbonate veins, and hematite alteration in probable hornblende metamonzodiorite and metatonalite. The fine-grained, red equigranular syenogranite cuts the foliation; tray 46; b) chlorite–epidote alteration of probable hornblende metamonzodiorite resulting in a laminated schist. The top shows hematite-altered fine-grained equigranular syenogranite; tray 43; c) strong red colouration and disseminated sulfide in metatonalite; tray 35; d) fresh pyrite and chalcopyrite stringer associated with hematite-stained feldspar; 490.53 m, tray 72

minor <0.3 mm subhedral epidote and <0.2 mm grains of chalcopyrite. In GSWA 206748 (492.60 – 492.74 m; ½ HQ core, 200 ppm Cu), sulfides are present in trace amounts and comprise <0.3 mm chalcopyrite and <0.1 mm galena. The sulfides are fresh in hematite-stained feldspar (Fig. 35d), suggesting that mineralization occurred under hypogene conditions on the pyrite–hematite fO_2 – fS_2 buffer, rather than during weathering.

In the red, hematite-stained syenogranite veins sulfides comprise pyrite, chalcopyrite and rare galena. In GSWA 206743 (441.98 – 442.10 m; ½ HQ core, 147 ppm Pb, 15.8 ppm Mo), a couple of 30 μ m galena grains adhere to a much larger subhedral grain of pyrite. Other sulfide occurrences include scarce chalcopyrite and pyrite with minor, late <0.3 mm magnetite on its margins. GSWA 206741 (441.12 – 441.25 m) contains disseminated, anhedral to subhedral <1 mm pyrite forming about 2% of the rock, and traces of chalcopyrite. The tan colour of the slightly degraded pyrite, and the approximately 0.2 mm stubby rutile, suggest that pyrite (or a pyrrhotite precursor) might have been present at the metamorphic peak.

Structural analysis of the FOR010 drillcore

The monzogranite gneiss and the metatonalite of the Undawidgi Supersuite have a moderate to strong foliation that mainly has a gentle to moderate, east-northeasterly to northeasterly dip (Fig. 36). Stereonet analysis of a best-fit great circle from poles to foliation planes in both lithologies combined gives a calculated fold axis of 20° towards 059° (Fig. 36b). However, when calculated separately, the monzogranite gneiss fold axis is 18° towards 025°, whereas the metatonalite is 17° towards 096° (Fig. 36c). This difference could be a function of the metatonalite being the dominant measured lithology in the upper part of the drillcore and the monzogranite gneiss being the dominant measured lithology in the lower part, suggestive of a change in orientation between the two lithologies. It could also indicate deviation of the drillhole, although the north-seeking gyro survey for this hole was successful for the full depth and the results show this not to be the case (Appendix 1), and any deviations were taken into account as the structural measurements

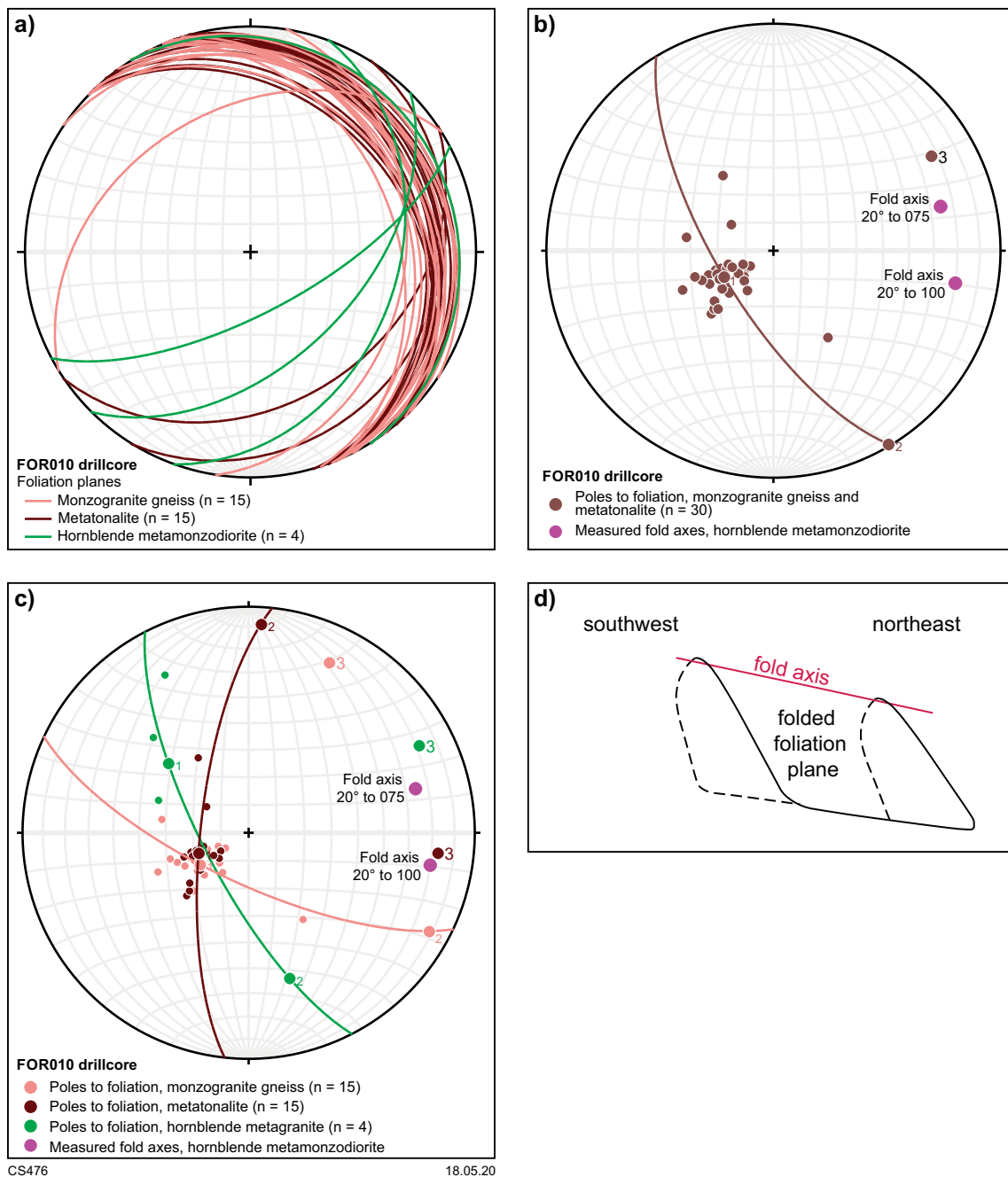


Figure 36. Equal area stereonet analysis of oriented drillcore FOR010: a) foliation planes measured in the monzogranite gneiss, metatonalite and hornblende metazonzodiorite; b) poles to foliation for the monzogranite gneiss and metatonalite in a), showing the calculated fold axis (denoted by Bingham analysis number 3), and measured fold axes; c) poles to foliation for the monzogranite gneiss, metatonalite, and hornblende metazonzodiorite shown separately, with respective calculated fold axes (denoted by Bingham analyses number 3), and measured fold axes; d) schematic diagram illustrating northeast-plunging tight to isoclinal folding of the monzogranite gneiss and metatonalite

were made. Fold axes measured in the hornblende metadiorite to metamonzodiorite, from the upper part of the drillcore, most closely match the calculated fold axis in the metatonalite (Fig. 36c), which would fit with the interpretation of a change in foliation and fold axis orientation with depth.

Evidence for folding in this drillcore is limited, and the two measured folds occur within chlorite–epidote schist interpreted to be intensely altered hornblende metadiorite to metamonzodiorite. The formation of chlorite–epidote schist in the upper part of the drillcore in both the hornblende metadiorite to metamonzodiorite and the metatonalite relates to metamorphic retrogression and associated deformation (Fig. 35a,b; Table 2). In the hornblende metadiorite to metamonzodiorite, the transition of biotite to chlorite indicates low or subgreenschist facies, likely related to shear zone activity and fluid mobility in the vicinity. Where the metatonalite is particularly strongly deformed in this upper section of drillcore, it is thinly layered and dark greenish grey due to modification into a chloritized biotite–epidote schist. The presence of biotite and the plagioclase composition suggests this deformation and alteration took place at low amphibolite facies metamorphic conditions, although the chlorite also indicates retrogression. It is therefore feasible that the measured folds are part of a younger deformation event, perhaps related to shear zone activity nearby, under greenschist facies metamorphic conditions. In contrast, the foliations measured in the monzogranite gneiss and the metatonalite elsewhere in the drillcore likely relate to an older deformation event, which the petrographic analysis indicates was at low amphibolite facies metamorphic conditions. The data are insufficient to characterize this older event, although the clustering of the poles to foliation (Fig. 36b,c) could indicate northeast-plunging tight to isoclinal folding with approximately parallel axial planes (Fig. 36d). Alternatively, the foliations could represent a northeast-dipping axially planar foliation related to

northwesterly trending, inclined or overturned large-scale folds, that is, larger than the drillhole itself. Although these foliations are locally strong, there are no microstructures that indicate formation within a shear zone.

The hornblende metadiorite to metamonzodiorite contains a variably developed metamorphic foliation that is similar in orientation to that measured in the monzogranite gneiss and the metatonalite, both of which it intrudes. However, veins of hornblende metadiorite to metamonzodiorite also clearly cut the foliation in both of these lithologies (Fig. 34c,f). Therefore, the foliation of moderate to strong intensity observed in the monzogranite gneiss and the metatonalite must pre-date intrusion of the hornblende metadiorite to metamonzodiorite, and the mostly less intense foliation in the hornblende metadiorite to metamonzodiorite likely formed during subsequent deformation (Table 2). Petrographic analysis of the metatonalite indicates the presence of a second, less well-developed biotite foliation at a high angle to the main foliation in some samples. If the interpretation of a second deformation event is correct, it is likely that strain was strongly partitioned resulting in variable development of the foliation in the hornblende metadiorite to metamonzodiorite, and recrystallization, for the most part, in a similar orientation to the first event in the metatonalite and monzogranite gneiss.

Aeromagnetic data show a dominantly northeast-trending magnetic fabric, although the magnetic fabric in the vicinity of drillhole FOR010 could be interpreted as a series of gently northeast-plunging tight to isoclinal folds, as shown schematically in Figure 36d. However, the more linear magnetic fabric and gravity ridge to the southeast is more suggestive of dominantly northeast-trending foliations, rather than northeast-dipping foliations (Fig. 30). It is possible that a northeast-trending shear zone exists between the two domains, which would fit with the surrounding structures interpreted in the geophysical data (Figs 29, 30).

Table 2. Structural and metamorphic synthesis of drillcore FOR010

<i>Event</i>	<i>Lithological unit</i>	<i>Feature</i>	<i>Estimated metamorphic grade</i>	<i>Interpretation</i>
Maralinga Event continued	Equigranular syenogranite	Intrusion of youngest Si-rich component of Bottle Corner Shoshonite	Unknown	Crosscuts all deformation
Third deformation event	Tonalitic metagranite and hornblende metagranite	Localized schistose foliation in retrogressed, altered rocks; small-scale folds	Greenschist facies	Related to shear zone activity
Second deformation event	Hornblende metagranite	Weak to moderate metamorphic foliation, locally produced	Low amphibolite facies	Unknown, data insufficient
Maralinga Event	Hornblende metagranite	Intrusion of mafic component of Bottle Corner Shoshonite	Unknown	Crosscuts foliation in first event
First deformation event	Undawidgi Supersuite; monzogranite gneiss and metatonalite	Moderate to strong metamorphic foliation	Low amphibolite facies	Tightly to isoclinally folded foliation within gently northeast-plunging folds, or axial planar foliation to northwest-trending folds



Figure 37. Photos of drillcore FOR011 (HQ core width 63.5 mm): a) amphibolite layer (top right) from which interpreted Toolgana Supersuite sample GSWA 213837 was collected; b) Undawidgi Supersuite metasyenite geochronology sample GSWA 206730; c) Bottle Corner Shoshonite from 412–417 m: the second row from the top contains Si-rich shoshonite (GSWA 213846), the two lowest rows contain hornblende-bearing shoshonite (GSWA 213847; geochronology sample GSWA 206729, lowest row); d) coarse-grained granite veins crosscutting foliated metamonzodiorite of the Undawidgi Supersuite; 400–402 m; e) grey breccia zone with K-feldspar-rich fragments in a biotite, chlorite and epidote matrix; about 317 m

Stratigraphic drillcore FOR011

Drillhole FOR011 is located within an area of west-northwesterly trending, linear magnetic fabric of moderate intensity, and within a large area of generally low-gravity response, locally with northeasterly trending, low- to moderate-response gravity ridges (Figs 26, 29, 30). The drillsite lies within an area flanked by two northwest-trending faults defined in magnetic data. The fault on the west side is the Tank Shear Zone — a curved, west- to northwest-dipping shear zone that cuts the northeast-trending Sleeper, Bluebush and Approach Mast Shear

Zones within its hangingwall, and also the antiformal structure near Forrest (Figs 10b, 29, 30). To the south, the Tank Shear Zone truncates the Mulyawara Shear Zone (Fig. 24).

The FOR011 drillcore is dominated by variably layered, leucocratic to mesocratic, foliated metagranite and, locally, melanocratic layers including amphibolite (Fig. 37). It comprises several lithological units belonging to two supersuites, and remnants of inferred Toolgana Supersuite

amphibolite. In order of relative age determined by crosscutting relationships in the drillcore, and also from geochronology (see Geochronology section), these are, from oldest to youngest: 1) sparse layers of amphibolite; 2) variably interlayered, equigranular to locally porphyritic metamonzogranite, metasyenite and metamonzodiorite; 3) metamonzogranite and metadiorite with shoshonitic compositions; 4) unfoliated granitic to pegmatitic veins. Apart from the amphibolite and the unfoliated granite veins, these units and lithologies are generally difficult to identify visually as they are intimately interlayered on a centimetre to several centimetre scale and only locally on a half-metre scale. In addition, most of the drillcore has a moderate to strong red colouration due to hematite alteration. Contacts have been transposed and modified during metamorphism and deformation and are now parallel to a moderate intensity, metamorphic foliation. Alteration and associated veins affect all lithologies and are therefore late. Based on geochronology and whole-rock geochemistry (see sections below) the metasyenite and some of the metamonzodiorite and metamonzogranite are assigned to the Undawidgi Supersuite. Other occurrences of metadiorite, metamonzodiorite and metamonzogranite are assigned to the Bottle Corner Shoshonite of the Moodini Supersuite. The crosscutting granite and pegmatite veins are also assigned to the Moodini Supersuite.

There are two distinct amphibolite layers at 385.50 – 386.10 m (Fig. 37a; GSWA 213837) and at about 439.90 m. These are assigned to the Toolgana Supersuite (see Whole-rock geochemistry section). GSWA 213837 contains abundant deep green hornblende (up to 4 mm), lightly illitized plagioclase (about An₂₅) and dark brown biotite, and lacks quartz. The texture and hornblende colour are typical of Fe-rich amphibolites of the middle amphibolite facies.

Undawidgi Supersuite: metamonzogranite, metasyenite and metamonzodiorite

The felsic layers in these metagranites vary from fine grained (average 1–3 mm) to coarse grained (average 3–5 mm) and are dominated by assemblages of plagioclase (locally myrmekitic), orthoclase (locally microcline), quartz, and biotite (locally overgrown by chlorite). The proportions of these minerals vary with the layering. The more mesocratic layers are fine grained (1–2 mm) to medium grained (2–4 mm), and are rich in dark green hornblende and olive-brown to dark biotite. Titanite is a common accessory mineral throughout. Hornblende and biotite are typically the major minerals that define the foliation.

The metasyenite typically contains orthoclase with weak strain-inversion to microcline, oligoclase, very dark brown (Fe-rich) biotite, and minor quartz (Fig. 37b). Accessory minerals include prominent titanite, magnetite, and minor apatite and zircon. The metamonzodiorite typically contains plagioclase (An_{20–30}), orthoclase (partly inverted to microcline), quartz, olive-brown biotite, and dark green hornblende. Accessory minerals include titanite, apatite and zircon.

Moodini Supersuite; Bottle Corner Shoshonite

This unit is difficult to distinguish from the Undawidgi Supersuite, particularly the more dioritic rocks, because

unlike in the FOR010 drillcore, here the unit is well foliated, and variable in grain size and composition (e.g. the Si-rich examples at 390 and 414 m; Fig. 37c). The unit is distinguished primarily by its whole-rock geochemistry and geochronology, and occurs as deformed veins or sheets within the Undawidgi Supersuite. Samples typically contain biotite and green hornblende aligned in the foliation, anhedral oligoclase mainly included in or at the margins of interstitial alkali feldspar, and minor quartz. Accessory minerals are typically titanite, magnetite and apatite.

Moodini Supersuite; granite veins

The layering and foliation in all units are cut by centimetre-scale to locally thicker, unfoliated granite or pegmatite veins (Fig. 37d). These veins vary from medium to coarse grained (average 3–5 mm) with feldspars up to 1 cm long, or are equigranular, to coarser grained varieties with feldspars up to 3 cm long. Some veins contain clots of biotite and probable magnetite up to about 5 mm, whereas others are quartz rich.

Sulfides and alteration

The rocks in drillcore FOR011 are typically red due to hematite staining on feldspars (locally sericite–hematite alteration of plagioclase) that is locally quite intense, as well as local hematite alteration of magnetite. Thin chlorite veins are common throughout and locally thin epidote and quartz veins are present, or thin cream-coloured probable carbonate veins. Chlorite alteration occurs in patches and is more prolific in the lower part of the drillcore where it occurs as a fine, blue-grey mineral. Brecciation and stockwork veining occur locally. For example, at about 317 m there is a 20 cm thick breccia zone with K-feldspar-rich fragments in a biotite, chlorite and epidote matrix (Fig. 37e). Just above this are thin chlorite and epidote veins, and below is a biotite-rich alteration zone, locally with thin biotite–chlorite veins.

Disseminated pyrite and chalcopyrite are reasonably common in minor quantities throughout the drillcore. The pyrite could be a late hypogene alteration product of pyrrhotite, and the chalcopyrite is commonly altered to bornite. Pyrite also occurs along fractures and biotite cleavages where it may be a mobilized retrograde alteration product of early pyrrhotite. One sample of biotite monzogranite (GSWA 206733; 7 cm ½ HQ core, 143.4 ppm Mo, 172.4 ppm Cu) contains minor <0.45 mm molybdenite flakes, disseminated subhedral <0.5 mm pyrite forming about 1% of the rock, and disseminated anhedral <0.1 mm chalcopyrite. The molybdenite suggests a fairly high-temperature origin for the sparse sulfides from magmatic fluid, and the presence of unaltered biotite associated with some sulfides suggests they pre-date chlorite.

Structural analysis of the FOR011 drillcore

Layering in the leucocratic, mesocratic and melanocratic rocks is mostly parallel to a well-developed, dominantly moderate intensity foliation (S₁), that has a predominant northwest or southeast dip (Fig. 38a). Stereonet analysis of a best-fit great circle from poles to planes of the foliation gives a calculated fold axis of 6° towards 061°, suggestive

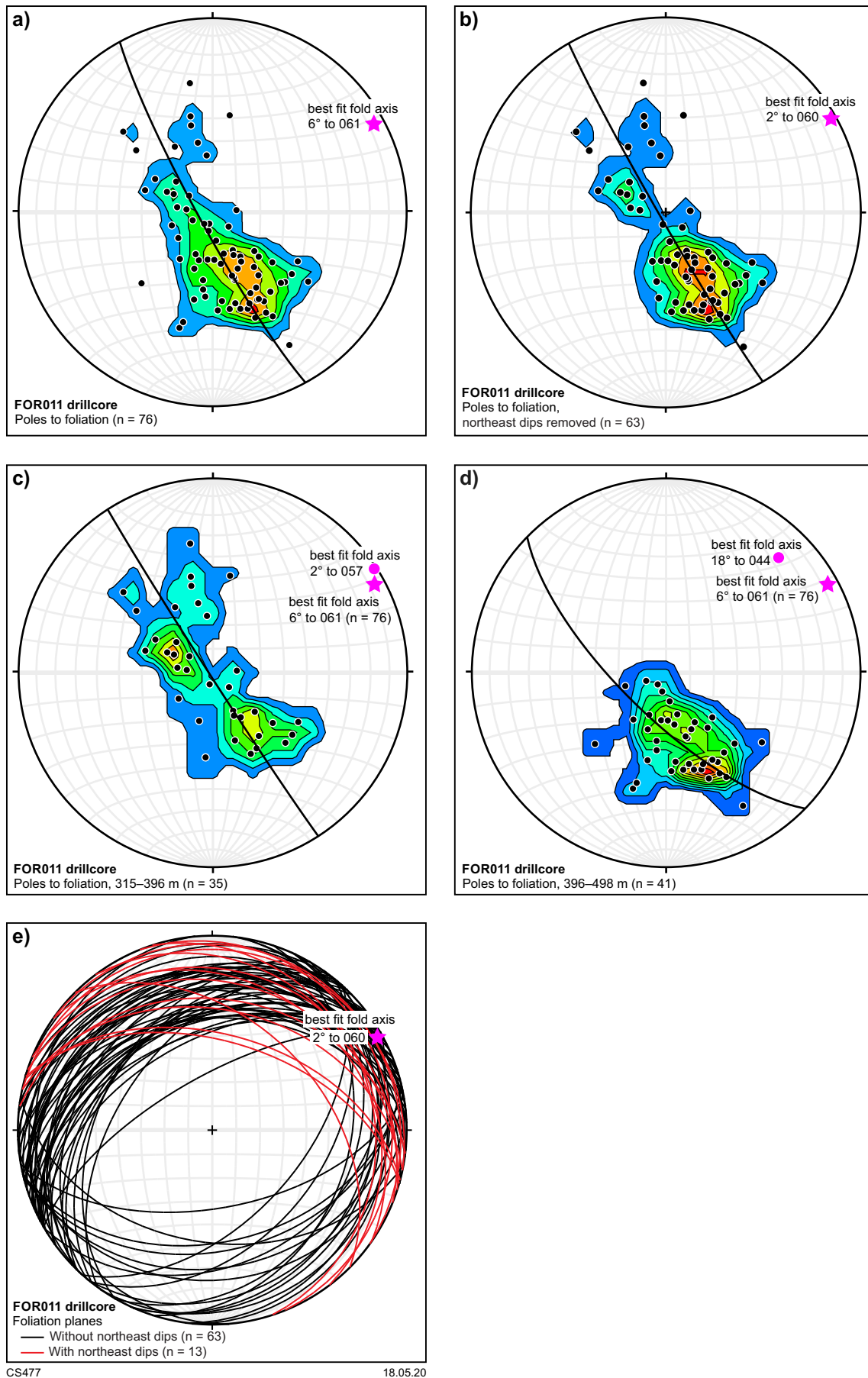


Figure 38. Equal area stereonet analysis of oriented drillcore FOR011: a) poles to foliation and calculated fold axis; b) poles to foliation with northeast-dipping measurements removed, and calculated fold axis; c) poles to foliation of measurements from the upper part of the drillcore; d) poles to foliation of measurements from the lower part of the drillcore; e) foliation planes, with northeast-dipping measurements in red, and calculated fold axis from b)

of gently northeast-plunging folds, and similar to the results in drillcore FOR010. At 409.3 m drilled depth the foliation and layering are folded into a small-scale, gently northeast-plunging, tight fold. This observation agrees with the stereonet analysis. Removing the northeast-dipping measurements, inferred to be fold hinge enveloping surfaces, yields a similar result for the calculated fold axis (Fig. 38b,e). There appears to be a minor difference between the upper and lower parts of the drillcore, where the foliation dips either northwest or southeast in the upper part, and mainly northwest in the lower part (Fig. 38c,d). This may represent a larger-scale fold hinge, estimated to lie at about 398 m drilled depth, corresponding with S_1 measurements of 9° towards 068° and 6° towards 036° (dip, dip direction of hinge zone), and the change to a dominant northwest dip direction below. Throughout the drillcore the foliation is cut by thin granite or pegmatite veins, and veins associated with alteration.

There does not appear to be any obvious relationship to the regional aeromagnetic data, which shows an area of west-northwesterly trending, linear magnetic fabric of moderate intensity (Fig. 29). However, as discussed in the FOR010 section above, northeasterly trending structural features are common in the region. There are also localized, subtle northeasterly trending gravity anomalies within a large area of generally low-gravity response (Fig. 30).

Stratigraphic drillcore FOR012

Drillhole FOR012 is located within a distinct, northeasterly trending wedge about 50 km long and 12 km wide defined by a moderate response magnetic fabric, and within an area of low-to-moderate gravity response (Figs 24, 26, 39). The wedge is interpreted to lie in the hangingwall of, and be truncated by, the Tank Shear Zone. The drillsite lies just south of a linear west-northwesterly trending magnetic feature interpreted to be a mafic dyke, potentially part of the c. 827 Ma Gairdner Dyke Swarm (Wingate et al., 1998). The FOR012 hole was drilled to test whether there was a tectonic boundary between drillsite FOR004 and the combined sites of FOR011 and FOR010, as samples from these drillcores yielded different ages (see Geochronology section).

Undawidgi Supersuite: metasyenogranite, mafic schist and metarhyolite

Drillcore FOR012 contains three distinct units: mylonitic metagranite, grey schist, and mafic to intermediate schist. The top section of the drillcore (310–377 m) is dominated by a fine- to medium-grained (1–4 mm) dark grey to reddish, felsic mylonite with abundant rounded pink feldspar or feldspar aggregate porphyroclasts (average about 4 mm, up to 1 cm) and abundant quartz (or felsic aggregate) eyes and ribbons (Fig. 40a,b). Dark layers generally 1–2 cm thick occur locally, are biotite rich, and in some instances appear to be ultramylonite layers. Some appear to cut the mylonite fabric and could be associated with alteration.

In thin section, the porphyroclasts are mostly subrounded mesoperthite, with less than half of them K-feldspar, and some of which show fine microcline twinning. Locally, albitized plagioclase porphyroclasts exhibit coarse albite twinning that is lightly crackle-brecciated

into subgrains with slightly disrupted orientations. Masses of fine-grained leucoxene, titanite, and magnetite (possibly after titanomagnetite) microporphyroclasts occur locally. The groundmass is a mixture of quartz, tabular to anhedral muscovite, biotite, and aggregates of very fine-grained K-feldspar, albite and quartz. Disseminated metamorphic magnetite occurs mainly in the fine-grained quartzofeldspathic aggregates. Fine-grained, anhedral acid-resistant carbonate (probably ankerite) occurs locally in the groundmass, and tiny carbonate inclusions are disseminated in most feldspar porphyroclasts. This section of drillcore is interpreted as mylonitic to ultramylonitic metasyenogranite. Petrographic analysis in Appendix 5 suggests this section of drillcore may be a metamorphosed porphyritic rhyolite, but when viewed in the drillcore itself the rock resembles a typical mylonitic granite (Fig. 40a,b). There has clearly been considerable grain size reduction, giving the appearance of a ‘glassy’ matrix, and rounding of porphyroclasts due to high strain. In addition, not all thin sections were cut perpendicular to the foliation, so the mylonitic fabric is not always apparent. However, the lower section of the drillcore, described below, likely had a felsic volcanic protolith.

The lower unit is a fine-grained (average 1–3 mm) mostly grey but locally darker and more biotite- and chlorite-rich schist with wispy pale felsic veinlets that are mostly parallel to the foliation, but locally transgress it. Locally, the grey schist contains a dark, millimetre-scale, biotite-rich spaced and anastomosing layering that is either parallel to the foliation or cuts it and also the wispy felsic veinlets (Fig. 40c,d). The schist is strongly deformed and mostly mylonitic. It comprises 0.5 – 5 mm, mostly eye-shaped, albitized plagioclase porphyroclasts wrapped by the foliation, which is dominated by variable proportions of white mica, and locally by chloritized biotite. Fine-grained quartz, albite and titanite are minor phases. Magnetite is common and occurs as microphenocrysts or is concentrated into <2 mm layers parallel to the foliation. One example (GSWA 219003) contains porphyroclasts of <2 mm recrystallized bipyramidal and round quartz. In this sample, the groundmass comprises fine white mica and minor, partly chloritized biotite, quartz, minor albite and titanite. Minor acid-resistant carbonate is probably ankerite, and metamorphic magnetite is locally altered to hematite and possibly ankerite. Very minor wispy lenses of fine rutile are probably relics of igneous Fe–Ti oxide microphenocrysts. Thin veins that cut the foliation at high angles consist of chlorite, K-feldspar, calcite, and minor ankerite or mixtures of chlorite, epidote and quartz.

This unit is interpreted as a felsic volcanic rock, possibly a metarhyolite, based on the overall fine grain size and variable texture that could be inherited to some degree from the protolith. In thin section, there are no coarse grains or masses of fine grains that could have been relicts of coarse igneous biotite. Alternatively, the unit is a strongly deformed to mylonitic metamonzogranite and has virtually the same granitic protolith as the unit above but is less porphyritic. Geochemically, there is little distinction between these two units (see Whole-rock geochemistry).

Below the upper metasyenogranite are several discrete horizons of mafic to intermediate schist that is similar in composition to the grey schist but contains a greater proportion of micaceous minerals, and possibly some fine amphibole (Fig. 40e,f,g).

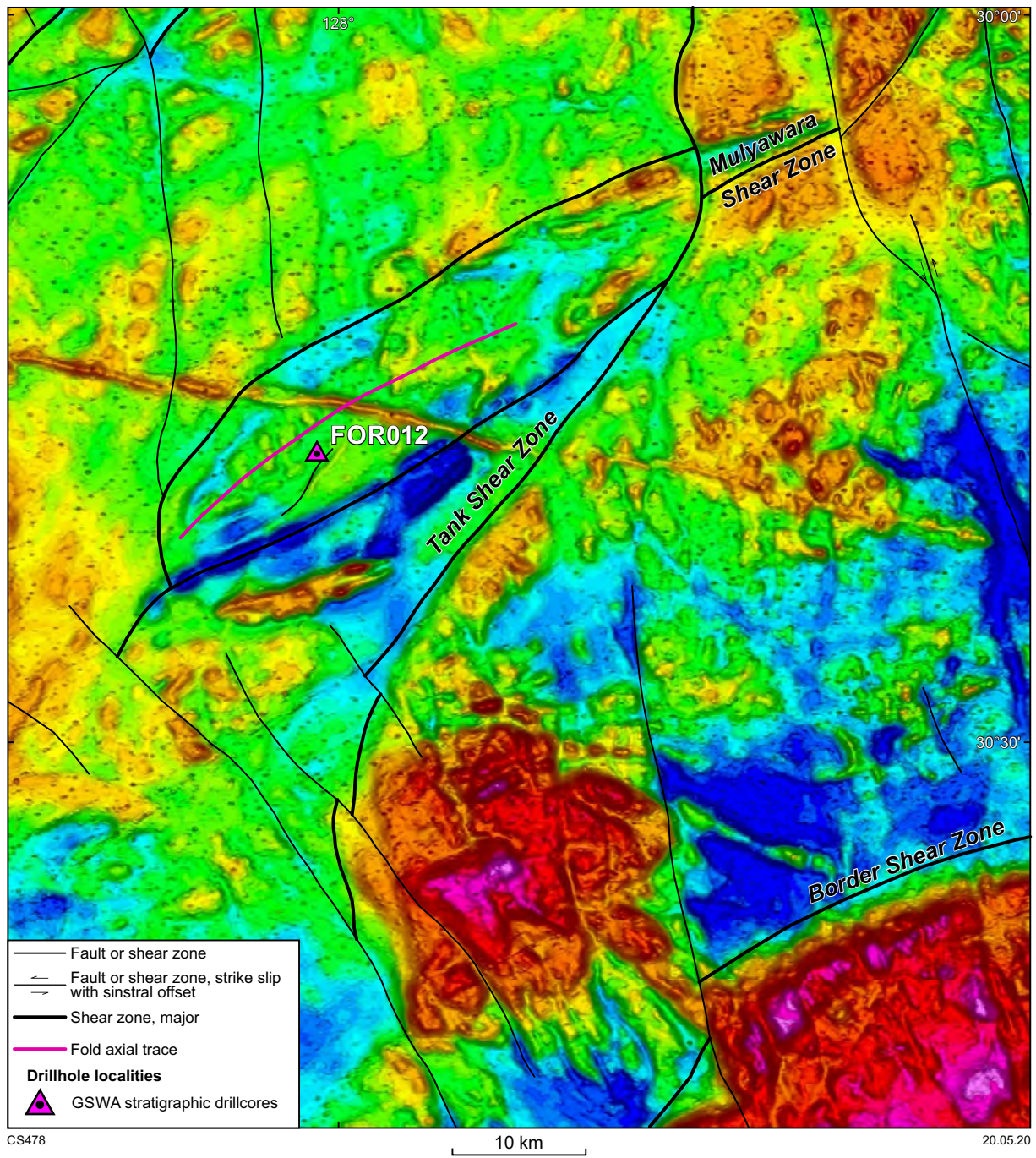


Figure 39. Geophysical images of drillsite FOR012 showing interpreted major structures: a) reduced-to-pole aeromagnetic image

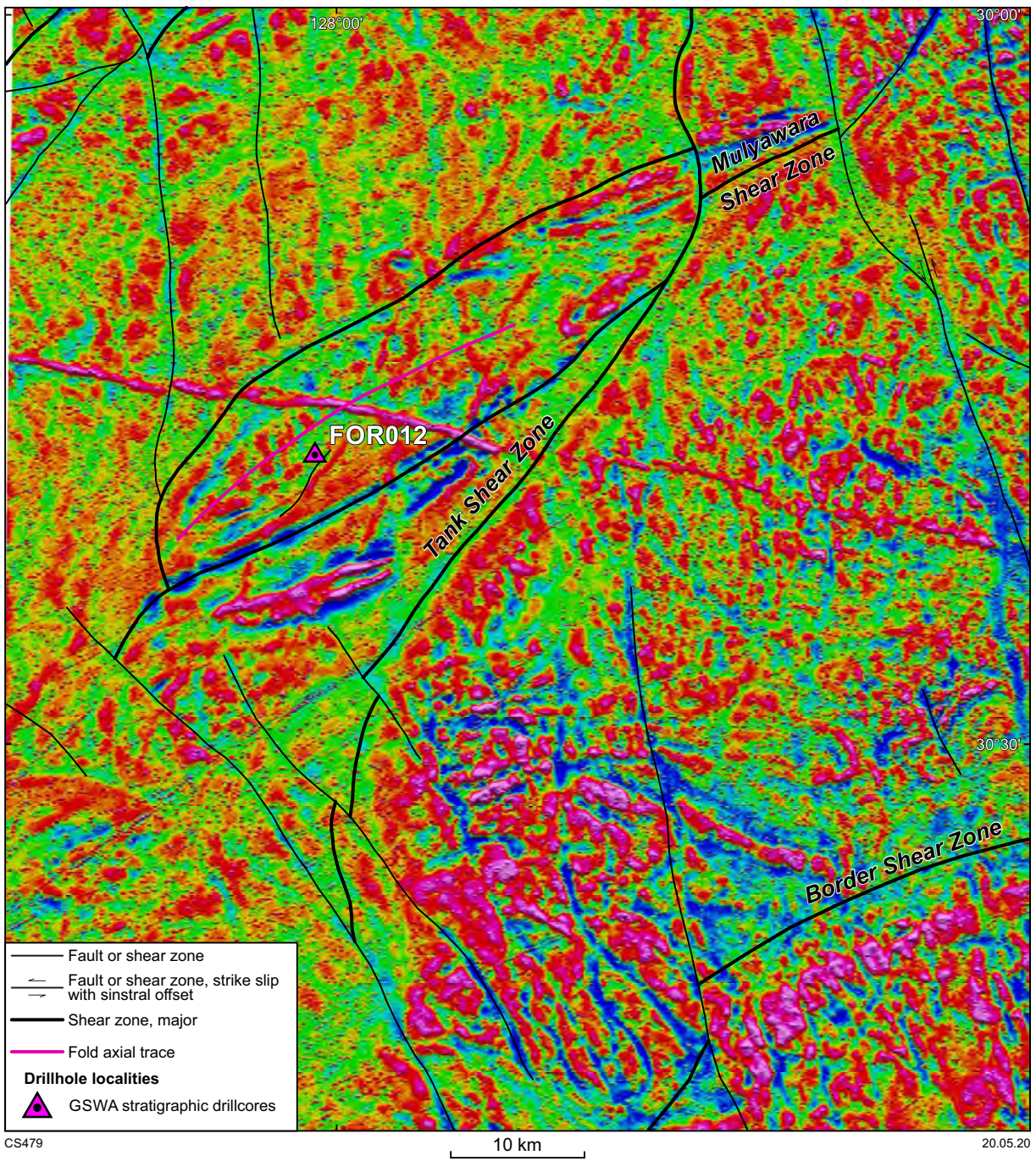


Figure 39. Continued: b) reduced-to-pole first vertical derivative aeromagnetic image

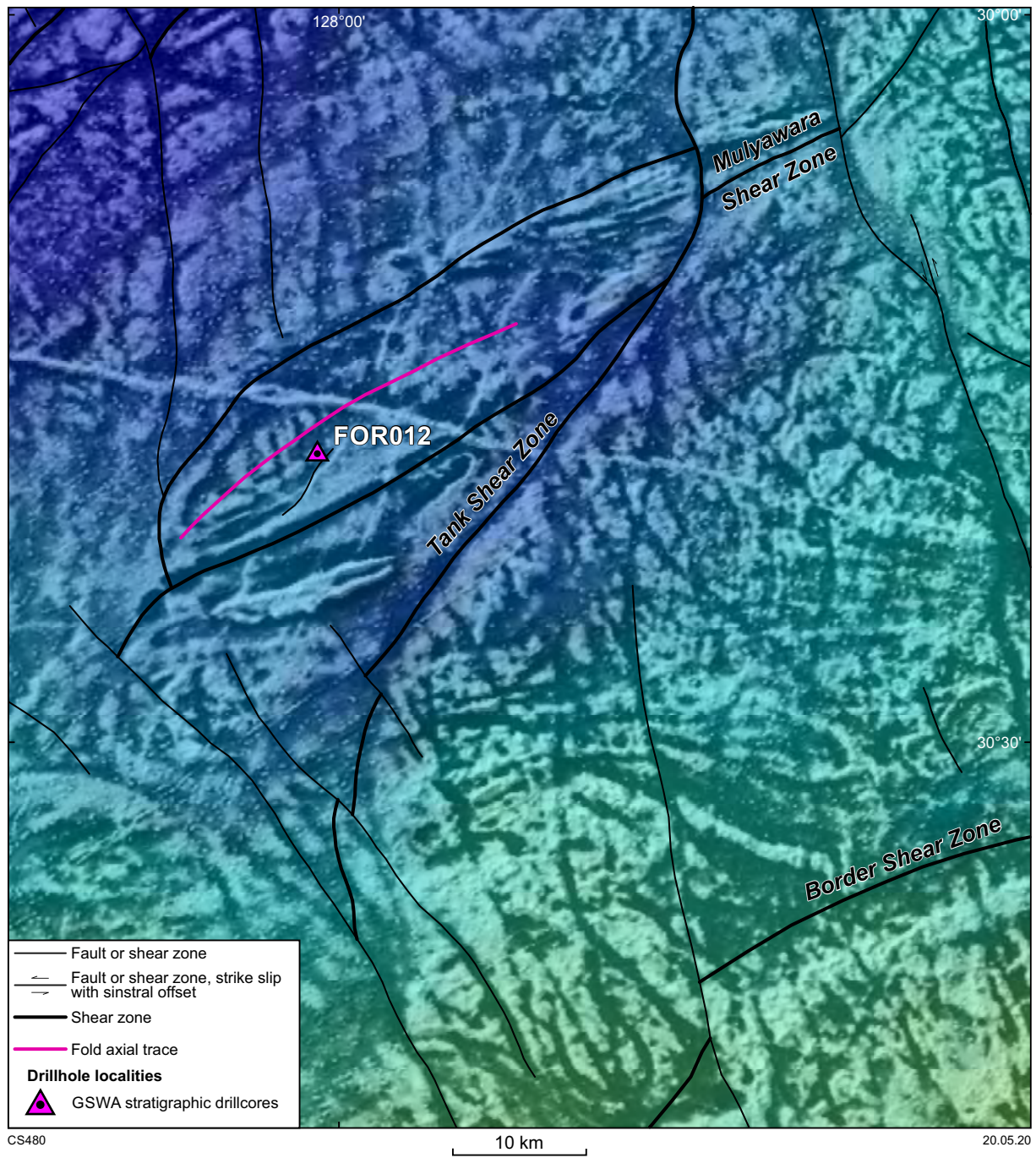


Figure 39. Continued: c) drape image of gravity (colour) and reduced-to-pole, first vertical derivative aeromagnetic data (greyscale)

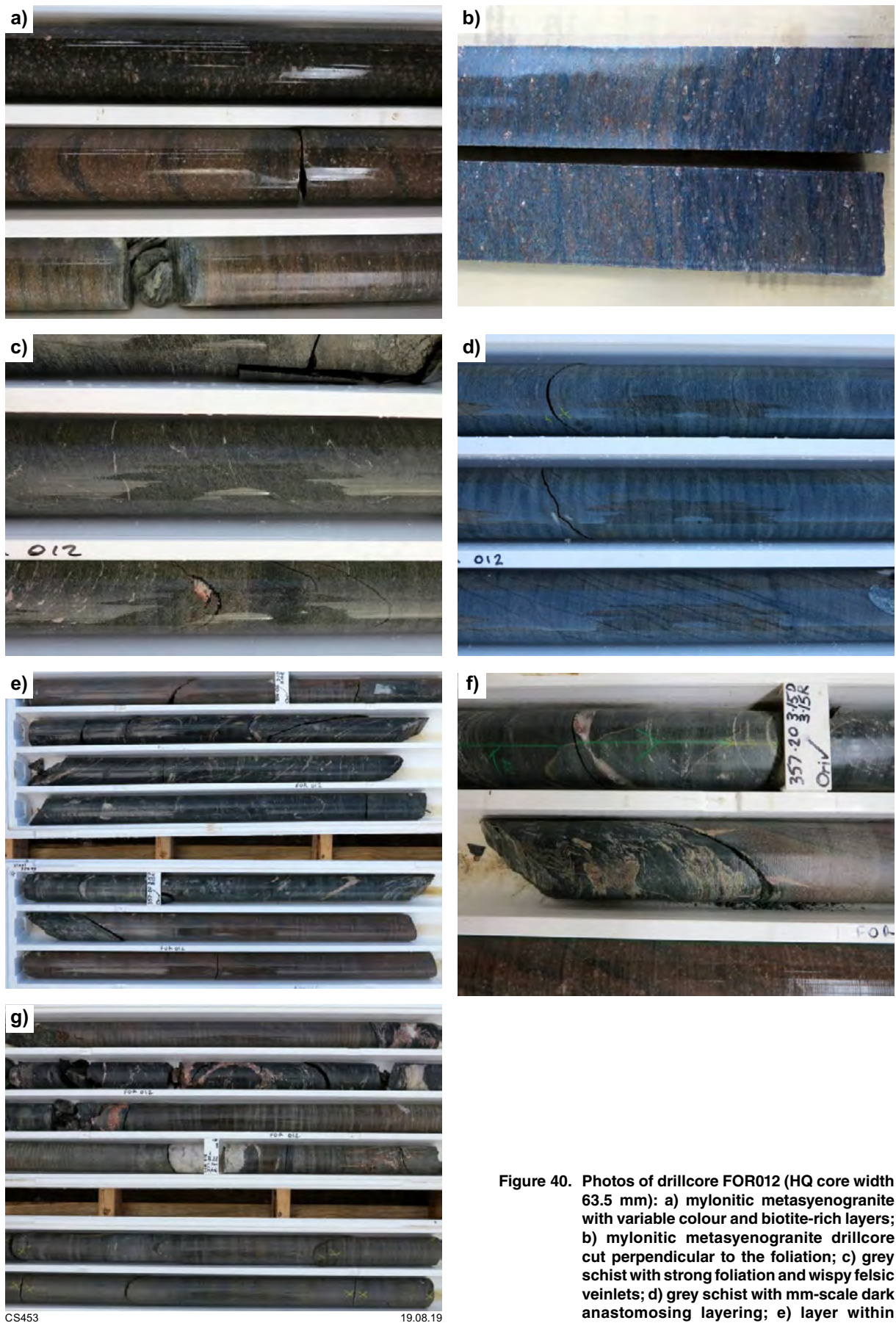


Figure 40. Photos of drillcore FOR012 (HQ core width 63.5 mm): a) mylonitic metasyenogranite with variable colour and biotite-rich layers; b) mylonitic metasyenogranite drillcore cut perpendicular to the foliation; c) grey schist with strong foliation and wispy felsic veinlets; d) grey schist with mm-scale dark anastomosing layering; e) layer within mylonitic metasyenogranite of folded mafic schist with wispy felsic veins; f) close-up of part of e), showing the sharp contact and folds within the mafic schist; g) transition from red to grey mylonitic metasyenogranite (top) to mafic schist, to grey schist

CS453

19.08.19

It has abundant white to pink wispy layering parallel to a very strong, anastomosing fabric with lozenges, some of which contain intrafolial folds in the necks. Locally, the wispy layering is tightly folded with the strong foliation.

Acid-resistant carbonate consistently present throughout FOR012 probably sets an upper limit to the metamorphic grade at the greenschist–amphibolite transition, and the biotite zone of the greenschist facies is the best estimate for the metamorphic grade of the shear zone this drillhole has intersected.

Sulfides and alteration

The mylonitic metasyenogranite contains thin, pink felsic veins, locally with minor chalcopyrite, and very thin (<1 mm) dark and/or red veins, locally with epidote rims. It also contains minor to locally abundant quartz or quartz–epidote veins, thin chlorite veins, locally with biotite or quartz, and thin chlorite–muscovite–epidote veins and networks, all of which cut the mylonite fabric. The mafic to intermediate schist has thin quartz or quartz–biotite–chlorite veins that cut the foliation. The grey schist has thin biotite–chlorite–quartz veins, dark veins and white veins, all of which cut the foliation. These veins locally contain minor epidote, pyrite and chalcopyrite. Thin quartz veins, dark hairline veins and felsic veins also cut the foliation. Locally, quartz-rich felsic (reddish) veins are up to 4 cm thick. Towards the bottom of the hole, where the grey schist is more greenish, there is possibly pervasive chlorite alteration.

In the grey schist, minor disseminated fine pyrite and associated anhedral chalcopyrite occur locally in the schistose groundmass, and are also typically associated with magnetite. Sulfides also occur in the thin dark wispy layering below 448 m, and in thin veins. For example, GSWA 206800 (435.23 – 435.46 m) is a dark grey schist with sulfide minerals parallel to the foliation and in hairline veinlets that contain carbonate–quartz–pyrite–magnetite–chalcopyrite. GSWA 206795 (394.67 – 394.92 m) is a grey schist with abundant thin quartz–chlorite veins and contains minor disseminated <0.2 mm pyrite and associated anhedral chalcopyrite in the schistose white mica-dominated matrix. This sample contains 1172 ppm Cu (25 cm $\frac{1}{2}$ HQ core). GSWA 206797 (406.61 – 406.77 m) is a grey schist with hairline veinlets and contains disseminated, lightly hematized octahedral <1 mm magnetite that forms about 1% of the rock. Cube-shaped pyrite, up to 1 mm in size, is concentrated in quartz–carbonate-rich lenses parallel to the foliation. Rarer <0.2 mm chalcopyrite is associated with pyrite and magnetite. More finely grained pyrite in a crosscutting 0.2 mm ankerite–quartz veinlet is probably younger. GSWA 206799 (422.07 – 422.29 m) is a grey schist with multiple thin quartz veins and is almost a breccia. It contains disseminated <1 mm roughly cube-shaped pyrite, which is rare compared with disseminated magnetite hematized at its margins and associated with fine rutile or anatase. Rare <0.1 mm anhedral chalcopyrite is associated with pyrite, but also occurs in and near sheeted veinlets that cut the foliation. The veinlets contain acid-resistant carbonate (probably ankerite) and calcite, locally contain <0.2 mm roughly prismatic to anhedral quartz, and are lined with fine chlorite.

Structural analysis of the FOR012 drillcore

The metasyenogranite in the upper part of the drillcore has a mylonitic foliation with a dominant, moderate northwesterly dip and less common southeasterly dip, and a subhorizontal to gentle northeasterly plunging mineral lineation, measured at 15° towards 060° (Fig. 41a). This lineation is rodded to some degree, so the mylonite is between an L-tectonite and L–S tectonite. The asymmetry of the porphyroclasts indicate both sinistral and dextral shear sense, suggesting a strong flattening and/or stretching component. Minor folds in this unit have a measured fold axis of 5° towards 040° and axial plane of 60° towards 130° (dip, dip direction). The minor switches in dip, from northwest to southeast, are likely to be due to S-folds.

The lower felsic unit also has a mylonitic foliation with moderate dip to both the southeast and northwest, and a measured mineral lineation of 3° towards 050° (Fig. 41b). The layers of mafic schist contain similar structures, with a dominant, moderate southeasterly dipping foliation, measured mineral lineation of 10° towards 049°, and tight folds plunging 5–10° towards 045–060° (Fig. 41c). Stereonet analysis of a best-fit great circle from poles to planes of the foliation in each unit gives calculated fold axes of 2° towards 048° (metasyenogranite), 1° towards 046° (grey schist), and 3° towards 226° (mafic schist). These data suggest all units have been affected by the same deformation event, consistent with similar metamorphic conditions and alteration of the matrix assemblages as the mylonite was formed. The mylonite itself appears to be folded about an upright, shallow northeasterly plunging axis subparallel to the mineral lineation, with a shallow to moderate southeasterly dipping axial plane. Stereonet analysis of a best-fit great circle from poles to foliation planes in all units gives a calculated fold axis of 2° towards 047° (Fig. 41d). On the larger scale, the fold geometry may be indicative of the overall shape of the northeasterly trending wedge that is visible in the aeromagnetic data (Fig. 39).

Exploration drillcores

In this section, we summarize the lithological units and relationships from sparse pre-existing exploration drillcores (Fig. 3, Table 3) to provide background information for samples collected for geochronology, whole-rock geochemistry, isotope analysis and petrography. The results are presented in the relevant sections below, or in previous publications (Spaggiari et al., 2015a, 2018; Kirkland et al., 2017).

Connie Sue Formation

The EIS co-funded drillcore NDDH002 was drilled by Teck Australia to test for base metals within an anomalous area of strong magnetic response defined as the NSD prospect (Figs 3, 17, 42; Table 3; Tillick, 2011b). Teck Australia also drilled NDDH001 about 10 km southwest of NDDH002, but this hole was terminated within the top of granitic basement due to logistical issues. The NDDH002 drillhole lies about 50 km west of the Rodona Shear Zone in the north–central

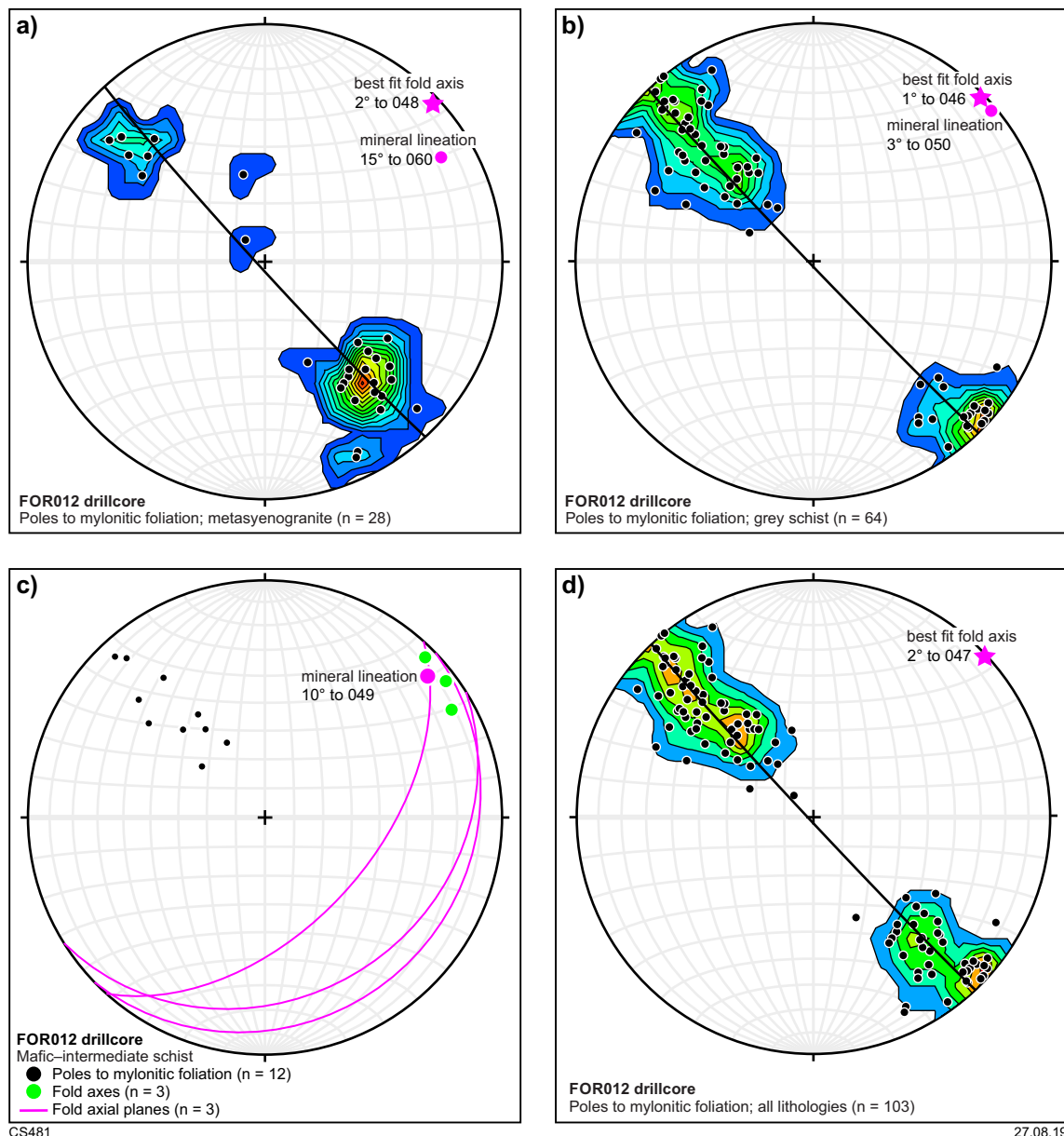


Figure 41. Equal area stereonet analysis of oriented drillcore FOR012: a) mineral lineation, poles to mylonitic foliation and calculated fold axis in mylonitic metasyenogranite, upper section of drillcore; b) mineral lineation, poles to mylonitic foliation and calculated fold axis in mylonitic grey schist, lower section of drillcore; c) mineral lineation, fold axes and poles to mylonitic foliation in mafic to intermediate schist; d) poles to mylonitic foliation and calculated fold axis in all lithologies, combined

region of the eastern Nornalup Zone of the Albany–Fraser Orogen, a region which also lies entirely under cover.

The NDDH002 drillcore is dominated by Ca–Mg-rich to Fe-rich metasedimentary rocks, mostly calc-silicate schists, interlayered with metabasalt and/or mafic metavolcaniclastic rocks (Fig. 43a, Table 4). This succession is intruded by weakly deformed, equigranular, pink metamonzogranite dated at 1169 ± 6 Ma (GSWA 192562, Wingate et al., 2018c) and undeformed, strongly altered, coarse-grained leucogabbro dated at 1180 ± 8 Ma (baddeleyite from GSWA 192563, Wingate et al., 2018d,e; Fig. 43b–d). The calc-silicate schist is fine to medium grained, pale green to grey, thinly layered to laminated, and is dominated by aggregates of clinopyroxene with typically lesser orthopyroxene, olive to green hornblende,

abundant Fe oxide minerals (mostly magnetite) and locally sulfide minerals (mostly pyrrhotite and/or pyrite, with sparse chalcopyrite), and plagioclase. Minor actinolite, cummingtonite, carbonate, biotite, quartz, rare garnet and trace apatite occur throughout, and layers of quartz–biotite–graphite schist occur locally (see also Tillick, 2011b). Thin quartz–carbonate veins also occur locally. The metabasalt is fine to medium grained (0.5 – 2 mm), thinly layered to laminated and dominated by clinopyroxene (locally overgrown by pleochroic olive-brown to green hornblende and minor actinolite), lesser orthopyroxene, plagioclase and Fe oxide minerals (probable ilmenite and/or sulfide), with minor biotite and epidote. It is locally cut by thin chlorite veins. The layering in the metabasalt and calc-silicate is mostly concordant, but locally oblique at some contacts, indicating it is primary, rather than metamorphic.

Table 3. Drillhole information for exploration drillcores from the Eucla basement

<i>Drillhole ID</i>	<i>Drilling; prospect</i>	<i>Company</i>	<i>Geophysical domain characteristics</i>	<i>Stratigraphic units intersected</i>	<i>Province</i>	<i>Drillcore type</i>	<i>Hole azimuth (°)</i>	<i>Inclination (°)</i>	<i>Depth to basement (m)</i>	<i>Basement drillcore (m)</i>	<i>Total depth of hole (m)</i>	<i>GDA 94 latitude/longitude</i>
NDDH002	EIS co-funded; NSD	Teck Australia Pty Ltd	Strong, linear magnetic anomaly; moderate gravity response	Connie Sue Formation, Esperance Supersuite	Kepa Kurl Booya	Diamond	315	-70	259.00	117.50	376.50	-30.1738110°S 125.4103400°E
BKD01	EIS co-funded; Burkin	Gunson Resources Limited	Folded, stripy, high-intensity magnetic layering; strong gravity response	Sleeper Camp Formation	Madura	Diamond	N/A	vertical	270.00	147.80	417.80	-30.3545483°S 126.2093848°E
BKD02	EIS co-funded; Burkin	Gunson Resources Limited	Folded, stripy, high-intensity magnetic layering; strong gravity response	Sleeper Camp Formation	Madura	Diamond	N/A	vertical	248.00	157.00	405.00	-30.3686979°S 126.1979682°E
LNGD001	Donated; Loongana	Helix Resources Limited	Folded, stripy, moderate-intensity magnetic layering; strong gravity response	Haig Cave Supersuite	Madura	Diamond	N/A	vertical	275.20	368.10	643.30	-30.8182890°S 126.4164610°E
LNGD002	Donated; Loongana	Helix Resources Limited	Folded, stripy, moderate-intensity magnetic layering; strong gravity response	Haig Cave Supersuite	Madura	Diamond	N/A	vertical	304.30	290.20	594.50	-30.8002850°S 126.4276730°E
LNGD003	Donated; Loongana	Helix Resources Limited	Folded, stripy, moderate-intensity magnetic layering; strong gravity response	Haig Cave Supersuite	Madura	Mud rotary collar; diamond	N/A	vertical	311.00	370.00	508.11	-30.8162160°S 126.4079457°E
LNGD003A	Donated; Loongana	MRG Metals Ltd	Folded, stripy, moderate-intensity magnetic layering; strong gravity response	Haig Cave Supersuite	Madura	Diamond	N/A	-89	Wedge off LNGDH003	370.00	370.00	-30.8162160°S 126.4079457°E
HDDH001	EIS co-funded; Haig	Teck Australia Pty Ltd	Folded, stripy, moderate-intensity magnetic layering; strong gravity response	Haig Cave Supersuite	Madura	Diamond	315	-80	426.90	209.10	636.00	-31.0534260°S 126.0790800°E
HDDH002	EIS co-funded; Haig	Teck Australia Pty Ltd	Linear, intense magnetic anomaly; strong gravity response	Haig Cave Supersuite	Madura	Diamond	315	-70	313.60	170.10	483.70	-30.9451330°S 126.1035300°E
SDDH001	EIS co-funded; Serpent	Teck Australia Pty Ltd	Linear, intense magnetic anomaly; strong gravity response	Haig Cave Supersuite	Madura	RC collar; diamond	N/A	vertical	480.00	105.40	585.40	-31.2138600°S 126.0715400°E
SDDH002	EIS co-funded; Serpent	Teck Australia Pty Ltd	Linear, intense magnetic anomaly; strong gravity response	Haig Cave Supersuite	Madura	RC collar; diamond	N/A	vertical	417.00	96.20	513.20	-31.2276100°S 126.0816100°E
Hannah 1	Donated; Hannah	Buffalo Gold Ltd	Elongate, boudin-shaped intense magnetic anomaly; strong gravity response	Esperance Supersuite	Kepa Kurl Booya (in Rodona Shear Zone)	Diamond	N/A	vertical	420.00	234.00	654.00	-32.1657446°S 125.1254261°E
MORCD001	Donated; Moodini	Venus Metals Corporation Ltd	Linear, strong magnetic anomaly; strong gravity response; within Mundrabilla Shear Zone	Moodini Supersuite	Madura	RC collar then diamond	N/A	vertical	228.00	381.30	609.70	-31.9113970°S 127.4162380°E
MORCD002	Donated; Moodini	Venus Metals Corporation Ltd	Linear, strong magnetic anomaly; strong gravity response; within Mundrabilla Shear Zone	Moodini Supersuite	Madura	RC collar then diamond	N/A	vertical	242.00	448.30	690.30	-31.9132750°S 127.4163220°E
Eucla No. 1	Donated; Eucla No. 1	Alliance Petroleum	Strong ovoid magnetic anomaly; moderate gravity response	Moodini Supersuite	Coompana	Chips from base of well	N/A	vertical	220.00	Chips from base of well	220.00	-31.8784084°S 128.2224979°E

Table 4. Summary of lithological and structural characteristics of metavolcanic and metasedimentary rocks of the Connie Sue Formation, Sleeper Camp Formation and coastal exposures of the Malcolm Metamorphics

<i>Prospect or location; Drillhole ID</i>	<i>Stratigraphic unit</i>	<i>Lithology</i>	<i>Mineralogy</i>	<i>Metamorphic facies</i>	<i>Structural features</i>
NSD; NDDH002	Connie Sue Formation	Foliated metabasalt; fine grained (0.5 – 2 mm); laminated to thinly layered	Clinopyroxene (locally overgrown by olive-brown to green hornblende, minor actinolite), lesser orthopyroxene, plagioclase, Fe oxides (probable ilmenite and/or sulfide); minor biotite, epidote	Amphibolite	Variably dipping, moderate to strong foliation, mostly subparallel to layering
NSD; NDDH002	Connie Sue Formation	Calc-silicate schist; fine to medium grained, laminated to thinly layered	Clinopyroxene with lesser orthopyroxene, olive to green hornblende, Fe oxides (mostly magnetite), plagioclase; minor actinolite, cummingtonite, carbonate, biotite, quartz, garnet, trace apatite; pyrrhotite and/or pyrite, sparse chalcopyrite; layers of quartz–biotite–graphite schist	Amphibolite	Variably dipping, moderate to strong foliation, mostly subparallel to layering
Burkin; BKD01 and 02	Sleeper Camp Formation	Mafic schist (metabasalt or mafic volcaniclastic); fine to medium grained (0.5 – 3 mm, locally coarser); massive to thinly layered	Green-blue hornblende (probably after pyroxene), sericite–epidote altered plagioclase; ilmenite, magnetite, titanite; late chlorite, quartz, epidote	Amphibolite	Weak to moderate intensity foliation; layering and foliation folded into small-scale, mostly subhorizontal open to tight folds
Burkin; BKD01 and 02	Sleeper Camp Formation	Metadolerite; foliated, fine to medium grained (1–5 mm; hornblende aggregates locally up to 10 mm)	Plagioclase, hornblende (with rare inclusions of quartz), ilmenite, magnetite, biotite, titanite; late chlorite, epidote, sericite, apatite	Amphibolite	Moderate intensity foliation
Burkin; BKD01 and 02	Sleeper Camp Formation	Schistose metasedimentary rock; fine to medium grained (typically 1–4 mm); layered to laminated	Quartz, chlorite, (probably after biotite), garnet, hematite, magnetite; apatite, pyrite	Amphibolite	Small-scale, mostly subhorizontal open to tight folds; weakly developed axially planar foliation defined by chlorite or chloritized amphibole; possible slump folds; refolded folds
Burkin; BKD01 and 02	Sleeper Camp Formation	Fe-rich, schistose metasedimentary rock; fine to medium grained (typically 1–4 mm); layered to laminated	Quartz, magnetite (or locally hematite), small pale yellow garnets, brown-green or blue-green hornblende (or locally actinolite ± cummingtonite); minor biotite, pyrite, chalcopyrite	Amphibolite	Small-scale, mostly subhorizontal open to tight folds; weakly developed axially planar foliation defined by chlorite or chloritized amphibole; possible slump folds; refolded folds
Burkin; BKD02	Sleeper Camp Formation	Crosscutting granite veins	Recrystallized quartz, plagioclase, K-feldspar; small garnet crystals, biotite, muscovite, fibrous sillimanite	Amphibolite	Typically layer-parallel and folded, but also locally cut the folded layering, or occur within axial planes of folds
Burkin; BKD01 and 02	Sleeper Camp Formation	Crosscutting basalt or dolerite; very fine grained (<20–50 µm; locally up to 0.2 mm)	All secondary phases: chlorite, quartz, possible quartzofeldspathic aggregates, Fe oxide	Lower greenschist	Locally foliated
Point Malcolm coastal exposures	Malcolm Metamorphics	Dark grey to black, foliated metabasalt with thin pale laminations or layers	Green-brown hornblende, clinopyroxene, plagioclase, ilmenite ± biotite, titanite, epidote, garnet, anthophyllite, quartz; pale layers dominantly plagioclase	Upper amphibolite to granulite	Steeply southwest plunging but locally northeast plunging, east-northeast trending, tight to isoclinal second generation folds
Point Malcolm coastal exposures	Malcolm Metamorphics	Calc-silicate; altered metabasalt	Garnet, quartz, clinopyroxene, plagioclase ± epidote, calcite, hornblende, wollastonite, clinozoisite; accessory titanite, magnetite, pyrite, chalcopyrite	Upper amphibolite to granulite	Steeply southwest plunging but locally northeast plunging, east-northeast trending, tight to isoclinal second generation folds
Point Malcolm coastal exposures	Malcolm Metamorphics	Psammitic and semipelitic schist	Quartz, K-feldspar, plagioclase, biotite; locally migmatitic	Upper amphibolite to granulite	Steeply southwest plunging but locally northeast plunging, east-northeast trending, tight to isoclinal second generation folds
Point Malcolm coastal exposures	Malcolm Metamorphics	Pelitic schist	Typically migmatitic; mesosomes contain biotite, quartz, K-feldspar, plagioclase, garnet ± muscovite, spinel, sillimanite	Upper amphibolite to granulite; 750°C and 4 kbar	Steeply southwest plunging but locally northeast plunging, east-northeast trending, tight to isoclinal second generation folds

NOTE: Additional information from Clark (1999), Clark et al. (2000), Tillick (2011a,b), Adams (2012) and Harley (2010)

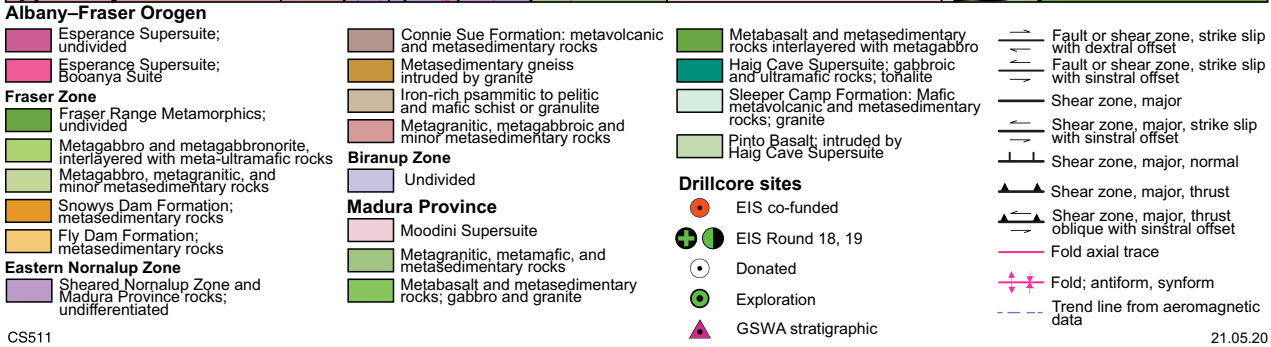
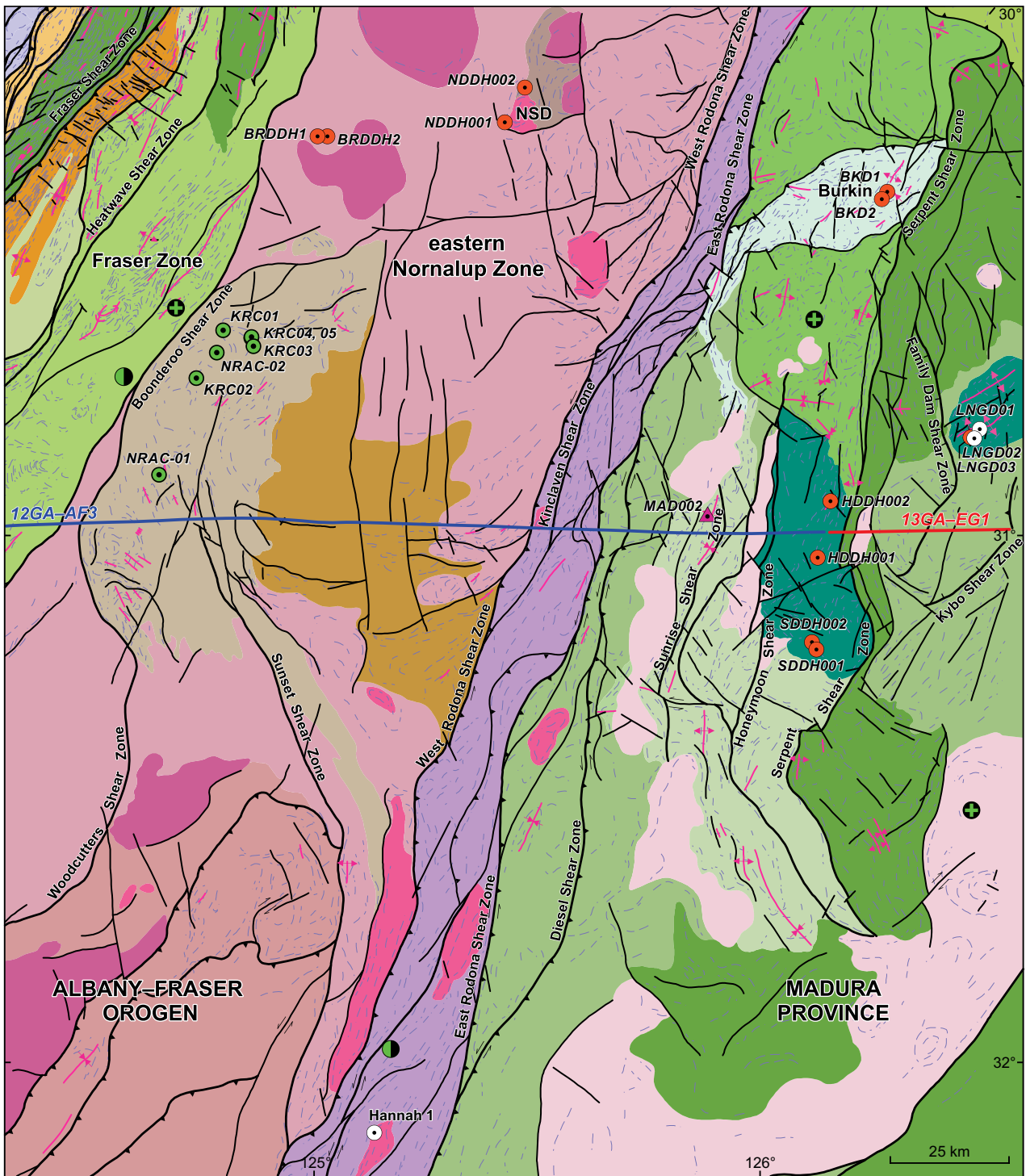
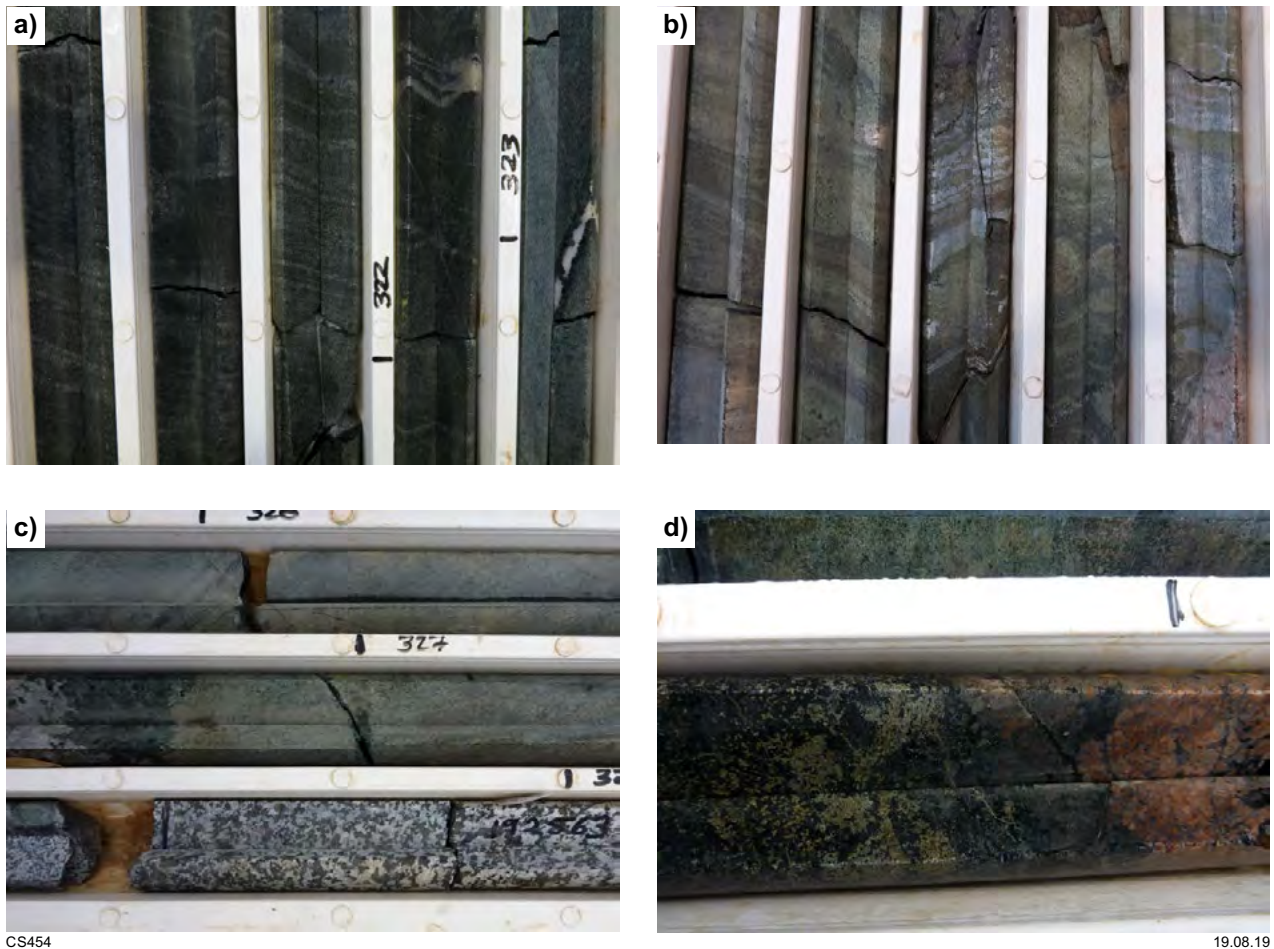


Figure 42. Interpreted bedrock geology and structures in the northern part of the eastern Nornalup Zone (modified from Spaggiari, 2016)



CS454

19.08.19

Figure 43. Photos of the Connie Sue Formation in drillcore NDDH002 (NQ core width 47.6 mm): a) layered mafic schist and calc-silicate (right-hand drillcore); b) layered Fe-rich sedimentary schist and crosscutting pink syenogranite (lower right); c) strongly altered leucogabbro crosscutting layering in calc-silicate schist; d) sulfides in mafic schist adjacent to pink syenogranite. NQ core is 47.6 mm diameter

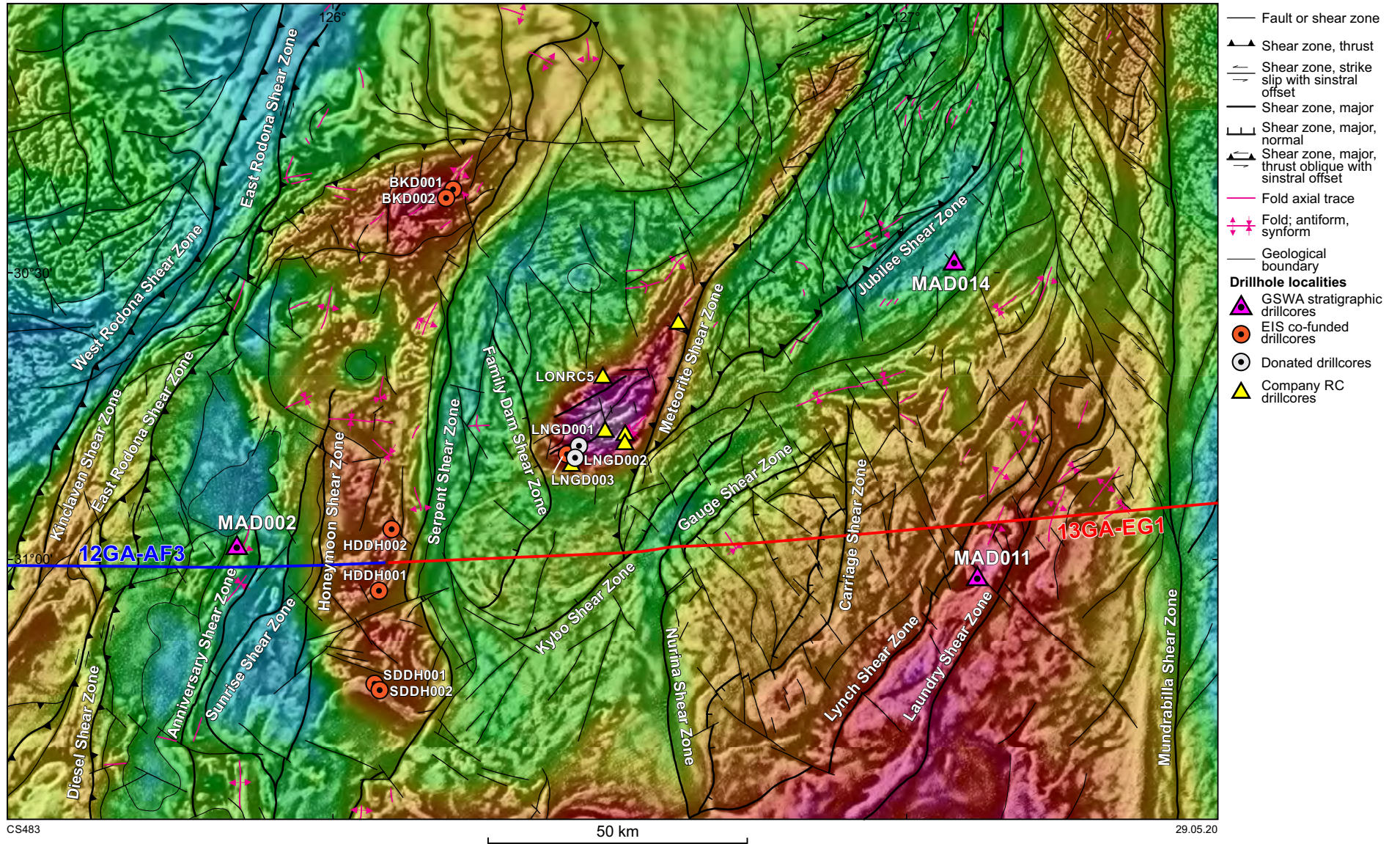


Figure 44. Structural interpretation and drillsite locations of the Loongana, Haig and Serpent prospects plotted on a drape image of gravity (colour) and reduced-to-pole, first vertical derivative aeromagnetic data (greyscale). Warm colours represent a strong gravity response, cool colours low response

A structurally distinct, west- to northwest-trending zone of comparable strong magnetic and gravity response southwest of the NSD prospect, bounded by the Woodcutters Shear Zone and in the vicinity of the Sunset Shear Zone, suggests similar rocks may cover a significant portion of this region (Figs 3, 42). The area near the northwestern end of the Sunset Shear Zone has been intersected by exploration drillholes. Magnetite-bearing mafic granulite (NRAC-01) and Mn-rich and Fe-rich sedimentary gneiss with the assemblage quartz–magnetite–spessartine garnet–phlogopite occur in drillhole NRAC-02 (Stephens, 2000) and occurrences of fine-grained mafic and quartz-rich amphibolite, layered Fe-rich metasedimentary rocks with elevated Mn and P values, and pelitic to psammitic schist occur in various drillholes (Smit, 2009). This region could be interpreted as an overthrust package of Madura Province rocks, potentially as a leading edge, frontal thrust preceding the Rodona Shear Zone itself. Alternatively, it could be an in situ component of the eastern Nornalup Zone, and the geophysically anomalous area in the vicinity of the NSD prospect could be part of a larger succession of strongly magnetic mafic and metasedimentary rocks that occur within the structurally distinct, west- to northwest-trending region southwest of NSD (Figs 3, 17, 42).

Sleeper Camp Formation

Two EIS co-funded drillholes, BKD01 and BKD02, were drilled by Gunson Resources to target a cluster of magnetic highs and a northeasterly trending gravity anomaly defined as the Burkin prospect for Ni–Cu mineralization (Figs 3, 44, Table 3; Harley, 2010). The magnetic anomalies are interpreted as a series of northeast-trending tight folds that are openly refolded by steeply plunging, west-northwesterly trending folds, similar to those described for the MAD002 drillcore location (Fig. 17). The interpreted trace of the Sleeper Camp Formation is folded about a west-northwesterly trending, open fold hinge. This folded package occurs within a northwest-vergent thrust sheet that is crosscut by the Rodona Shear Zone.

The drillcores comprise fine- to medium-grained (typically 1–4 mm), layered to laminated, sedimentary schists of variable composition, including graphite-bearing layers, Fe-rich horizons similar to banded iron-formation (BIF), and Mn-rich layers (Fig. 45a, Table 4, Appendix 8). These are interlayered with fine- to medium-grained (typically 0.5 – 3.0 mm), generally thinly layered mafic schist with a moderate intensity foliation (Fig. 45b), and fine- to medium-grained (typically 1–4 mm) metadolerite (Fig. 45c). All are metamorphosed to amphibolite facies. The sedimentary schists are dominated by quartz, and the Fe-rich horizons contain magnetite (or locally hematite), pale yellow garnet, brown-green or blue-green hornblende (or locally actinolite±cummingtonite), and minor biotite, pyrite and chalcopyrite. The mafic schist is dominated by green-blue hornblende (probably after pyroxene), fresh to sericitized or saussuritized (sericite–epidote altered) plagioclase, ilmenite, and fine-grained magnetite accompanied by titanite and epidote (cf. Harley, 2010). The metadolerite has a moderate intensity foliation and typically contains plagioclase, hornblende, magnetite, biotite, chlorite, epidote and sericite. The thinly layered mafic schist is likely to be a volcanic or volcanoclastic component of the succession. Late chlorite,

locally as massive aggregates of very fine, decussate, chlorite crystals and quartz, quartz veins, epidote and possibly smectite indicate hydrothermal alteration (cf. Harley, 2010).

The contacts are typically sharp or brecciated, although locally they are obscured by alteration. Brecciated contacts contain jigsaw-fit mafic clasts, and the breccia zones are locally up to 15 cm thick (Fig. 45d). They typically contain epidote veins and occur at the base and tops of mafic schist layers. They are clearly not tectonic breccias or fault gouges, and could be interpreted as autobreccias formed by the deposition of mafic subvolcanic flows into the sedimentary pile. The succession is suggestive of below wave-base, possibly deep sea, locally Fe- and Mn-rich sedimentation associated with basaltic magmatism, potentially as interflow sediments adjacent to exhalative volcanic activity.

Quartzofeldspathic layers, patches and wispy stringers occur at various horizons in the sedimentary and mafic schists. These are typically layer parallel and folded, but also locally cut the folded layering, or occur within axial planes of folds. Although initially interpreted as local migmatization (Kirkland et al., 2012b), further work indicates that they are granite veins (Fig. 45e). They lack selvages typical of in situ melts, and the mineral assemblages and textures in both drillcores indicate amphibolite facies metamorphism. The granite veins contain assemblages dominated by recrystallized quartz with ragged grain boundaries and well-developed undulose extinction, plagioclase and K-feldspar, and locally, small garnets, biotite, muscovite and fibrous sillimanite.

The sedimentary schists, mafic schists and granite veins are crosscut by undeformed to locally foliated, very fine-grained basalt (Fig. 45f). These rocks are highly altered, contain no primary minerals, and are dominated by chlorite with quartz, possible quartzofeldspathic aggregates and Fe oxide minerals, suggestive of lower greenschist facies metamorphism.

Structural features of the BKD01 and BKD02 drillcores

Both drillcores locally contain small-scale, mostly subhorizontal, open to tight folds in both the sedimentary schist and the layered mafic schist, defined by folded layering. The drillholes were vertical and the drillcores were not oriented so it is not possible to determine fold orientations. These folds locally have a weakly developed axially planar foliation defined by chlorite or chloritized amphibole. The folds appear to be discontinuous and irregular, and could be recrystallized sedimentary slump folds. Their subhorizontal orientations cannot be correlated with the larger scale folds evident in the aeromagnetic data, although the BKD01 drillcore contains a tight upright fold that appears to be refolded by a second upright fold at a high angle to the first. Thin granite veins in this drillcore are also folded, but the folded layering is also locally cut by thicker granite veins.

Haig Cave Supersuite

The Haig Cave Supersuite has been intersected in several drillholes in the Loongana, Haig and Serpent prospects (Table 3), and is interpreted to cover a significant portion



CS455

19.08.19

Figure 45. Photos of the Sleeper Camp Formation (NQ core width 47.6 mm): a) layered Fe-rich and Mn-rich metasedimentary schists. Drillcore BKD01; b) thinly layered mafic schist interpreted as metavolcaniclastic. Sample GSWA 219093 is from the centre upper section (361.75 – 362.23 m), with corresponding geochemistry sample GSWA 201277 (362.23 – 362.46 m) downhole to the right. Tray 39, drillcore BKD02; c) metadolerite sample GSWA 219092, Tray 60, drillcore BKD01; d) epidote-altered brecciated contacts between mafic and metasedimentary schists containing jigsaw-fit mafic clasts. Drillcore BKD02; e) granite veins intruded into mafic volcaniclastic rocks, from near where sample GSWA 182485 was collected. Drillcore BKD002; f) crosscutting fine-grained basalt. NQ drillcore diameter is 47.6 mm

of the Madura Province (Figs 3, 17, 44). Seismic reflection data indicate these rocks have strong reflectivity and extend to a depth of about 4.5 km in the vicinity of the Haig prospect (Fig. 10a; Spaggiari et al., 2017a). The Haig Cave Supersuite is dominated by a series of gabbros and mafic to ultramafic rocks, denoted by their strong gravity and moderate to strong magnetic response. These rocks are intruded by dominantly trondhjemitic granites interpreted as oceanic plagiogranite (Kirkland et al., 2017; Spaggiari et al., 2018). In addition to these rocks, the adakite intersected in the MAD002 drillhole is also assigned to the Haig Cave Supersuite. Based on geochemical characteristics, the Haig Cave Supersuite has been interpreted as part of an oceanic arc (the Loongana Arc; Spaggiari et al., 2015a).

Loongana prospect

The Loongana prospect is defined as the distinctive, northeast-trending gravity and magnetic feature east of the northwest-dipping Family Dam Shear Zone and west of the northwest-dipping Meteorite Shear Zone (Fig. 44). Aeromagnetic data indicate a series of northeast-trending folds within the prospect, truncated by, but potentially related to, oblique thrust and sinistral movement along the Meteorite Shear Zone. The Family Dam Shear Zone is interpreted as a younger, extensional shear zone.

The broader, southwestern portion of the prospect is where diamond drillholes LNGD001, LNGD002 (Helix Resources; Bunting and McIntyre, 2003) and LNGD003 and its wedge LNGD003a (MRG Metals Pty Ltd; McIntyre and Weston, 2015) were located (Fig. 44). Exploration has focused on potential for Ni, Cu and platinum group elements (PGE) based on interpretations that drillcores LNGD001 and LNGD002, and the associated gravity and magnetic features, indicated a large mafic–ultramafic layered intrusion prospective for stratiform reef-style PGE or Voisey's Bay-style Ni–Cu–PGE mineralization in massive or disseminated sulfide (Bunting and McIntyre, 2003).

Richmond Mining Ltd undertook an RC drilling campaign to investigate the lateral extent of the southwestern area and continuation of the succession and prospect to the northeast, interpreted as a 'tail' or feeder dyke, predominantly focusing on Ni sulfide exploration (Richmond Mining Limited, 2012). The drillholes intersected gabbro, variably serpentinized ultramafic rocks and tonalite, confirming continuation of the succession and its relationship to the gravity and magnetic features. Although the results for Ni sulfides were not encouraging, Au mineralization with associated elevated Cu values were intersected in one hole in a quartz–feldspar vein (drillhole LONRC5, Fig. 44). The best intercept was 1 m at 2.67 g/t Au from 368 m. Quartz veining between 370–372 m contained on average 0.13% Cu and the interval from 371–372 m contained 0.74 g/t Au (Richmond Mining Ltd, 2012).

Drillcore LNGD001 is dominated by medium-grained gabbros layered with peridotite (dunite and wehrlite), pyroxenite and feldspathic pyroxenite, and quartz gabbros grading to coarse-grained tonalitic plagiogranites (Fig. 46a,b; Bunting and McIntyre, 2003; McIntyre and Weston, 2015). Highly anomalous PGE results were

recorded in the upper portion of drillcore LNGD001, where an intersection from 275.2 to 281 m commences at 117 ppb Pt + Pd grading down to a cut-off of 20 ppb Pt + Pd (Bunting and McIntyre, 2003; McIntyre and Weston, 2015). Finer grained rocks comprising gabbro and granite, interpreted as lamprophyre, were also intersected.

Drillcore LNGD002 contains medium- to coarse-grained melanocratic gabbro, fine- to medium-grained pyroxene-rich gabbro, and lesser fine-grained talc-altered dolerite or microgabbro (Bunting and McIntyre, 2003). The drillcore also contains typically massive amphibole- or biotite-bearing plagiogranites and finer grained rocks interpreted as lamprophyre similar to those in LNGD001. Petrographic reports for samples from both LNGD001 and LNGD002 are provided in appendices 7 and 8 in Bunting and McIntyre (2003). The petrographic work indicates that protoliths included olivine, pyroxene and plagioclase cumulates that were likely gabbros, pyroxenites and feldspathic pyroxenites (possibly harzburgites), and that olivine cumulates contain fine aggregates of pyrrhotite, chalcopyrite and pentlandite. It also describes extensive retrograde alteration of the mafic phases comprising assemblages containing tremolite–actinolite, epidote–clinozoisite, sericite and magnesian chlorite. Metamorphism in both drillcores is estimated at greenschist to lower amphibolite facies (Bunting and McIntyre, 2003; Nelson, 2005a,b). The variable degree of fabric formation indicates that deformation was strongly partitioned, particularly into localized mylonite zones.

Drillcore LNGD003 is dominated by gabbroic rocks reported as cyclically layered on a centimetre to 5 m scale, with thin pyroxenitic bases grading through melanogabbro to mesogabbro, and locally, pyroxenites and feldspathic pyroxenites (McIntyre and Weston, 2015). The layering is interpreted to dip about 45°, and generally northwards, which matches the gross magnetic layering in this area of the prospect. Coarse- to very coarse-grained leucogabbro and granite crosscut the gabbroic succession. Geochemical data indicates a Cr-rich pyroxenite with Cr values up to about 2000 ppm contains a 4.5 m zone of anomalous PGE concentrations, which has been cut and excised by an approximately north-dipping, extensional mylonitic shear zone (McIntyre and Weston, 2015). Visible pyrrhotite–chalcopyrite–pyrite mineralization was observed and anomalous PGE intervals were recorded from 388.9 to 389.4 m at 52 ppb Pt + Pd over 0.5 m, and a single spike at 4.75 m at 23 ppb Pt + Pd (McIntyre and Weston, 2015).

Serpent prospect

The Serpent prospect is defined as a coincident, northwest-trending, strong magnetic and gravity anomaly and is intersected by two diamond drillcores, SDDH001 and SDDH002 (Figs 16, 17, 44; Tillick, 2010). Although coincident in this area, the strong gravity anomaly has greater lateral extent than the discrete magnetic anomaly and is a north-trending ridge about 55 km long, which includes the Haig prospect. Exploration was focused on Cu–Au (Fe oxide – copper – gold [IOCG]-style) and Ni (\pm Cu; magmatic sulfide) mineralization (Tillick, 2010). The approximately 13 km-long Serpent magnetic anomaly was targeted due to its unusual sinusoidal shape and excellent linear continuity, with a peak amplitude of around 4200 nT (Tillick, 2010).

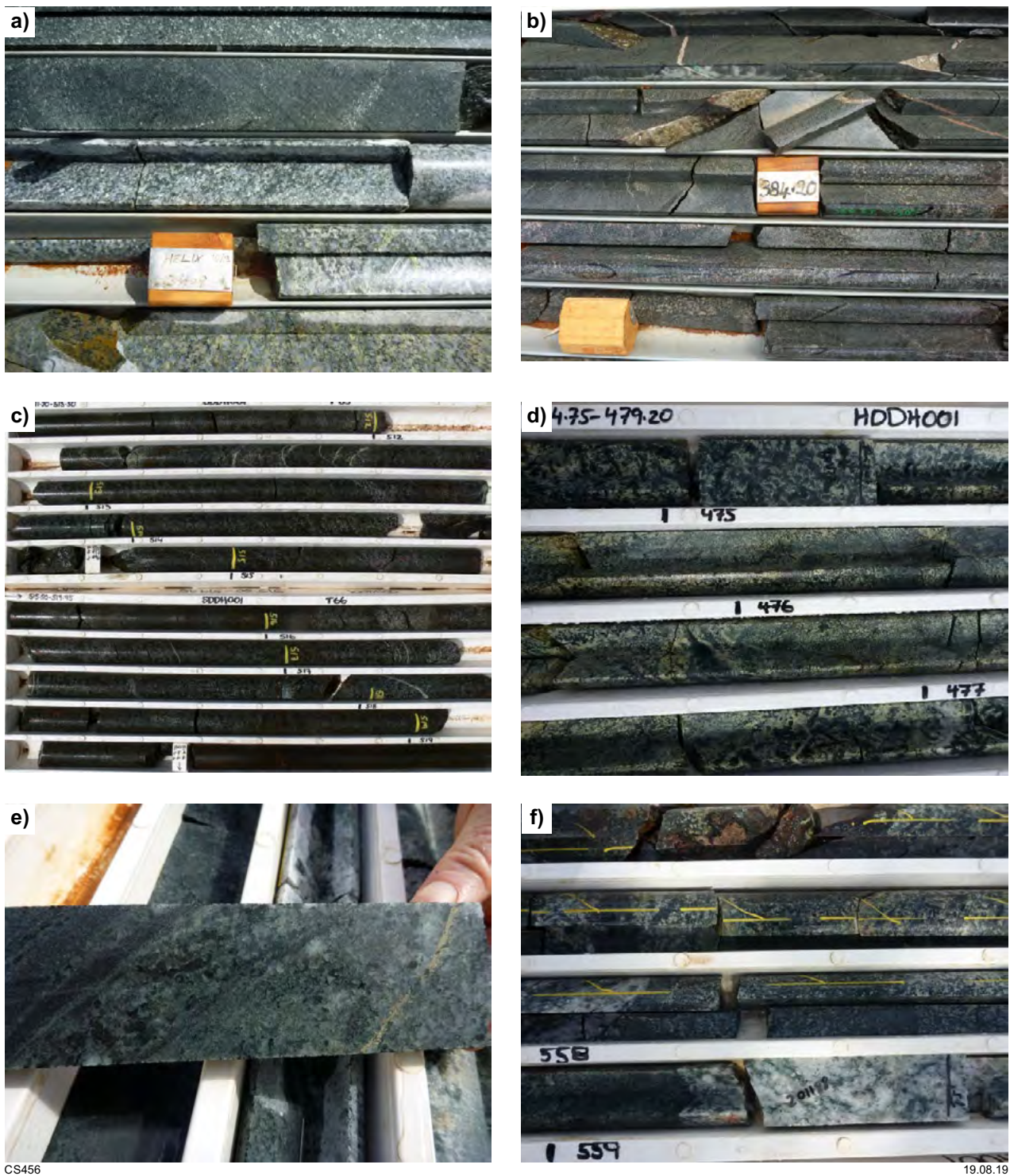


Figure 46. Photos of drillcores containing Haig Cave Supersuite (NQ core width 476 mm): a) fine- to medium-grained metagabbro and coarse-grained tonalitic plagiogranite with blue quartz; drillcore LNGD001, Loongana prospect; b) fine- to medium-grained, variably textured and layered metagabbro; drillcore LNGD001, Loongana prospect; c) metagabbro and metagabbro-norite in drillcore SDDH001, Serpent prospect; d) weakly layered medium- to coarse-grained metagabbro, locally with long hornblende laths; drillcore HDDH001, Haig prospect; e) fine layering and sulfide vein in metagabbro; drillcore HDDH001, Haig prospect; f) variably textured metagabbro intruded by 30 cm-wide plagiogranite vein (geochemistry sample GSWA 201188); drillcore HDDH001, Haig prospect

Drillholes SDDH001 and SDDH002 intersected medium- to coarse-grained metamorphosed gabbro and gabbro-norite with disseminated and layered primary magnetite and ilmenite, and locally disseminated pyrrhotite, interpreted to lie in the upper, highly fractionated portion of a zoned mafic intrusion (Tillick, 2010). The gabbro and gabbro-norite are massive to weakly foliated or layered, with the foliation or layering typically defined by plagioclase, hornblende or actinolite after pyroxene, and Fe oxide minerals (Fig. 46c). Augite norite with primary hornblende occurs locally in SDDH001. Thin carbonate veins cut the layering locally. Conglomerate that lies unconformably above contains clasts rich in coarse-grained hematite and magnetite (Tillick, 2010).

Haig prospect

The Haig prospect lies to the north of the Serpent prospect along the same gravity ridge, and within a series of northeast-trending magnetic layers (Figs 17, 44). As with the Serpent prospect, exploration was focused on Cu–Au (IOCG-style) and Ni (\pm Cu; magmatic sulfide) mineralization.

Drillhole HDDH001 intersected dominantly gabbroic rocks of variable grain size and composition. These include medium-grained, mesocratic to melanocratic gabbro interleaved and veined by acicular gabbro, fine-grained gabbro intruded by veins of fine- to medium-grained leucogabbro, and medium- to coarse-grained acicular leucogabbro with hornblende from 8 mm to 2 cm (Fig. 46d,e). Some occurrences of mesocratic homogeneous gabbro are well layered, from coarse-grained to fine-grained acicular gabbro. The gabbros are intruded by medium- to coarse-grained leucogranite veins that are locally foliated (Fig. 46f), and are variably altered to hematite–epidote–chlorite–sericite–actinolite–albite and stockwork veined. Alteration intensity generally increases towards the bottom of the hole, with K concentrations increasing significantly (up to 2.5%) below 589 m (Tillick, 2011a).

Drillhole HDDH002 intersected medium-grained, mesocratic, equigranular gabbro, locally with crude layering including fine-grained mesocratic to melanocratic gabbro, medium-grained mesocratic to melanocratic gabbro with anhedral plagioclase to 4 mm, and fine- to medium-grained mesocratic gabbro. The gabbros are intruded by locally foliated, coarse- to medium-grained leucogranite. Limited quartz veining and zones of weak sericite \pm chlorite \pm epidote alteration occur locally. Strongly altered intervals contain anomalous Ni, Cr and PGE concentrations (Tillick, 2011a). Minor pyrite and trace chalcopyrite occur in both drillcores.

Moodini Supersuite at the Moodini prospect

The Moodini prospect lies within the Mundrabilla Shear Zone, which separates the Madura and Coompana Provinces (Figs 3, 21, 24). The prospect is defined by strong, coincident magnetic and gravity anomalies that have a north–south trend parallel to the shear zone. These are similar to north-northeasterly trending

anomalies to the northwest that have been dragged into the shear zone with sinistral movement sense (Fig. 21). The anomalies are interpreted to be, at least in part, due to intrusions of the Moodini Supersuite. On the eastern side of the Mundrabilla Shear Zone, similar anomalies form part of a large, northeasterly trending chain of intrusions bounded by the Border Shear Zone and are also dragged into the shear zone with sinistral shear sense (Fig. 24). These intrusions include the granite intersected at the base of the Eucla No. 1 petroleum well, dated at 1140 ± 8 Ma (GSWA 194773, Kirkland et al., 2011c). The magnetic and gravity responses of these intrusions are very similar to that at the Hannah 1 drillsite, and also intrusions of Boonya Suite granites within the Albany–Fraser Orogen (Fig. 47). These intrusions are mostly circular to ovoid, and have well-defined magnetic rims or layering, which is typically parallel to a magmatic fabric (e.g. at Afghan Rock, Quentin de Gromard et al., 2017).

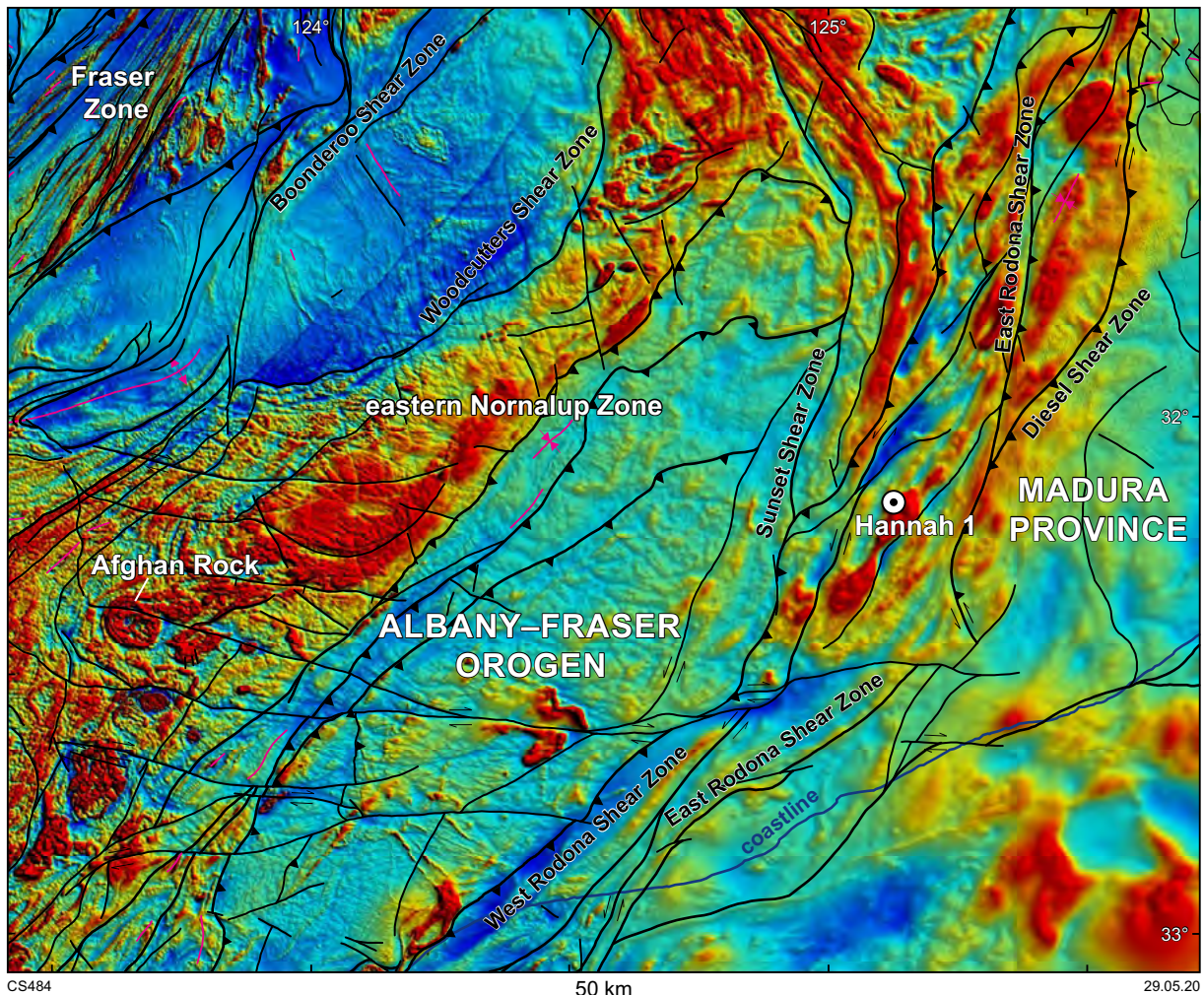
Venus Metals investigated the Moodini prospect for IOCG potential. The company drilled two diamond holes, MORCD001 and MORCD002 (Table 3; Sasi, 2011, 2012). The drillholes intersected altered, fractured and locally sulfidic granitic basement (Fig. 48a), which yielded anomalous assay results for Ag, elevated Ba, Ti and Zn, and locally, U (Sasi, 2011, 2012). Drillcore MORCD001 yielded anomalous Ag values of 23.27 g/t from 408 to 409 m, 12.86 g/t from 504 to 508 m, 34.14 g/t from 544 to 545 m and 5.13 g/t from 553 to 554 m. Drillcore MORCD002 yielded anomalous Ag values of 3.52 g/t from 323 to 324 m, 6.81 g/t from 341 to 342 m, 8.4 g/t from 373 to 374 m and 31.91 g/t from 376 to 377 m (Sasi, 2012).

Drillcores MORCD001 and MORCD002 are dominated by medium- to coarse-grained, seriate-textured to porphyritic, biotite–hornblende–magnetite metamonzogranite, locally with a fine-grained quench texture suggestive of rapid cooling. Rare elongate xenoliths of mesocratic granite also occur. Coarse-grained pegmatite veins with large K-feldspars and white micas intrude the metamonzogranite. The metamonzogranite is dominated by K-feldspar, plagioclase, quartz and biotite in variable proportions, and small mafic blebs occur towards the base of the drillcore in MORCD001.

The metamonzogranite contains a well-developed subhorizontal foliation or linear fabric with a rod-like morphology (L–S tectonite; Fig. 48b). Alteration, which crosscuts the fabric, is localized and comprises zones of quartz, epidote and possible prehnite in veins. The lower part of drillcore MORCD001 is more heavily altered and brecciated, and the fabric is closer to an S tectonite than an L tectonite. At 518 m, this fabric changes to be steeply dipping. The metamonzogranite has a high magnetic susceptibility, up to 249×10^{-3} SI, which is significantly lower in alteration zones and within the pegmatite veins.

Malcolm Metamorphics

Although exposed in outcrop, the Malcolm Metamorphics are included in this Report because they are associated



CS484

50 km

29.05.20

- | | | | | | |
|-----|---|-----|---|---|---------------------|
| — | Fault or shear zone | ↔↔↔ | Shear zone, major, thrust oblique with dextral offset | — | Geological boundary |
| ↔↔↔ | Shear zone, strike slip with sinistral offset | ↔↔↔ | Shear zone, major, thrust oblique with sinistral offset | ⊙ | Donated drillcores |
| ↔↔↔ | Shear zone, strike slip with dextral offset | ↔↔↔ | Fold axial trace | | |
| — | Shear zone, major | ↔↔↔ | Fold; antiform, synform | | |
| ↔↔↔ | Shear zone, major, thrust | | | | |

Figure 47. Reduced-to-pole aeromagnetic image showing strongly magnetic granitic and dioritic intrusions of the Boanya Suite, as denoted by the Hannah 1 drillsite, exposures at Afghan Rock, and similar circular to ovoid features within the eastern Nornalup Zone

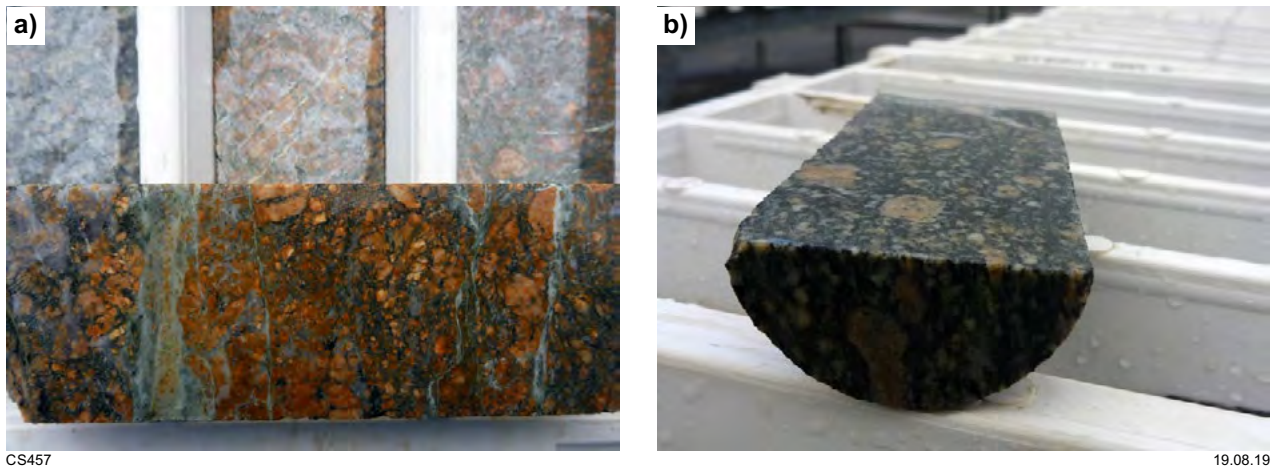


Figure 48. Photos of Moodini prospect drillcores (NQ core width 476 mm): a) strongly altered and fractured metamonzogranite in drillcore MORCD001; b) L-tectonite fabric in metamonzogranite from the drillcore MORCD002. The hole was drilled vertically, so the long axis of the cut core represents the vertical surface, and the short axis (half-moon cut shape with strong linear fabric) represents the horizontal surface

with the Rodona Shear Zone and represent the only onshore exposure of Madura Province rocks. They crop out on coastal platforms from Cape Pasley through to Point Malcolm, which is the easternmost coastal exposure of basement rocks before the coastline turns to the northeast, forming Israelite Bay (Figs 3, 49). The Malcolm Metamorphics lie within a northeast-trending fault slice that is about 40 km long and 8 km wide. The fault slice is bounded to the northwest by the southeast- to east-dipping Daringdella Shear Zone, and to the southeast by the Franklin Shear Zone, interpreted as a splay off the East Rodona Shear Zone (Spaggiari, 2016).

The Malcolm Metamorphics comprise folded, psammitic, semipelitic and pelitic schistose to gneissic rocks interlayered with fine-grained, laminated metabasalt and calc-silicate rocks (Fig. 50a, Table 4). Metabasalt accounts for up to 50% of the outcrop towards the southwest, whereas the metasedimentary rocks are dominant towards the northeast (Clark, 1999). Peak metamorphic conditions of the metasedimentary rocks are estimated at about 750°C and 4 kbar (Clark et al., 2000). Metasedimentary rocks with pelitic compositions are typically migmatitic, biotite rich, and contain garnets that are wrapped by a second-generation foliation that is axially planar to the dominant fold sequence. The metasedimentary rocks typically contain mesosomes comprising biotite–quartz–K-feldspar–plagioclase–garnet ± muscovite, spinel and locally sillimanite, and leucosomes dominated by quartz and K-feldspar (Clark, 1999; Adams, 2012). Metasedimentary rocks with semipelitic to psammitic compositions are medium grained and strongly foliated. They are dominated by assemblages of quartz–K-feldspar–plagioclase–biotite and are also migmatitic (Adams, 2012).

The metabasalt is fine to medium grained and dark grey to black with thin pale laminations that are folded (Fig. 50b; see also Quentin de Gromard et al., 2017). It locally contains strongly altered horizons comprising green, layered calc-silicate rocks that are also folded (Fig. 50c). The calc-silicate rocks are volumetrically minor, and occur as pods or layers. Within a low-strain zone at Cape Pasley, sharp curved contacts between metabasalt and

metasedimentary rock, and angular fragments of metabasalt within metasedimentary rock (Clark, 1999) are suggestive of pillow basalts intruded into wet sediments forming hyaloclastite.

The metabasalt contains the assemblage green-brown hornblende–clinopyroxene–plagioclase–ilmenite ± biotite, titanite, epidote, garnet, anthophyllite and quartz (c.f. Clark, 1999). Clinopyroxene is mostly overgrown by hornblende, some of which is very strongly pleochroic (brown – olive green – blue-green), and the fine-grained pale layers are dominated by plagioclase. Garnet is restricted to thin layers and small pods of metasedimentary rocks within the metabasalt. The calc-silicate rocks contain the assemblage garnet–quartz–clinopyroxene–plagioclase ± epidote, calcite, hornblende, wollastonite, clinozoisite, with accessory minerals titanite and magnetite, and locally pyrite and chalcopyrite (Clark, 1999). Magnetic susceptibility readings are highly variable and range from 0.00 to 58.50×10^{-3} SI. In the Point Malcolm area, the metabasalt yields magnetic susceptibility readings of zero.

The main layering in the Malcolm Metamorphics, including the migmatitic leucosomes in the pelitic to semipelitic rocks and the pale laminations and segregations in the metabasalt, forms second-generation, tight to isoclinal, steeply southwest or locally northeast-plunging, east-northeasterly trending folds that define the dominant structures (cf. Clark, 1999; Adams, 2012). To the southwest of Point Malcolm at Cape Pasley, these folds generally have more moderate plunges (Clark, 1999). Locally, refolded older folds are visible in both the metabasalt and metasedimentary rocks (Fig. 50b; see also Quentin de Gromard et al., 2017). The second-generation folds are cut by small shear zones, and both pegmatitic and fine-grained equigranular granitic veins. There is also at least one generation of older pegmatite that is also folded and locally boudinaged in the east-northeast direction of the main fabric.

Towards the southwest at Point Malcolm, a fine-grained, equigranular, northeasterly trending (040°) granite vein up to about 1 m wide crops out continuously over about 85 m

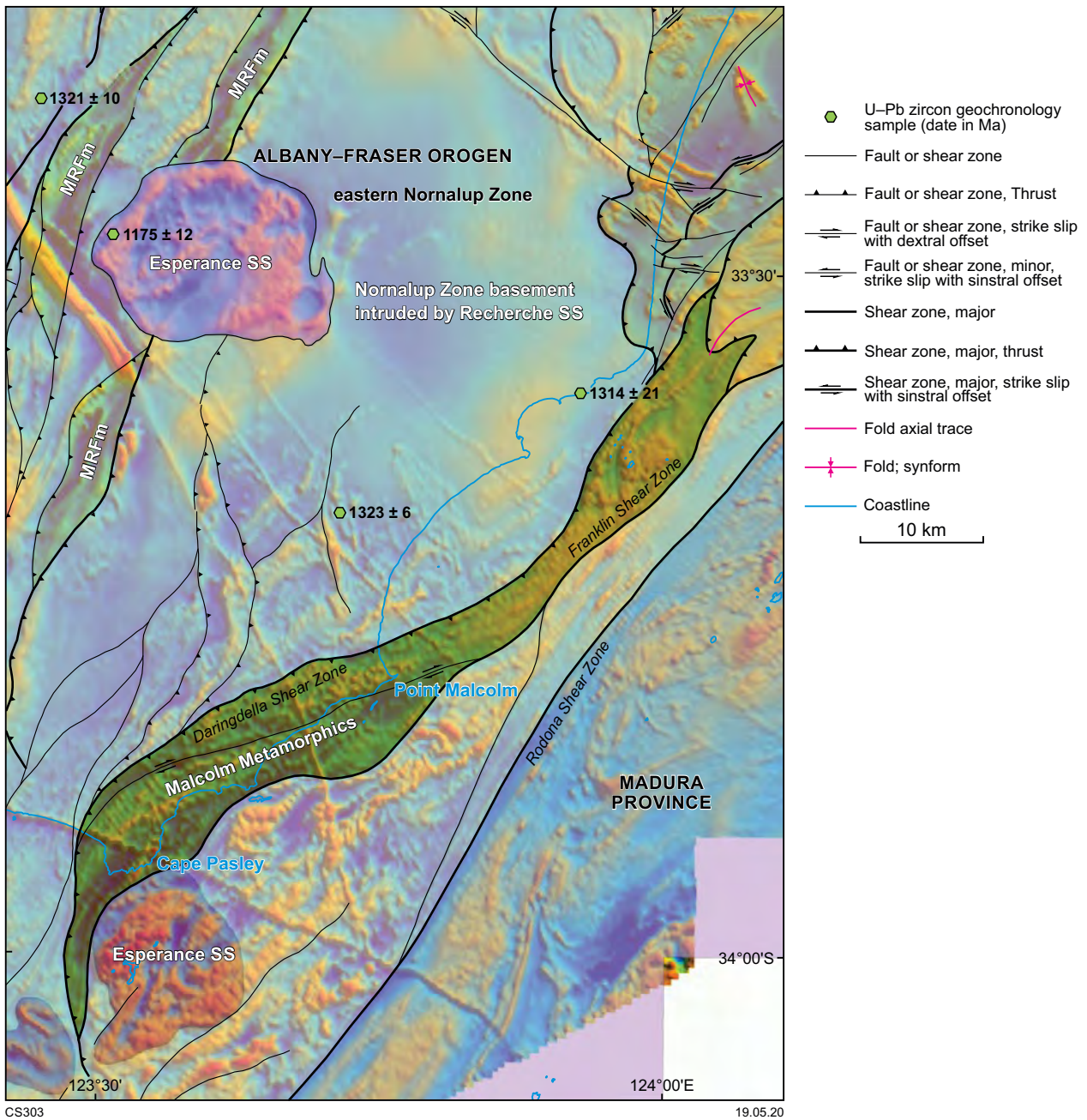


Figure 49. Reduced-to-pole aeromagnetic image overlain by semitransparent interpreted bedrock geology (Spaggiari, 2016) of the region in the vicinity of the exposures of the Malcolm Metamorphics. The green hexagons show the locations of dated samples of the Recherche and Esperance Supersuites. Abbreviations: MRFm, Mount Ragged Formation; SS, Supersuite



CS458

19.08.19

Figure 50. Photos of the Malcolm Metamorphics: a) folded migmatitic semipelitic to pelitic schist interlayered with fine-grained metabasalt; Point Malcolm; b) laminated metabasalt showing two generations of folding; Cape Pasley. Photo courtesy of Dan Clark; c) folded green calc-silicate alteration in metabasalt; Point Malcolm; d) dated sample site of the fine-grained granite vein parallel to the main fabric, but locally crosscutting it and the folds; Point Malcolm; e) coarse-grained pegmatite (foreground) crosscutting both folding phases and the fine-grained granite vein (centre) shown in d). The pegmatite trends 175°, but is the same intrusion as one trending east; Point Malcolm

and is dated at 1313 ± 16 Ma (Fig. 50d; Clark et al., 2000). Although this granite vein crosscuts both folding phases, it is also foliated and layered and locally pinches into foliated metasedimentary rocks parallel to the foliation. This granite vein is one of several similar veins, some of which are locally sheared, but none of which are folded. The structural relationships suggest the granite veins may have intruded during the final stages of the second folding event, subparallel to the axial planes of the folds. This is consistent with a mean monazite age of 1311 ± 4 Ma from three diverse samples of metasedimentary rocks, interpreted as dating the refolded, peak metamorphic fabric (Adams, 2012). Coarse-grained pegmatite veins crosscut both phases of folds and also the fine-grained granite veins (Fig. 50e). These are up to several metres wide and contain K-feldspar, quartz, biotite, and locally, garnet. Late, locally occurring, northwest-trending open folds pre-date the large, second-generation pegmatite veins (Clark, 1999; Adams, 2012).

The maximum depositional age and the age of the dominant detrital component in the metasedimentary succession at Point Malcolm is constrained at c. 1470 Ma (Spaggiari et al., 2018), based on ages of 1467 ± 11 Ma for semipelitic schist (GSWA 194867, Wingate et al., 2020a) and 1474 ± 9 Ma for psammitic schist (GSWA 207001, Wingate et al., 2020c). Zircon rims in GSWA 194867 yielded a date of 1315 ± 11 Ma, interpreted as the age of high-grade metamorphism and a minimum age for sediment deposition (Wingate et al., 2020a).

About 6 km southwest of Point Malcolm, off the Telegraph Track, is another area of coastal platforms exposing the same succession as that at Point Malcolm. Interlayered psammitic and pelitic schistose to gneissic rocks are fine to medium grained with well-developed layering and a strong foliation. The psammitic metasedimentary rocks contain a greater abundance of leucosomes and metagranitic veins than at Point Malcolm (e.g. GSWA 194869, Wingate et al., 2020b). Metasedimentary rocks of pelitic composition are biotite rich and contain garnet that is wrapped by the foliation. As at Point Malcolm, the metasedimentary rocks are interlayered and folded with fine-grained metabasalt and pegmatite veins. In the metabasalt, the foliation is strong and parallel to the thin layering. Both are folded, and there are small felsic veinlets parallel to the axially planar foliation. The folds are tight, northeast-trending, and have steeply southwest- or northeast-plunging fold axes. A weak to moderate mineral lineation plunging 22° towards 045° is developed in the more highly strained rocks. These rocks are crosscut by large, very coarse-grained pegmatite veins that are locally sheared. Magnetic susceptibility readings in the psammitic metasedimentary rocks are highly variable and range from 0.00 to 11.00×10^{-3} SI, with most in the range 4.00 – 5.00 $\times 10^{-3}$ SI.

To the southeast, the foliation is more intense and is related to a steeply dipping, northeast-trending dextral shear zone. The shear zone contains sheared lenses of pegmatite that cut the layering with dextral asymmetry, and the pegmatite contains felsic porphyroclasts with dextral asymmetry. Elongate, stretched calc-silicate pods occur locally.

Towards the southwest, the mineral lineation changes from northeast-plunging to southwest-plunging (18° towards 240° in metabasalt). The metabasalt contains

thin layering that is tightly chevron-folded with vertical fold axes, suggesting the mineral lineation is not related to these folds. The metasedimentary rocks are dominated by psammitic compositions and are intruded by large pegmatite veins that are also deformed. A second generation of large, very coarse-grained pegmatite veins cut the main foliation but are also foliated and locally sheared.

Geochronology

In this section, U–Pb zircon geochronology conducted using the sensitive high resolution ion microprobes (SHRIMP) II at Curtin University, using procedures described by Wingate and Lu (2017), is summarized. Reflected light, transmitted light and cathodoluminescence (CL) images were used to ensure analyses were made on discrete zircon growth phases. Analyses $>5\%$ discordant are generally considered to be less reliable or to have undergone secondary alteration processes and are not normally included in determining the age of each sample or zircon grain. Sampling was conducted after detailed logging of the GSWA stratigraphic drillcores and care was taken to document the geological context of each sample from all drillcores. Fractions of each geochronology sample were isolated for petrography and geochemistry where sufficient material remained or where a previous geochemical sample had not been collected. Interpretation of geochronology results takes into account relevant petrographic, geochemical, isotope and structural data for all samples and intervening drillcore material, as detailed in Appendices 2, 5 and 7–9. Isotopic ages discussed in this Report are quoted with 95% confidence intervals, unless noted otherwise.

Sample information for the GSWA stratigraphic and exploration drillcores and their ages are provided in Table 5, and published reports for each sample can be downloaded from the Geochronology webpage on the DMIRS website (www.dmirs.wa.gov.au/geochron).

Madura Province

In this section, the age constraints are summarized for recognized units within the Madura Province (Fig. 51), from oldest to youngest.

Sleeper Camp Formation (1536–1471 Ma)

This unit has been identified at the Burkin prospect in drillcores BKD01 and BKD02 (Fig. 44). Sample GSWA 219093 is a fine-grained amphibolite schist with folded thin layering and a subparallel foliation, and is representative of the mafic volcanoclastic component of the Sleeper Camp Formation (Fig. 45b). The sample contained only 10 zircons and yielded a date of 1536 ± 13 Ma for the youngest group of five analyses, interpreted as a maximum depositional age (Wingate et al., 2018g). The youngest zircon yielded a date of 1512 ± 14 Ma (1σ). Two older detrital zircons in this sample yielded dates (1σ) of 1806 ± 5 and 1616 ± 6 Ma.

Sample GSWA 219092 (Fig. 45c) is a medium-grained metadolerite representative of the mafic subvolcanic component of the Sleeper Camp Formation interlayered

Table 5. U–Pb zircon geochronology results and sample information

GSWA Sample ID	Drillcore ID	Depth (m)		Lithology	Unit	Location	Province	Inheritance (Ma)	Protolith (Ma)	Metamorphic age (Ma)	Zone	MGA Easting/northing	Latitude/longitude
		From	To										
192594 [†]	FOR004	497.67	498.18	Granodiorite gneiss	Toolgana Supersuite	Northwest of Eucla	Coompana	1724 ± 13; 1671 ± 19	1611 ± 7		52	457543E/6539272N	-31.280077°S/128.553959°E
213822 [†]	FOR004	484.54	485.10	Medium-grained, schlieric biotite metasyenogranite	Toolgana Supersuite	Northwest of Eucla	Coompana		1613 ± 4	1179 ± 10	52	457543E/6539272N	-31.280077°S/128.553959°E
216276 [†]	FOR008	552.21	552.91	Migmatitic granodiorite gneiss	Toolgana Supersuite	East of Reid	Coompana		1613 ± 13	1153 ± 9	52	469985E/6589321N	-30.828872°S/128.686155°E
216261 [†]	FOR008	476.31	476.81	Migmatitic monzogranite gneiss (leucosome)	Toolgana Supersuite	East of Reid	Coompana		1604 ± 6	1151 ± 6	52	469985E/6589321N	-30.828872°S/128.686155°E
206788 [†]	FOR012	433.00	433.50	Strongly deformed felsic volcanic schist	Undawidgi Supersuite	Southwest of Forrest	Coompana		1499 ± 9		52	403478E/6536633N	-31.300658°S/127.985768°E
206751 [†]	FOR010	432.75	433.10	Fine-grained foliated metatonalite	Undawidgi Supersuite	Northeast of Forrest	Coompana		1492 ± 9		52	439176E/6623576N	-30.518604°S/128.366042°E
206730 [†]	FOR011	419.20	419.40	Metasyenite	Undawidgi Supersuite	Northeast of Forrest	Coompana		1488 ± 7	1174 ± 12	52	421006E/6612536N	-30.617158°S/128.175832°E
192592 [†]	FOR010	474.32	475.09	Foliated porphyritic monzogranite gneiss	Undawidgi Supersuite	Northeast of Forrest	Coompana		1487 ± 9		52	439176E/6623576N	-30.518604°S/128.366042°E
216239 [†]	FOR012	341.59	342.05	Mylonitic metamonzogranite	Undawidgi Supersuite	Southwest of Forrest	Coompana		1479 ± 8		52	403478E/6536633N	-31.300658°S/127.985768°E
219092	BKD01	373.85	374.40	Medium-grained metadolerite	Sleeper Camp Formation	Burkin prospect	Madura		1479 ± 8		52	231761E/6638624N	-30.354548°S/126.209385°E
219093	BKD02	361.75	362.23	Mafic volcanoclastic schist	Sleeper Camp Formation	Burkin prospect	Madura	1806–1531	*1536 ± 13		52	230702E/6637028N	-30.368700°S/126.197970°E
219094	BKD02	263.26	263.63	Metagranite vein	Sleeper Camp Formation	Burkin prospect	Madura	1772; 1542	1471 ± 5		52	230702E/6637028N	-30.368700°S/126.197970°E
182485 [†]	BKD02	271.38	272.08	Metagranite vein	Sleeper Camp Formation	Burkin prospect	Madura	2408–2293; 1538 ± 17	1477 ± 4		52	230702E/6637028N	-30.368700°S/126.197970°E
178070	LNGD002	363.52	364.00	Granite intruded into amphibolite	Haig Cave Supersuite	Loongana prospect	Madura		1415 ± 7		52	253880E/6589700N	-30.800290°S/126.427670°E
178071	LNGD001	611.80	612.50	Biotite microtonalite	Haig Cave Supersuite	Loongana prospect	Madura		1408 ± 7		52	252720E/6587520N	-30.819700°S/126.415030°E
178072	LNGD001	637.60	640.00	Biotite tonalite gneiss	Haig Cave Supersuite	Loongana prospect	Madura		1407 ± 7		52	252720E/6587520N	-30.819700°S/126.415030°E
192558 [†]	LNGD002	465.30	466.20	Granitic gneiss	Haig Cave Supersuite	Loongana prospect	Madura		1411 ± 6		52	253880E/6589700N	-30.800290°S/126.427670°E
192557 [†]	LNGD002	371.00	371.50	Metagabbro	Haig Cave Supersuite	Loongana prospect	Madura		1403 ± 6		52	253880E/6589700N	-30.800290°S/126.427670°E
192560	HDDH001	490.63	490.95	Granite vein in metagabbro	Haig Cave Supersuite	Haig prospect	Madura		1400 ± 11		52	221250E/6560810N	-31.053426°S/126.079084°E
192561	HDDH002	426.77	427.10	Granite vein cutting metagabbro	Haig Cave Supersuite	Haig prospect	Madura		1397 ± 9		52	223271E/6572880N	-30.945133°S/126.103530°E
206754 [†]	MAD002	488.58	488.83	Adakite (metagranodiorite)	Haig Cave Supersuite	Gunnadorrah Station	Madura	2487–1455	1389 ± 7		51	770428E/6569645N	-30.975748°S/125.831448°E
206753 [†]	FOR010	490.14	490.48	Fine-grained equigranular syenogranite	Bottle Corner Shoshonite; Moodini Supersuite	Northeast of Forrest	Coompana	1576–1511	1192 ± 13		52	439176E/6623576N	-30.518604°S/128.366042°E
213838 [†]	FOR011	388.02	388.26	Coarse, quartz-rich monzogranite vein	Moodini Supersuite	Northeast of Forrest	Coompana	1552–1462	1189 ± 6		52	421006E/6612536N	-30.617158°S/128.175832°E
206752 [†]	FOR010	482.42	483.02	Porphyritic syenogranite	Bottle Corner Shoshonite; Moodini Supersuite	Northeast of Forrest	Coompana	1558 ± 21	1184 ± 8		52	439176E/6623576N	-30.518604°S/128.366042°E
206729 [†]	FOR011	415.80	416.19	Metadiorite with hornblende-biotite foliation	Bottle Corner Shoshonite; Moodini Supersuite	Northeast of Forrest	Coompana		1180 ± 6		52	421006E/6612536N	-30.617158°S/128.175832°E
192593 [†]	FOR010	459.77	460.25	Hornblende metagranite	Bottle Corner Shoshonite; Moodini Supersuite	Northeast of Forrest	Coompana		1175 ± 5		52	439176E/6623576N	-30.518604°S/128.366042°E
194773 [†]	Eucla No. 1	215.00	221.00	Felsic drill cuttings (granite)	Moodini Supersuite	Kuthala Pass	Coompana	1598 ± 14	1140 ± 8		52	426457E/6473617N	-31.870840°S/128.222500°E
192595 [†]	MAD014	433.27	433.87	Equigranular, biotite–hornblende granodiorite	Moodini Supersuite	North of Loongana	Madura		1182 ± 7		52	316247E/6626622N	-30.478606°S/127.085712°E
206778 [†]	MAD011	491.00	491.92	Coarse-grained monzogabbro	Kestrel Cavern Gabbro; Moodini Supersuite	Near Loongana	Madura		1143 ± 5		52	320871E/6565566N	-31.029952°S/127.123209°E
206779 [†]	MAD011	562.01	562.32	Medium-grained monzogabbro	Kestrel Cavern Gabbro; Moodini Supersuite	Near Loongana	Madura		1144 ± 7		52	320871E/6565566N	-31.029952°S/127.123209°E
192566 [†]	MORCD002	592.83	593.39	Metamonzogranite	Moodini Supersuite	Moodini prospect	Madura		1132 ± 9		52	350264E/6468083N	-31.913275°S/127.416322°E
192565 [†]	MORCD001	497.37	497.94	Metamonzogranite	Moodini Supersuite	Moodini prospect	Madura		1127 ± 7		52	350253E/6468291N	-31.911397°S/127.416238°E

NOTES: * maximum depositional age, † Analysed for Lu–Hf

with the mafic volcanic and volcanoclastic schist. The sample yielded only 12 zircons, and 11 analyses indicated a date of 1479 ± 8 Ma, interpreted as the magmatic crystallization age of the dolerite (Wingate et al., 2018f).

The mafic volcanoclastic schist and metadolerite are crosscut by granite veins (Fig. 45e), samples of which yielded crystallization ages of 1477 ± 4 Ma (GSWA 182485, Wingate et al., 2019) and 1471 ± 5 Ma (GSWA 219094, Wingate et al., 2018h). However, the c. 1477 Ma zircons from GSWA 182485 yield extremely variable evolved initial ϵ_{Hf} ratios that range from -1.2 to -12.3 , which likely reflect metamorphic (hydrothermal) fluid infiltration during emplacement of the granite veins (see Hf isotope geology section below). In GSWA 182485, zircon cores that yield a mean age of 1538 ± 17 Ma are interpreted as inherited and are within uncertainty of the main age component of 1536 ± 13 Ma in the host mafic volcanoclastic schist (GSWA 219093). Three older inherited zircon cores indicated dates between 2408 and 2293 Ma (Fig. 51).

Together, the four samples constrain the age of the Sleeper Camp Formation to be in the range 1536–1471 Ma. However, it is unknown whether crosscutting, highly altered, very fine-grained basalt is part of the same formation (Fig. 45f). A sample of thinly layered, red and grey quartz-rich sedimentary schist did not yield any zircons (GSWA 219091, Appendix 8).

Haig Cave Supersuite (1415–1389 Ma)

This unit has been identified in several drillcores from the Loongana, Haig and Serpent prospects, and in the MAD002 GSWA stratigraphic drillcore (Fig. 44). Five samples of recrystallized metagabbro and granitic gneiss in two drillcores from the Loongana prospect, LNGD001 and LNGD002, yielded igneous crystallization ages 1415–1403 Ma (Fig. 52a, Table 5). In each case, the data are single-component, mainly concordant and well grouped, yielding precise protolith ages. The ages of five samples are in statistical agreement, and yield a weighted mean of 1409 ± 6 Ma.

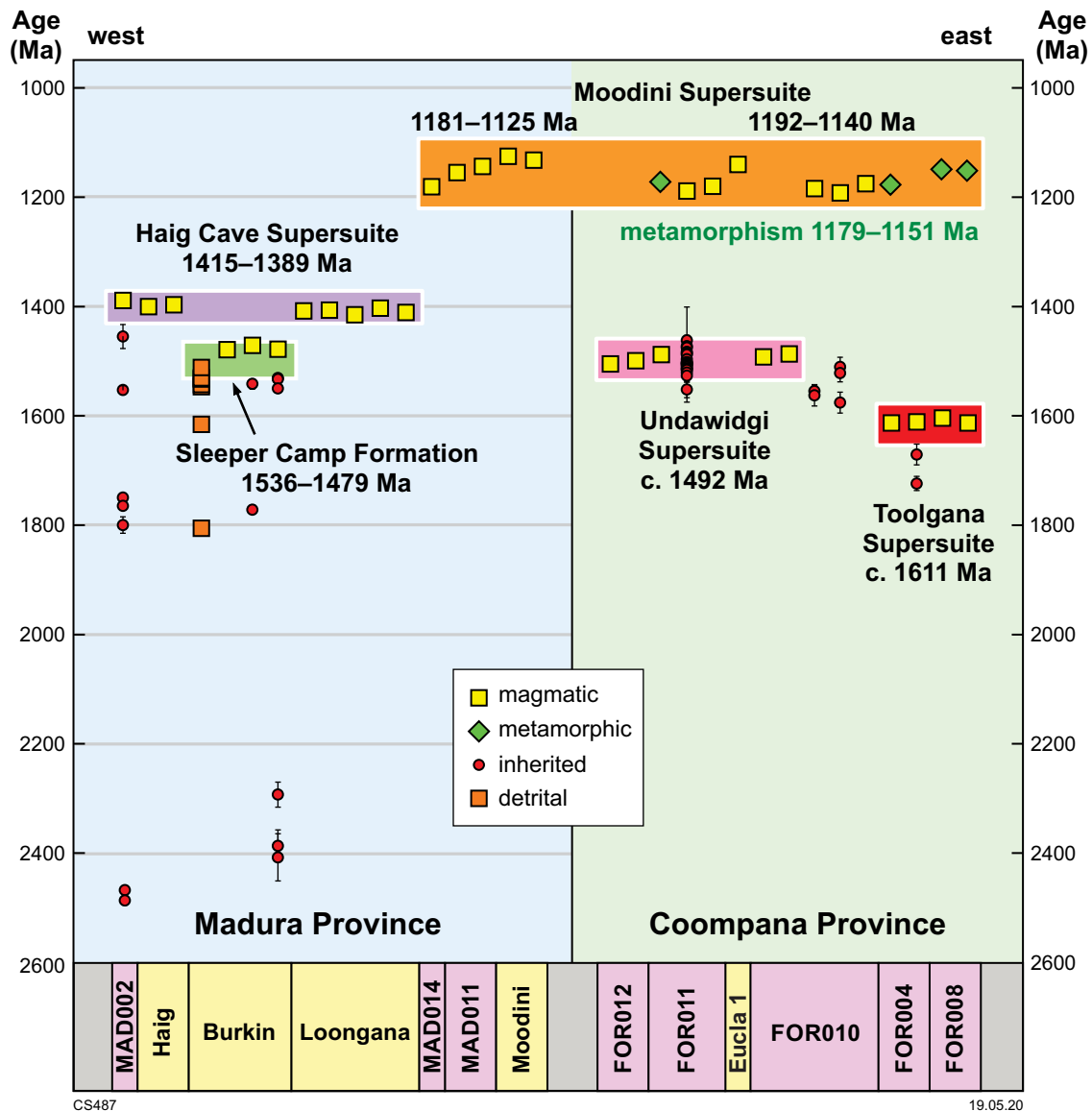


Figure 51. Summary of geochronology results from drillcore samples from the Madura and Coompana Provinces. Symbols represent mean ages of samples, except for red circles which represent the ages of individual analyses of inherited zircons

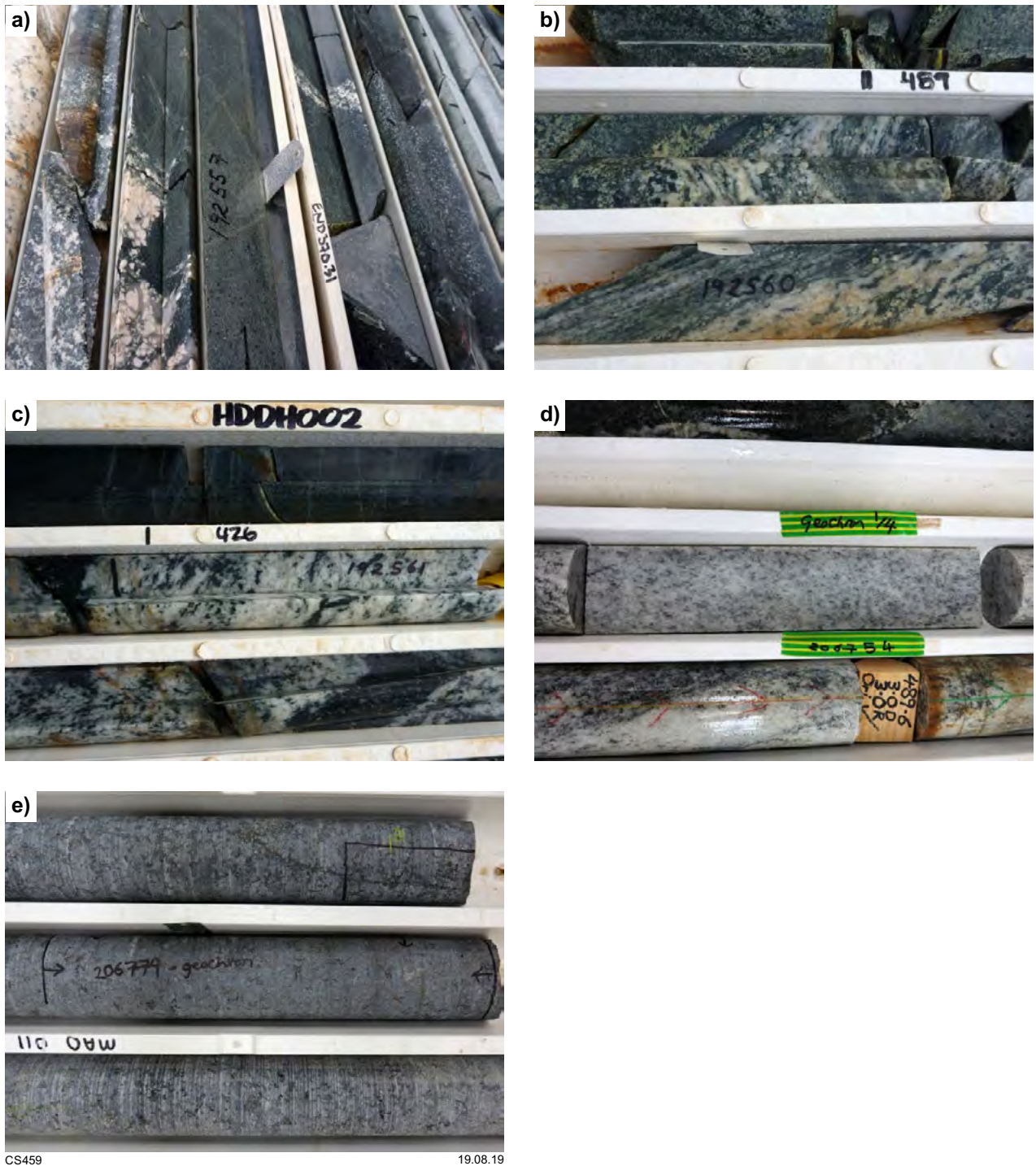


Figure 52. Photos of dated rocks from the Madura Province: a) metagabbro sample GSWA 192557 from the Loongana prospect, NQ drillcore LNGD002; b) strongly deformed biotite–amphibole metatonalite sample GSWA 192560; Haig prospect, NQ drillcore HDDH001; c) biotite–amphibole metatonalite sample GSWA 192561 with plagioclase crystals up to 8 mm long; Haig prospect, NQ drillcore HDDH002; d) metagranodiorite (adakite) sample GSWA 206754, HQ drillcore MAD002; e) medium-grained monzogabbro of the Kestrel Cavern Gabbro, Moodini Supersuite, GSWA 206779, HQ drillcore MAD011

Two tabesamples of metatonalite veins from the Haig prospect (Fig. 52b,c) yielded dates of 1400 ± 11 Ma (GSWA 192560, Wingate et al., 2018a) and 1397 ± 9 Ma (GSWA 192561, Wingate et al., 2018b). Metagranodiorite with the composition of adakite (see Whole-rock geochemistry section below), sampled from one of the thickest metagranite veins in drillcore MAD002 (Fig. 52d), provided a crystallization age of 1389 ± 7 Ma (GSWA 206754, Wingate et al., 2016b). Seven analyses of seven zircon cores yield dates of 2487–1750 and 1553–1455 Ma, interpreted as the ages of inherited components.

Moodini Supersuite (1182–1127 Ma)

This unit has been identified in GSWA stratigraphic drillcores MAD014 and MAD011, and in exploration drillholes MORCD001 and MORCD002 from the Moodini prospect (Figs 21, 44). A sample of unfoliated, equigranular, medium- to coarse-grained biotite–hornblende granodiorite representative of the main lithology in drillcore MAD014 (Fig. 23b) yielded a mean age of 1182 ± 7 Ma (GSWA 192595, Wingate et al., 2016a). Metamonzogranites with L–S tectonite fabric from the Mundrabilla Shear Zone, intersected in drillcores MORCD002 and MORCD001 at the Moodini prospect, yielded well-defined crystallization ages of 1132 ± 9 Ma (GSWA 192566, Wingate et al., 2015c) and 1125 ± 7 Ma (GSWA 192565, Wingate et al., 2015b), respectively. The results provide a direct constraint for the maximum age of c. 1128 Ma for sinistral movement on the shear zone.

Kestrel Cavern Gabbro

This unit was intersected in drillcore MAD011. GSWA 206778 is from a very coarse-grained, plagioclase-rich pegmatitic leucogabbro vein (Fig. 22a). The sample contained high U (median = 1750 ppm ^{238}U), low Th/U (median = 0.05), largely metamict zircons that nevertheless yielded a well-defined crystallization age of 1143 ± 5 Ma, thanks to the high spatial resolution of the SHRIMP primary beam (about 20 mm diameter), which allowed the damaged parts of the zircons to be avoided (Wingate et al., 2016c). GSWA 206779 is a medium-grained monzogabbro representative of the main rock type intersected in the drillcore (Figs 22b, 52e). The sample provided much lower U (median = 94 ppm ^{238}U), high Th/U (median = 2.3), undamaged zircons that yielded an essentially identical crystallization age of 1144 ± 7 Ma (Wingate et al., 2016d).

Coompana Province

In this section, the age constraints are summarized for recognized units within the Western Australian part of the Coompana Province (Fig. 51), from oldest to youngest.

Toolgana Supersuite (1613–1604 Ma)

This unit has been identified in drillcores FOR004 and FOR008 (Figs 24, 26). The samples from drillcore FOR004 are representative of layered granodioritic to monzogranitic gneiss (Fig. 27a; GSWA 192594), and foliated, schlieric biotite metasyenogranite (Fig. 27c; GSWA 213822).

Sample GSWA 216276 from drillcore FOR008 is from migmatitic granodiorite gneiss with strongly flattened K-feldspar porphyroclasts (Fig. 31). Sample GSWA 216261 from drillcore FOR008 is from the same unit as that represented by GSWA 216276, but contains a large component of leucosome, interpreted as derived from partial melting during high-temperature metamorphism.

In metasyenogranite sample GSWA 213822, the zircons consist of concentrically zoned cores overgrown by high-U rims, whereas in the other three samples zoned zircon cores are overgrown by rims of low-U zircon that also fills fractures in many crystals. Zircon cores in the four samples yield dates between 1613 and 1604 Ma, interpreted as the crystallization ages of granitic protoliths. These ages agree to within uncertainty, with a weighted mean of 1611 ± 7 Ma. In three samples (GSWA 213822, 216276 and 216261), analyses of low-Th/U zircon rims indicated ages for high-grade metamorphism of 1179 ± 10 , 1153 ± 9 and 1151 ± 6 Ma (Table 5). Two zircon cores in GSWA 192594 provide dates of c. 1724 and 1671 Ma, interpreted as the ages of inherited zircons.

Undawidgi Supersuite (1499–1479 Ma)

This unit has been identified in drillcores FOR010, FOR011 and FOR012 (Figs 24, 26, 29, 30). Zircons in all samples are subhedral to euhedral, and concentrically zoned and except for GSWA 206730 none of the samples exhibit zircon rims. In each case, most data indicate a mainly well-grouped, concordant component, yielding a precise protolith age. The apparent oldest sample in the age range is a grey, schistose felsic metavolcanic rock from the lower part of drillcore FOR012 that yielded an igneous crystallization age of 1499 ± 9 Ma (GSWA 206788, Wingate et al., 2016e). Mylonitic metamonzogranite from the upper part of drillcore FOR012 yielded an igneous crystallization age of 1479 ± 8 Ma (GSWA 216239, Wingate et al., 2016g), defining the younger end of the age range.

A sample of fine-grained metatonalite (GSWA 206751) from drillcore FOR010 yielded an igneous crystallization age of 1492 ± 9 Ma (Wingate et al., 2015h). Interlayered with the metatonalite is a monzogranite gneiss (GSWA 192592) that yielded an igneous crystallization age of 1487 ± 9 Ma (Wingate et al., 2015d). GSWA 206730 is a hornblende-bearing metasyenite from drillcore FOR011 and contains zircon cores that provided an igneous crystallization age of 1488 ± 7 Ma (Wingate et al., 2015g). The cores are overgrown by thin zircon rims, six analyses of which indicate very low Th/U ratios (0.01 – 0.07) and a concordia age of 1174 ± 12 Ma, interpreted as the age of high-grade metamorphism.

Moodini Supersuite (1192–1140 Ma)

This unit was intersected in drillcores FOR010 and FOR011, and also occurs at the base of the Eucla No. 1 petroleum well (Fig. 3), a sample from which yielded a magmatic crystallization date of 1140 ± 8 Ma, and one inherited zircon dated at 1598 ± 14 Ma (1σ) (GSWA 194773, Kirkland et al., 2011c).

A sample from a coarse, quartz-rich monzogranite vein identified as the youngest magmatic rock type in drillcore FOR011 yielded an igneous crystallization age of 1189 ± 6 Ma (GSWA 213838, Wingate et al., 2015k). These analyses indicate very low Th/U ratios (median 0.008). The sample is dominated by zoned zircon cores with dates of 1552–1462 Ma, and moderate to high Th/U ratios (median 1.1). These zircon cores are derived from the host hornblende-bearing metasyenite of the Undawidgi Supersuite that the monzogranite vein intrudes (dated at 1488 ± 7 Ma, GSWA 206730, Wingate et al., 2015g). The monzogranite vein crosscuts the foliation in the metasyenite, providing a minimum age for deformation.

As is the case with the Moodini Supersuite samples in the Madura Province (1182–1127 Ma), the mean ages for the Coompana Province samples are scattered well beyond analytical precision (1192–1140 Ma), indicating that Moodini Supersuite magmatism was protracted.

Bottle Corner Shoshonite

In drillcore FOR010, mafic shoshonite (variably foliated hornblende metadiorite to metamonzodiorite) and two phases of Si-rich shoshonite (syenogranite veins) are assigned to the Bottle Corner Shoshonite. Based on lithological relationships in the drillcore, the second youngest unit is an unfoliated red porphyritic syenogranite and the youngest unit is an unfoliated, fine-grained, pink to red equigranular syenogranite. In drillcore FOR011, the Bottle Corner Shoshonite is more difficult to distinguish without geochemical data, and occurs as deformed veins or sheets of metamonzodiorite that typically contain biotite and green hornblende aligned in the foliation. In both drillcores, the Bottle Corner Shoshonite intrudes the Undawidgi Supersuite.

A sample of each of the three lithologies of Bottle Corner Shoshonite in drillcore FOR010 was dated. The hornblende metadiorite to metamonzodiorite (mafic shoshonite sample GSWA 192593) yielded an igneous crystallization age of 1175 ± 5 Ma (Wingate et al., 2015e). The porphyritic syenogranite yielded an igneous crystallization age of 1184 ± 8 Ma (GSWA 206752, Wingate et al., 2015i). Two analyses of a single zircon core from this sample indicate inheritance at 1558 ± 21 Ma. The fine-grained equigranular syenogranite (GSWA 206753) yielded an igneous crystallization age of 1192 ± 13 Ma (Wingate et al., 2015j). Three inherited zircon cores from this sample yielded ages (1σ) of 1576 ± 19 , 1522 ± 16 and 1511 ± 18 Ma, which are all older than the c. 1490 Ma Undawidgi Supersuite in the same drillcore.

A metadiorite with a hornblende–biotite foliation from drillcore FOR011 (GSWA 206729) yielded an igneous crystallization age of 1180 ± 6 Ma (Wingate et al., 2015f). The igneous crystallization ages for all four samples of Bottle Corner Shoshonite agree to within uncertainty and yield a mean of 1179 ± 9 Ma. Together with the relative age relationships and lithological relationships described above, this suggests that deformation and metamorphism of the mafic shoshonite occurred just prior to intrusion of the Si-rich, unfoliated, syenogranite veins.

Whole-rock geochemistry

Results of whole-rock major and trace element geochemistry are available for 189 samples collected from the eight stratigraphic drillcores and from exploration diamond drillcores, including EIS co-funded drillcores (Fig. 3). Whole-rock Sm–Nd isotope data were determined on selected samples from many, but not all, lithological or geochemical groups (Tables 6, 7) and these data are also integrated here. All whole-rock data and sample information are provided in Appendix 7 Tables A7.1 and 7.2. Assay data from altered samples are provided in Appendix 7 Table A7.3. The data are also available from the online Western Australian geochemistry ([WACHEM](#)) database.

Major element oxides and selected trace elements were determined by X-ray fluorescence (XRF). Other trace elements, and rare earth elements (REE) were measured by inductively coupled plasma mass spectrometry (ICP-MS) either at the University of Queensland, Geoscience Australia or ALS Laboratories (Perth, Australia). Based on multiple analyses of in-house reference materials, and on sample duplicates, precision and accuracy of major elements and trace elements by XRF is estimated at better than 4% relative standard deviation (RSD), and trace elements and REE by ICP-MS better than 5% RSD in most cases.

Sm–Nd isotope values were determined on crushed whole-rock samples by isotope dilution at the University of Rennes (France) or by ICP-MS at the University of Queensland. At the University of Rennes, samples were spiked with a ^{150}Nd – ^{149}Sm mixed solution and dissolved in HF–HNO₃. REE were separated using cationic resin and then Sm and Nd were collected by passing the solution through an additional set of ion exchange columns loaded with Ln spec Eichrom resin. Sm and Nd were loaded with HNO₃ reagent on to double Re filaments and analysed via multicollector mass spectrometry in static collection mode. All analyses of the unknowns are adjusted to a nominal $^{143}\text{Nd}/^{144}\text{Nd}$ value of 0.511850 for the La Jolla standard. At the University of Queensland, Nd isotopes were analysed by multi-collector ICP-MS using a Nu Plasma system. Instrument bias and mass fractionation were corrected by normalizing raw ratios to $^{146}\text{Nd}/^{144}\text{Nd} = 0.7219$. Additional details for each batch are provided on WACHEM. Two-stage depleted mantle model ages (T_{DM}^2) are calculated after Liew and Hofmann (1988), and assume an average crustal Sm/Nd ratio for the first stage of their evolution.

Whole-rock geochemistry of Madura Province rocks

In addition to the stratigraphic drillcores MAD002, MAD011 and MAD014, drillcores sampled in the Madura Province include those from the Burkin, Haig, Serpent, Loongana and Moodini prospects. Reference will also be made to samples of the Connie Sue Formation from the NSD prospect in the eastern Nornalup Zone of the Albany–Fraser Orogen, the Hannah prospect in the Rodona Shear Zone, and outcrop samples from coastal exposures at and southwest of Point Malcolm (Figs 3, 17, 21, 49). Collectively, this sample set can be divided into four major

rock groups; basalts and fine-grained mafic rocks, gabbroic rocks and peridotites, sodic granites, and potassic granites. All samples are metamorphosed to at least greenschist facies. The analysed samples represent the least altered and texturally and lithologically most homogeneous material available, covering the full lithological range encountered in each drillcore. Where sampling of altered material has been unavoidable, geochemical interpretation has been mainly based on variations in typically fluid-immobile elements. In all cases, major element data have been recalculated volatile free.

Basalts and fine-grained mafic rocks

Basalts and fine-grained mafic rocks were sampled from MAD002 (Pinto Basalt), MAD011 (Narilya Bore Basalt), the Burkin prospect (Sleeper Camp Formation), the NSD prospect (Connie Sue Formation) and Point Malcolm (Malcolm Metamorphics). Some samples show petrographic signs of extensive alteration or metamorphism (typically epidote, chlorite and actinolite), and some are schistose. Samples of the Narilya Bore Basalt, however, are typically massive and preserve igneous textures, and all of the rocks are interpreted to be either volcanic, volcanoclastic or subvolcanic based on preserved textures (see relevant sections above, and Appendices 2, 5 and 8).

Metamorphism and alteration

The effects that either, or both, metamorphism and alteration have had on primary geochemical variations are assessed by viewing variations in elements that are typically mobile under such conditions (e.g. large ion lithophile elements [LILE], such as Sr, Ba, Rb) against both analytical loss on ignition (LOI) and elements that are typically immobile (e.g. high field strength elements [HFSE], such as Nb, Zr, Ti).

The only relatively clear trends against LOI are positive correlations with MgO, Mg# (molecular MgO/[MgO+Total FeO] with all Fe calculated as Fe²⁺) and possibly CaO shown by the Pinto Basalt and metabasalt of the Malcolm Metamorphics (Fig. 53). These trends likely reflect chlorite+actinolite and epidote alteration of mafic minerals and plagioclase. The Pinto Basalt can be broadly divided into low- and high-MgO groups, and there is an indication that Rb, Cs and Li decrease with increasing LOI in both of these groups (Fig. 53). Positive correlations between Cs, Rb and possibly also K₂O are clear within and between the high- and low-MgO rocks of the Pinto Basalt, but none of these trace elements shows any clear correlation with concentrations of HFSE (e.g. Zr) or Th within either of these rock groups.

Samples of the Pinto Basalt with >13 wt% MgO (calculated on an anhydrous basis) typically also have higher concentrations of K₂O (Fig. 54), Cs, Rb, (Ba) and Li than lower MgO basalts, although the correlations are not systematic. There are relatively weak negative correlations between MgO (and Mg#) and HFSE within and between the high- and low-MgO basalts. This suggests that alteration and metamorphism had a more significant effect on the LILE than on other elements, as expected. Hence, any variations in concentrations of LILE (including K) in these rocks are not considered to reliably reflect igneous processes and high LILE concentrations in the high-MgO

basalts (and those of the Malcolm Metamorphics) most likely accompanied hydrous alteration of mafic minerals within those rocks, although the degree of alteration is not necessarily represented by present LOI values.

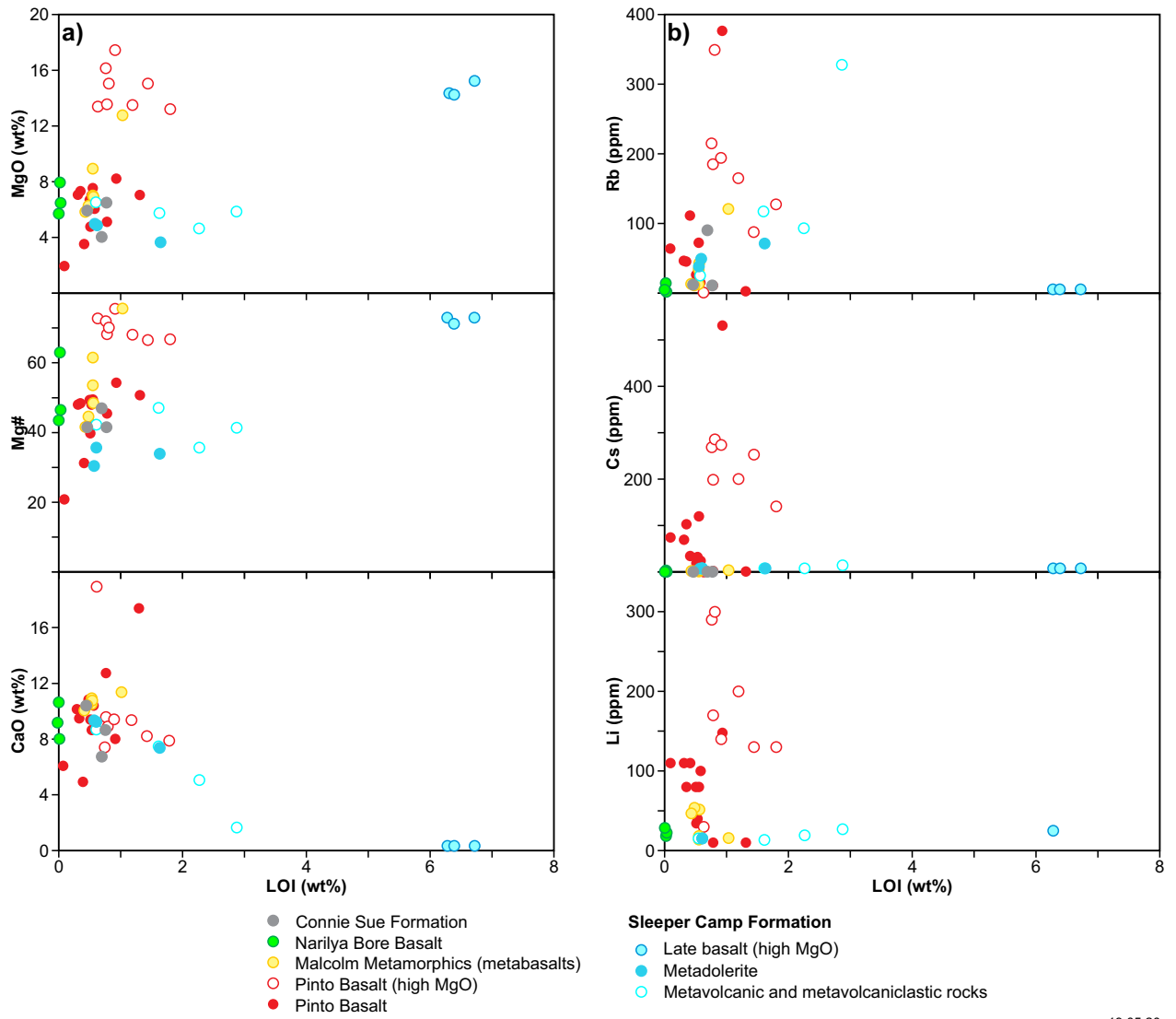
Poor correlations between HFSE, Th and both MgO and Mg# (Fig. 55) for all groups of basalts likely reflects a range of factors, including intrinsically low concentration ranges for many of these elements. However, it is also likely that a significant amount of compositional dispersion, in addition to that seen for the LILE elements, is a result of alteration and metamorphism. There is also the possibility that some of the fine-grained samples include a metasedimentary or volcanosedimentary component. However, reasonably well-constrained trends between HFSE (including Th) limit the amount of metasedimentary input and also provide confidence that compositional variation between these typically immobile trace elements has not been significantly disturbed.

Major element variations (all groups)

Major element compositions have been plotted against Mg# (Fig. 54). For most element oxides, the data for most of the rock groups are rather scattered, pointing to compositional modification attributable to hydrothermal alteration and/or metamorphism. All groups, however, show general trends to increasing FeO^T (total Fe calculated as FeO) with decreasing Mg# reflecting tholeiitic trends.

For the Pinto Basalt, some of the observed dispersion can be attributed to two samples with anomalously high CaO (>17 wt%) and low Al₂O₃, likely reflecting carbonate alteration, and two low-MgO samples with Mg# <32, high Na₂O (>3.5 wt%; Fig. 54) and very high HFSE concentrations. The latter two samples have compositions expected of fractionated liquids leaving magnetite–feldspar cumulates. The remaining samples of Pinto Basalt can be divided between a low-MgO group (MgO <9 wt%) and a high-MgO group (MgO >13wt%), as described above. Samples from both groups occur throughout much of the length of the drillcore, although low-MgO basalts dominate the upper and lowest parts of the core, and high-MgO basalts dominate the middle to lower parts. The high-MgO rocks have Mg# from 75 to 67. SiO₂ varies between 43.93 and 51.03 wt%, MgO between 17.81 and 13.54 wt%, and FeO^T between 13.93 and 9.14 wt%. Decreasing Mg# correlates with increasing concentrations of Al₂O₃ (4.81 – 13.61 wt%), TiO₂ (0.48 – 1.78 wt%), Na₂O (0.44 – 1.34 wt%) and P₂O₅ (0.06 – 0.19 wt%) and decreasing concentrations of Ni (1430–315 ppm) and Cr (2520–770 ppm) (Fig. 55), with increasing Cr/Ni ratios.

The low-MgO Pinto Basalt samples have Mg# from 54 to 40 (excluding the two strongly fractionated samples described above). SiO₂ varies between 45.07 and 48.81 wt%, MgO between 8.37 and 4.80 wt%, and FeO^T between 15.01 and 11.10 wt%. The other element oxides show little systematic variation against Mg# and vary within relatively narrow ranges (Al₂O₃ 16.59 – 12.54 wt%; TiO₂ 2.84 – 1.51 wt% [but mostly between 2.84 and 2.62 wt%]; CaO 12.74 – 8.16 wt%; Na₂O 3.38 – 2.59 wt%; P₂O₅ 0.44 – 0.13 wt%). Concentrations of Ni (<91 ppm) and Cr (<225 ppm) are low and decrease with decreasing Mg#.



CS440

19.05.20

Figure 53. Trends in various elements with loss on ignition (LOI) for metabasalts of the Madura Province: a) selected major elements and Mg#; b) selected fluid-mobile trace elements

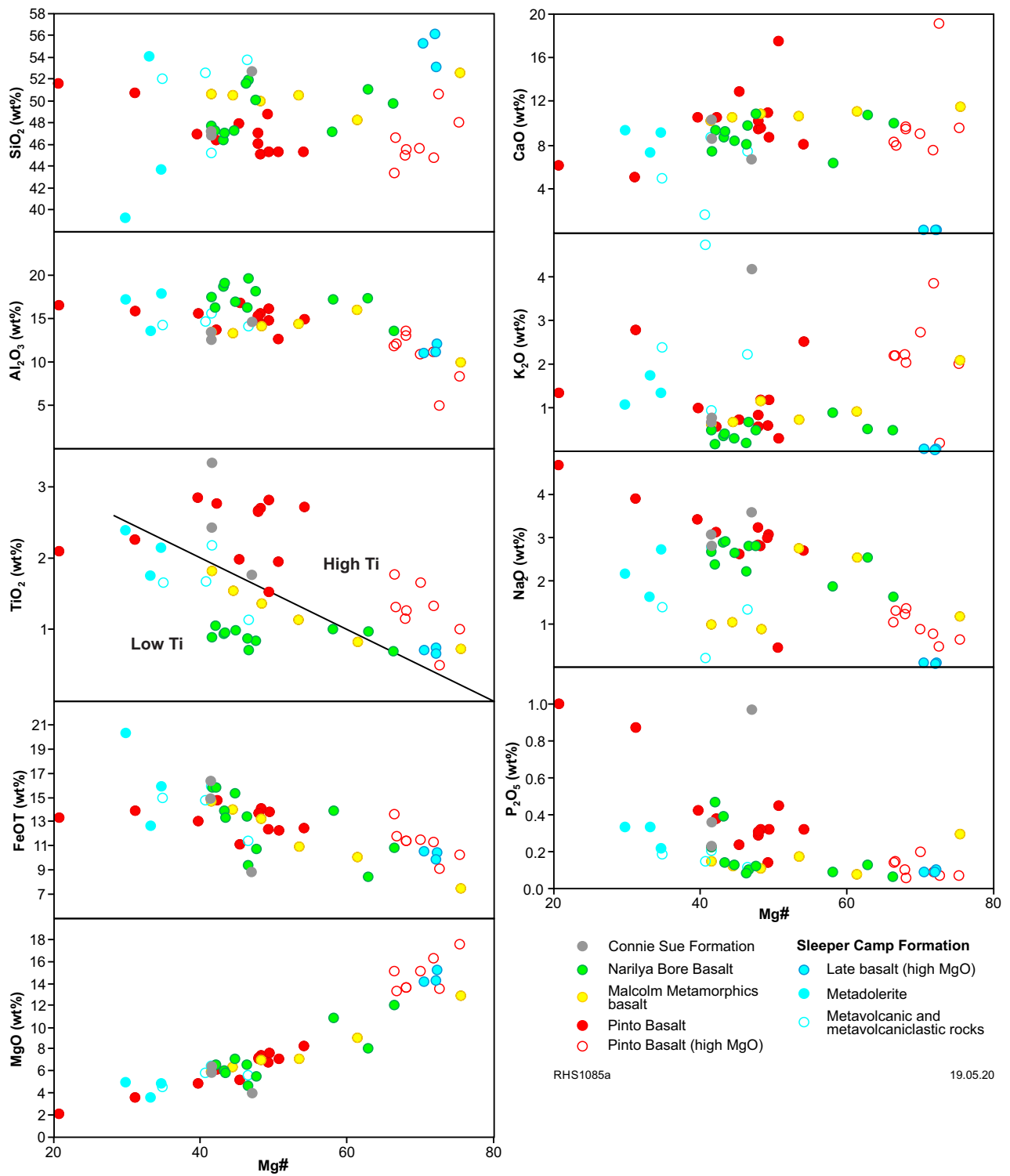


Figure 54. Variation in major element concentrations with Mg# for metabasalts of the Madura Province. The line in the plot of TiO₂ vs Mg# separates notationally high- from low-Ti groups

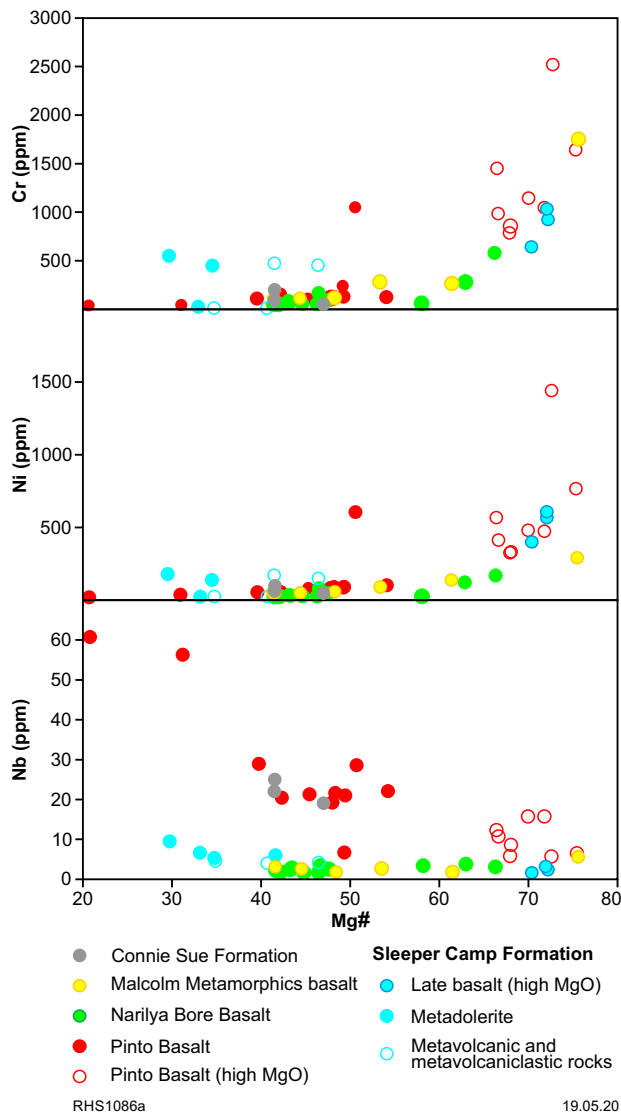


Figure 55. Variation in the concentrations of selected trace elements with Mg# for metabasalts of the Madura Province

Of the other groups, the Narilya Bore Basalt and the Malcolm Metamorphics basalt both include samples with MgO >10 wt%, with correspondingly high Mg# (Narilya Bore Basalt: 66; Malcolm Metamorphics basalt: 76) and Cr and Ni concentrations (Narilya Bore Basalt: 558 and 157 ppm, respectively; Malcolm Metamorphics basalt: 1751 and 279 ppm, respectively; Figs 54, 55). Both groups also show reasonably well-defined major element oxide trends against Mg#. In the case of the Narilya Bore Basalt, Al₂O₃ (19.35 – 13.47 wt%), FeO^T (8.38 – 15.92 wt%), Na₂O (1.60 – 2.87 wt%) and P₂O₅ (0.06 – 0.46 wt%) all increase as Mg# decreases to 42, while concentrations of CaO (10.63 – 6.26 wt%) and TiO₂ (1.03 – 0.68 wt%) show no trend. The Malcolm Metamorphics basalt shows a systematic increase in FeO^T (7.50 – 14.89 wt%) and TiO₂ (0.72 – 1.81 wt%) as Mg# decreases to 42 (Fig. 54), whereas CaO (11.52 – 10.10 wt%) decreases slightly, and P₂O₅ (0.07 – 0.29 wt%) and Na₂O (2.73 – 0.83 wt%) show no trend. The concentration of Al₂O₃ is low (9.82 wt%) in the most MgO-rich sample of the Malcolm Metamorphics basalt, but in the

more evolved rocks, Al₂O₃ decreases in concentration (15.88 – 13.28 wt%) as Mg# decreases from 61 to 42. The Sleeper Camp Formation mafic rocks lie in an MgO range from 15.1 to 3.52 wt% (Mg# 72–30). Notably, the three lithological groups of mafic rocks within the Sleeper Camp Formation each have samples falling within the high- and low-Mg# groups, with the metadolerite the lowest, and the late crosscutting basalt the highest. The Connie Sue Formation metabasalt has an MgO range of 6.50 – 4.05 wt% (Mg# 47–41).

Trace element variations (all groups)

Considering all groups, the rocks can be broadly divided, at a given Mg#, into high-Ti and low-Ti basalts (Fig. 54). The former division includes most rocks of the Pinto Basalt and Connie Sue Formation, which are also clearly distinguished from the other rocks by their very high Nb concentrations (Fig. 55). Samples falling into each of these two divisions also form very different primitive mantle (PM)-normalized trace element patterns (Fig. 56). In plotting these diagrams, we neglect LILE, which were shown above to be disturbed by alteration or metamorphic mobilization. The relatively smooth incompatible trace element pattern shown by most of the samples supports the suggestion that relative variations in the concentrations of REE and HFSE have not been significantly altered from primary igneous concentrations.

The only available whole-rock Sm–Nd data for basaltic rocks from the Madura Province are from the Pinto Basalt and the Narilya Bore Basalt (Table 6). The Pinto Basalt has a Nd isotope composition in the range of ϵ_{Nd} +2.54 to +3.33, when calculated at an inferred age of c. 1600 Ma, and an average T_{DM}^2 age of c. 1.87 Ga. The Nd isotope composition of the Narilya Bore Basalt, calculated at an inferred age of c. 1400 Ma, lies within the range ϵ_{Nd} +1.02 to +1.14, with an average two-stage depleted mantle model age of c. 1.85 Ga.

High-Ti basalts

The high-Ti Pinto Basalt and Connie Sue Formation metabasalt show smooth and quite fractionated PM-normalized patterns with normalized values consistently between those of enriched mid-ocean ridge basalt (E-MORB) and ocean-island basalt (OIB). Heavy rare earth element (HREE) concentrations vary from ~2–5 times PM values for the high-MgO Pinto Basalt samples to 6–10 times PM for the low-MgO samples, and reflect decreasing degrees of partial melting of a mantle source. On a plot of Th/Yb vs Nb/Yb (Pearce, 2008), all Pinto Basalt samples lie within or very close to the mantle (MORB–OIB) array (Fig. 57), indicating very little crustal material in their bulk source, and potentially an oceanic setting. Contamination by a small amount of crust might provide an explanation for the anomalously high Th/Yb ratios observed in the three Connie Sue Formation samples, compared with the Pinto Basalt. The radiogenic Nd isotope compositions of the Pinto Basalt also suggest very limited crustal contamination.

During partial melting of spinel lherzolite, Yb and Ti are similarly incompatible, but during partial melting of deeper mantle sources, Yb is preferentially partitioned into garnet. Hence, Ti/Yb ratios greater than those of normal mid-ocean ridge basalt (N-MORB) or E-MORB (~2600; Sun and McDonough, 1989) in primitive magmas can reflect deep (e.g. >2.8 Gpa; Pearce, 2008) melting of garnet lherzolite.

Table 6. Whole-rock Sm–Nd data and sample information from the Madura Province

GSWA sample ID	Series name	Stratigraphic unit	Lithology	Drillcore ID	T (Ma)	Sm (ppm)	Nd (ppm)	$^{147}\text{Sm}/^{144}\text{Nd}^*$	Standard-corrected $^{143}\text{Nd}/^{144}\text{Nd}^*$	$^{143}\text{Nd}/^{144}\text{Nd}_{(T)}$	CHUR _(T)	DM _(T)	$\epsilon\text{Nd}_{(T)}$	T_{DM} (Ga)	T_{DM}^2 (Ga)
201190	Haig 1 gabbro	Haig Cave Supersuite	Medium- to coarse-grained acicular leucogabbro	HDDH001	1400	2.30	8.83	0.157729 ± 0.000158	0.512302 ± 0.000005	0.510851	0.510841	0.511198	0.21		1.91
201191	Haig 1 gabbro	Haig Cave Supersuite	Medium-grained mesocratic gabbro; interlayered with medium-grained leucogabbro	HDDH001	1400	3.04	10.85	0.169415 ± 0.000169	0.512413 ± 0.000006	0.510855	0.510841	0.511198	0.27		1.91
201204	Haig 2 gabbro	Haig Cave Supersuite	Medium-grained melanocratic gabbro; anhedral plagioclase to 4mm	HDDH002	1400	1.30	4.38	0.179910 ± 0.000180	0.512492 ± 0.000006	0.510837	0.510841	0.511198	-0.08		1.93
201208	Haig 2 gabbro	Haig Cave Supersuite	Fine- to medium-grained mesocratic gabbro	HDDH002	1400	1.52	4.98	0.184062 ± 0.000184	0.512536 ± 0.000006	0.510843	0.510841	0.511198	0.04		1.92
201209	Haig plagiogranite	Haig Cave Supersuite	Granite vein	HDDH002	1400	0.80	4.38	0.109781 ± 0.000526	0.511766 ± 0.000008	0.510756	0.510841	0.511198	-1.65	2.04	2.05
201295	Haig plagiogranite	Haig Cave Supersuite	Foliated, medium-grained leucogranite	HDDH002	1400	1.26	10.37	0.073626 ± 0.000051	0.511460 ± 0.000006	0.510783	0.510841	0.511198	-1.14	1.85	2.01
201300	Haig plagiogranite	Haig Cave Supersuite	Weakly foliated, coarse- to medium-grained leucogranite	HDDH001	1400	0.73	3.06	0.143916 ± 0.000935	0.512122 ± 0.000008	0.510798	0.510841	0.511198	-0.83		1.99
201146	Loongana 1 gabbro	Haig Cave Supersuite	Medium-grained equigranular leucogabbro	LNGD001	1410	1.79	5.84	0.185243 ± 0.000185	0.512678 ± 0.000006	0.510962	0.510828	0.511184	2.63		1.74
201148	Loongana 1 gabbro	Haig Cave Supersuite	Medium-grained equigranular gabbro	LNGD001	1410	3.42	9.05	0.228545 ± 0.000229	0.513092 ± 0.000006	0.510975	0.510828	0.511184	2.87		1.72
201150	Loongana 1 gabbro	Haig Cave Supersuite	Fine- to medium-grained equigranular gabbro	LNGD001	1410	1.2	5.1	0.143732 ± 0.000144	0.512263 ± 0.000005	0.510931	0.510828	0.511184	2.02		1.78
201123	Loongana 1 peridotite	Haig Cave Supersuite	Fine- to medium-grained equigranular gabbro	LNGD001	1410	0.46	1.36	0.204035 ± 0.001144	0.512842 ± 0.000008	0.510952	0.510828	0.511184	2.44		1.75
201124	Loongana 1 peridotite	Haig Cave Supersuite	Fine- to medium-grained equigranular gabbro	LNGD001	1410	0.69	2.19	0.190818 ± 0.000897	0.512678 ± 0.000008	0.510910	0.510828	0.511184	1.61		1.81
201129	Loongana 1 peridotite	Haig Cave Supersuite	Fine- to medium-grained equigranular gabbro	LNGD001	1410	0.56	2.18	0.154683 ± 0.000727	0.512398 ± 0.000011	0.510965	0.510828	0.511184	2.68		1.73
201170	Loongana 2 gabbro	Haig Cave Supersuite	Fine- to medium-grained equigranular gabbro	LNGD002	1410	1.01	3.51	0.173635 ± 0.001631	0.512506 ± 0.000006	0.510897	0.510828	0.511184	1.36		1.83
201156	Loongana plagiogranite	Haig Cave Supersuite	Massive mesocratic granodiorite; subhedral plagioclase to 5mm	LNGD001	1410	3.09	12.46	0.149856 ± 0.000150	0.512315 ± 0.000006	0.510927	0.510828	0.511184	1.94		1.79
201160	Loongana plagiogranite	Haig Cave Supersuite	Foliated mesocratic granodiorite; anhedral plagioclase to 5mm	LNGD001	1410	3.03	12.70	0.144276 ± 0.000144	0.512232 ± 0.000006	0.510895	0.510828	0.511184	1.33		1.84
201164	Loongana plagiogranite	Haig Cave Supersuite	Foliated medium- to coarse-grained mesocratic granite – blue quartz	LNGD001	1410	1.69	8.35	0.122482 ± 0.000122	0.512058 ± 0.000006	0.510923	0.510828	0.511184	1.86	1.84	1.80
201169	Loongana plagiogranite	Haig Cave Supersuite	Foliated equigranular leucogranite	LNGD002	1410	2.43	15.57	0.094426 ± 0.000094	0.511632 ± 0.000006	0.510757	0.510828	0.511184	-1.38	1.95	2.04
201267	Loongana plagiogranite	Haig Cave Supersuite	Unfoliated, medium- to coarse-grained leucocratic metagranite	LNGD002	1410	3.10	20.32	0.092121 ± 0.000299	0.511615 ± 0.000006	0.510762	0.510828	0.511184	-1.29	1.94	2.03
213891	MAD002 adakite	Haig Cave Supersuite	Medium-grained, foliated, leucogranite; wisps of biotite	MAD002	1389	0.34	1.92	0.105613 ± 0.000718	0.511619 ± 0.000009	0.510655	0.510855	0.511214	-3.91	2.17	2.21
213898	MAD002 adakite	Haig Cave Supersuite	Medium-grained, weakly to moderately foliated, equigranular biotite leucogranite	MAD002	1389	0.90	5.42	0.100625 ± 0.000625	0.511645 ± 0.000007	0.510727	0.510855	0.511214	-2.51	2.04	2.11
216210	MAD002 adakite	Haig Cave Supersuite	Medium-grained, weakly to moderately foliated, equigranular and mesocratic biotite granite	MAD002	1389	1.13	6.46	0.105638 ± 0.000630	0.511794 ± 0.000008	0.510830	0.510855	0.511214	-0.49	1.93	1.95

Table 6. Continued

GSWA sample ID	Series name	Stratigraphic unit	Lithology	Drillcore ID	T (Ma)	Sm (ppm)	Nd (ppm)	$^{147}\text{Sm}/^{144}\text{Nd}^*$	Standard-corrected $^{143}\text{Nd}/^{144}\text{Nd}^*$	$^{143}\text{Nd}/^{144}\text{Nd}_{(T)}$	CHUR _(T)	DM _(T)	$\epsilon\text{Nd}_{(T)}$	T _{DM} (Ga)	T _{DM} ² (Ga)
182467	Serpent 1 gabbro	Haig Cave Supersuite	Metagabbro	SDDH1	1400	1.75	6.47	0.163800 ± 0.000164	0.512504 ± 0.000006	0.510998	0.510841	0.511198	3.07		1.70
182471	Serpent 2 gabbro	Haig Cave Supersuite	Metagabbro	SDDH1	1400	2.10	7.02	0.180713 ± 0.000181	0.512596 ± 0.000005	0.510934	0.510841	0.511198	1.82		1.79
213884	MAD002 E-MORB	Pinto Basalt	Fine-grained mafic with mm-scale laminations and 1–3 cm layers defined by mineralogical variations	MAD002	1600	5.00	21.19	0.142766 ± 0.000430	0.512253 ± 0.000006	0.510751	0.510581	0.510916	3.33		1.84
213888	MAD002 E-MORB	Pinto Basalt	Fine-grained mafic with well-developed mm-scale laminations; moderately foliated; minor carbonate veins	MAD002	1600	5.61	21.95	0.154562 ± 0.000195	0.512392 ± 0.000007	0.510766	0.510581	0.510916	3.63		1.82
213887	MAD002 high Mg E-MORB	Pinto Basalt	Fine-grained mica-rich mafic with mm-scale laminations; foliated; locally brecciated	MAD002	1600	3.71	13.56	0.165191 ± 0.000720	0.512441 ± 0.000007	0.510703	0.510581	0.510916	2.39		1.91
216201	MAD002 high Mg E-MORB	Pinto Basalt	Fine-grained mafic with 1–2 cm layering defined by mica content	MAD002	1600	3.03	11.90	0.154126 ± 0.000253	0.512332 ± 0.000007	0.510711	0.510581	0.510916	2.54		1.90
216226	MAD011 basalt	Narilya Bore Basalt	Fine-grained, massive, non-layered rock containing <5% biotite; inclusion in medium- to coarse-grained leucogabbro with lobate contacts	MAD011	1400	2.12	9.94	0.128937 ± 0.000751	0.512085 ± 0.000005	0.510899	0.510841	0.511198	1.14	1.93	1.84
216229	MAD011 basalt	Narilya Bore Basalt	Fine-grained mafic with <5% biotite; well-developed layering is contorted and semicontinuous on a 1–2 mm scale	MAD011	1400	2.56	9.62	0.160745 ± 0.000881	0.512371 ± 0.000007	0.510893	0.510841	0.511198	1.02		1.85
216221	MAD011 high-KFe	Kestrel Cavern Gabbro	Medium- to coarse-grained, grey, plagioclase-rich leucogabbro; subhedral to euhedral plagioclase to 1 cm	MAD011	1144	14.9	66.4	0.135321 ± 0.000182	0.512038 ± 0.000006	0.511022	0.511173	0.511559	–2.95	2.18	1.93
192595	MAD014 High-KFe	Moodini Supersuite	Unfoliated granodiorite	MAD014	1182	20.2	116.5	0.104884 ± 0.000105	0.511738 ± 0.000006	0.510924	0.511124	0.511505	–3.91	1.99	2.04
201282	MAD014 High-KFe	Moodini Supersuite	Unfoliated, mesocratic, medium- to coarse-grained, equigranular biotite–hornblende granodiorite to monzogranite	MAD014	1182	17.9	101.9	0.106114 ± 0.000082	0.511717 ± 0.000006	0.510894	0.511124	0.511505	–4.49	2.04	2.08
201283	MAD014 High-KFe	Moodini Supersuite	Unfoliated, medium- to fine-grained equigranular biotite syenogranite; later phase	MAD014	1182	2.4	13.5	0.105733 ± 0.000117	0.511688 ± 0.000006	0.510867	0.511124	0.511505	–5.02	2.08	2.12
201284	MAD014 High-KFe	Moodini Supersuite	Fine-grained biotite monzogranite (transitional to GSWA 201283)	MAD014	1182	5.1	36.5	0.083714 ± 0.000430	0.511559 ± 0.000008	0.510909	0.511124	0.511505	–4.19	1.88	2.06
201289	MAD014 High-KFe	Moodini Supersuite	Unfoliated, mesocratic, medium- to coarse-grained, equigranular biotite–hornblende granodiorite to monzogranite	MAD014	1182	16.9	95.7	0.107009 ± 0.000421	0.511731 ± 0.000008	0.510900	0.511124	0.511505	–4.37	2.04	2.07
201293	MAD014 High-KFe	Moodini Supersuite	Unfoliated, mesocratic, medium- to coarse-grained, equigranular biotite–hornblende granodiorite to monzogranite	MAD014	1182	21.6	122.1	0.106799 ± 0.000849	0.511724 ± 0.000007	0.510896	0.511124	0.511505	–4.46	2.05	2.08
201216	Moodini High-KFe	Moodini Supersuite	Medium- to coarse-grained, seriate to porphyritic mesocratic granite	MORC001	1125	24.0	109.0	0.132888 ± 0.000133	0.512053 ± 0.000006	0.511071	0.511197	0.511586	–2.47	2.09	1.88
201220	Moodini High-KFe	Moodini Supersuite	Coarse-grained seriate to porphyritic mesocratic granite	MORC001	1125	9.9	45.4	0.132353 ± 0.000132	0.512025 ± 0.000006	0.511047	0.511197	0.511586	–2.94	2.13	1.92
201223	Moodini High-KFe	Moodini Supersuite	Fine- to medium-grained, equigranular to seriate, mesocratic to melanocratic granite	MORC002	1132	9.2	46.6	0.119642 ± 0.000120	0.511927 ± 0.000005	0.511038	0.511188	0.511576	–2.95	2.00	1.92
182479	Hannah High-KFe	Booanya Suite	Metamonzodiorite	Hannah 1	1170	20.7	134.8	0.092630 ± 0.000093	0.511577 ± 0.000005	0.510865	0.511139	0.511522	–5.35	1.99	2.14
182483	Hannah High-KFe	Booanya Suite	Metamonzodiorite	Hannah 2	1170	24.4	160.5	0.092048 ± 0.000092	0.511568 ± 0.000006	0.510861	0.511139	0.511522	–5.44	1.99	2.14

NOTE: Model age parameters ($^{147}\text{Sm}/^{144}\text{Nd}$)_{DM} = 0.2136, ($^{143}\text{Nd}/^{144}\text{Nd}$)_{DM} = 0.513163, ($^{147}\text{Sm}/^{144}\text{Nd}$)_{CHUR} = 0.1967, ($^{143}\text{Nd}/^{144}\text{Nd}$)_{CHUR} = 0.512638; decay constant of ^{147}Sm = $6.54 \times 10^{-12} \text{ T}_{\text{DM}}$ is not calculated for samples with $^{147}\text{Sm}/^{144}\text{Nd}$ ratio >0.14. * Reported uncertainties are 2σ. Abbreviations: T, age of Nd calculation; T_{DM}, single-stage depleted mantle model age; T_{DM}², two-stage depleted mantle model age

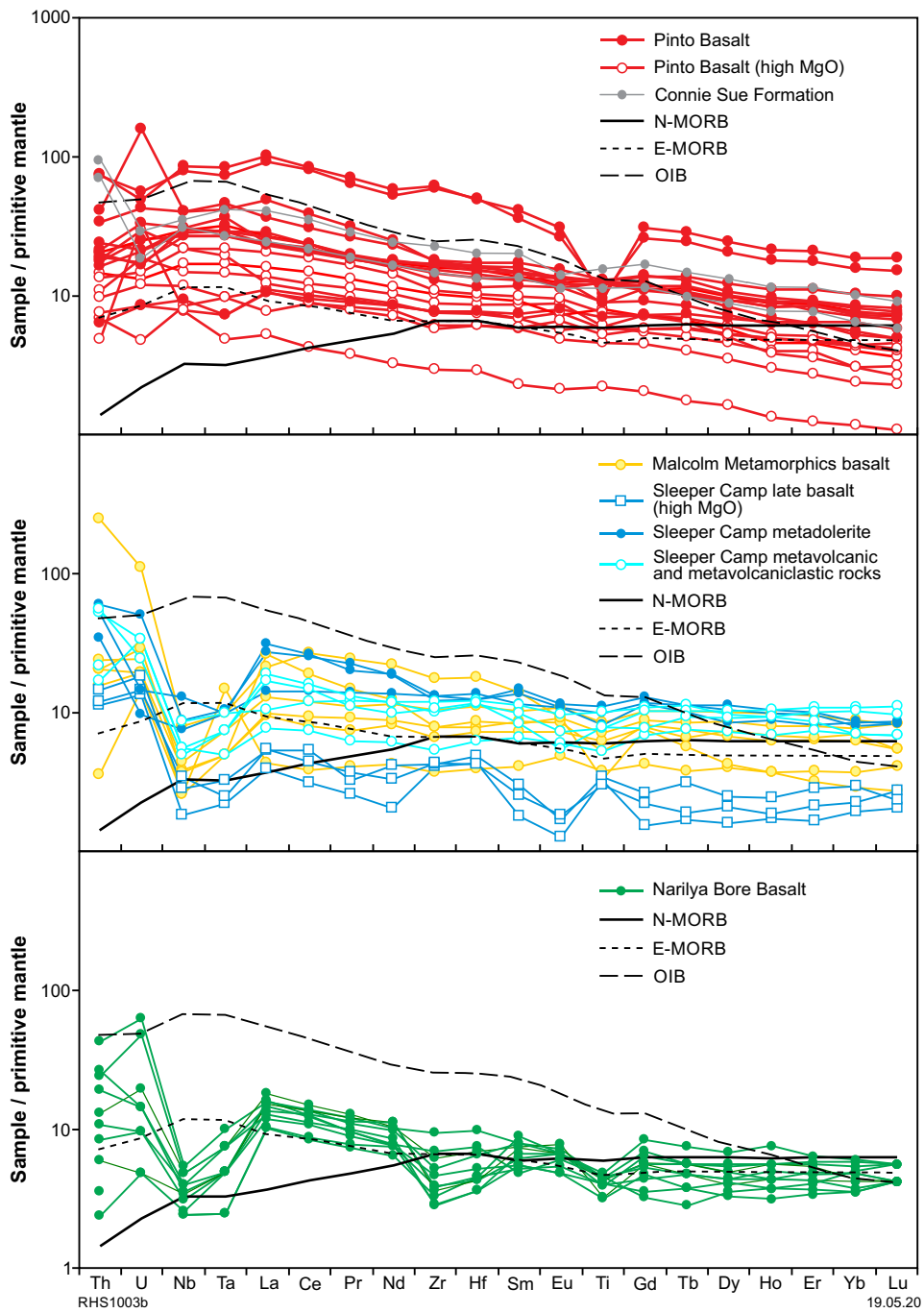


Figure 56. PM-normalized trace element spider diagrams for metabasalts from the Madura Province (normalizations after Sun and McDonough, 1989). Abbreviations: E-MORB, enriched mid-ocean ridge basalt; N-MORB, normal mid-ocean ridge basalt; OIB, ocean-island basalt

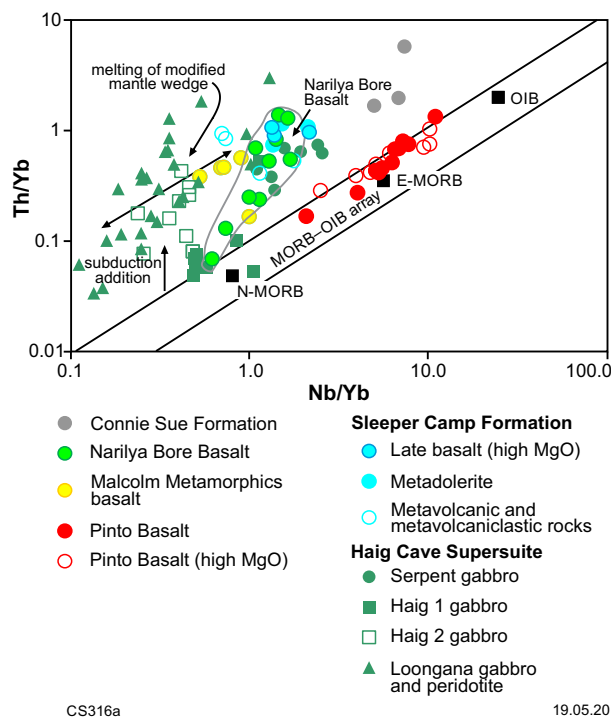


Figure 57. Logarithmic Th/Yb vs Nb/Yb diagram (after Pearce, 2008) for mafic rocks of the Madura Province. Modified from Spaggiari et al. (2015a, 2018)

The range of Ti/Yb ratios from the Pinto Basalt is from 2820 to 6511, exceeding that of E-MORB and spanning much of the gap between E-MORB and OIB. These variations are largely independent of the Mg# or MgO content of the rocks. Samples from the Connie Sue Formation also have high Ti/Yb ratios of 4061–4600. Thus, both groups have compositions consistent with low-degree partial melting of a fertile mantle source at deep levels within the garnet lherzolite stability field, and are likely a result of deep asthenospheric upwelling. Such compositional trends resemble those expected during plume–ridge interactions or ocean–continent transition zones (e.g. Pearce 2008), although such interpretations are very speculative based on sampling from such a geographically restricted area. The important geodynamic constraints here include the limited degree of crustal influence, the significant inferred depth (>90 km) of melting (e.g. thick lithosphere) and likely higher than ‘normal’ mantle temperatures (required to begin melting at higher pressure).

Low-Ti basalts

The low-Ti basalts (Narilya Bore Basalt, Sleeper Camp Formation, Malcolm Metamorphics) have PM-normalized patterns that contrast significantly with those of the high-Ti basalts of the Pinto Basalt and Connie Sue Formation (Fig. 56). The normalized patterns for the low-Ti basalt are relatively flat, with concentration ranges for most elements typically between 3 and 30 times PM values (mostly <10 times N-MORB), and Th/Yb_(PM) ratios from 0.4 to 8. Ratios of HFSE/Yb are typically close to N-MORB values, reflecting a depleted mantle source. HFSE / light rare earth elements (LREE) and HFSE/Th ratios, however, are much lower than N-MORB values, requiring the addition of an enriched, or crustal, component to the bulk source. These patterns closely resemble those of tholeiitic basalts

derived from a weakly subduction-modified depleted mantle source in a fore-arc or back-arc region. The effect of crustal addition to a subduction-related mantle source can usually be identified on a Th/Yb – Nb/Yb diagram (Fig. 57); addition of the subduction-mobile element Th produces sources with high Th/Nb ratios that melt to produce magma series with Th/Yb – vNb/Yb trends that parallel the mantle array (Pearce, 2008). Most samples of the Malcolm Metamorphics and Sleeper Camp Formation have Th/Yb ratios ~1, consistent with derivation from a subduction-modified source, although a trend that parallels the mantle array is only weakly developed. The samples of the Narilya Bore Basalt, however, show a very different trend, which emanates from a point very close to N-MORB and just above the mantle array, and then shows systematically increasing Th/Yb > Nb/Yb (Fig. 57). Such trends can reflect continuous magma–crust interaction, although the crust component is not necessarily continental crust, but may be contemporaneous, or only slightly older, subduction-related crust with a high Th/Nb ratio (i.e. contamination of basalt derived from a mantle-wedge source, which may or may not be weakly subduction-modified, by overlying young arc crust).

The Narilya Bore Basalt falls into two groups based on depth within the drillcore, an upper unit (579–601 m) and a lower unit (629–642 m). The upper unit occurs as inclusions within a monzogabbro intrusion (the Kestrel Cavern Gabbro of the Moodini Supersuite), whereas the lower unit occurs by itself in the drillcore. The upper unit has low Mg# (46–42). The lower unit includes samples with Mg# as high as 66, and most samples have higher Th/Yb, Nb/Yb, Zr (Hf) (Fig. 58), Th, U and Nb, and typically also K, Ba, Cs and Rb than those of the upper basalt unit. Both groups of the Narilya Bore Basalt differ further from the other low-Ti basalts in having distinctive negative Zr (Hf) anomalies in PM-normalized diagrams (Fig. 56), typically with Nb/Zr ratios > N-MORB values of 0.031. The Zr/Zr* ratio is a measure of the mantle-normalized Zr anomaly and for the Narilya Bore Basalt this decreases (i.e. the Zr anomaly becomes more negative) as Th/Yb, Mg#, Th and Zr decrease (Fig. 59). Hence, the explanation for the negative Zr anomaly is either unrelated to, or is negatively correlated with, the process leading to Th enrichment in the more MgO-rich samples of the Narilya Bore Basalt.

In detail, samples of the Sleeper Camp Formation define two patterns: a trace element depleted group that corresponds with samples that have high (>73) Mg#, and a lower Mg# group that shows more enriched trace element patterns. As noted previously, the three lithological groups of mafic rocks within the Sleeper Camp Formation each have samples falling within both trace element groups, providing no clear geochemical distinction between these lithological types.

Alteration of Sleeper Camp Formation metasedimentary rocks

Geochemical data initially obtained from the two Burkin prospect drillcores was essentially limited to six elements: Co, Cr, Cu, Fe, Ni and Zn (Gunson Resources; Harley, 2010). The data identified several horizons with anomalously high concentrations of Cu (e.g. BKD01 292–310 m with Cu between 131 and 394 ppm; 350–360 m with Cu between 106 and 995 ppm), with corresponding

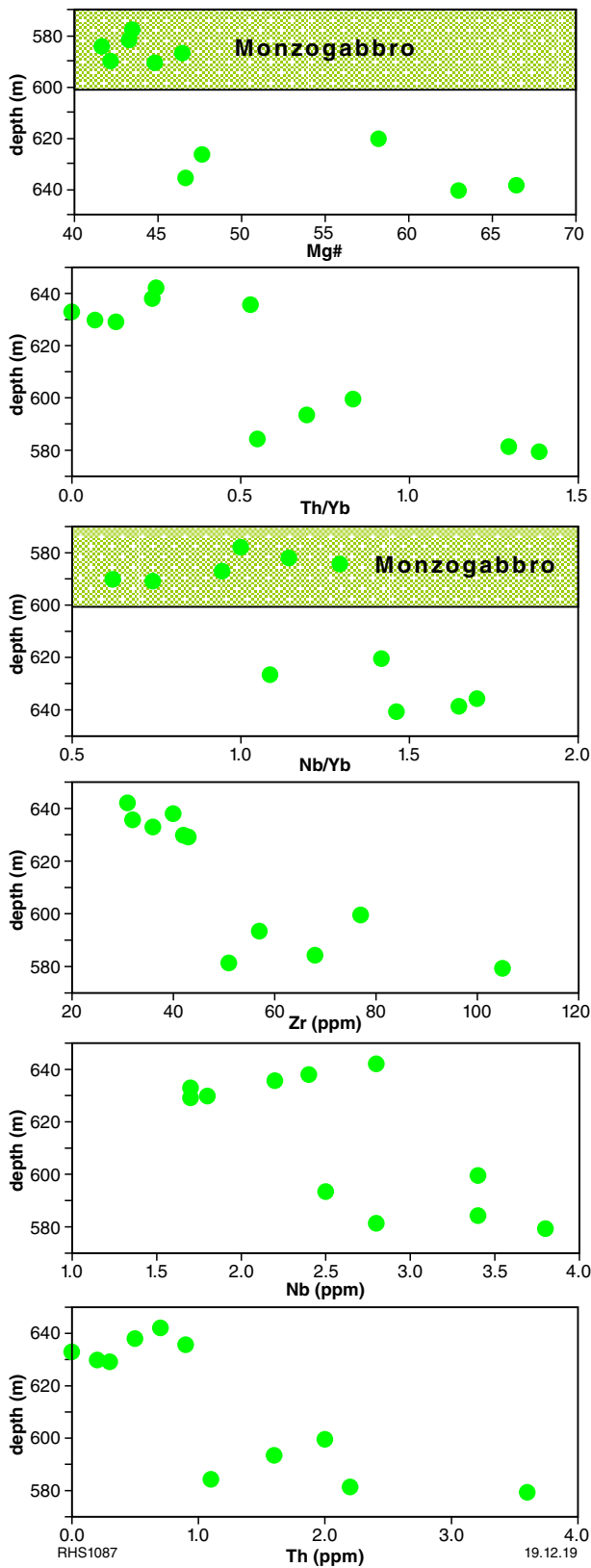


Figure 58. Geochemical groups of the Narilya Bore Basalt associated with depth intervals within drillcore MAD011. The unit above drillcore depth 599 m occurs as inclusions within monzogabbro of the Kestrel Cavern Gabbro

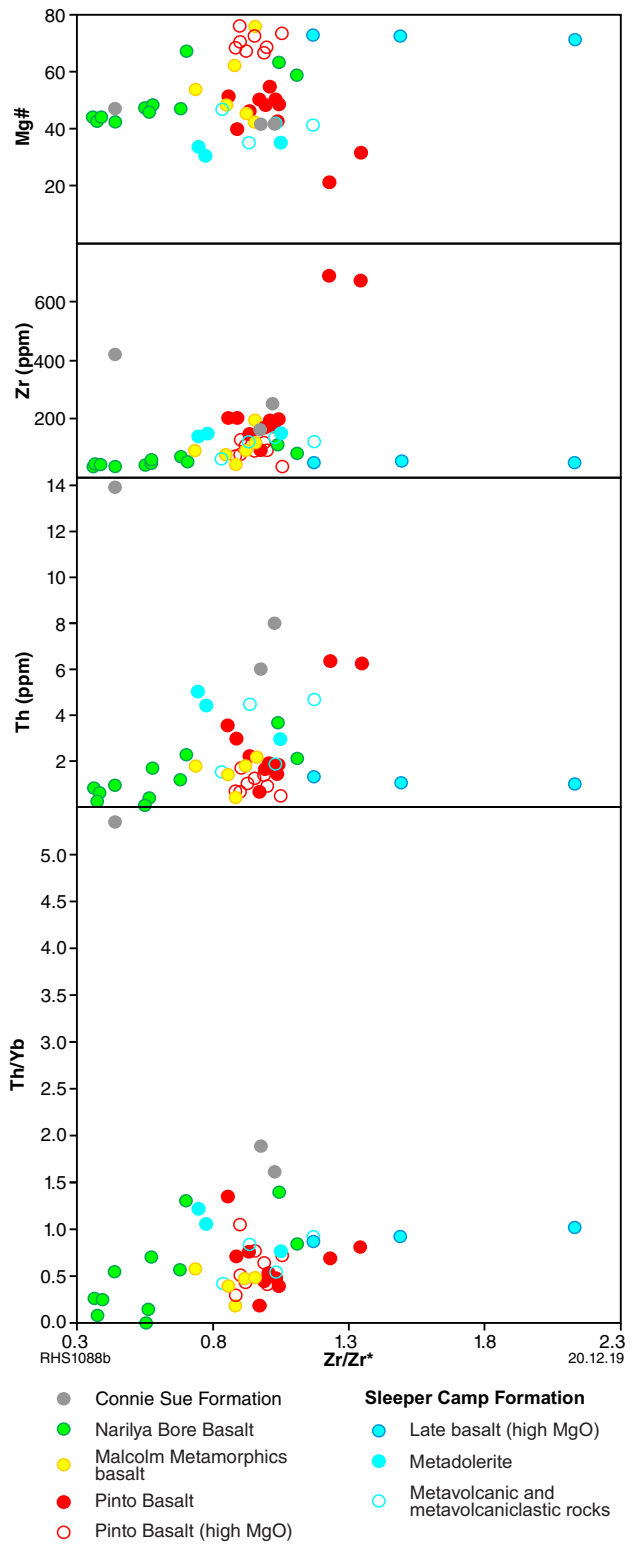


Figure 59. Variation in Mg#, Zr, Th and Th/Yb with Zr/Zr^* for metabasaltic rocks of the Madura Province. $Zr^* = (Nd_{(PM)} + Sm_{(PM)})/2$; PM, PM-normalized

FeO and Cr analyses suggesting a broadly basaltic or basaltic volcanosedimentary lithology. Narrower horizons had FeO and Ni concentrations consistent with more primitive (high Mg#) basaltic lithologies and anomalous Ni and Cu were mutually exclusive, suggesting Ni was not hosted in sulfide minerals.

Importantly, however, it appears that the magnetite horizons in the metasedimentary rocks (see above) were initially not analysed. We sampled two such horizons from BKD01 (GSWA 201271 and 201274; Appendix 7, Table A7.1) with FeO from 40 to 48 wt%. One sample has anomalous Cu (>300 ppm) and both samples have MnO between 4.8 and 8.7 wt%.

Ultramafic, mafic and intermediate (monzonitic) intrusive rocks

Mafic and/or ultramafic intrusive rocks were sampled in drillcore MAD011 and in six of the exploration diamond drillcores (Loongana prospect: LNGD001, LNGD002; Haig prospect: HDDH001, HDDH002; Serpent prospect: SDDH001, SDDH002; Fig. 17, Table 3). Monzodiorite and monzonite intersected in the Hannah 1 exploration drillcore yielded a date of 1170 ± 4 Ma, interpreted as the age of magmatic crystallization coeval with a high-grade metamorphic event forming zircon rims (GSWA 182203; Kirkland et al., 2012a). These rocks are assigned to the Booanya Suite of the Esperance Supersuite (Smithies et al., 2015b).

Haig Cave Supersuite: Loongana, Haig and Serpent prospects

Weakly layered, medium-grained, mafic cumulate rocks form the basement lithology at the Serpent prospect. They also greatly dominate the basement geology defined by the two Haig drillcores, but there are intruded by medium- to coarse-grained trondhjemitic plagiogranite. Each of the drillcores for both Haig and Serpent sampled geochemically distinct mafic cumulate rocks. The two drillcores from Loongana cannot be distinguished from each other on the basis of lithological variation or geochemistry, although few samples were taken from LNGD002. This indicates at least five, geochemically distinct, but more or less contemporaneous, mafic intrusive units within this region of the Madura Province.

The Loongana LNGD001 drillcore was the most extensively sampled. The upper portion of the basement component of this core is dominated by weakly layered, medium-grained, mafic rocks but also includes an approximately 13 m-thick interval of medium-grained, peridotitic cumulate rocks. The lower part of the drillcore is dominated by medium- to coarse-grained trondhjemitic plagiogranite, which is also the dominant lithology in LNGD002. In the mafic to ultramafic interval, compositional trends with increasing depth include repeated intervals over which MgO and Mg# increase and Rb decreases (Fig. 60). These trends suggest that the intrusion is the right way up; that is fractionation trends increase upwards. The basal part of the peridotite layer shows trends reflecting mixing with the upper part of the underlying mafic layer, suggesting both units were at least partially liquid at the same time (i.e. the peridotite

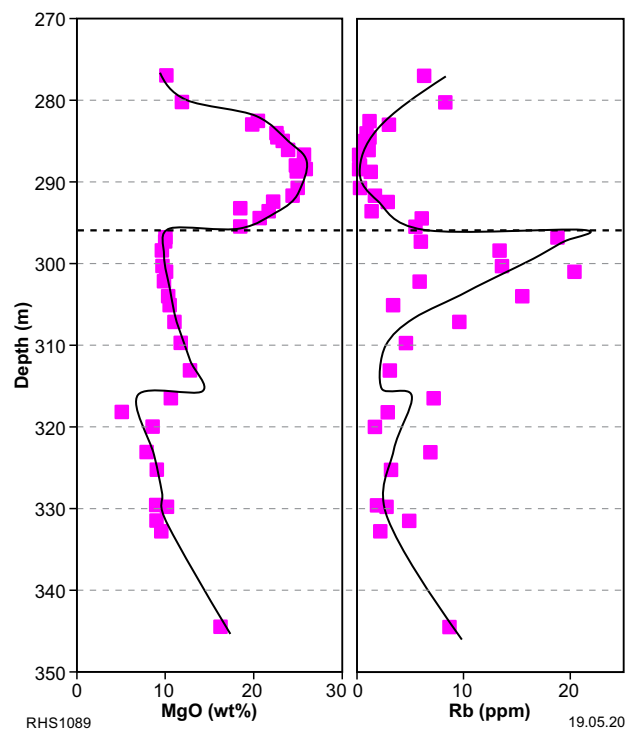


Figure 60. Variation of MgO and Rb with depth for samples of drillcore LNGD001 from the Loongana prospect. The upper portion of this core is dominated by metagabbroic rocks but also includes an approximately 13 m-thick interval of peridotitic cumulate rocks. The lower part is dominated by trondhjemitic plagiogranite. Compositional trends with increasing depth include repeated intervals over which MgO and Mg# increase and Rb decreases, suggesting that the intrusion is the right way up

unit was not a dyke or sill emplaced into an already fully crystallized rock).

Trends to Fe-enrichment (Fig. 61) and low K₂O contents show that the Haig Cave Supersuite intrusions from the Serpent, Haig and Loongana prospects are derived from low- to medium-K, tholeiitic parental magmas. Two anomalously high-Ti samples from Haig 1 (Fig. 61) are magnetite cumulates. With Mg# >60, the Loongana and Haig 2 rocks possibly crystallized from near-primary magmas, whereas the compositions in Haig 1, Serpent, Hannah 1 and the Kestrel Cavern Gabbro are far from those of a primary parental magma.

N-MORB-normalized trace element plots for the Loongana and Haig intrusions (Fig. 62) show 'spiky' patterns typical of mafic cumulate rocks. For the Loongana intrusion, the normalized concentration range for the mafic and ultramafic cumulates overlaps completely for most trace elements, although the mafic rocks generally occupy the higher part of that range. The most significant difference is that the mafic rocks show positive Sr anomalies and no negative Eu anomaly, consistent with a higher modal plagioclase content. For both mafic and ultramafic rocks, there are pronounced negative Nb (Ta) and Zr (Hf) anomalies, although Nb/Zr ratios remain below N-MORB values, and normalized REE patterns are relatively flat to slightly enriched in LREE. The Loongana rocks all contain a high proportion of cumulate minerals and so

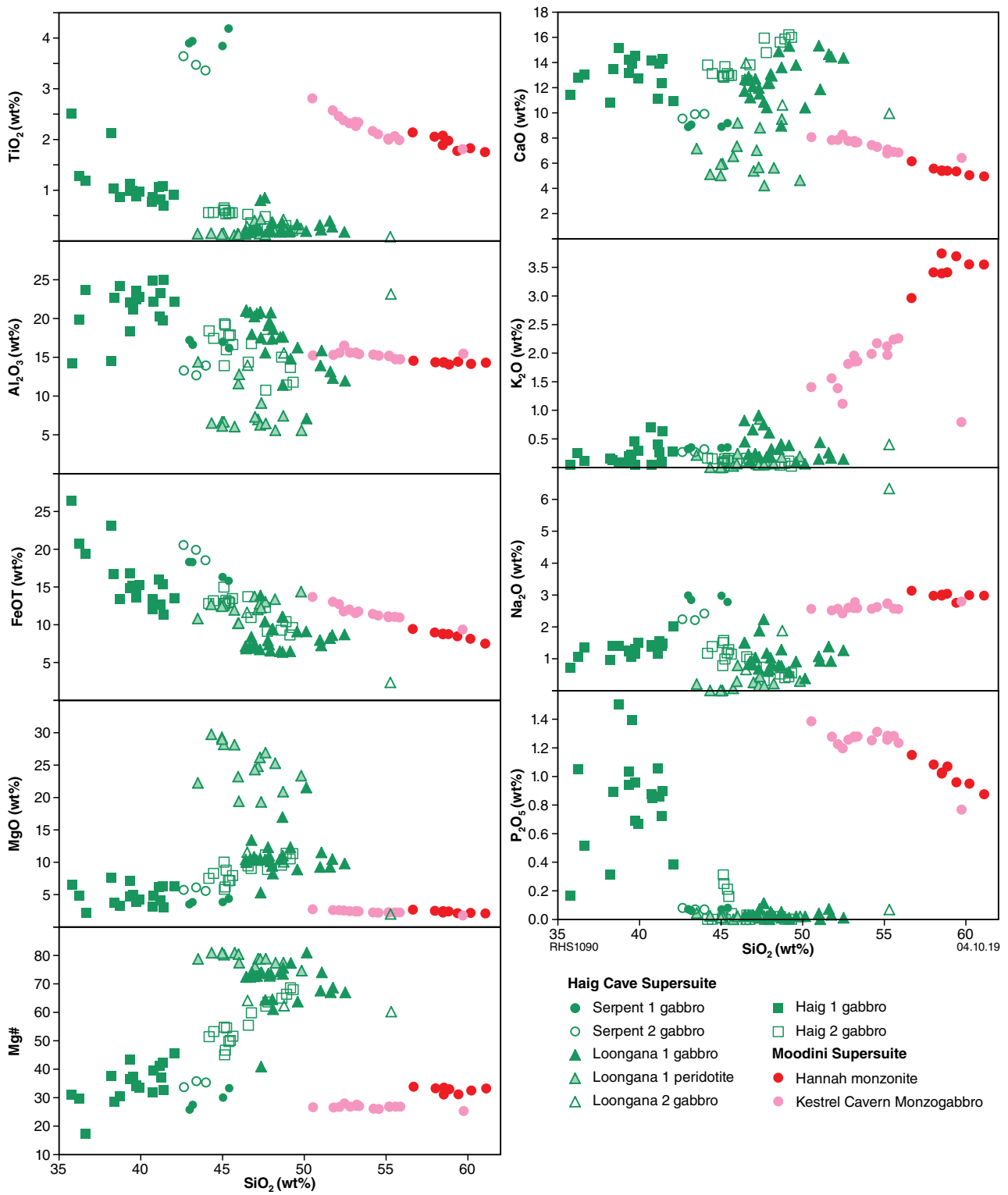


Figure 61. Compositional variation diagrams for mafic and intermediate intrusive rocks from the Madura Province

their abundance patterns do not directly reflect that of the parental liquid. Nevertheless, in most cases, there is a systematic increase in normalized concentrations in the order Nb, Zr, Ti, Yb, a pattern that possibly indicates magma derivation from a source more depleted than that of an N-MORB source. Mineral/melt partition coefficients (D) for all major minerals in these rocks are such that $D_{\text{Nb, La, Th, Zr}} < D_{\text{Yb}}$. Hence, the slight enrichments in Th, HFSE and LREE relative to HREE are an underestimate of magmatic values, although the significant negative Nb anomalies and Nb/Yb and Zr/Yb ratios below N-MORB values will still broadly characterize the magmatic compositions. Thus, although the source was likely similar to, or more depleted than, N-MORB source, the magmas from which the Loongana rocks crystallized had higher Th/HFSE and LREE/HFSE ratios than N-MORB.

The two Haig intrusions are mineralogically distinct from each other. Haig 1 has an essentially anhydrous, pyroxene-dominated mafic mineralogy, whereas Haig 2 contains hornblende. These differences correspond to significant differences in major element compositions (Fig. 61). Compared with Haig 1, rocks from Haig 2 have higher SiO_2 (>43 wt% cf. <43 wt%), MgO, Mg# (45–69 cf. 17–46) and lower Al_2O_3 , FeO and P_2O_5 concentrations. These compositional differences reflect the more plagioclase-rich mineralogy of Haig 1, but it is also clear that this intrusion crystallized from a much more evolved magma with a significantly better-developed, tholeiitic Fe-enrichment trend. Despite these mineralogical and major element differences, the normalized trace element patterns for these two intrusions (Fig. 62) are reasonably similar, although there are some subtle and systematic differences. Haig 2, for example, has generally lower concentrations of the less incompatible trace elements (e.g. MREE and HREE), and higher concentrations of Pb, Th and U. This results in, for example, higher LREE/HREE and Th/Nb ratios in Haig 2, as well as lower Gd/Yb ratios, which might reflect evolution dominated by hornblende removal.

When trace elements that are significantly affected by cumulate processes within mafic magmas are not considered, normalized trace element patterns for Loongana gabbros and Haig 2 gabbros are similar (Fig. 63). Lower Pb, Th and U in Haig 2 might reflect a less significant 'crustal' or 'subduction' component and the same argument might also apply for Zr (Hf). Concentrations of Zr and Hf are lower in Haig 2; however, Yb concentrations are also at the low end of the range for gabbros from Loongana. In addition, only a few samples from Haig 2 have Nb concentrations at or above the lower level of analytical detection, and so it is quite likely that most Haig 2 rocks also have significantly lower Nb concentrations than the Loongana gabbros. Thus, although Nb, Zr and Yb might be at lower concentrations in Haig 2, ratios of these elements are probably quite similar to those in Loongana gabbros, reflecting a similarly depleted mantle source.

The two Serpent intrusions have compositions significantly more Ti-enriched than gabbro from Haig or Loongana, likely reflecting cumulate Ti-rich magnetite. The Serpent rocks are also unusually enriched in Na_2O (to 2.98 wt%), Nb and Zr compared with Haig and Loongana gabbros (Figs 61, 62). Their normalized trace element patterns are tightly constrained, with only slight negative Nb anomalies and relatively marked positive Pb, Sr, Eu and Ti anomalies (Fig. 62). The Sr, Eu and Ti anomalies most

likely reflect cumulate plagioclase and Ti-magnetite or ilmenite. Ignoring trace elements significantly influenced by cumulate mineralogy, the Serpent gabbros have N-MORB-normalized patterns similar to the low-Ti basalts of the Malcolm Metamorphics (Fig. 63), but with slightly higher Nb/Yb ratios likely reflecting a slightly less-depleted mantle source component. The patterns reflect weak 'crustal' or 'subduction' influences superimposed on a HFSE pattern that suggest a source slightly depleted with respect to PM, but not as depleted as an N-MORB source.

Using the Th/Yb – Nb/Yb projections of Pearce (2008), gabbroic intrusions sampled from the Madura Province can be divided into at least two groups (Fig. 57). The first group contains a single gabbro body (Haig 1) with relatively low Th/Nb ratios (and low Th/Yb and Nb/Yb) lying close to MORB values. This intrusion formed from low-K tholeiitic magmas derived from a mantle source that was similar to N-MORB source, although Th/Nb ratios slightly above N-MORB values probably require at least a very minor crustal component, either as a subduction contribution to the source or as a younger contaminant.

The second group contains the Serpent and Loongana intrusions and the hornblende-bearing Haig 2 intrusion. These bodies collectively form a trend that parallels the mantle array but at higher Th/Nb ratios. In this analysis, the trends for individual intrusions cannot be considered as they might include the effects of variations in cumulate mineralogy at constant Th/Nb ratios. Nevertheless, there is no indication that the overall trend collectively shown by the bodies has been greatly influenced by interaction with continental crustal material, which should produce a trend to significantly elevated Th/Nb ratios. The observed trend is best interpreted in terms of individual magma batches derived via different degrees of partial melting of a subduction-enriched mantle source with a narrow range of Th/Nb ratios. The difference between the two groups of intrusions is also seen on a plot of Ti vs V, which can be used to distinguish typically V-enriched arc (oceanic) basalts from non-subduction-related basalts (e.g. Shervais, 1982; Fig. 64). The application of the Ti–V diagram to rocks potentially containing cumulate Ti or V oxides requires caution. Nevertheless, the 'tholeiitic' Haig 1 gabbros have relatively high Ti/V ratios (14–28) within or marginal to the field for N-MORB-like basalts derived from relatively dry and reduced mantle (e.g. Shervais, 1982), whereas the other intrusions plot within the arc field. Thus, in terms of their ranges in Th/Nb and V/Ti ratios, it can be suggested that the Group 1 gabbro (Haig 1) was derived from a depleted mantle source with only very minor prior subduction enrichment, whereas the magmas forming Group 2 bodies were most likely derived from a subduction-enriched mantle source.

Kestrel Cavern Gabbro and Hannah 1 intrusion

At a given SiO_2 content, mafic intrusive rocks of the Kestrel Cavern Gabbro and from the Hannah prospect have unusually high FeO, TiO_2 and P_2O_5 concentrations, and low and remarkably constant Mg# (<35; range for Kestrel Cavern Gabbro is 25–28 and for Hannah is 31–34). They show normal igneous trends of systematically decreasing TiO_2 , FeO, MgO and CaO, increasing K_2O and roughly constant Al_2O_3 and Na_2O , with increasing SiO_2 (Fig. 61). Compared with the gabbroic rocks of the Haig,

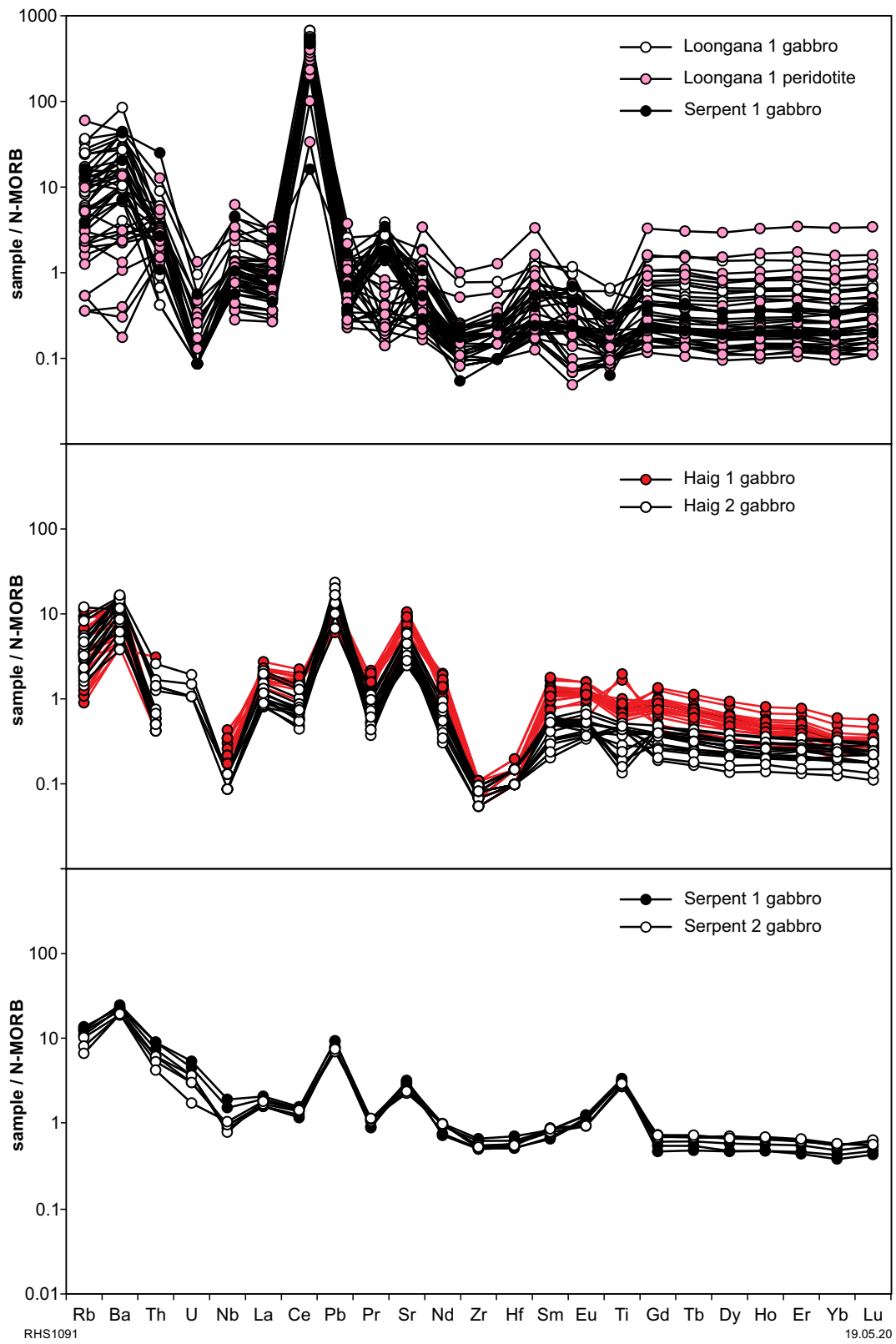


Figure 62. PM-normalized trace element spider diagrams for mafic and intermediate intrusive rocks from the Madura Province (normalizations after Sun and McDonough, 1989)

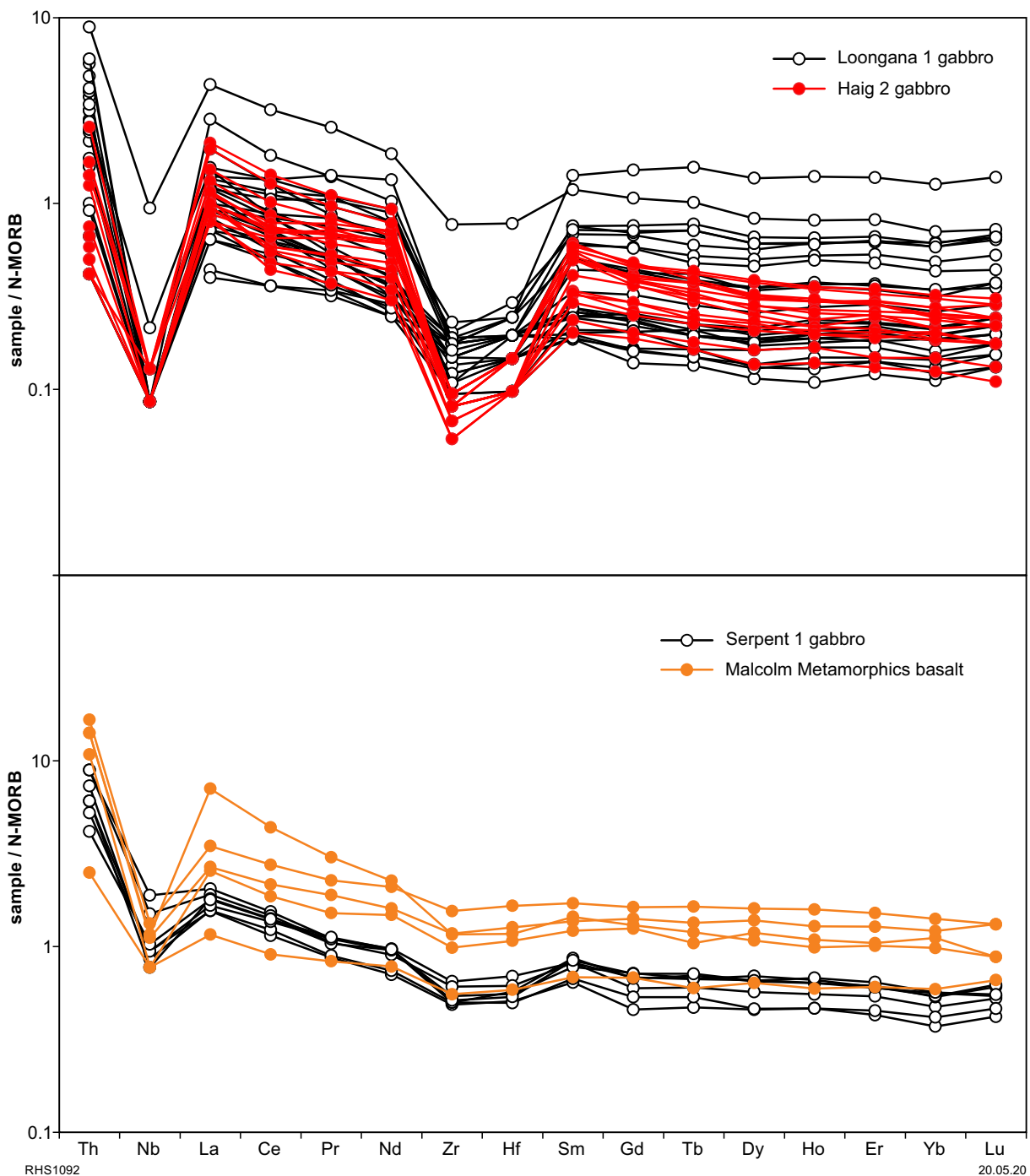


Figure 63. PM-normalized trace element spider diagrams for mafic and intermediate intrusive rocks from the Madura Province with trace elements that are typically significantly affected by cumulate processes (e.g. Sr in plagioclase) removed (normalizations after Sun and McDonough, 1989)

Loongana and Serpent intrusions, they also show extreme enrichments in LILE, HFSE, REE (cf. Figs 62, 65), Ga and Zn, particularly given the low SiO₂ range of the Kestrel Cavern Gabbro (typically <55 wt%), consistent with strongly fractionated tholeiitic or A-type magmatic evolution. Many of the samples from the Hannah 1 drillcore plot in the compositional field of monzonite and samples of the Kestrel Cavern Gabbro are monzogabbro.

In contrast with the scattered compositional trends of the Haig and Loongana intrusions dominated by various cumulate mineral assemblages, major and trace element variations against SiO₂ from the Kestrel

Cavern Gabbro and Hannah intrusions have more linear trends (Figs 61, 66). This suggests that not only do the Kestrel Cavern Gabbro and Hannah monzonite reflect a compositionally distinct style of magmatism, but their mode of emplacement might also be significantly different. Additionally, although the well-constrained major element 'Kestrel Cavern Gabbro – Hannah trend' reflects melting and/or crystallization controlled by quite a specific mineralogy or process, contrasting trace element and trace element ratio trends (e.g. La, La/Yb; Fig. 66) indicate a unique source composition for each of these two intrusions.

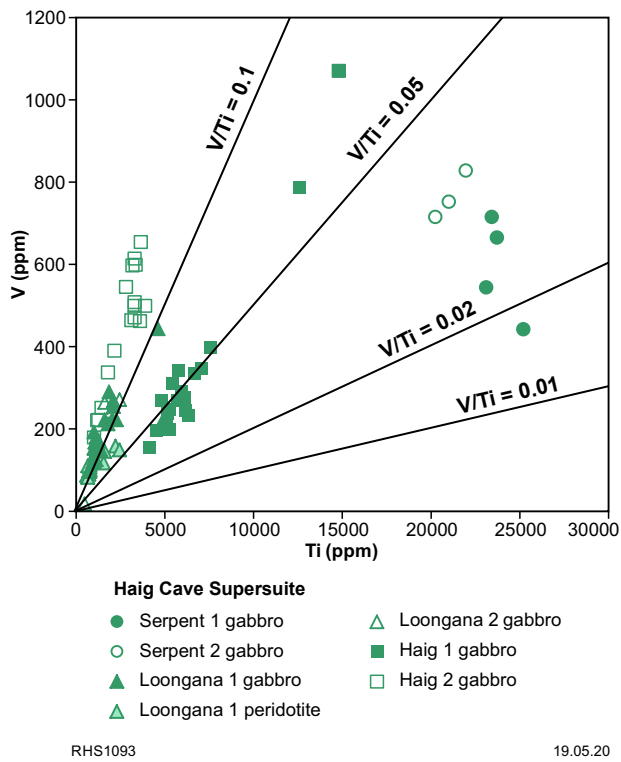


Figure 64. Comparison of V/Ti ratios for Haig Cave Supersuite mafic and ultramafic intrusions (after Spaggiari et al., 2018)

The high Fe contents (up to 13.52 wt% Fe₂O₃ for Kestrel Cavern Gabbro) and low MgO (<2.8 wt% for Kestrel Cavern Gabbro) make Mg# (or Fe* = wt%FeO/[wt%FeO+wt%MgO] with total Fe as FeO) a poor index of compositional evolution. Major elements and many trace elements show systematic variations with SiO₂ (albeit at constant Mg#), and in the case of Kestrel Cavern Gabbro, the concentration of strongly incompatible elements such as K (K₂O; Fig. 61), Rb, La and Th, and ratios such as La/Sm and Rb/Sr, all increase with increasing SiO₂ (Fig. 66), reflecting fractional crystallization. In addition, concentrations of Th and Rb double over a relatively narrow SiO₂ interval (51.8 – 55.9 wt%), suggesting magma volume at least halved, through some form of crystal–liquid separation. Duchesne and Charlier (2005) describe the formation of gabbronoritic cumulate sequences with relatively constant Mg# (Mg# of 40–45 over a SiO₂ range of 20 wt%) and attributed this to a balance between accumulation of Fe–Ti oxides and pyroxene. A similar petrogenetic model may apply to the Kestrel Cavern Gabbro and is consistent with compositional changes with depth within the Kestrel Cavern Gabbro intrusion. The Kestrel Cavern Gabbro (monzogabbro) becomes systematically less evolved (i.e. SiO₂, K₂O, REE, Th, Nb and Zr decrease, and FeO, MgO, TiO and CaO increase) with depth, but subtle cyclic changes in La/Sm ratios superimposed on the continuous changes in SiO₂ allow the sampled portion of the intrusion to be divided into several cryptic zones (Fig. 67). These compositional relationships suggest periodic

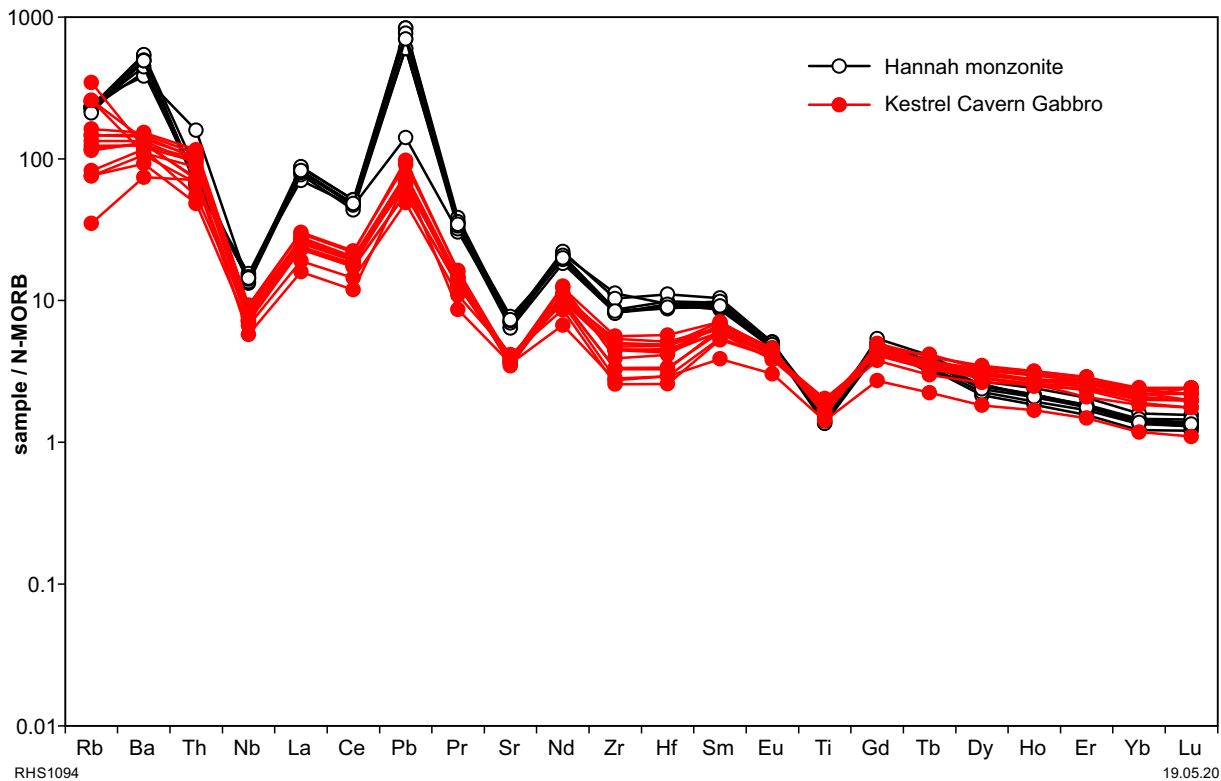


Figure 65. PM-normalized trace element spider diagrams for the Kestrel Cavern Gabbro and Hannah monzonite (normalizations after Sun and McDonough, 1989)

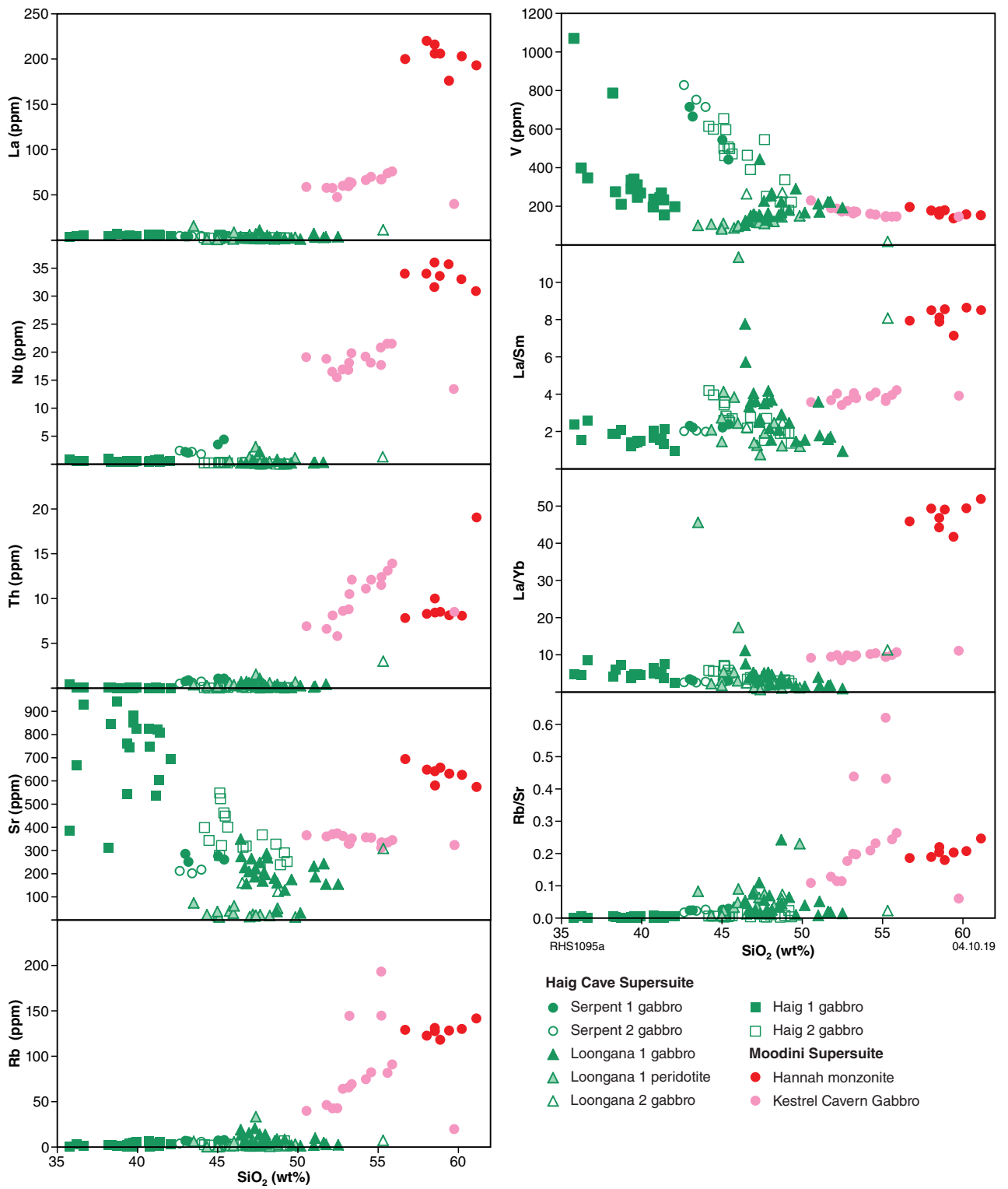


Figure 66. Variation in selected trace elements and ratios against SiO_2 for mafic and intermediate intrusive rocks from the Madura Province

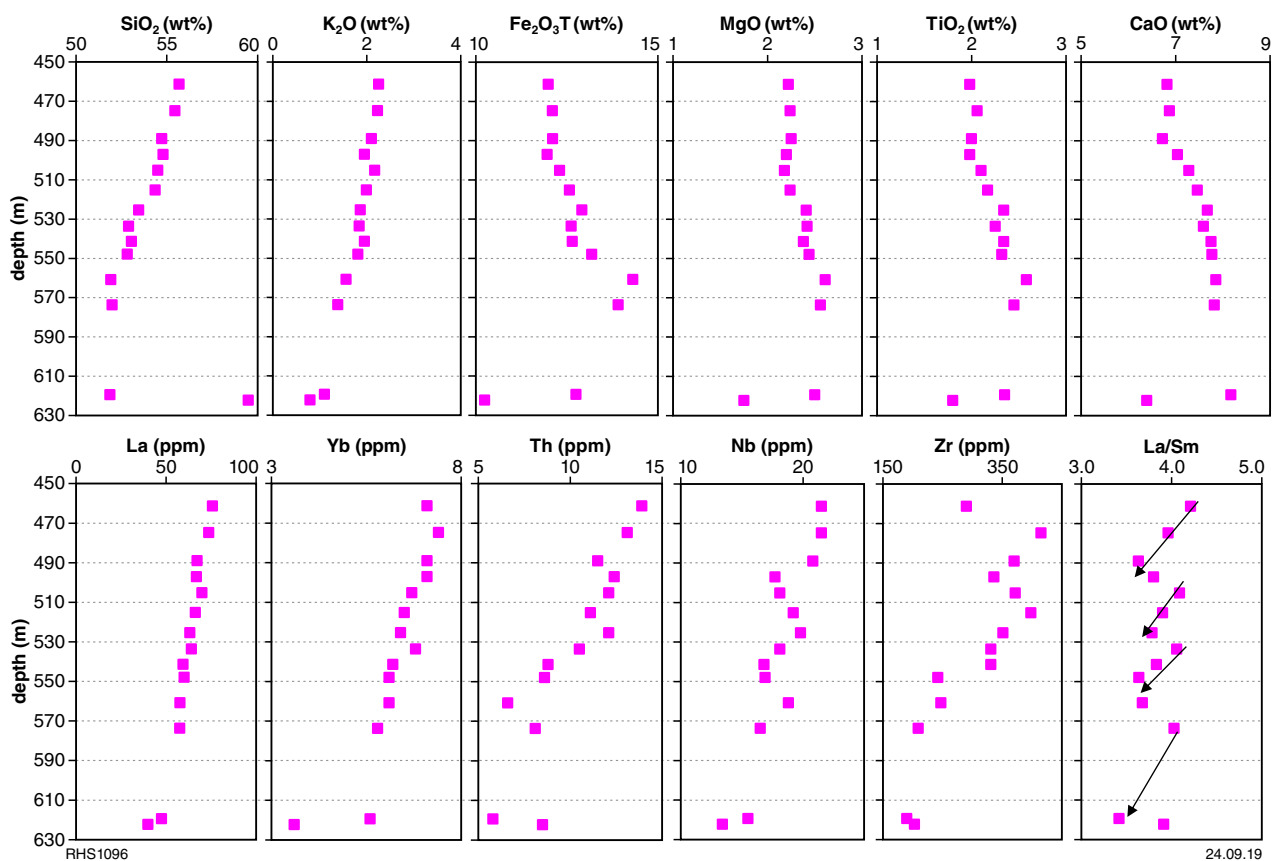


Figure 67. Plots of selected elements and La/Sm ratios with depth of the sampled portion of the Kestrel Cavern Gabbro in the drillcore MAD011. Systematic compositional variations are seen with depth for many elements and reflect a system becoming increasingly evolved upwards, although there is an indication of secondary rhythmic variations in some elements (e.g. Nb) and variations in La/Sm confirm these secondary variations

small-volume recharge and homogenization of the Kestrel Cavern Gabbro from a larger underlying chamber, or from an evolving source region.

The Hannah monzonite shows similar major element and compatible trace element (Ni, V, Sr) trends to the Kestrel Cavern Gabbro, albeit at differing concentrations (Fig. 66). However, concentrations of REE and HFSE decrease over the limited SiO_2 interval (56.7 – 61.2 wt%), whereas concentrations of the most incompatible trace elements (e.g. Th, Rb) increase only marginally (Rb 120 to 140 ppm) as do such indices of compositional evolution as La/Sm (7.9 to 8.5) and Rb/Sr (0.19 to 0.25). Although more SiO_2 -rich and alkaline than the Kestrel Cavern Gabbro, the Hannah monzonite is more primitive, with high-MgO trends and higher concentrations of Cr, Ni and Co. The magma from which the Hannah monzonite crystallized was also significantly enriched in LILE, LREE, Nb and Zr, and had much higher La/Yb ratios, than the magmas that crystallized the Kestrel Cavern Gabbro.

Nevertheless, the high Fe-, Ti- and P-character of the Kestrel Cavern Gabbro and Hannah monzonite (Figs 61, 66) is in strong contrast with other gabbroic rocks of the Madura Province. The primary mineralogy of the Kestrel Cavern Gabbro included orthopyroxene and possibly also pigeonite. These compositions and mineralogy are characteristic of high-temperature, Fe-rich orthopyroxene–monzonite (jotunite) suites

described mainly from Mesoproterozoic terranes of Norway, Ukraine and Quebec (Duchesne and Wilmart, 1997). Although the Kestrel Cavern Gabbro and Hannah monzonite are similar in age to many of the published accounts of jotunites, they appear to differ significantly in that they lack the clear association with massif-style anorthosite bodies (discussed below).

Relationship between Narilya Bore Basalt and Kestrel Cavern Gabbro in drillcore MAD011

Low-Ti basaltic rocks of the Narilya Bore Basalt occur as inclusions within the monzogabbroic rocks that form part of Kestrel Cavern Gabbro – Hannah trend. Although some of the basaltic inclusions contain a foliation not observed in the gabbro, and display evidence of granulite or mafic hornfels metamorphism (Appendices 2, 5), it remains possible that this foliation and recrystallization developed within a short period separating extrusion of the basalts from intrusion of more evolved magmas from a broadly comagmatic parental magma. However, the extreme enrichments in TiO_2 , FeO and P_2O_5 seen in the monzogabbro at similar concentrations of SiO_2 and at only slightly higher MgO (Fig. 68) almost certainly rule out a direct genetic relationship between these two groups. In addition, when calculated at 1140 Ma, the Narilya Bore Basalt has significantly more radiogenic Nd isotope compositions ($\epsilon_{\text{Nd}} -1.10$ to -0.17) than the Kestrel Cavern Gabbro ($\epsilon_{\text{Nd}} -2.95$; Table 6).

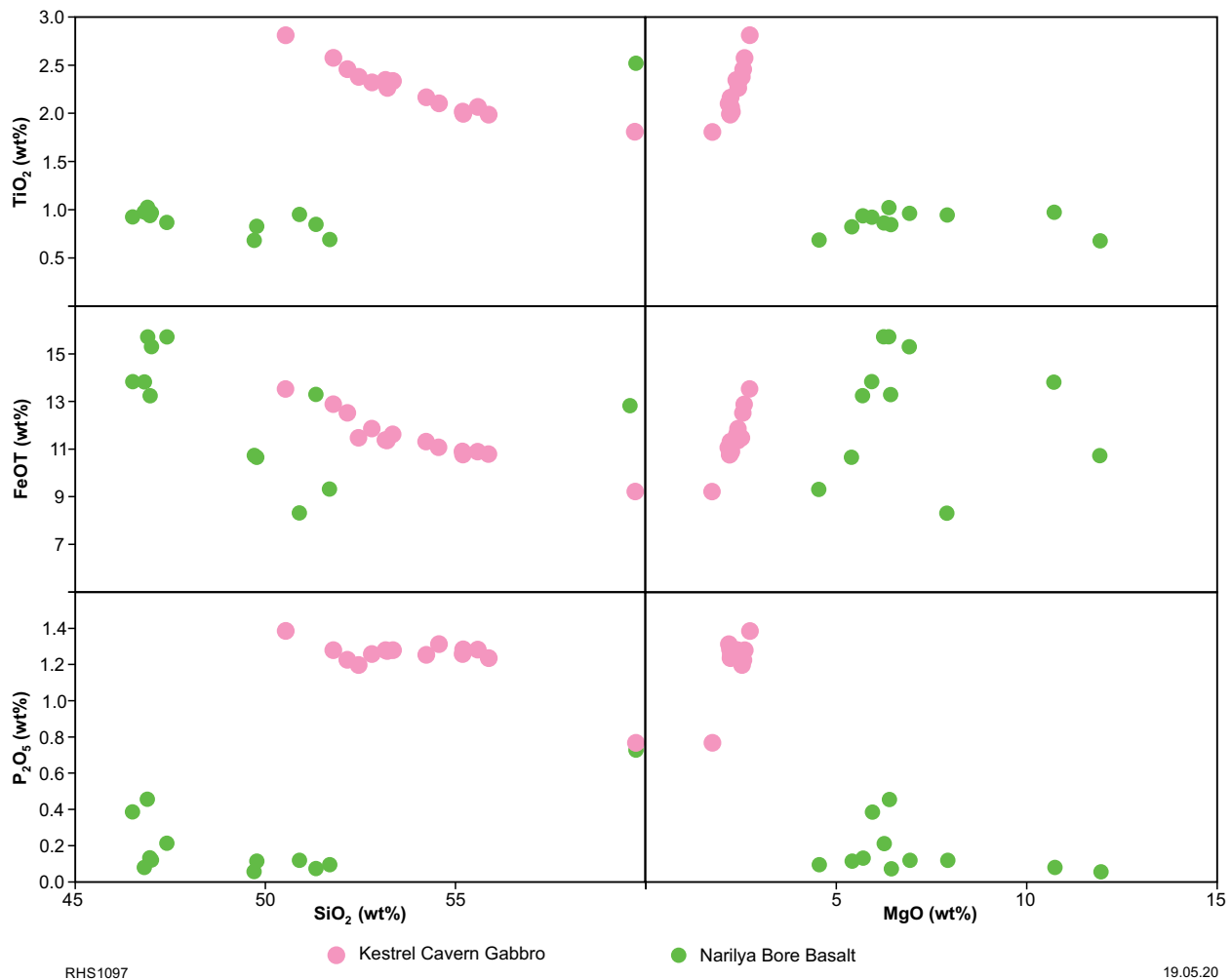


Figure 68. Variation in TiO_2 , total Fe (FeO^{T}) and P_2O_5 with both SiO_2 and MgO for the Kestrel Cavern Gabbro and Narilya Bore Basalt

Shoshonites in LNGD001 from the Loongana prospect

Two samples from the LNGD001 drillcore (at 385.4 and 382.1 m depth) containing acicular crystals are fine- to medium-grained dykes that intrude both the metagabbro and metagranite of the Haig Cave Supersuite. These dykes were initially interpreted as lamprophyre (Bunting and McIntyre, 2003). They have a basic to intermediate chemistry (SiO_2 52.04 and 59.95 wt%), with 9.7 – 11.0 wt% MgO and Mg\# of 72. They are also strongly enriched in K_2O (3.82 and 4.69 wt%), Na_2O (2.16 and 2.39 wt%), and LILE (e.g. Ba >1700 ppm). These dykes have the composition of shoshonites (possibly shoshonitic lamprophyres). In many respects, their geochemistry is similar to the rocks forming the Kestrel Cavern Gabbro – Hannah trend described above (Fig. 69), which also represent strongly enriched, K-rich basic to intermediate magmas. The shoshonites are, however, distinctive in their high Mg\# (cf. the ferroan nature of the Kestrel Cavern Gabbro – Hannah trend).

Sodic leucogranites

Metagranites in the compositional range of tonalite to trondhjemite intrude metagabbro at the Loongana prospect

(drillcores LNGD001 and LNGD002) and at the Haig prospect (drillcores HDDH001 and HDDH002), and also intrude the Pinto Basalt (drillcore MAD002). These metagranites form only a minor component of the Haig drillcores, occurring as veins on a centimetre scale and up to 1 m scale, locally incorporating the gabbroic wallrock. In the Loongana drillcores, sodic granite intrusions vary from centimetre-sized veins to layers that dominate large sections of the drillcores and in LNGD002 are the primary lithology. In drillcore MAD002, sodic granite forms centimetre- to metre-scale veins, dominating some portions of the middle to lower parts of the drillcore (Appendix 2). These granites are part of the 1415–1389 Ma Haig Cave Supersuite.

The metagranites are typically very SiO_2 -rich, with those from the Loongana prospect showing the widest range (Fig. 70). One sample from drillcore LNGD002 has SiO_2 <65 wt%, but the remainder show a restricted range at >73 wt%. Samples from LNGD001 (Loongana 1) show a continuous range between 67 and 78 wt% SiO_2 . Apart from a single sample from HDDH002 (Haig 2), all remaining metagranites have SiO_2 contents >72.5 wt%. In terms of other major elements, samples from Loongana (1 and 2) are distinctive in that they range to higher K_2O contents (up to 1.7 wt%) at higher SiO_2 contents and have the highest $\text{K}_2\text{O}/\text{Na}_2\text{O}$ ratios of up to 0.41 (although still very sodic).

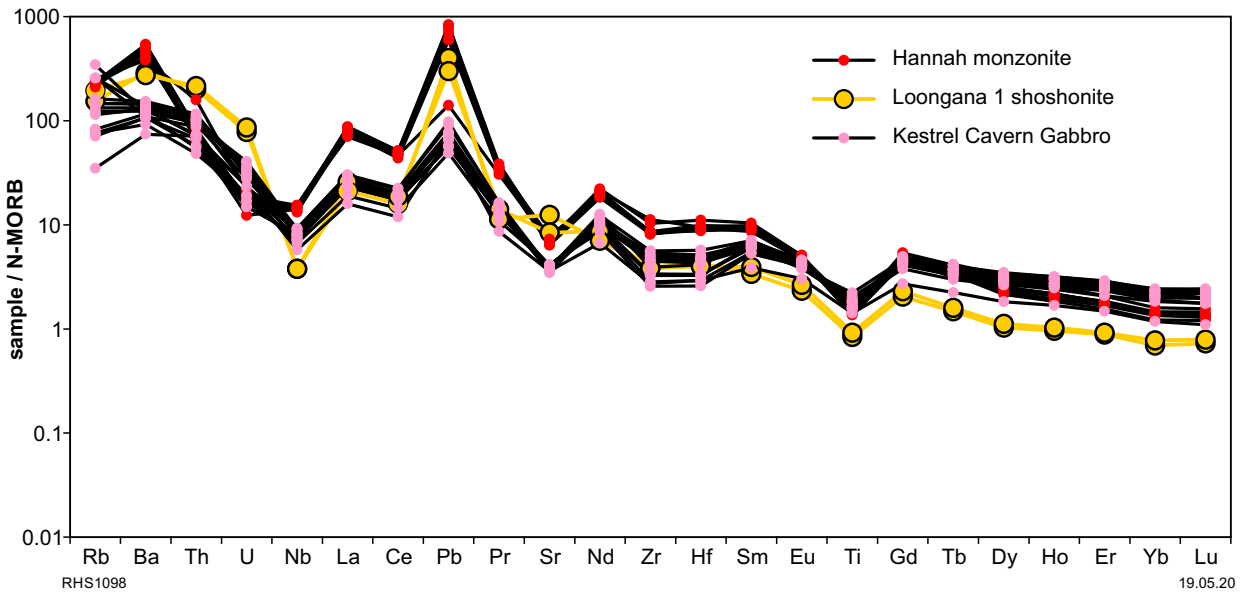


Figure 69. N-MORB normalized trace element spider diagram for the Hannah monzonite, shoshonite from Loongana prospect drillcore LNGD001, and the Kestrel Cavern Gabbro (normalizations after Sun and McDonough, 1989)

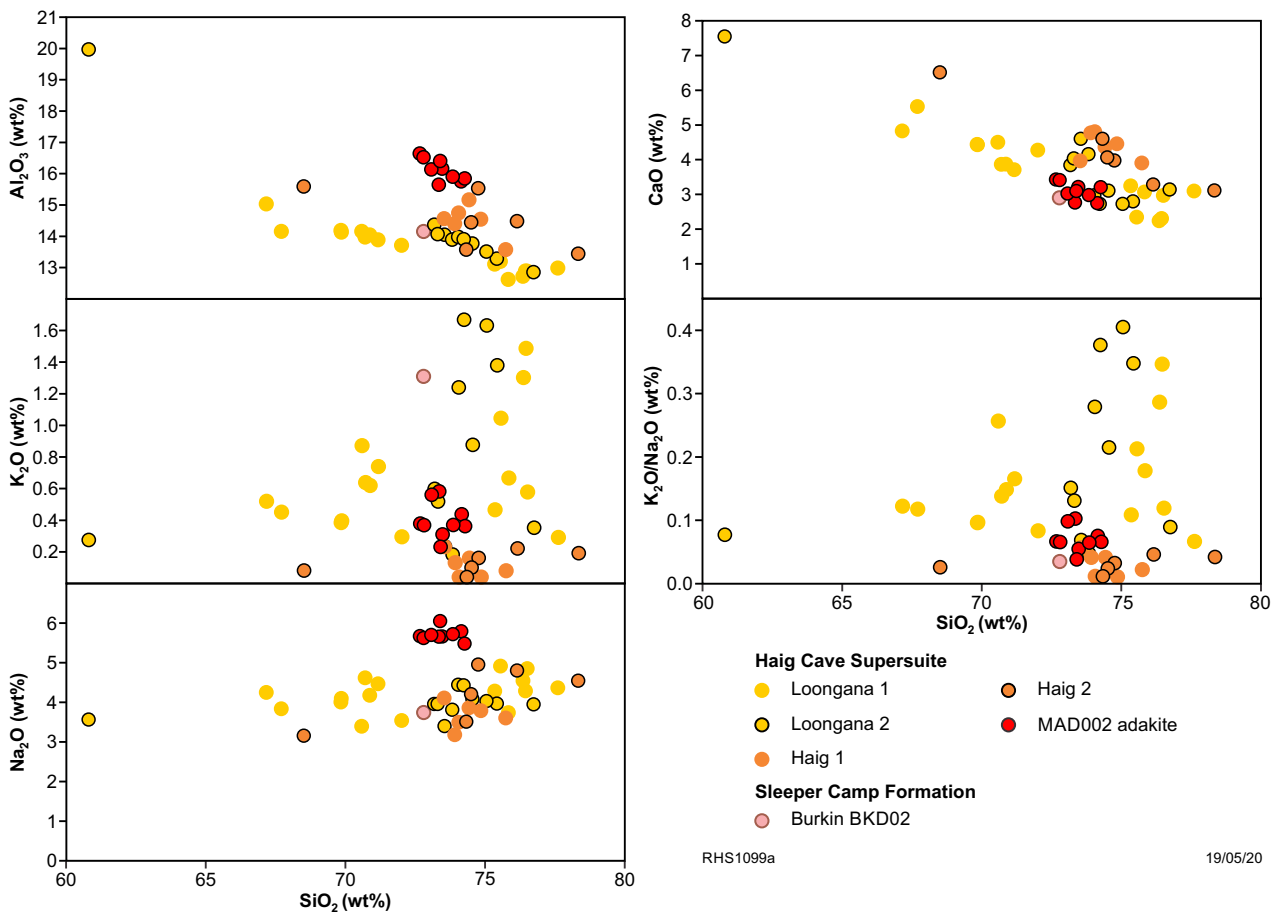


Figure 70. Variation in selected major elements and element ratios with SiO_2 for metagranitic rocks of the Haig Cave Supersuite and Sleeper Camp Formation

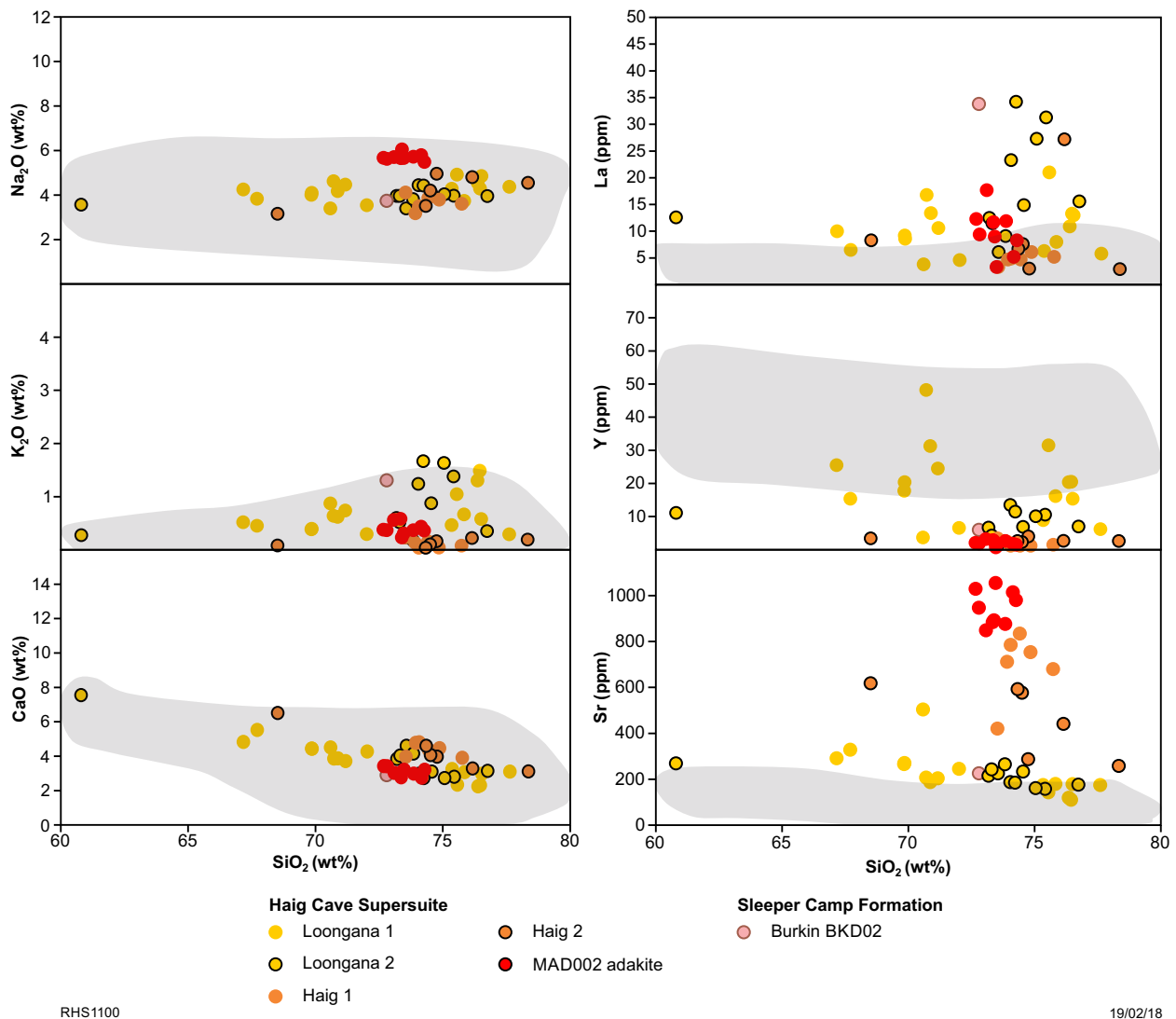


Figure 71. Variation in selected major and trace elements with SiO_2 for metagranitic rocks of the Haig Cave Supersuite and Sleeper Camp Formation. Grey field reflects the compositional range of oceanic plagiogranites compiled from data obtained from the Geochemistry of Rocks of the Oceans and Continents (GEOROC) online database (<http://georoc.mpch-mainz.gwdg.de/georoc/>)

The samples from drillcore MAD002 show distinctly Al-rich trends and are significantly enriched in Na_2O (5.48 – 6.05 wt%), with maximum $\text{K}_2\text{O}/\text{Na}_2\text{O}$ ratios of 0.1.

As is typical of highly evolved sodic granites, those of the Madura Province are mostly depleted in LREE, HFSE and Rb and have variable concentrations of Ba. They share these features with sodic felsic magmatic rocks from a range of oceanic tectonic settings, including ‘oceanic plagiogranites’ from ophiolite complexes (Fig. 71). Metagranites from the Loongana prospect, in particular, show major element trends resembling oceanic plagiogranites, including a more extended SiO_2 range.

In terms of variations in concentrations of Sr, Y and HREE, the metagranites show a range of patterns (Fig. 72). Metagranite in drillcore MAD002 and from the Haig prospect contain anomalous concentrations of Sr (MAD002 = 849–1055 ppm; Haig 1 = 420–835 ppm; Haig 2 = 258–618 ppm) compared with the other Madura Province metagranites and with sodic granites from oceanic settings (Fig. 71). Conversely, concentrations of

HREE and Y are anomalously low in metagranites from MAD002 (Yb 0.08 – 0.29 ppm), Haig 1 (Yb 0.2 – 0.4 ppm) and Haig 2 (Yb 0.17 – 0.6 ppm) compared with concentrations within Loongana 1 (Yb 0.28 – 5.41 ppm) and Loongana 2 (Yb 0.28 – 1.5 ppm), which are more representative of the range for oceanic sodic granites. In the case of the metagranite from MAD002, the more restricted SiO_2 range, lower TiO_2 and FeO and higher Al_2O_3 contents are also in contrast with oceanic plagiogranites.

Leucocratic metagranite veins also form part of the Sleeper Camp Formation and were sampled from drillcore BKD02. These also have low $\text{K}_2\text{O}/\text{Na}_2\text{O}$ ratios (<0.4), similar to the sodic granites of the Haig Cave Supersuite, and in particular from MAD002, with which they also share textural similarities and show Sr, Yb, and Y concentrations transitional between the two groups described above. It is therefore feasible that these metagranite veins in the Sleeper Camp Formation are also oceanic plagiogranites, although about 60–70 million years older.

In Figure 73, the composition of the various metagranites is compared to the composition of the mafic crust into which they intrude. It is clear that the high Sr and low Yb characteristics of the Haig metagranites are shared by the Haig metagabbro and similarly, the Loongana metagranites and metagabbros share low Sr and high Y characteristics. The high Sr, low Y characteristics of the MAD002 metagranite, however, are opposite to those of the E-MORB-like Pinto Basalt into which it intrudes.

Plagiogranites are thought to either represent low-fraction partial melts of mafic crust or the products of extended fractional crystallization of mafic magmas. In either case, it might be expected that distinctive compositional features of the mafic parental rocks or magmas can be inherited in the felsic liquids. This certainly would explain the similarities in trace element patterns between metagranites and metagabbro at Loongana and Haig, particularly given the low (depleted) Th and LREE concentrations in the gabbros (cumulates) and extreme Sr concentration seen in the Haig gabbros — all of which are mirrored in the associated metagranites. Because these metagabbros are cumulate-rich rocks, the associated metagranites are more likely to be related to them via a low-fraction partial melt than via fractional crystallization of residual liquids. Certainly, in the case of the Haig intrusions, this is consistent with the very low volumes of extremely silicic leucogranite.

The patterns for the metagranite in MAD002 contrast strongly with those of the associated basalts, particularly in terms of the very high La/Yb ratios and strongly developed negative Nb and Ti anomalies observed in the latter (Fig. 73). The notably Al_2O_3 and Na_2O enriched compositions of these metagranites (Fig. 70) together with the very high Sr and very low Y and HREE concentrations (Fig. 72), that is, very high Sr/Y and La/Yb ratios, are characteristics of adakites and Archean tonalite–trondhjemite–granodiorite (TTG), resulting through high-pressure melting of mafic crust leaving a garnet-present but plagioclase-free residuum (e.g. Martin et al., 2005). The high Sr/Y ratios of Haig 1, however, can be better explained in terms of compositional inheritance from gabbroic melting sources that share certain compositional similarities — as outlined above. Indeed, relatively flat HREE patterns with low Dy/Yb ratios (Fig. 74) ranging to values lower than those of associated gabbros and other oceanic leucogranites, are consistent with low-pressure fractionation or source retention of hornblende, rather than equilibrium with peritectic garnet.

Potassic granites and associated mafic rocks of the Moodini Supersuite

Potassium-rich, ferroan (high-KFe) granites are the sole basement lithology encountered in the MAD014 drillcore and in the two drillcores from the Moodini prospect (Figs 3, 21). The granites at Moodini range from quartz diorite and granodiorite to biotite±hornblende monzogranite whereas those from MAD014 are mainly biotite±hornblende monzogranite (Figs 22a,b, 23). Granites from both localities are part of the Moodini Supersuite.

Samples from the Moodini prospect cover a much wider SiO_2 range (57.64 – 74.68 wt%) than those from MAD014 (69.77 – 76.08 wt%). With increasing SiO_2 contents, concentrations of all major element oxides

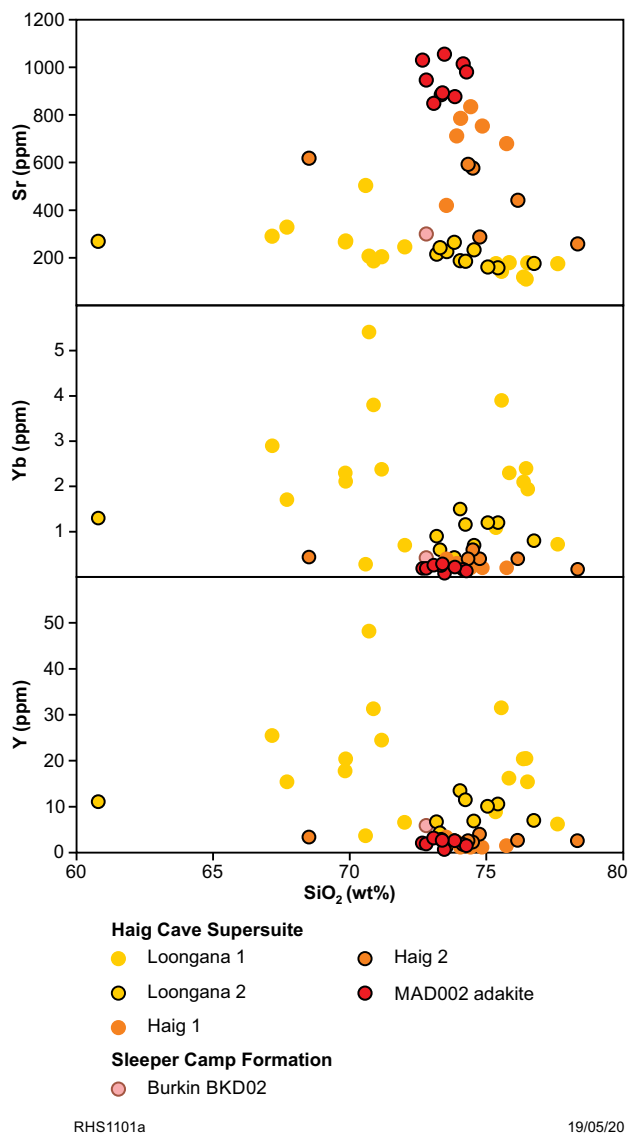


Figure 72. Variation in selected trace elements with SiO_2 for metagranitic rocks of the Haig Cave Supersuite and Sleeper Camp Formation

decrease, except for K_2O , which increases, and Na_2O , which increases in the MAD014 rocks and is constant in the Moodini prospect granites (Fig. 75). The minor rock types at each location (forming the five most SiO_2 -rich samples from MAD014 and the four most SiO_2 -poor samples from Moodini) form slightly different trends for many elements, at least in the case of MAD014, suggesting slightly distinct magma compositions consistent with the crosscutting relationships. In the case of the Moodini prospect, the distinctly less silicic minor group, forming layers of older mesocratic rock, more likely relate to preserved rafts and inclusions of older cumulate-rich assemblages. There are, however, some slight, but distinct, differences between the main rock types at each locality. In particular, the MAD014 granites are enriched in both K_2O and Na_2O and have distinctly lower CaO contents than the Moodini prospect granites. This results in the MAD014 granites being mainly alkali-calcic whereas the Moodini prospect granites are mainly calc-alkalic.

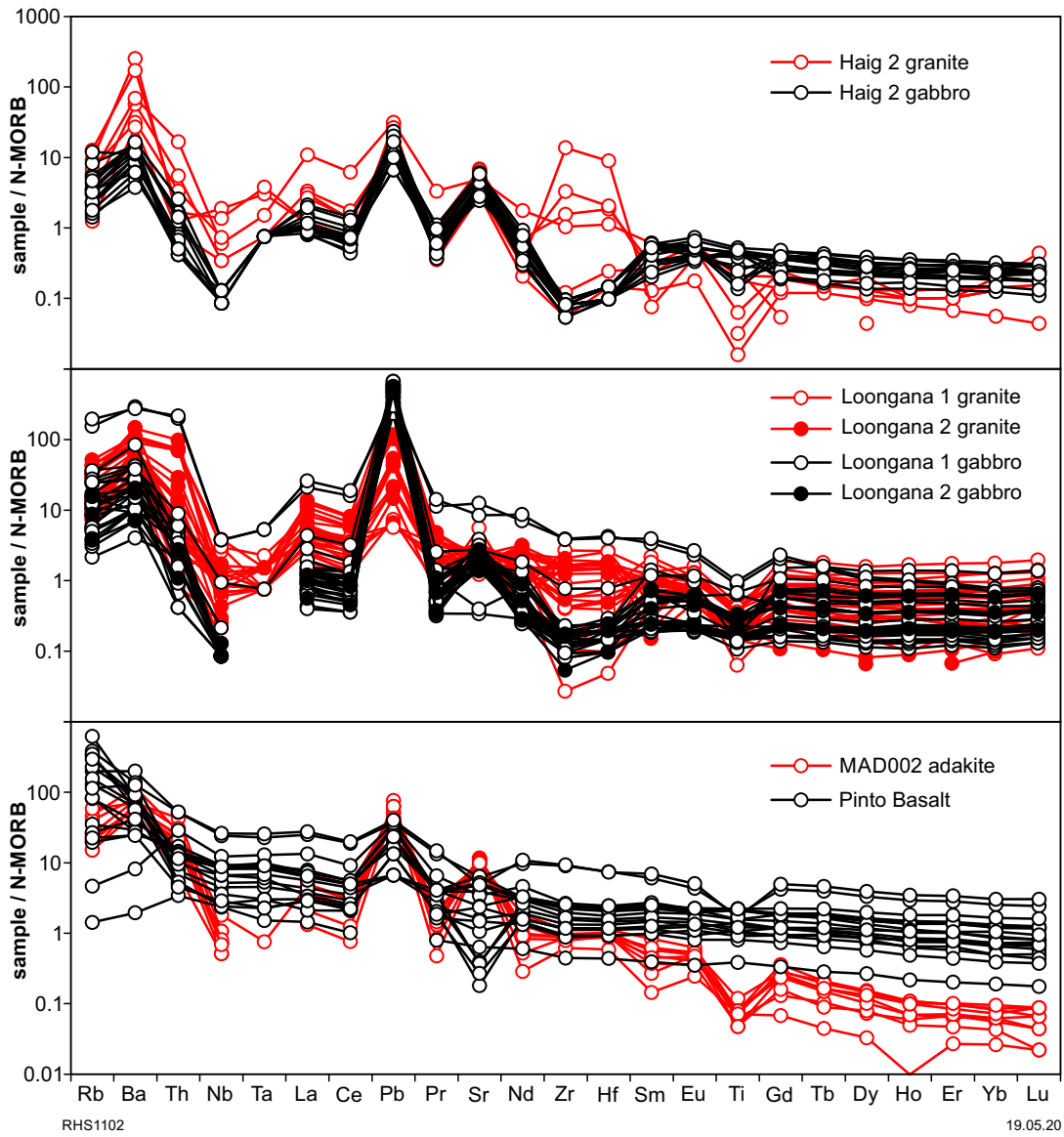


Figure 73. N-MORB normalized trace element spider diagrams for the Haig Cave Supersuite and Pinto Basalt (normalizations after Sun and McDonough, 1989)

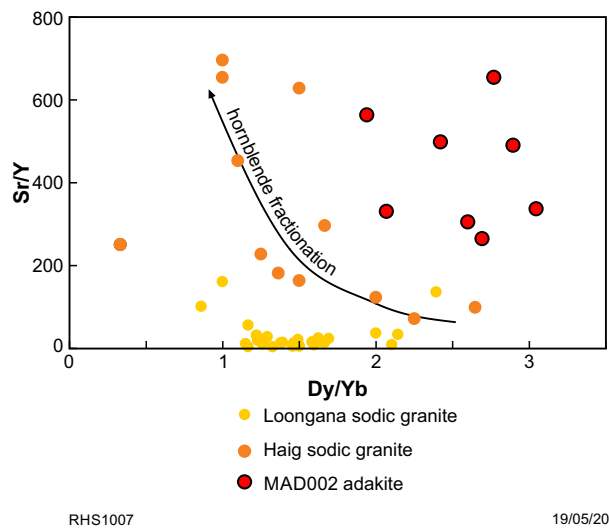


Figure 74. Variation in Sr/Y with Dy/Yb for metagranitic rocks of the Haig Cave Supersuite

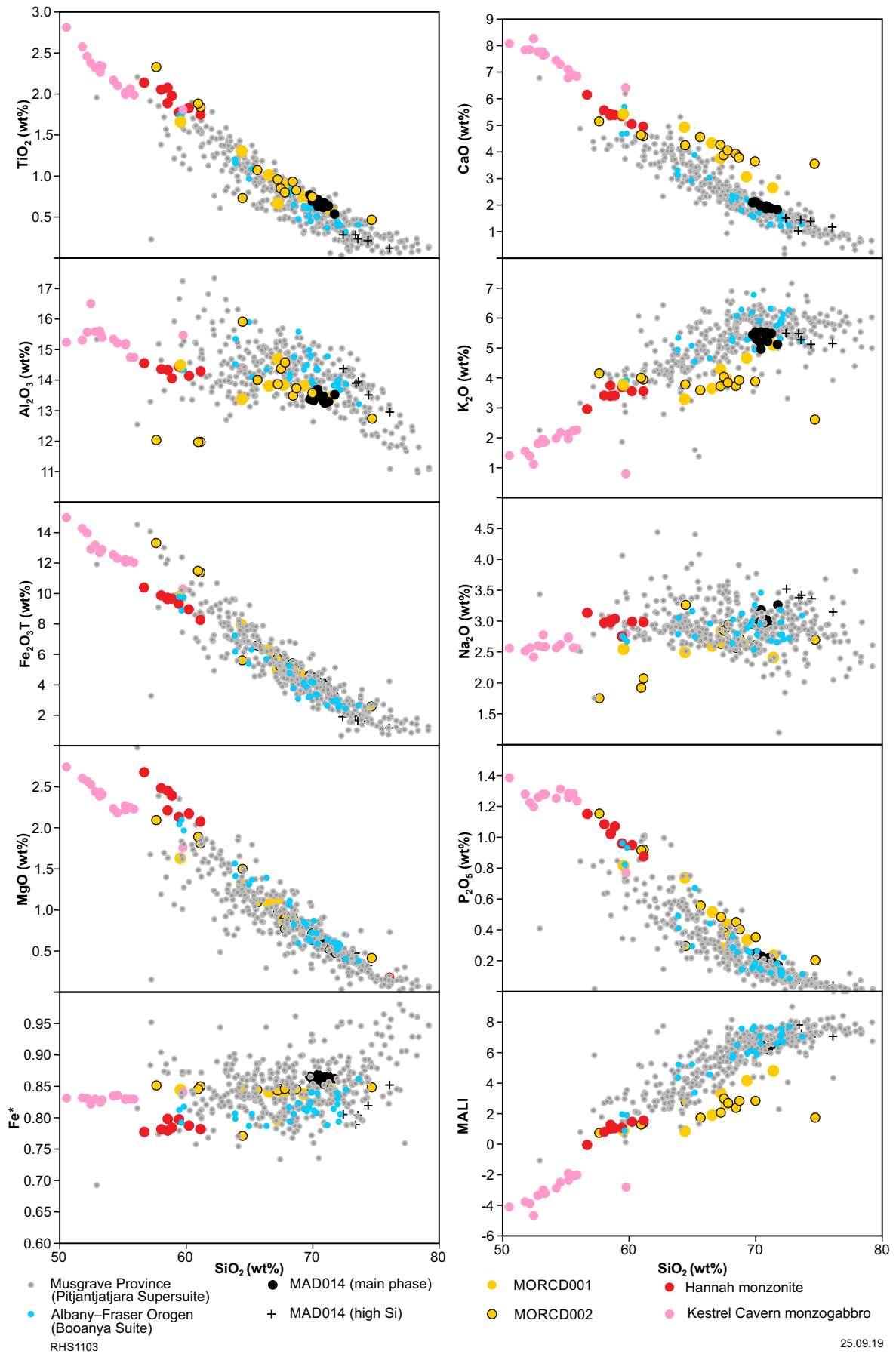


Figure 75. Compositional variation diagrams for Moodini Supersuite rocks of the Madura Province compared to intrusive rocks of similar age in the Musgrave Province (Pitjantjatjara Supersuite) and the Albany-Fraser Orogen (Booanya Suite). Additional data sources from Smithies et al. (2010, 2015). Abbreviation: MALI, modified alkali-lime index

The MAD014 granites also form a slightly lower P_2O_5 trend, are enriched in Pb, Rb, Ga, REE (particularly LREE), HFSE, Th and U and depleted in Sr and Ba (Fig. 76). In all cases, however, all granites from the Moodini prospect and the MAD014 drillcore form part of a distinctly TiO_2 - and P_2O_5 -rich trend of mainly metaluminous, ferroan composition (the silicic rocks from MAD014 are weakly magnesian).

For the MAD014 granites, the concentration of Rb appears to decrease with increasing SiO_2 (and with decreasing MgO, not shown; Fig. 76) — opposite to trends expected through normal igneous magma compositional evolution. However, the main group (low SiO_2) of MAD014 samples shows very little variation in either SiO_2 or Rb (or MgO) and so the apparent trend is really defined by the high- SiO_2 rocks that intrude this main group, and which, based on other trends (e.g. Mg# vs SiO_2 , Mg# vs Th, SiO_2 vs Al_2O_3 , Rb vs Sr, LREE vs SiO_2 , Ce/Pb vs SiO_2 , K vs Rb, K_2O/Na_2O vs SiO_2 , not shown), are not directly related to the main group. The trends to lower Rb concentration with increasing SiO_2 in the high- SiO_2 samples (Fig. 76) is, nonetheless, intriguing and are also accompanied by slight decreases in K_2O contents. They potentially reflect biotite-destructive silicification, although no petrographic evidence exists for this. Alternatively, the trend may reflect partial melting controlled by dehydration melting of Mg (and F)-rich biotite as suggested for similar high- SiO_2 , high-KFe granites from the Musgrave Province (e.g. Smithies et al., 2011).

When samples from the Moodini prospect are divided into Moodini 1 (samples from MORCD001) and Moodini 2 (samples from MORCD002), trends for Moodini 1 also become more apparent and rational in terms of normal igneous differentiation. For example, although the trend in Rb vs SiO_2 is flat for the combined group (i.e. little variation in Rb), when the data from the two drillcores are separated, a significant increase in Rb (98–171 ppm) in Moodini 1 over a SiO_2 interval from 64.24 to 71.38 wt% is revealed (Fig. 76). The SiO_2 range for Moodini 2 is greater (64.45 – 74.68 wt%), but the high- SiO_2 point has anomalous concentrations of several trace elements (Ba, Sr, Rb). The remaining Moodini 2 samples show a very flat trend (no variation in Rb), and it is possible that this is also a result of biotite-destructive silicification.

The mesocratic, lower SiO_2 component of the Moodini prospect drillcores typically lies at the low- SiO_2 extension of the trends defined by the main granites for all major and most trace elements. These trends are consistent with the suggestion that the lower SiO_2 rocks are simply older, cumulate-rich assemblages. The combined trends for typically incompatible trace elements such as Zr and REE (Fig. 76) suggests this magma series became saturated in accessory phases such as zircon and apatite at relatively low SiO_2 concentrations (<64 wt%), with trends to decreasing concentrations of Nb potentially reflecting saturation in ilmenite or rutile (or both).

As was also observed for monzogabbroic samples of the Kestrel Cavern Gabbro from MAD011 and monzonite from the Hannah prospect, Mg# and hence Fe^* for samples from the Moodini prospect (~25 and ~ 0.85,

respectively) and the main group of rocks from MAD014 (~22 and ~0.87, respectively) vary within a remarkably narrow range (Fig. 75). In the case of the Moodini prospect, this is not resolved by dividing the data into Moodini 1 and 2. Both Mg# and Fe^* are probably poor indicators of evolution within such strongly evolved, MgO-poor magmas, and such trends are common in ferroan magma series that crystallize abundant, late Fe oxides (e.g. Frost and Frost, 2008, 2011).

The rocks from MAD014 and the Moodini prospect show high, but scattered, concentrations of Ba, but relatively low and decreasing concentrations of Sr (<400 ppm for Moodini; <200 ppm MAD014; Fig. 76). For the REE, U, Th and HFSE analyses the main group from MAD014 tend to cluster with a faint trend to lower concentrations of all trace elements with increasing SiO_2 . The remaining MAD014 samples (five most SiO_2 rich) and all samples from Moodini show a moderately well-defined trend with increasing SiO_2 of low and decreasing LREE, high and decreasing HREE and HFSE, and low and increasing U and Th concentrations. Again, trends for Moodini 1 are better defined than those for Moodini 2. At high SiO_2 contents (>70 wt%), there are extreme enrichments in Th (i.e. >50 ppm, up to 92 ppm) at very high Th/U (>10).

The high-KFe rocks from MAD014 and the Moodini prospect all have clear A-type characteristics, including high Ga/Al ratios, high HFSE, Ga, Zn concentrations and ferroan compositions (Figs 75, 77). Within the general A-type classification, the distinctive high TiO_2 and P_2O_5 trends suggest these rocks are members of a 'charnockite-series' (Kilpatrick and Ellis, 1992), although none are mineralogically charnockites. The charnockite-series comprises magmas derived from dry and reduced lower crustal source regions incorporating a large mantle component (e.g. Smithies et al., 2011). Zirconium-saturation thermometry (Watson and Harrison, 1983) suggests the MAD014 and Moodini prospect high-KFe magmas became saturated in zircon at apparent temperatures above 900°C.

The high TiO_2 and P_2O_5 concentrations and strong enrichments in REE and HFSE in the high-KFe granites are distinctive (Fig. 77) and are clearly shared by the slightly older c. 1143 Ma Kestrel Cavern Gabbro from the MAD011 drillcore and also the c. 1180 Ma monzonite from the Hannah prospect (Fig. 75). Both are very high-temperature intrusions that contain primary orthopyroxene and possibly also pigeonite, and belong to the jotunite class of rocks. The implications of these potential relationships are presented in the Discussion section.

Whole-rock Sm–Nd data for the Haig Cave and Moodini Supersuites

The Nd isotope compositions of the Haig Cave Supersuite intrusions lie in the range $\epsilon_{Nd(1400\text{ Ma})}$ –3.91 to +3.07, with the felsic rocks nearly as radiogenic as those in the coeval metagabbros ($\epsilon_{Nd(1400\text{ Ma})}$ –0.08 to +3.07; Table 6). The adakite in the MAD002 drillcore yields the most evolved Nd signature of $\epsilon_{Nd(1400\text{ Ma})}$ –3.91 to –0.49. Two-stage model ages of the Haig Cave Supersuite intrusions range from 2.21 to 1.70 Ga, with an average model age of c. 1.89 Ga.

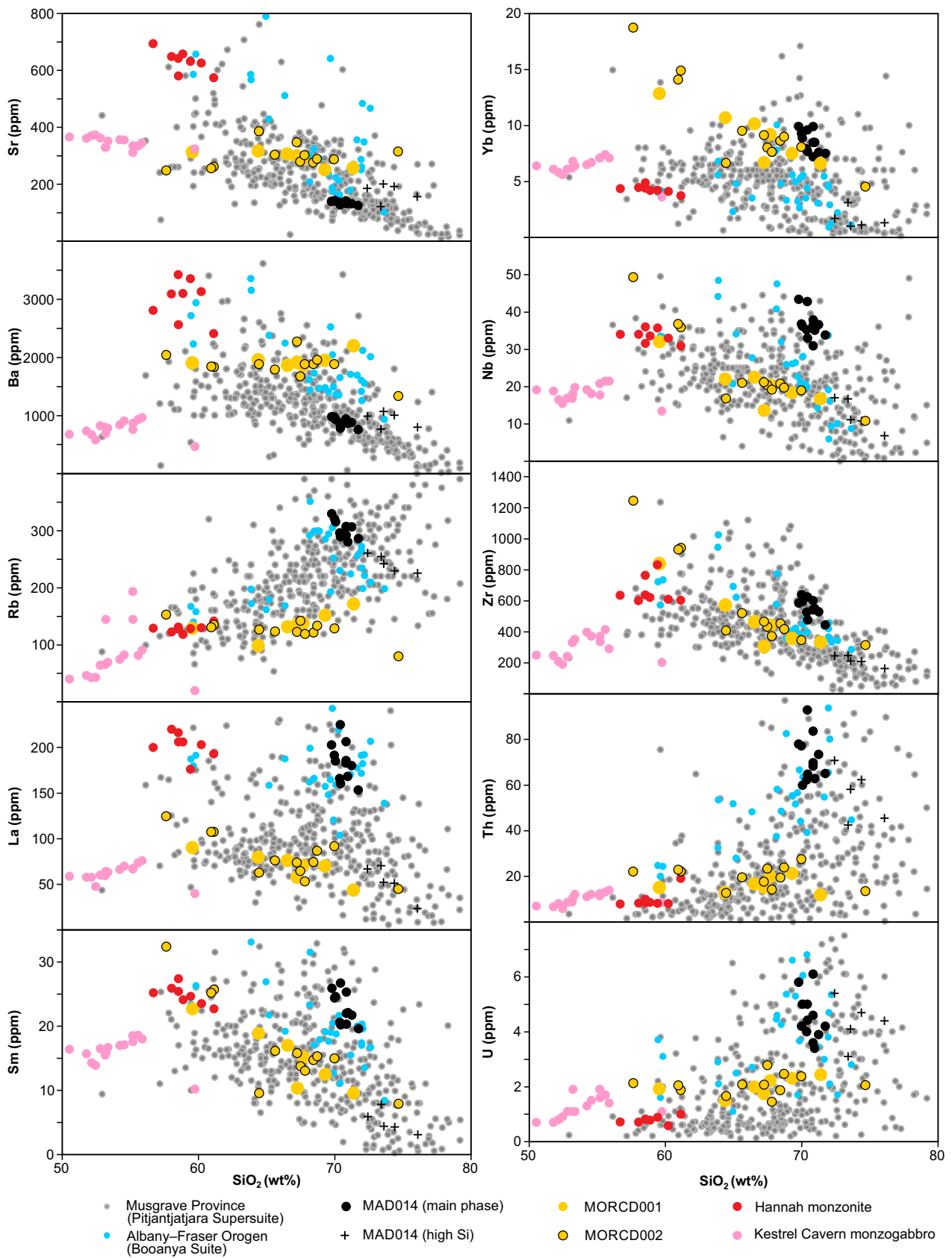


Figure 76. Trace element variation diagrams for Moodini Supersuite rocks of the Madura Province compared to intrusive rocks of similar age in the Musgrave Province (Pitjantjatjara Supersuite) and the Albany-Fraser Orogen (Booanya Suite). Additional data from (Smithies et al., 2010; 2015a). Abbreviation: MALI, modified alkali-lime index

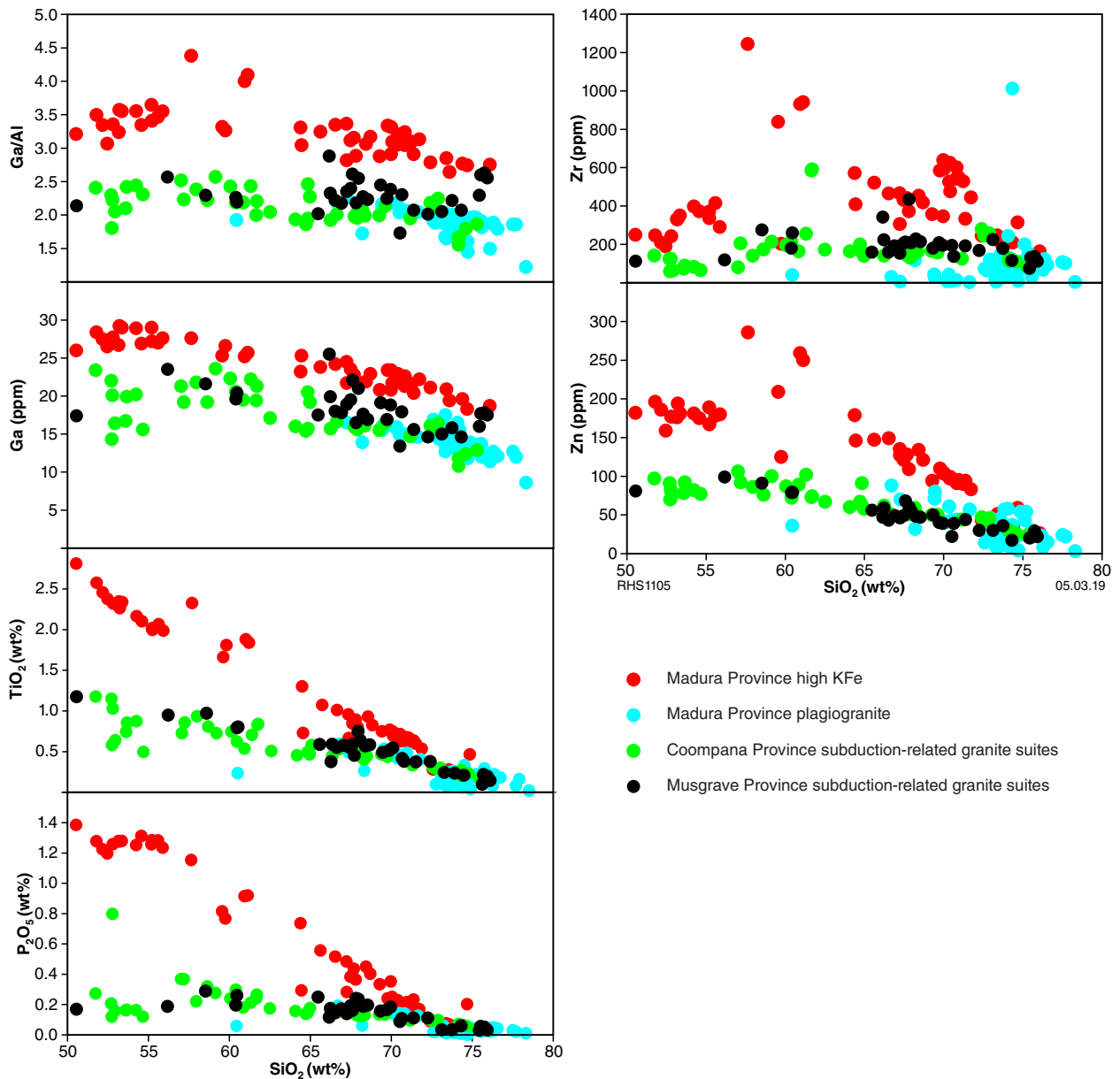


Figure 77. Variation in selected major and trace elements with SiO_2 , comparing metagranitic rocks of the Madura Province with rocks interpreted to be subduction-related from the Coompana and Musgrave Provinces. Additional data from Smithies et al. (2010, 2015a)

The whole-rock ϵ_{Nd} isotopic values from Moodini Supersuite magmatic rocks range from -5.02 to -2.47 , with a median two-stage model age of 2.0 Ga (Table 6). These intrusions tend to become more juvenile with decreasing age.

Samples from drillcores SDDH1 (Serpent prospect) and LNGD001 and LNGD002 (Loongana prospect) define a Nd errorchron of 1437 ± 160 Ma (mean square weighted deviation [MSWD] = 61) with an initial $^{143}\text{Nd}/^{144}\text{Nd}$ of 0.51091 ± 0.00019 (Fig. 78, Table 6). The individual samples yield an average $\epsilon_{\text{Nd}(i)}$ of 2.3 ± 0.6 , corresponding to T_{DM^2} of $1.8 - 1.7$ Ga. Although imprecise, the errorchron is only slightly older than the known age of these rocks from U–Pb zircon geochronology of $1415\text{--}1389$ Ma (see Geochronology section). Hence, the errorchron age is consistent with only a minor component of evolved material assimilation

into a melt dominated by a juvenile mantle source. Assuming that a precursor Nd reservoir was broadly of average crustal composition, then the age of at least one evolved contaminant can also be inferred, and must be older than 1.8 Ga given the maximum T_{DM^2} age. Assuming a more mafic precursor Nd reservoir would tend to increase the minimum age of this contaminant.

In contrast to the Nd isotopic systematics of the Haig Cave Supersuite gabbros, which support juvenile input at c. 1400 Ma and incorporation of at least one older component, the evolution pattern of granitic rocks of the Haig Cave and Moodini Supersuites of the Madura Province is generally further influenced by the older source. Nd isotopic values from granites scatter from evolved components with T_{DM^2} ages of up to c. 2.0 Ga to more radiogenic values, consistent with additional new mantle input during magmatism (Fig. 79).

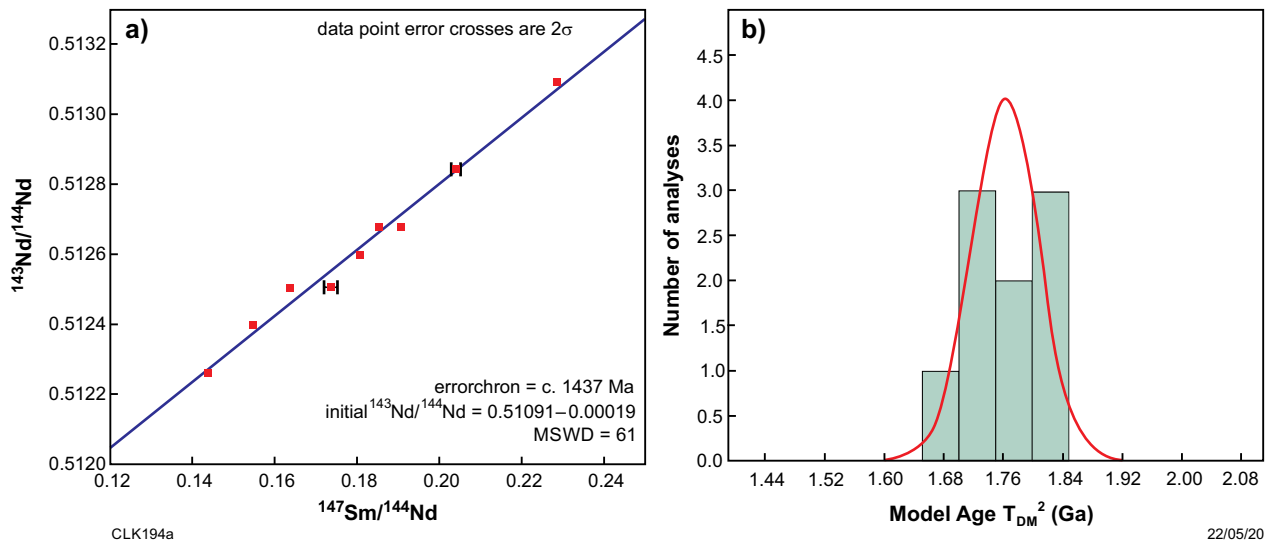


Figure 78. Sm–Nd data for gabbros of the Haig Cave Supersuite, Serpent and Loongana prospects: a) Sm–Nd isochron (errorchron); b) histogram of two-stage depleted mantle model ages (T_{DM}^2) with reference normal probability curve

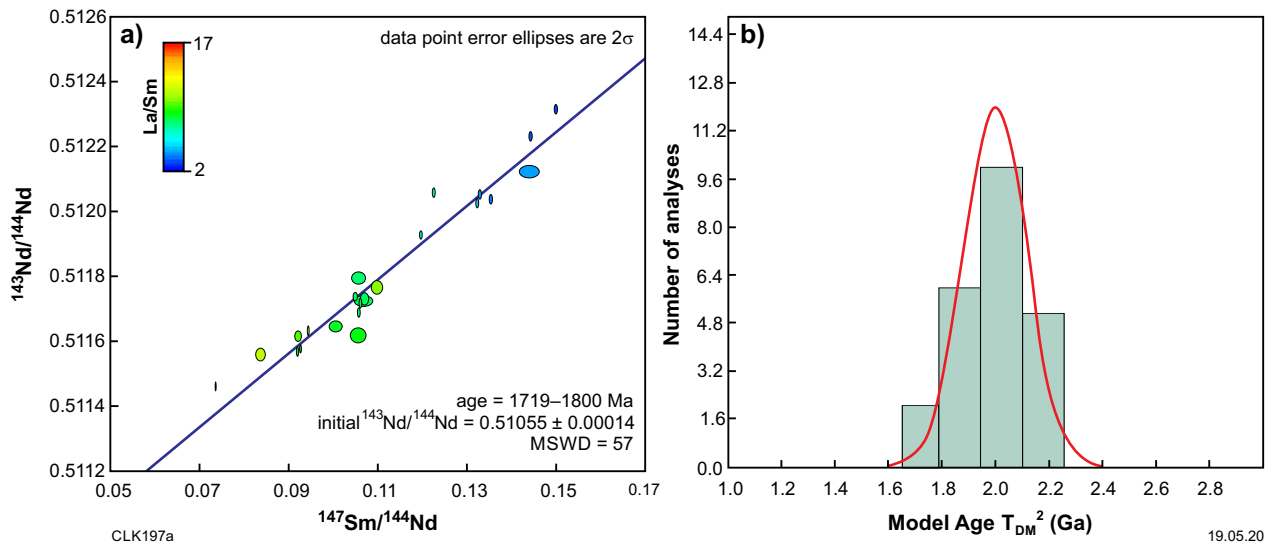


Figure 79. Sm–Nd data for granites of the Haig Cave and Moodini Supersuites, Madura Province: a) Sm–Nd isochron (errorchron), which yields a geologically meaningless age. The array within the data reflects a mixing line between granites with greater crustal contamination (with higher La/Sm ratios) and less contaminated granites (with lower La/Sm ratios); b) histogram of TDM2 with reference normal probability curve

Whole-rock geochemistry of Coompana Province rocks

No mineral exploration drillcores are available from the Coompana Province in Western Australia, and all of the whole-rock geochemical data presented here was sampled from the five GSWA stratigraphic drillcores (Figs 3, 24, 26, 29). As for the Madura Province, the samples represent the least altered and texturally and lithologically most homogeneous material available, covering the full lithological range encountered in each drillcore. Where sampling of altered material has been unavoidable, geochemical interpretation has been mainly based on variations in typically fluid-immobile elements. In all cases, major element data (e.g. SiO_2 wt%) has been recalculated volatile free (e.g. a SiO_2 wt%).

Rocks from the five FOR-prefix drillcores are presented mainly in terms of decreasing age, rather than by individual drillhole or in terms of geographical location. As presented above in the Geochronology section, three broad age groups and supersuites have been identified. One of these, the Moodini Supersuite, also occurs in the Madura Province (Figs 8, 10, 17).

Geochemistry of the Toolgana Supersuite

The 1613–1604 Ma Toolgana Supersuite was intersected in drillcores FOR004 and FOR008, and is also interpreted to be present as sparse layers of amphibolite in drillcore FOR011. The geochemistry of these rocks is described below, from felsic through to more mafic varieties.

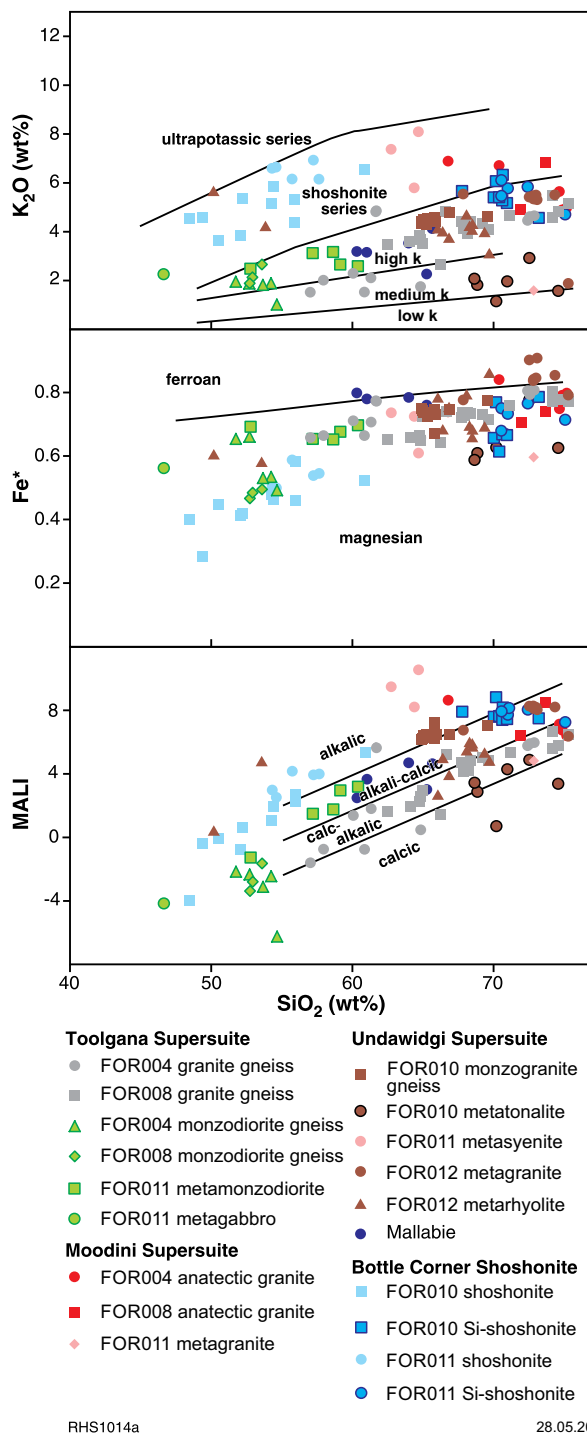


Figure 80. Variation in K_2O , Fe number (Fe^*) and modified alkali-lime index (MALI) with SiO_2 for felsic to intermediate rocks of the Coompana Province. Fe^* and MALI after Frost et al. (2001)

Granite gneisses

Both drillcores FOR004 and FOR008 are dominated by feldspar-porphyrific granite gneisses interleaved with fine- to medium-grained metamonzodiorite, metamorphosed to at least amphibolite facies between 1180 and 1150 Ma (see Lithological, petrographic and structural analysis of the stratigraphic drillcores). In drillcore FOR008, the gneisses are locally migmatitic. All sampled components of these drillcores show a narrow range of relatively juvenile Nd isotope compositions, with $\epsilon_{Nd(1600\text{ Ma})}$ ranging from +1.49 to -0.86 (Table 7), with the monzodiorite lying in the middle of this range.

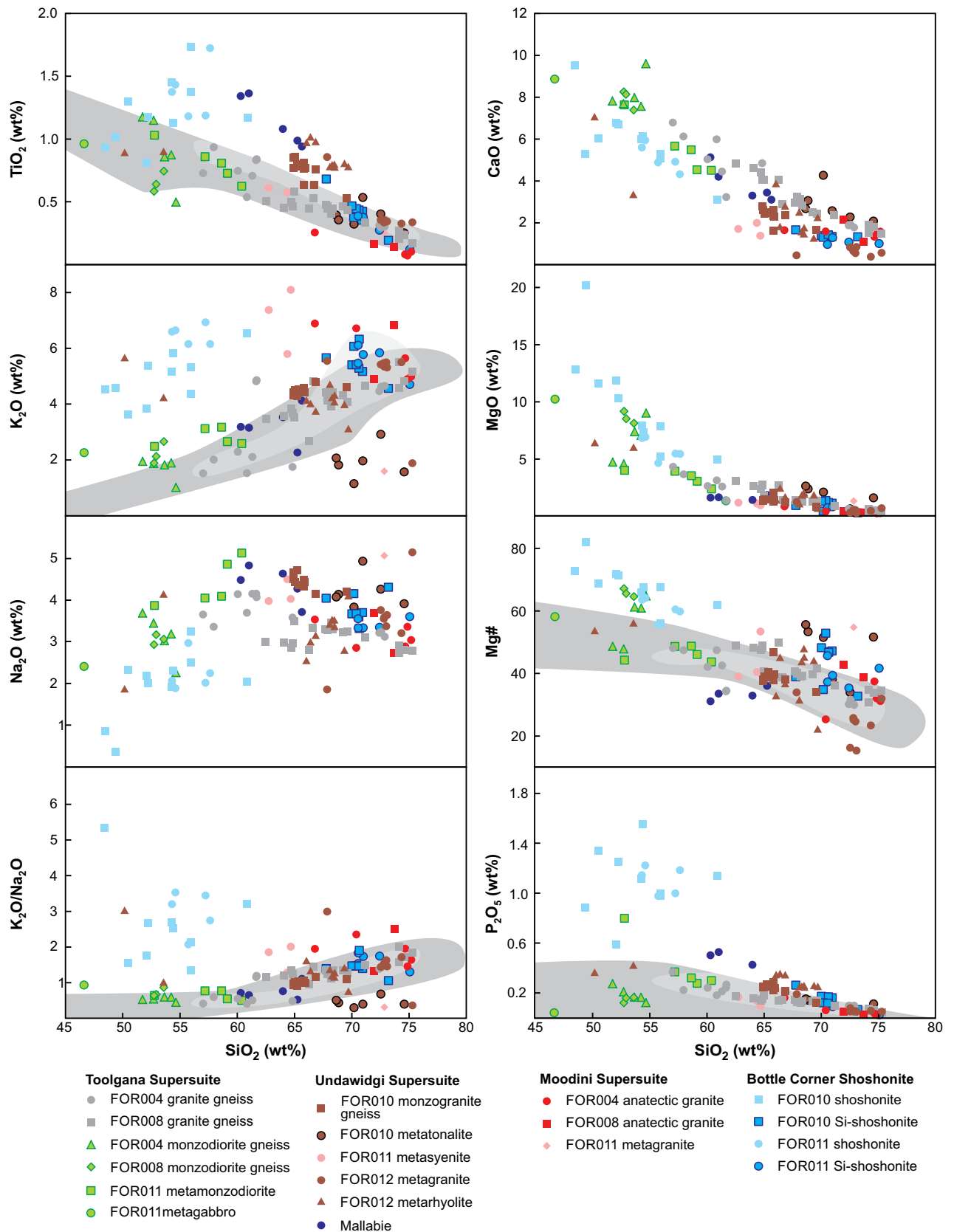
The granite gneisses are all magnesian and mainly calc-alkalic (terminology of Frost et al., 2001; Fig. 80). Those from FOR008 are mainly high-K, whereas those from FOR004 are mainly medium-K at lower SiO_2 contents (57–65 wt%), and high-K at higher SiO_2 contents. Two samples from FOR004 (with ~61.7 wt% SiO_2) are anomalous in that they plot in the shoshonitic field and are additionally rich in Ba and Zr, but otherwise are similar to the main group (Figs 80–82). It is possible that these anomalous samples contain cumulate K-feldspar and zircon. Granite gneisses from FOR008 show an extended SiO_2 range from 62.51 to 75.29 wt%. However, in some Harker plots two groups can be distinguished; a low- Na_2O , low- TiO_2 , high-MgO group with low SiO_2 contents (62.51 – 66.25 wt%) and a higher SiO_2 main group with only minimal SiO_2 overlap (64.98 – 75.29 wt%; Fig. 81). Samples from FOR004 show more compositional scatter than those from FOR008 and include a main group with lower SiO_2 (57.02 – 61.7 wt%; texturally transitional with the monzodiorite gneiss) and a smaller group with a high and narrow SiO_2 range (72.19 – 72.88 wt%; in addition to the two high Ba and Zr samples noted above). At least some of the scatter (particularly for LILE) is almost certainly the result of variable mixing between leucosomal and refractory portions of migmatite, allowing only broad generalizations about the compositional characteristics of these rocks.

Compared with the other FOR-prefixed granite groups, the Toolgana Supersuite granite gneisses from FOR008 and FOR004 typically have low TiO_2 , K_2O and Na_2O , low K_2O/Na_2O , and high CaO contents. Compositional variations typical of normal calc-alkaline granites are similar to other central and southern Australian Proterozoic suites thought to be subduction-related (e.g. c. 1300 Ma Wankanki Supersuite of the Musgrave Province; Smithies et al., 2010, 2011; Howard et al., 2015; Fig. 81). These compositional characteristics include high ratios of both LILE and LREE against HFSE, producing significant negative HFSE anomalies on mantle-normalized trace element plots (Fig. 83). Except for the high- SiO_2 granite gneisses from FOR004 (see below), the Toolgana Supersuite granite gneisses also show low Dy/Yb ratios that imply a significant role for hornblende fractionation during compositional evolution. A plot of Zr vs SiO_2 , in particular, contrasts these potentially subduction-related suites (low Zr) from more extreme Zr-enriched suites (Fig. 82) more likely derived through high-temperature melting of crust or subduction-enriched lithosphere (e.g. high-KFe suites and shoshonites; see below). However, the granite gneisses do show considerable scatter in LILE

Table 7. Whole-rock Sm–Nd data and sample information from the Coompana Province

GSWA sample ID	Series name	Stratigraphic unit	Lithology	Drillcore ID	T (Ma)	Sm (ppm)	Nd (ppm)	$^{147}\text{Sm}/^{144}\text{Nd}^*$	Standard-corrected $^{143}\text{Nd}/^{144}\text{Nd}^*$	$^{143}\text{Nd}/^{144}\text{Nd}_{(T)}$	CHUR _(T)	DM _(T)	$\epsilon\text{Nd}_{(T)}$	T _{DM} (Ga)	T _{DM} ² (Ga)
192594	FOR004 granite	Toolgana Supersuite	Granodiorite gneiss	FOR004	1610	6.7	39.0	0.103781 ± 0.000104	0.511742 ± 0.000006	0.510643	0.510568	0.510902	1.48	1.97	1.99
213826	FOR004 granite	Toolgana Supersuite	Granodiorite gneiss: medium-grained, foliated granodiorite	FOR004	1610	7.2	42.1	0.102847 ± 0.000112	0.511727 ± 0.000006	0.510638	0.510568	0.510902	1.37	1.97	2.00
213829	FOR004 granite	Toolgana Supersuite	Granodiorite gneiss: medium-grained, leucocratic to mesocratic, weakly to moderately foliated biotite granodiorite	FOR004	1610	9.0	40.1	0.135876 ± 0.000253	0.512002 ± 0.000008	0.510564	0.510568	0.510902	-0.08	2.27	2.11
213830	FOR004 granite	Toolgana Supersuite	Granodiorite gneiss: medium-grained, leucocratic to mesocratic, strongly foliated biotite granodiorite	FOR004	1610	5.3	25.1	0.126760 ± 0.000450	0.511866 ± 0.000006	0.510524	0.510568	0.510902	-0.86	2.27	2.17
213835	FOR004 granite	Toolgana Supersuite	Granodiorite gneiss: medium-grained, leucocratic to mesocratic, strongly foliated biotite granodiorite	FOR004	1610	7.8	35.9	0.131213 ± 0.000300	0.511954 ± 0.000007	0.510565	0.510568	0.510902	-0.06	2.23	2.11
213821	FOR004 monzodiorite	Toolgana Supersuite	Monzodiorite gneiss	FOR004	1610	4.4	20.3	0.129668 ± 0.000479	0.511966 ± 0.000007	0.510593	0.510568	0.510902	0.49	2.17	2.07
213828	FOR004 monzodiorite	Toolgana Supersuite	Monzodiorite gneiss	FOR004	1610	5.8	27.7	0.127471 ± 0.000626	0.511955 ± 0.000007	0.510606	0.510568	0.510902	0.74	2.13	2.05
216256	FOR008 granite	Toolgana Supersuite	Granodiorite gneiss: medium- to coarse-grained, well-foliated, mesocratic, K-feldspar (pink)–biotite–hornblende granodiorite; feldspar strongly flattened	FOR008	1604	6.9	40.1	0.103207 ± 0.000362	0.511670 ± 0.000006	0.510582	0.510576	0.510911	0.12	2.05	2.09
216276	FOR008 granite	Toolgana Supersuite	Granodiorite gneiss: medium- to coarse-grained, well-foliated, mesocratic, K-feldspar (pink)–biotite–hornblende granodiorite; porphyritic with strongly flattened K-feldspar to 2.5 cm	FOR008	1604	6.9	34.5	0.120402 ± 0.000410	0.511844 ± 0.000006	0.510574	0.510576	0.510911	-0.03	2.15	2.10
216267	FOR008 monzodiorite	Toolgana Supersuite	Metamonzodiorite: medium-grained, weakly foliated, very mesocratic (to melanocratic), hornblende-rich granite	FOR008	1604	3.6	17.7	0.123885 ± 0.000354	0.511896 ± 0.000007	0.510590	0.510576	0.510911	0.28	2.14	2.08
213843	FOR011 monzodiorite/ granodiorite	Toolgana Supersuite?	Metamonzodiorite: weakly foliated, fine-grained red granite; ~8–10% fine-grained mafic minerals (?hornblende>biotite); weak layering on a <1 cm scale	FOR011	1610	6.4	34.8	0.111119 ± 0.000258	0.511773 ± 0.000007	0.510597	0.510568	0.510902	0.57	2.06	2.06
213852	FOR011 monzodiorite/ granodiorite	Toolgana Supersuite?	Metamonzodiorite: fine- to medium-grained, mesocratic biotite–hornblende granite; up to 30% mafic minerals forming poorly defined 2–10 mm layers	FOR011	1610	4.8	27.1	0.106736 ± 0.000256	0.511647 ± 0.000007	0.510517	0.510568	0.510902	-1.00	2.15	2.18
213836	FOR011 syenite	Undawidgi Supersuite	Metasyenite: weakly foliated, fine-grained red granite; ~8–10% fine-grained mafic minerals (?hornblende>biotite); weak layering on a <1 cm scale	FOR011	1488	12.3	79.4	0.093611 ± 0.000126	0.511538 ± 0.000006	0.510623	0.510726	0.511074	-2.03	2.06	2.15
192592	FOR010 sodic	Undawidgi Supersuite	Monzogranite gneiss	FOR010	1488	7.6	48.7	0.093973 ± 0.000094	0.511643 ± 0.000005	0.510724	0.510726	0.511074	-0.05	1.93	2.00
213864	FOR010 sodic	Undawidgi Supersuite	Monzogranite gneiss: strongly foliated, porphyritic, medium- to coarse-grained biotite-granite; elongate feldspar phenocrysts to 1.2 cm	FOR010	1488	11.2	68.7	0.098950 ± 0.001769	0.511703 ± 0.000006	0.510735	0.510726	0.511074	0.16	1.94	1.99
213857	FOR010 high K	Undawidgi Supersuite	Metatonalite: foliated, fine- to medium-grained, grey granite; weakly porphyritic; strongly flattened feldspar phenocrysts to 8 mm	FOR010	1488	3.0	16.1	0.112744 ± 0.000313	0.511846 ± 0.000006	0.510744	0.510726	0.511074	0.34	1.98	1.97
216242	FOR012 high K	Undawidgi Supersuite	Metamonzogranite: fine- to medium-grained, pink mylonitic felsic rock with indistinct (ghost-like), subrounded phenocrysts to 6 mm	FOR012	1500	13.1	68.3	0.115627 ± 0.000259	0.511956 ± 0.000007	0.510816	0.510711	0.511057	2.05	1.87	1.86
216250	FOR012 high K	Undawidgi Supersuite	Felsic volcanic schist: grey slate	FOR012	1500	4.1	19.3	0.128361 ± 0.000516	0.512099 ± 0.000006	0.510833	0.510711	0.511057	2.39	1.90	1.83
216251	FOR012 high K	Undawidgi Supersuite	Felsic volcanic schist: grey schist; strongly flattened 'wispy' micaceous rock (white mica and chlorite) with remnant pink feldspar to 2 mm	FOR012	1500	10.2	52.4	0.117411 ± 0.000211	0.511962 ± 0.000006	0.510805	0.510711	0.511057	1.84	1.90	1.87
213817	FOR004 anatectic granite	Moodini Supersuite anatectic granite?	Medium-grained, weakly foliated, equigranular to seriate-textured, biotite leucogranite	FOR004	1180	19.2	82.7	0.140647 ± 0.000468	0.512002 ± 0.000007	0.510913	0.511126	0.511508	-4.18		2.06
213825	FOR004 anatectic granite	Moodini Supersuite anatectic granite?	Medium-grained, weakly foliated, seriate-textured, leucogranite	FOR004	1180	2.2	12.8	0.105294 ± 0.000284	0.511762 ± 0.000006	0.510946	0.511126	0.511508	-3.52	1.97	2.01
216261	FOR008 anatectic granite	Moodini Supersuite anatectic granite?	Leucosome from migmatitic monzogranite gneiss; blocky, subhedral to euhedral feldspar to 5 mm	FOR008	1150	4.2	27.3	0.092749 ± 0.000310	0.511598 ± 0.000006	0.510898	0.511165	0.511550	-5.23	1.97	2.11
192593	FOR010 shoshonite	Bottle Corner Shoshonite	Hornblende metadiorite	FOR010	1180	16.6	100.5	0.100079 ± 0.000100	0.511893 ± 0.000005	0.511118	0.511126	0.511508	-0.17	1.70	1.76
213846	FOR011 SiO ₂ -rich shoshonite	Bottle Corner Shoshonite	Weakly to moderately foliated, fine-grained biotite–hornblende metamonzodiorite	FOR011	1180	6.6	53.7	0.074736 ± 0.000091	0.511583 ± 0.000007	0.511004	0.511126	0.511508	-2.39	1.73	1.92
213847	FOR011 shoshonite	Bottle Corner Shoshonite	Fine-grained, mesocratic biotite–hornblende metamonzodiorite	FOR011	1180	18.5	103.2	0.108129 ± 0.000306	0.511965 ± 0.000006	0.511127	0.511126	0.511508	0.02	1.73	1.74
213848	FOR011 shoshonite	Bottle Corner Shoshonite	Weakly to moderately foliated, fine-grained mesocratic biotite–hornblende metamonzodiorite	FOR011	1180	17.1	97.2	0.106135 ± 0.001674	0.511959 ± 0.000007	0.511137	0.511126	0.511508	0.21	1.70	1.73
213858	FOR010 SiO ₂ -rich shoshonite	Bottle Corner Shoshonite	Fine- to medium-grained granite, unfoliated and equigranular (to locally granofelsic-textured) syenogranite	FOR010	1180	11.8	85.6	0.083496 ± 0.000762	0.511722 ± 0.000006	0.511076	0.511126	0.511508	-0.99	1.68	1.82
213867	FOR010 SiO ₂ -rich shoshonite	Bottle Corner Shoshonite	Fine-grained, unfoliated, 'felsitic-textured' syenogranite vein within foliated porphyritic granite (GSWA 213866; Appendix 8)	FOR010	1180	3.1	22.5	0.084534 ± 0.000346	0.511708 ± 0.000007	0.511053	0.511126	0.511508	-1.43	1.71	1.85
213868	FOR010 shoshonite	Bottle Corner Shoshonite	Fine- to medium-grained, 'spotty' to equigranular grey-brown (mesocratic) biotite–hornblende metamonzodiorite	FOR010	1180	25.2	153.4	0.099485 ± 0.000886	0.511818 ± 0.000007	0.511047	0.511126	0.511508	-1.55	1.79	1.86
213871	FOR010 SiO ₂ -rich shoshonite	Bottle Corner Shoshonite	Unfoliated, medium-grained porphyritic syenogranite; euhedral feldspar phenocrysts to 1 cm	FOR010	1180	5.5	36.5	0.091747 ± 0.000071	0.511737 ± 0.000007	0.511026	0.511126	0.511508	-1.96	1.78	1.89

NOTE: Model age parameters $^{147}\text{Sm}/^{144}\text{Nd} = 0.2136$; $^{143}\text{Nd}/^{144}\text{Nd} = 0.513163$; decay constant of $^{147}\text{Sm} = 6.54 \times 10^{-12}$. $\text{Sm}/\text{Nd} = ([^{147}\text{Sm}/^{144}\text{Nd}]_{\text{sample}}/[^{147}\text{Sm}/^{144}\text{Nd}]_{\text{CHUR}}) - 1$, where $^{147}\text{Sm}/^{144}\text{Nd}$ CHUR = 0.1967. Abbreviations: T, age of Nd calculation; T_{DM}, single-stage depleted mantle model age; T_{DM}², two-stage depleted mantle model age. * Reported uncertainties are 2σ



RHS1015

26.05.20

Figure 81. Variation in selected major elements and ratios with SiO₂ for felsic rocks of the Coompana Province. Shown for comparison are fields for subduction-related rocks of the c. 1300 Ma Wankanki Supersuite of the Musgrave Province (darker grey; Smithies et al., 2010) and rocks of the 1640–1600 Ma St Peter Suite of the Gawler Craton (lighter grey; D Champion, 2016, written comm., May 2016)

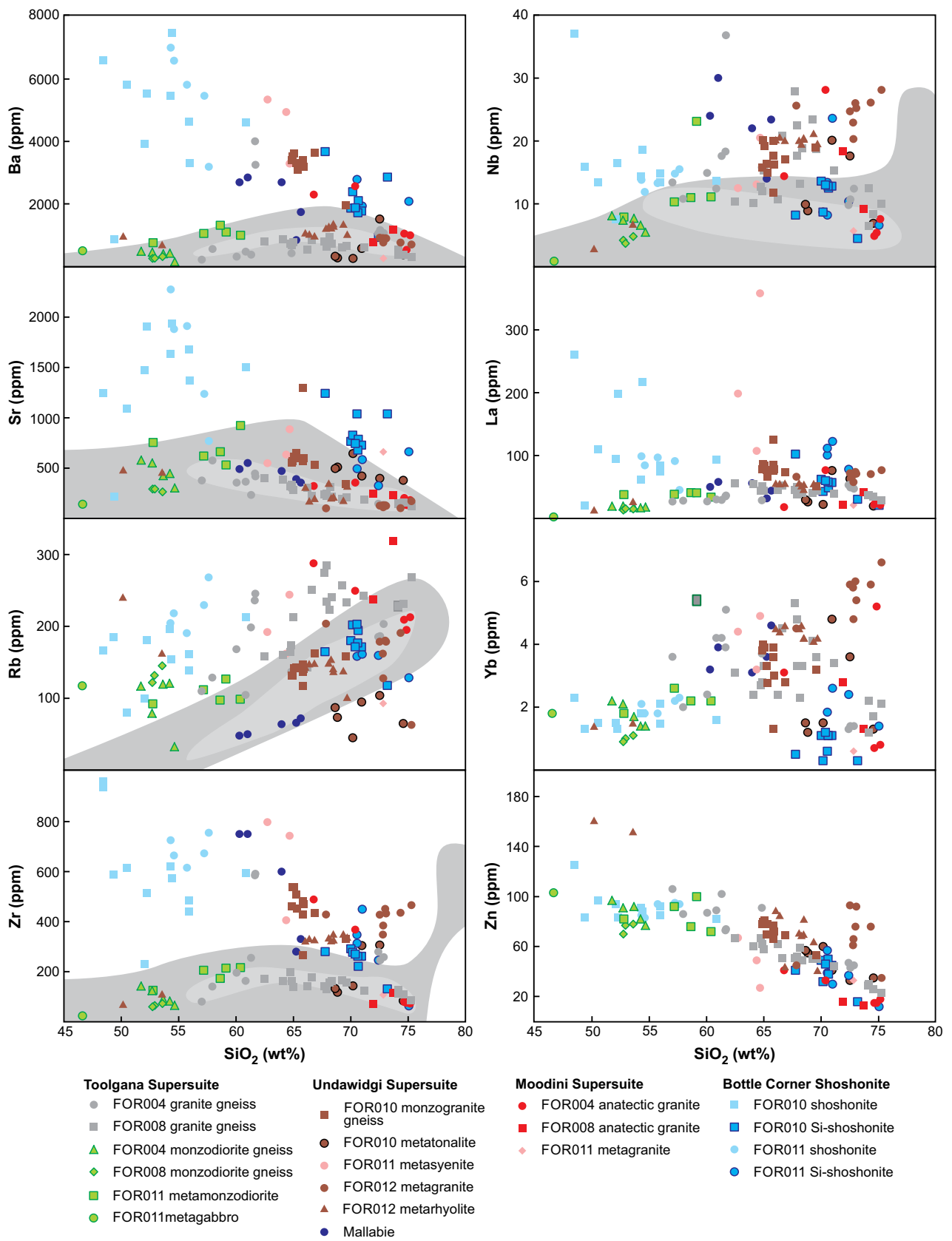


Figure 82. Variation in selected trace elements with SiO₂ for felsic rocks of the Coompana Province. Shown for comparison are fields for subduction-related rocks of the c. 1300 Ma Wankanki Supersuite of the Musgrave Province (darker grey; Smithies et al., 2010) and rocks of the 1640–1600 Ma St Peter Suite of the Gawler Craton (lighter grey; D Champion, 2016, written comm., May 2016)

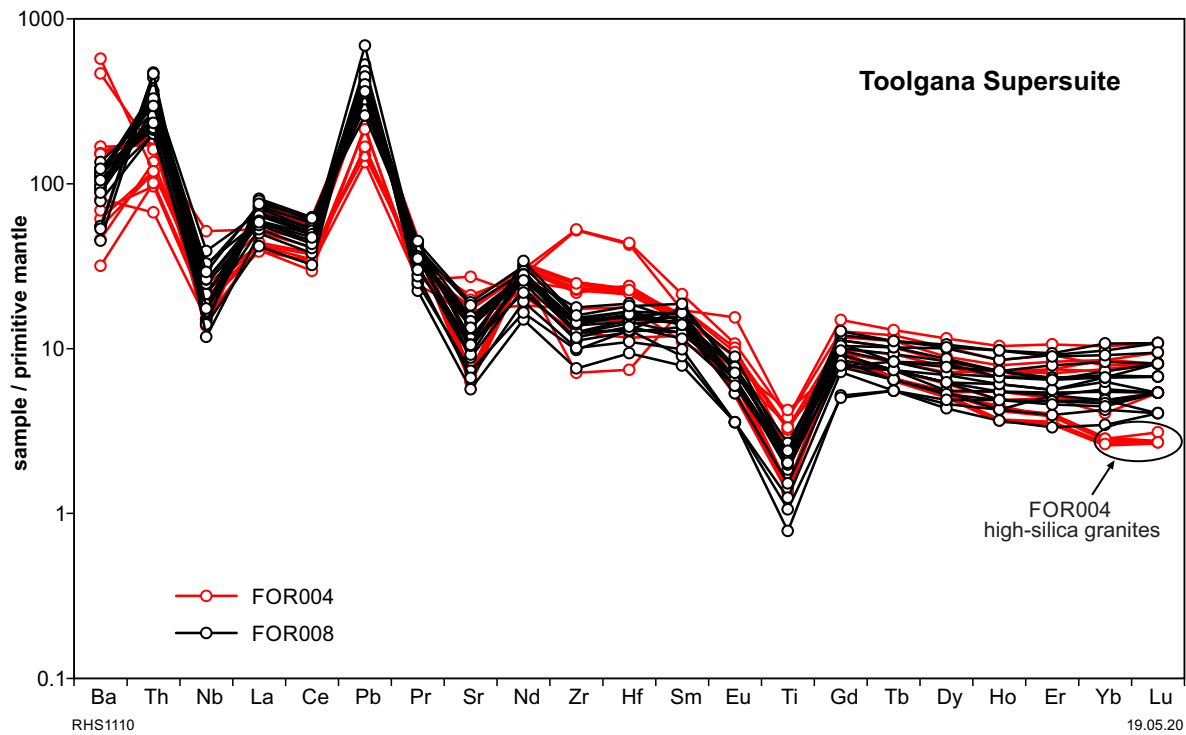


Figure 83. PM-normalized trace element spider diagrams for the Toolgana Supersuite (normalizations after Sun and McDonough, 1989)

concentrations and are particularly depleted in Ba (Fig. 82). This is probably at least partly attributable to metamorphism, likely involving biotite breakdown (i.e. biotite $D_{Ba > Rb, Sr, La}$ etc). Their compositions are, nevertheless, consistent with a subduction origin or re-melting of a subduction-derived source, or incorporation of crustal material into a mantle-derived melt (i.e. they are relatively typical of calc-alkaline granites).

The Nd isotope composition for most of the Toolgana Supersuite granite gneisses (excluding the high-SiO₂ group from FOR004, see below) varies only slightly (within ~1.7 ϵ_{Nd} units) over a wide SiO₂ range (53.6 – 68.37 wt%; Fig. 84, Table 7), becoming less radiogenic with increasing SiO₂. This suggests progressive contamination (i.e. assimilation-fractional crystallization [AFC] processes) and the presence of older SiO₂-rich material (perhaps the 1724–1671 Ma inherited component identified in the zircon geochronology). However, either the amount of progressive contamination was very small or the contaminant itself was only slightly less radiogenic and/or was mafic in composition.

It is also interesting to note, however, that the monzodiorite gneisses found in both FOR004 and FOR008 form the primitive (mafic) continuation of the AFC trend defined by the Toolgana Supersuite granite gneisses (Fig. 84), and on that basis might be parental to them. The probability that the monzodiorite gneisses are at least comagmatic with the granite gneisses is high because in drillcore FOR004, the monzodiorite and low-SiO₂ granite gneisses have a similar structural fabric and are also texturally and mineralogically transitional. The suggestion that the monzodiorite gneisses are primitive or parental members of the granite suites is also consistent with all geochemical trends (which are more or less continuous) and isotopic trends between these groups.

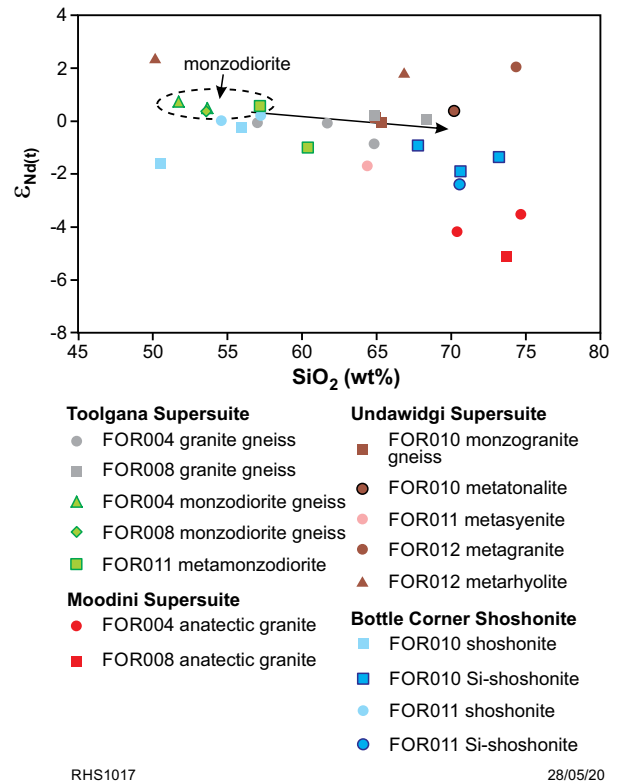


Figure 84. Variations with SiO₂ of ϵ_{Nd} at the relevant crystallization age for the c. 1611 Ma Toolgana Supersuite, depicted by the arrow, compared with younger anatectic granites from the same drillcores, the c. 1490 Ma Undawidgi Supersuite and c. 1180 Ma Bottle Corner Shoshonite

Notably, the Nd isotope composition of the high-SiO₂ granite gneisses from FOR004 (two Nd isotope data points) is ~1.5 ε_{Nd} units higher (i.e. significantly more radiogenic) than the other granite gneisses and comagmatic monzodiorite gneiss, reflecting a greater juvenile contribution to the bulk source. These high-SiO₂ rocks are still magnesian and calc-alkalic, with no evidence of a tholeiitic liquid line of descent. However, they have higher La/Yb and Dy/Yb ratios (Fig. 85) than all of the other Toolgana Supersuite granite gneisses suggesting that amphibole fractionation played a lesser role in the compositional evolution of the high-SiO₂ group. Hence, it is quite likely that although the high-SiO₂ FOR004 granite gneisses formed at a similar time as the other granite gneisses and the monzodiorite gneiss, they are not genetically directly related to those rocks — perhaps reflecting a slightly drier (less subduction-metasomatized?) source.

Monzodiorites

The geochemical data for these fine- to medium-grained, monzogabbroic to monzodioritic, typically gneissic rocks are widely dispersed, probably at least in part due to metamorphism. However, these rocks are generally quite similar in composition and the data likely reflect a similar style of magmatism. Their MgO contents range from 9.17 to 8.13 wt% for drillcore FOR008 and 9.01 to 4.56 wt% for drillcore FOR004, with a corresponding maximum Mg# of 67 and 65, and Ni concentrations of 187 and 131 ppm, respectively. The most primitive of these rocks (from FOR008) have compositions very similar to those expected of primary mantle-derived melts. Such near-primary compositions rule out significant contamination or fractionation. However, the near-primary composition also contrasts with considerable enrichments in incompatible trace elements. These enriched patterns include high LILE/HFSE ratios indicative of a subduction, or crustal, contribution to the bulk source (Fig. 86), consistent with the Nd isotope requirement for a non-radiogenic source component (e.g. ε_{Nd(1600 Ma)} ~0; Fig. 84). If this enriched component were added at a crustal level, then it is unlikely to have been the same component producing the AFC trends in the Toolgana Supersuite granite gneisses. An alternative that is more consistent with the primitive nature of the monzodiorite gneisses is that the mantle source itself was contaminated (i.e. subduction enrichment).

Probable Toolgana Supersuite amphibolites in drillcore FOR011

Drillcore FOR011 contains several mafic amphibolite horizons that have not been isotopically dated, but are an early component of the drillcore, based on textural relationships (e.g. their crystallization pre-dates development of the earliest preserved deformation fabric; see Lithological, petrographic, and structural analysis of the stratigraphic drillcores, Fig. 37a). In addition, Nd isotope data from younger metagranites in FOR011 suggest a c. 1610 Ma mafic crustal basement source component (see below).

The first of these mafic amphibolites is a series of low-SiO₂ (52.78 – 60.39 wt%) metamonzodiorites. These are sodic (Na₂O 3.87 – 5.13 wt% and K₂O/Na₂O <0.8) but also high-K, magnesian and alkali-calcic, and show

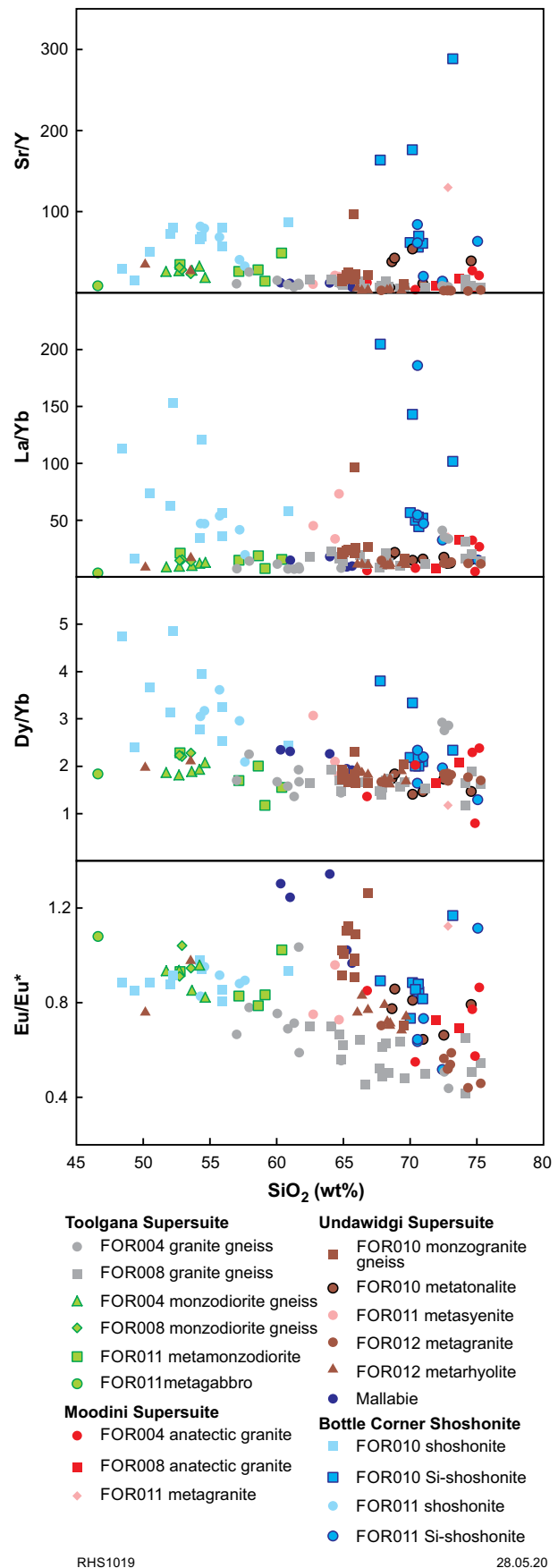


Figure 85. Variation in selected trace element ratios with SiO₂ for felsic rocks of the Coompana Province

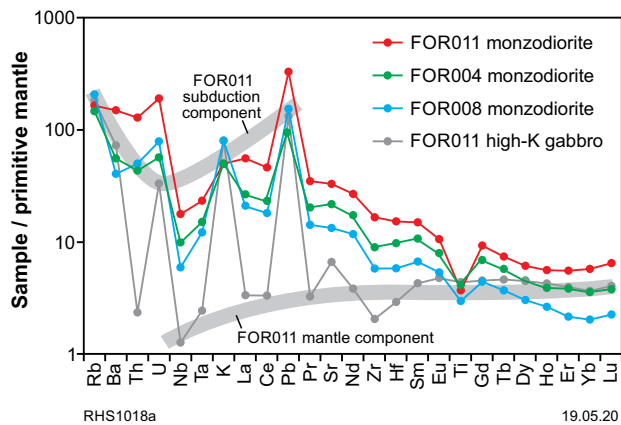


Figure 86. PM-normalized trace element spider diagrams for primitive rocks of the Toolgana Supersuite, including samples from drillcore FOR011 (normalizations after Sun and McDonough, 1989)

close compositional similarities with the Toolgana Supersuite primitive monzodiorite gneisses from drillcores FOR004 and FOR008, including equivalent Nd isotope compositions (Table 7; data with all of these rocks being isotopically equivalent at 1600 Ma: FOR011 $\epsilon_{\text{Nd}(1600 \text{ Ma})} +0.46$ to -1.11 ; FOR004 and FOR008 $\epsilon_{\text{Nd}(1600 \text{ Ma})} +0.65$ to $+0.24$).

The second mafic amphibolite is a high-K gabbro (46.63 wt% SiO_2 , 2.26 wt% K_2O) containing 10.22 wt% MgO. Having a Mg# of 58 indicates it has undergone a degree of fractionation, although a Ni concentration of 295 ppm suggests the rock remains relatively primitive. Mantle-normalized trace element patterns for this sample identify a mantle source that was depleted (based on MORB-like Nb/La and La/Sm ratios: Fig. 86), but also significantly enriched in fluid-mobile trace elements (e.g. LILE) without any accompanying enrichment in melt-mobile incompatible trace elements such as Th and LREE. No crustal addition is recognized. This pattern strongly resembles arc or fore-arc basalt derived from a previously depleted mantle source refertilized with a fluid-mobile (i.e. shallow) subduction component. The fluid-mobile enrichment pattern strongly resembles enrichment patterns in the Toolgana Supersuite monzodiorite gneisses.

Geochemistry of the Undawidgi Supersuite

Rocks of 1499–1479 Ma age form the sole magmatic component in drillcore FOR012, and a magmatic component in FOR010 and FOR011. In FOR010, crystallization ages of 1492 ± 9 and 1487 ± 9 Ma appear to relate to two compositionally discrete groups that are interlayered, the metatonalite and the porphyritic monzogranite gneiss, respectively. Neither appears to carry any inheritance (Table 5). The two ages are within uncertainty and it is unknown which is the oldest phase because the contacts are parallel to the foliation.

The c. 1492 Ma metatonalite is SiO_2 rich (68.65 – 74.58 wt%), with medium K, is calc-alkalic and magnesian (Fig. 80). It typically has among the highest MgO, Na_2O and CaO contents (and among the highest

Mg# [up to 56 but mainly between 56 and 51]) and lowest FeO and K_2O (and also $\text{K}_2\text{O}/\text{Na}_2\text{O}$ mainly ≤ 0.5) of all of the FOR-prefix granites at a given SiO_2 content (Fig. 81). These sodic metagranites are enriched in Sr (378–645 ppm) and depleted in Pb (mainly < 23 ppm) and Rb (< 104 ppm; Fig. 82). Low concentrations of Yb (< 1.5 ppm) and Y (< 13 ppm) and high La/Yb (> 15 [La up to 30 ppm]) and Sr/Y ratios (38–54; Figs 82, 85) suggest a broadly adakitic paragenesis. However, the c. 1492 Ma metatonalite has low Dy/Yb and Sr/Y ratios (Fig. 85) compared with true adakites, probably indicative of moderate-pressure hornblende fractionation rather than extraction from a high-pressure garnet–hornblende-bearing source.

The c. 1487 Ma monzogranite gneiss from drillcore FOR010 has a narrower and lower SiO_2 range (mainly 64.89 – 66.86 wt%), is high-K to shoshonitic, but remains magnesian (Fig. 80). It is TiO_2 rich, CaO poor, has high Na_2O (4.73 – 4.14 wt%) and $\text{K}_2\text{O}/\text{Na}_2\text{O}$ (~ 0.9 – 1.1) and is enriched in P_2O_5 over nearly all other FOR-prefix metagranites, except for the c. 1499 Ma felsic metavolcanic rocks from FOR012 (Fig. 81). The monzogranite gneiss has high Ba, Sr and Pb concentrations but is relatively depleted in Rb, and shows weak to moderate enrichments in Nd and Ta and strong enrichments in Zr, Hf and REE (Fig. 82). Overall, it shows transitional A-type characteristics (including high Ga and Zn), but is distinct in that it remains magnesian.

The c. 1492 Ma metatonalite and c. 1487 Ma monzogranite gneiss are isotopically similar (Fig. 87). Their isotope compositions may have resulted from reworking of Toolgana Supersuite crust, isotopically similar to that found in drillcores FOR004 and FOR008, and the amphibolites in FOR011. If an A-type petrogenetic interpretation is correct, a lack of c. 1600 Ma zircon inheritance in the c. 1487 Ma monzogranite gneiss might be related to high melting temperatures. Alternatively, the melting source might have been at the zircon-poor mafic end of the c. 1600 Ma material (or its source).

Several fine-grained, felsic metavolcanic schists in the lower part of drillcore FOR012 (Fig. 40c,d) are strongly depleted in alkalis (particularly in the SiO_2 range from 66–70 wt%) and are peraluminous, probably as a result of alteration. Undawidgi Supersuite rocks from FOR012 (i.e. both intrusive and felsic volcanic types) share many compositional features with the c. 1487 Ma monzogranite gneiss from FOR010, but they are slightly less alkali (mainly alkali-calcic), are high-K (rather than ‘shoshonitic’), and trend to more ferroan compositions at SiO_2 above 70 wt% (Fig. 80). They show significant enrichments (over most other FOR-prefix rocks) in HFSE and REE (particularly HREE) and in this respect, and in terms of elevated Ga and Zn concentrations (Fig. 88) and more ferroan compositions, most samples show well-developed A-type granite characteristics. Extended trace element trends, high trace element concentrations and significant Sr and Eu anomalies suggest the Undawidgi Supersuite rocks from FOR012 are more fractionated than the c. 1487 Ma monzogranite gneiss from FOR010. Nd isotope compositions also indicate a greater juvenile component at 1500 Ma ($\epsilon_{\text{Nd}} +0.82$ to 1.51, cf. -0.95 for the c. 1487 Ma monzogranite gneiss; Fig. 87). Although Nd isotope

data indicate that the c. 1492 metatonalite and 1487 Ma monzogranite gneiss for FOR010 could be a result of remelting of c. 1600 Ma crust (or its source), formation of the Undawidgi Supersuite rocks from FOR012 would require the addition of a more radiogenic component (e.g. mantle), consistent with their more ferroan, A-type compositions.

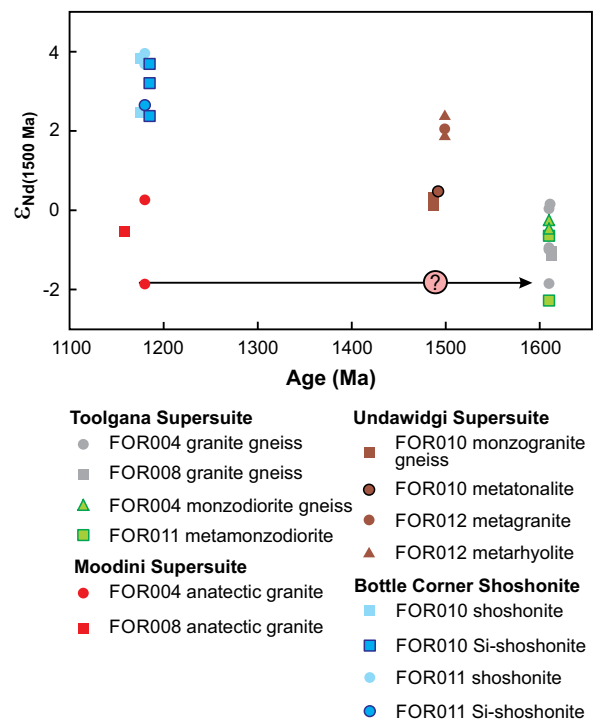
The magmatic rocks in drillcore FOR012 and the c. 1487 Ma monzogranite gneiss in FOR010 show similarities to c. 1500 Ma granite gneiss sampled from the Mallabie 1 drillcore in the southern part of the Coompana Province in South Australia (Wade et al., 2007; Figs 80–82). These are also isotopically primitive ($\epsilon_{\text{Nd}(1500 \text{ Ma})} +1.2 - 3.3$), marginally ‘A-type’ in composition, and straddle the ferroan/magnesian boundary.

The A-type signature of most of the Undawidgi Supersuite and Mallabie 1 granite gneiss is interesting given the large proportions of magnesian compositions, and suggests a strongly magnesian and likely oxidized and hydrated crustal source. These rocks represent three instances of similar-age rocks with similar compositional features that distinguish them from other magma compositions including typical subduction compositions. In many respects, these resemble post-collisional granites, with the more magnesian compositions (of the c. 1487 Ma monzogranite gneiss in particular) perhaps correlating with their more crustal, or perhaps mantle-lithospheric, isotope compositions. It is inviting to suggest that these rocks formed through high-temperature melting of juvenile, mafic arc-related crust or included melts of subduction-modified mantle-lithosphere, during extensional collapse.

Metasyenite in drillcore FOR011

Drillcore FOR011 includes a small group of metamorphosed and deformed alkali-rich syenites and leucosyenogranites. One of these contains zircon rims dated at 1174 ± 12 Ma and cores dated at 1488 ± 4 Ma (GSWA 206730, Wingate et al., 2015g; Table 5). The younger rims have very low Th/U ratios and comprise only 12% of the zircon analyses. If the c. 1174 Ma age is interpreted to represent the age of igneous crystallization, rather than metamorphism, the overwhelming dominance of the c. 1488 Ma zircon age component (which could be interpreted as inheritance) suggests that felsic crust of that age was the main Zr-contributing component of the melt source. Irrespective of how the age data are interpreted, it appears likely that c. 1488 Ma crust was a quite proximal, if not significant, component of drillcore FOR011. It is also present in nearby drillcore FOR010.

The metasyenites have a narrow SiO_2 range (62.75 – 64.68 wt%) but with very high K_2O (5.80 – 8.09 wt%), high Na_2O (3.98 – 4.50 wt%) and low CaO. They are magnesian and ‘alkaline’, lying at the upper end on the ‘shoshonite’ field near the ultrapotassic series (Figs 80, 81). They are strongly enriched in Ba (and to a lesser degree Sr, Rb and Pb), LREE (>MREE [middle rare earth elements] >HREE) and Zr and Hf, but do not show significant enrichments in Nb, Ta, Y, Ga or Zn expected of typical A-type magmas (Fig. 82). Their non-radiogenic Nd ($\epsilon_{\text{Nd}(1500 \text{ Ma})} -1.87$;



RHS1020 28/05/20

Figure 87. Variation in ϵ_{Nd} at 1500 Ma for felsic rocks of the Coompana Province. The metasyenite in drillcore FOR011, denoted by the pink dot and question mark regarding its c. 1500 Ma age, has a similar ϵ_{Nd} value at 1500 Ma to Toolgana Supersuite rocks (denoted by the arrow)

$\epsilon_{\text{Nd}(1200 \text{ Ma})} -5.86$; Figs 87, 89) require a dominantly ‘crustal’ origin, possibly strongly metasomatized crust. Whereas c. 1488 Ma crust is the main source of Zr, the non-radiogenic Nd-isotope composition is inconsistent with derivation from known c. 1500 Ma sources, which are too radiogenic (Fig. 87). However, it is consistent with derivation from c. 1610 Ma crust. Although no inherited zircons of that age are found in the metasyenite, it is possible that the source was c. 1610 Ma mafic crust (possibly monzodiorite). Thus, possible scenarios for these rocks are c. 1610 Ma mafic crust strongly alkali-metasomatized and partially melted at c. 1488 Ma, and then either remelted and remobilized or simply recrystallized, at c. 1174 Ma. Although strongly alkali rich, these metasyenites are not quite peralkaline. Their relatively low Nb (Ta) and Y concentrations distinguish them from typical sodic A-type felsic rocks often associated with alkali magmatism in rift settings, but this could be a reflection of a particularly juvenile (depleted in Nb, Ta, etc), subduction-related, crustal source component. However, the metasyenites do show strong enrichments in Zr and LREE, reflecting the type of trace element decoupling expected in subduction-related crust.

Geochemistry of the Moodini Supersuite

Magmatic rocks with ages of 1192–1175 Ma occur in drillcores FOR010 and FOR011 (Table 5). Some samples of granitic gneiss from drillcores FOR004 and FOR008

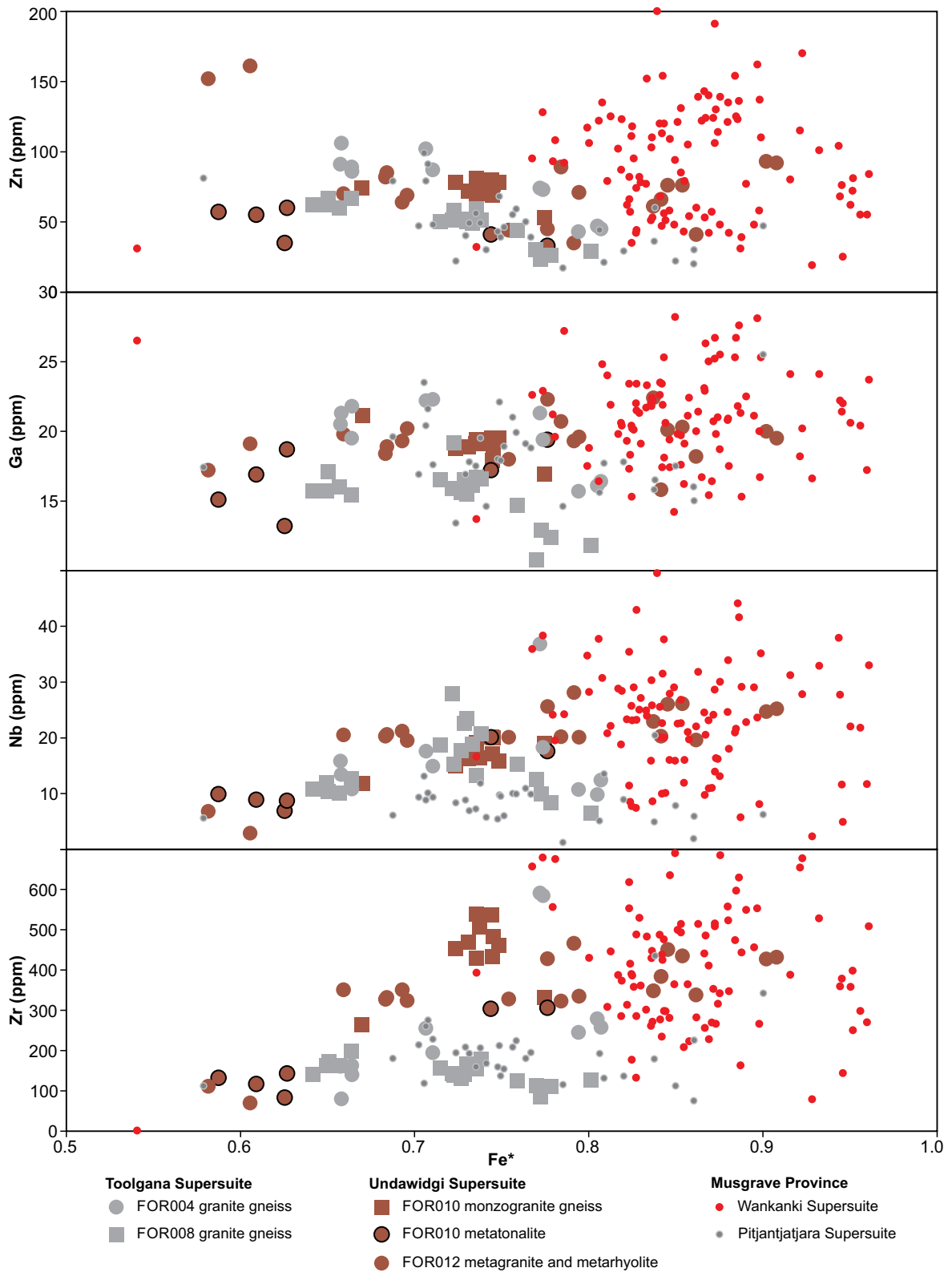


Figure 88. Variation in selected trace elements with Fe*, comparing rocks of the Toolgana and Undawidgi Supersuites with rocks of the Musgrave Province (from Smithies et al., 2010)

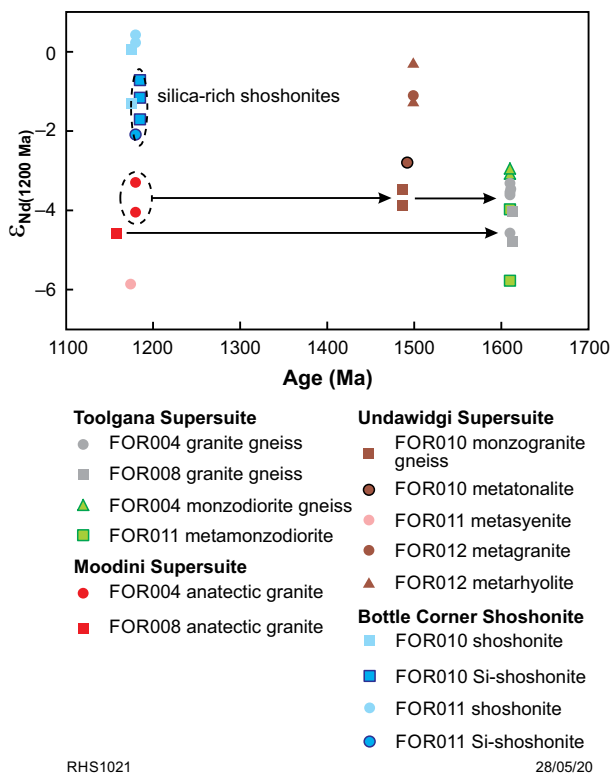


Figure 89. Variation in ϵ_{Nd} at 1200 Ma for felsic rocks of the Coompana Province. Note that in this diagram the metasyenite sample (GSWA 213836) from drillcore FOR011 is interpreted to have a magmatic crystallization, rather than metamorphic, age of c. 1174 Ma

can be interpreted as anatectic melts formed at a similar time within the Toolgana Supersuite (Appendix 7, Table A7.2; e.g. the interpreted metamorphic dates of c. 1179 Ma in GSWA 213822 and c. 1151 Ma in GSWA 216261 could represent crustal melting). Nd isotope data clearly distinguish two groups for these rocks (Fig. 89): 1) evolved (unradiogenic) samples from FOR004, FOR008 and FOR011; 2) primitive samples from FOR010 and FOR011. The isotopically primitive group can be broadly grouped into a ‘shoshonite’ series known as the Bottle Corner Shoshonite.

Crustal melting or metamorphic resetting at 1192–1150 Ma?

A granite vein dated at 1189 ± 6 Ma (GSWA 213838, Wingate et al., 2015k; no Nd isotope data) crosscuts all other lithologies and structures in drillcore FOR011. This is a sodic (5.07 wt% Na_2O) high- SiO_2 (72.85 wt% SiO_2) granite with low K_2O (1.59 wt%), high Sr (661 ppm), Sr/Y (129) and La/Yb (35), and low Y (5.1 ppm) and Yb (0.6 ppm) (Figs 81, 82) strongly reminiscent of adakite. However, it has among the lowest Dy/Yb of all FOR-prefix rocks (Fig. 85), reflecting a strong hornblende rather than garnet control. It is likely a low- to moderate-pressure melt of mafic basement (arguments presented above would point to a 1600–1500 Ma crustal source).

Schlieric leucogranites in FOR004 form a distinct geochemical group — one sample (GSWA 213822, Wingate et al., 2016f) has zircons and rims dated at

1179 ± 10 Ma (Table 5). This is interpreted as the age of in situ leucosome development in the c. 1613 Ma host. These leucogranites are SiO_2 -rich (>66 wt% and most ~75 wt%), have low TiO_2 , FeO, MgO (even for a given SiO_2 content) and CaO, have similar Na_2O to the host but are enriched in K_2O , Ba and Rb (but not Sr or Pb; Figs 81, 82). The lack of Sr and Pb enrichment and the distinctly unradiogenic Nd isotope compositions ($\epsilon_{Nd(1200 \text{ Ma})}$ from -4.56 to -3.28 ; Fig. 89) clearly distinguish these rocks from the SiO_2 -rich members of the shoshonite series (see below). At c. 1200 Ma, the leucogranites are isotopically equivalent to 1600–1500 Ma crust. Similarly, two leucogranites in FOR008 are migmatitic melts of the c. 1600 Ma host, formed between c. 1158 and 1150 Ma.

Bottle Corner Shoshonite

Rocks with shoshonitic composition form a major component (up to 25%) of both FOR010 and FOR011 and can be broadly divided into mafic samples (SiO_2 48.45 – 60.87 wt%) and felsic samples (SiO_2 67.78 – 75.08 wt%), each type occurring in both cores.

The mafic group typically has between 5.0 and 10.0 wt% MgO, but up to 20.18 wt% (aMgO with LOI of 2.18 wt%; Fig. 81). Corresponding Mg# ranges from mainly >66 up to 82 in FOR010, and between 56 and 65 in FOR011, with high Ni (1019–80 ppm in FOR010; 181–71 ppm in FOR011) and Cr (987–93 ppm in FOR010; 216–60 ppm in FOR011). Mafic shoshonites from FOR011 typically overlap the less primitive end of the range for the mafic shoshonites from FOR010. The mafic shoshonites lie within the upper part of the ‘shoshonite series’ field in the K_2O vs SiO_2 diagram of Peccerillo and Taylor (1976; Fig. 80) although none cross into the ultrapotassic field. They are strongly enriched in TiO_2 , P_2O_5 , LILE (particularly Ba and Sr), Zr, Hf, (to a lesser extent Nb, Ta), Th, U, and L-MREE, but are depleted (or at least not enriched) in HREE, with correspondingly high La/Yb ratios (Figs 81, 82, 85). Nd isotope data for the Bottle Corner Shoshonite appear to require a source component slightly more radiogenic than any sampled FOR-prefix material at c. 1200 Ma (Fig. 89), and slightly more radiogenic than bulk Earth — that is, likely an asthenospheric component.

The more felsic rocks of the shoshonite group show slight enrichments in TiO_2 and P_2O_5 compared with all other FOR-prefix granites (except those with A-type affinity) at similar SiO_2 levels, have higher Mg# (53–33) than most FOR-prefix granites, are distinctly magnesian and alkali-calcic to alkali and straddle the shoshonite series high-K boundary (Figs 80–82). Compared to other FOR-prefix granites at similar SiO_2 contents, the felsic shoshonites are also enriched in LILE (except Rb), Zr and Hf (but not Nb and Ta) and LREE (but not HREE) and hence show the same enrichment patterns as the mafic shoshonites. The less radiogenic Nd isotope compositions of the felsic shoshonites are consistent with the presence of inherited zircons, but there is no clear correlation between SiO_2 and ϵ_{Nd} that would indicate significant contamination or AFC style processes.

Lu–Hf isotope geology

This section documents Lu–Hf isotope data for the drillcores, comprising >300 Hf isotope analyses on dated zircons from 24 samples (Appendix 9; Kirkland et al., 2017; Spaggiari et al., 2018). The Lu–Hf data can also be downloaded from GeoVIEW.WA (www.dmirns.wa.gov.au/geoview).

Isotope systematics can withstand the effects of overprinting and provide a means to assess the timing and nature of early crust formation processes in the Madura and Coompana Provinces. Hf isotope measurements in zircons are ideal for characterizing sources of magmatism (Kemp et al., 2009; Payne et al., 2016). When coupled with U–Pb geochronology, the Hf isotope compositions of zircons provide information about the timing and relative roles of juvenile mantle input or reworking of older crust. Hf isotopes provide a useful tool in constraining geodynamic models because they can indicate temporal trends in source composition, which, when coupled with geological understanding, provides valuable information to assess tectonic setting.

Analytical methods

Hf isotope analyses were conducted on previously dated zircons from a range of Eucla basement drillcores (Table 5) using a New Wave / Merchantek LUV213 laser ablation microprobe, attached to a Nu Plasma multicollector inductively coupled plasma mass spectrometer (LA-MC-ICP-MS). The method has been discussed in detail elsewhere (Griffin et al., 2000). Analyses involved a laser beam diameter of about 40 µm with ablation pits 40–60 µm deep. The ablated sample material was transported from the laser cell to the ICP-MS torch in a He gas flow. Interference of ^{176}Lu on ^{176}Hf was corrected by measurement of the interference-free ^{175}Lu and using an invariant $^{176}\text{Lu}/^{175}\text{Lu}$ correction factor. Isobaric interference of ^{176}Yb on ^{176}Hf was corrected by measurement of the interference-free ^{172}Yb isotope and using the $^{176}\text{Yb}/^{172}\text{Yb}$ ratio to calculate the intensity of interference-free ^{176}Yb . The appropriate value of $^{176}\text{Yb}/^{172}\text{Yb}$ was determined by successive doping of the JMC475 Hf standard with various amounts of Yb.

Samples were measured over four analytical sessions. Zircons from the Mud Tank carbonatite were analysed alongside the samples in each session as a measure of the accuracy of the results. Most of the data and the mean $^{176}\text{Hf}/^{177}\text{Hf}$ value of each session (session 1: 0.282515 ± 24 , $n = 14$; session 2: 0.282513 ± 36 , $n = 21$; session 3: 0.282529 ± 28 , $n = 16$; session 4: 0.282531 ± 30 , $n = 38$) are within 2 standard deviations (SD) of the recommended value (0.282522 ± 42 [2σ]; Griffin et al., 2007). Temora 2 zircon was also run as an independent check on the accuracy of the Yb correction. Temora 2 has an average $^{176}\text{Yb}/^{177}\text{Hf}$ ratio of 0.04, which is similar to the mean $^{176}\text{Yb}/^{177}\text{Hf}$ ratio of zircon in this study (0.04). The average $^{176}\text{Hf}/^{177}\text{Hf}$ ratio for Temora 2 in each session is (session 1: 0.282672 ± 22 , $n = 2$; session 2: 0.282695 ± 46 , $n = 19$; session 3: 0.282689 ± 40 , $n = 20$; session 4: 0.282670 ± 36 , $n = 23$) consistent with the published value for the Temora 2 standard

(0.282687 ± 24 , LA-ICP-MS, Hawkesworth and Kemp, 2006). Calculation of ϵ_{Hf} values employs the decay constant of Scherer et al. (2001) and the chondrite uniform reservoir (CHUR) values of Blichert-Toft and Albarède (1997). T_{DM}^2 ages are calculated assuming a crustal $^{176}\text{Lu}/^{177}\text{Hf}$ ratio of 0.015.

Lu–Hf isotope results

Analysed samples are listed in Table 5, and analytical results are presented in Appendix 9 and in an initial Hf evolution diagram in Figure 90. Statistics for the ϵ_{Hf} values of individual stratigraphic units analysed in the Madura and Coompana Provinces are provided in Table 8.

Madura Province

Sleeper Camp Formation

Only one sample from the Sleeper Camp Formation has been analysed for zircon Lu–Hf isotopes, a granite vein that crosscuts mafic volcanoclastic schist and metadolerite (Figs 45e, 91a). GSWA 182485 is medium to coarse grained and hydrothermally altered. Its visually estimated mineralogy comprises 60% feldspar, 30% quartz, 4% epidote, 3% muscovite, 2% garnet and accessory biotite, muscovite, Fe oxide minerals, zircon and chlorite. Fine- to medium-grained feldspar and quartz grains are corroded and resorbed, and feldspars are heavily saussuritized. Garnets form isolated corroded grains partly rimmed by epidote, muscovite and chlorite, and Fe oxide minerals are altered to chlorite. The zircons from GSWA 182485 are mainly subhedral, variably rounded, and most exhibit faint indications of oscillatory zoning and many have homogeneous patches and rims with low CL response (Kirkland et al., 2012b; Wingate et al., 2019).

GSWA 182485 yielded an igneous crystallization age of 1477 ± 4 Ma from 14 zircon cores and rims (Kirkland et al., 2012b; Wingate et al., 2019), similar to the 1471 ± 5 Ma crystallization age of another granite vein in the same drillcore (GSWA 219094, Wingate et al., 2018h; Spaggiari et al., 2018). In GSWA 182485, four zircon cores that provided a mean age of 1538 ± 17 Ma and three older zircon cores that were dated at 2408–2293 Ma are interpreted as inherited from the host rock (Fig. 51).

Although the date of 1477 ± 4 Ma in GSWA 182485 is interpreted as an igneous crystallization age, it could also be interpreted as metamorphic (e.g. Kirkland et al., 2017). The c. 1477 Ma zircons yielded highly variable and evolved initial ϵ_{Hf} values, from -1.5 to -12.3 (Fig. 91b,c; Appendix 9.1). This implies growth or crystallization from fluids of highly variable Lu content, but could also be consistent with hydrothermal (metamorphic) alteration, because magmatic growth within a single granite vein may be unlikely to result in such a wide range of $\epsilon_{\text{Hf}(i)}$ values.

The $\epsilon_{\text{Hf}(i)}$ value of two inherited zircons are $\epsilon_{\text{Hf}(2293 \text{ Ma})} -4.6$ and $\epsilon_{\text{Hf}(2387 \text{ Ma})} +4.1$. A single analysis on a third inherited core yields an $\epsilon_{\text{Hf}(2408 \text{ Ma})}$ value of $+12.2$ when calculated at its apparent $^{207}\text{Pb}/^{206}\text{Pb}$ age. However, on post-analysis inspection of the ablation spot, the U–Pb analysis may have incorporated some younger material and, when recalculated

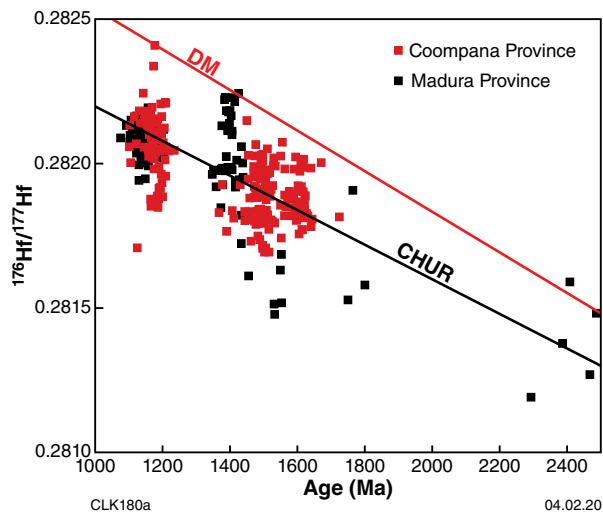


Figure 90. Hf evolution diagram for samples from the Coompana and Madura Provinces (modified from Kirkland et al., 2017). Abbreviations: CHUR, chondrite uniform reservoir; DM, depleted mantle

Table 8. Summary statistical description of Hf isotope signature (ϵ_{Hf}) of the Madura and Coompana Provinces (modified from Kirkland et al., 2017)

Province/ unit	N	Minimum	Maximum	Average	Standard error	Variance	Standard deviation	Median	25th percentile	75th percentile	Skewness	Kurtosis
Madura Province												
Moodini Supersuite	76	-4.4	5.1	0.8	0.2	2.6	1.6	0.6	-0.1	2.0	-0.4	1.3
Sleeper Camp Formation	17	-12.3	12.2	-6.2	1.6	41.1	6.4	-7.3	-11.0	-4.3	1.7	3.4
Haig Cave Supersuite	44	-40.4	13.0	3.2	1.3	72.7	8.5	3.1	1.2	8.7	-3.2	15.5
Coompana Province												
Moodini Supersuite	84	-12.8	9.9	0.8	0.4	14.7	3.8	1.0	-1.7	3.4	-0.5	0.9
Toolgana Supersuite	70	-0.8	111.0	6.9	1.8	226.5	15.1	3.3	2.2	5.1	5.5	34.6
Undawidgi Supersuite	82	-6.8	10.2	2.0	0.4	12.3	3.5	2.6	-0.7	4.5	-0.2	-0.4

NOTES: N, number of samples. 25th percentile: the value such that 25% of the sample is below, 75% above; 75th percentile: the value such that 75% of the sample is below, 25% above. Skewness: measure of the lack of symmetry in the population with a normal distribution assigned a skewness of zero; positive values indicate a tail to the more radiogenic ϵ_{Hf} side of a distribution. Kurtosis: measure of whether the data are peaked or flat relative to a normal distribution, where a parametric distribution is equal to zero

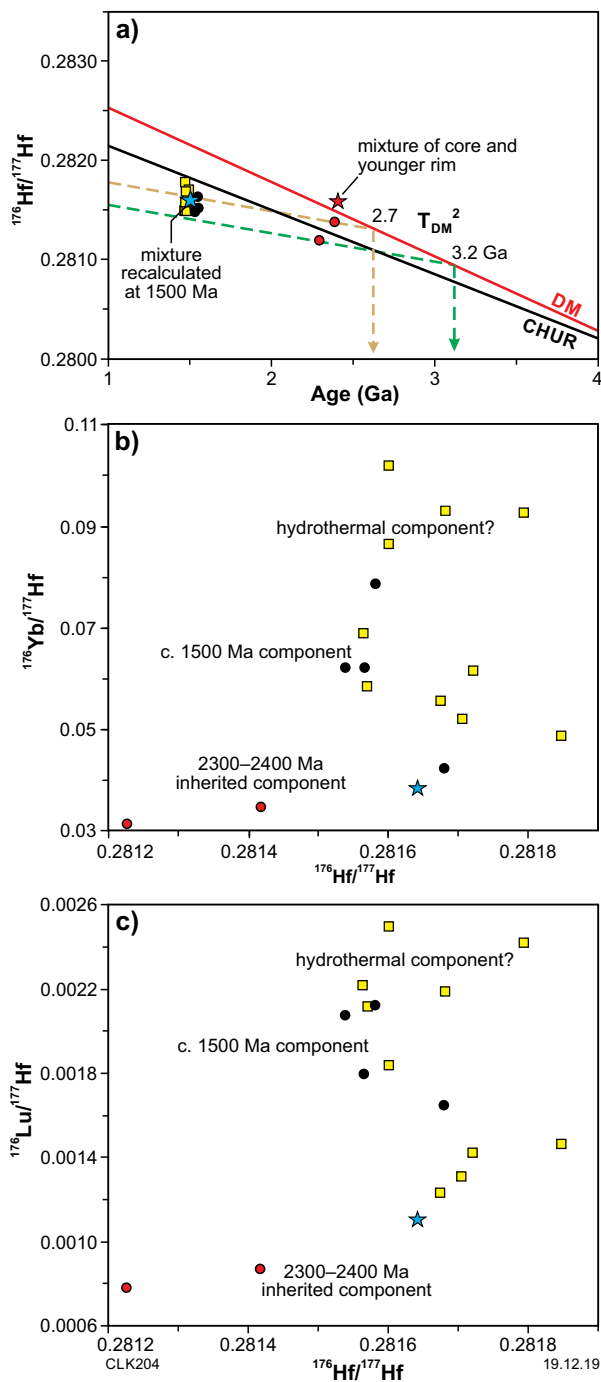


Figure 91. Zircon Lu–Hf data for granite vein sample GSWA 182485 (Sleeper Camp Formation): a) $^{176}\text{Hf}/^{177}\text{Hf}_{(i)}$ evolution plot. The blue star reflects recalculation of inherited zircon spot 18.1 (red star), interpreted to reflect a mixture with a metamorphic rim at c. 1500 Ma; b) measured $^{176}\text{Yb}/^{177}\text{Hf}$ vs $^{176}\text{Hf}/^{177}\text{Hf}$; c) measured $^{176}\text{Lu}/^{177}\text{Hf}$ vs $^{176}\text{Hf}/^{177}\text{Hf}$. Red dots reflect older inherited zircon; black dots reflect c. 1538 Ma inherited and recrystallized zircon; yellow squares reflect c. 1477 Ma magmatic and recrystallized zircon; blue star indicates the analysis with a possible mixture (modified from Kirkland et al., 2017)

at a nominal age of 1500 Ma, the $^{176}\text{Hf}/^{177}\text{Hf}_{(i)}$ value is within the range of other analyses (Fig. 91a). The younger group of c. 1538 Ma inherited zircons yields $\epsilon_{\text{Hf}(i)}$ values between -11.8 and -6.0 .

The Hf–Yb–Lu isotope signature of zircons can be used to assess the recrystallization process of zircon and whether HREE such as Lu and Yb, rather than Hf, are preferentially partitioned into garnet (Chen et al., 2010; Zhang et al., 2010). Garnet crystallization during high-temperature metamorphism can significantly deplete the associated metamorphic medium in HREE, and thus zircon formed from that medium will acquire a lower $^{176}\text{Lu}/^{177}\text{Hf}$ and $^{176}\text{Yb}/^{177}\text{Hf}$ ratio than in older zircon in isotopic equilibrium with the whole-rock composition (Hoskin and Schaltegger, 2003). Conversely, if garnet preferentially breaks down at the same time that zircon grows, elevated HREE in the zircon may be expected, and the $^{177}\text{Hf}/^{176}\text{Hf}$ isotope ratio of the zircon will vary widely depending on the time elapsed between garnet precipitation and subsequent breakdown. In the simplest scenario of crystallization of solely magmatic zircon, the $^{176}\text{Hf}/^{177}\text{Hf}$ ratio would be essentially identical to that of magmatic crystals because the Lu/Hf ratio of zircon is very low (e.g. Payne et al., 2016). The older inherited zircon crystals in GSWA 182485 have generally lower $^{176}\text{Yb}/^{177}\text{Hf}$ and $^{176}\text{Lu}/^{177}\text{Hf}$ compared to the younger c. 1538 Ma inherited zircon and also the c. 1477 Ma zircon component (Fig. 91). The elevated HREE content in the c. 1538 Ma inherited zircon may reflect garnet corrosion and zircon recrystallization during metamorphism and hydrothermal alteration of the host rock at c. 1477 Ma, as the granite veins were emplaced. Such a situation would also be consistent with elevated Yb and Lu in the c. 1477 Ma zircon component.

Haig Cave Supersuite

Two samples analysed for zircon Lu–Hf isotopes from drillcore LNGD002 from the Loongana prospect (Table 5) yielded crystallization ages of 1411 ± 6 Ma (granite gneiss sample GSWA 192558; (Kirkland et al., 2013c) and 1403 ± 6 Ma (metagabbro sample GSWA 192557; Kirkland et al., 2013b). Metagranodiorite of adakite composition from drillcore MAD002 analysed for zircon Lu–Hf isotopes yielded a slightly younger igneous crystallization age of 1389 ± 7 Ma as well as inherited zircon cores dated at 2487–1455 Ma (GSWA 206754, Wingate et al., 2016b).

The ϵ_{Hf} values for c. 1410 Ma magmatic zircons range from $+13.0$ to -5.3 and are bimodal, with peaks at about $+10$ and $+2$ (Fig. 92). One outlying analysis with an apparent ϵ_{Hf} value of -40 is excluded (analysis ID 206754-11.2; Appendix 9, Table A9.1), interpreted to have sampled an undetected inherited core. The T_{DM}^2 model ages are c. 2.0 and 1.5 Ga, although some are close to the c. 1400 Ma magmatic crystallization age. Adakite sample GSWA 206754, from the MAD002 drillcore, includes inherited zircons that yield ϵ_{Hf} as evolved as -8.8 , indicative of the influence of older crust in the source (Kirkland et al., 2017).

Moodini Supersuite

Five Moodini Supersuite samples from the Madura Province, from four drillcores, analysed for zircon Lu–Hf isotopes yield igneous crystallization ages of 1182–1127 Ma (Table 5). When plotted on an evolution plot of ϵ_{Hf} vs 204-corrected $^{207}\text{Pb}/^{206}\text{Pb}$ age, an apparent evolution array is evident; however, a strong correlation is also evident between f_{204} and 204-corrected $^{207}\text{Pb}/^{206}\text{Pb}$ ages (Fig. 93; Kirkland et al., 2017). f_{204} is the percentage of common or non-radiogenic Pb within measured ^{206}Pb , which carries the chronometric signal of interest. This correlation is likely a result of overcorrecting for common Pb, and is an issue that affects all secondary ion mass spectrometry measurements taking the approach that common Pb correction should be made for all analyses in which ^{204}Pb is measured. In this approach, when low counts of ^{204}Pb are at or below the background level, correlations with f_{204} and corrected ages can become manifest. The alternative, where correction of common Pb is only applied when counts are above a statistically defined threshold, raises issues of where that threshold should be set, but also means a potential correction distribution bias towards under correction could occur as, statistically, the same number of over-counts as under-counts could be predicted.

In the situation of the Moodini Supersuite, with low levels of common Pb and highly concordant data, ^{207}Pb corrected $^{238}\text{U}/^{206}\text{Pb}$ ages are preferred and avoid this issue. This preferred age selection issue has implications for the distribution of time-corrected Hf data, and is directly relevant to the interpretation of the data. In the case of the Moodini Supersuite zircons, with their low and hence difficult to measure ^{204}Pb , 204-corrected $^{207}\text{Pb}/^{206}\text{Pb}$ ages are both undercorrected (where 204 counts are below background resulting in negative f_{204} and a resultant increase in the corrected $^{207}\text{Pb}/^{206}\text{Pb}$ age) but also overcorrected (where 204 counts are spuriously above background resulting in excessive reduction in the $^{207}\text{Pb}/^{206}\text{Pb}$ age). The net effect of this, when plotting age against ϵ_{Hf} , is an apparent array with no crustal evolution significance (Fig. 94; Kirkland et al., 2017). When corrected using 207-corrected ages this array disappears and a cluster of data ranging from +5 to –5 is revealed.

Coompana Province

Toolgana Supersuite

All four dated samples of Toolgana Supersuite from drillcores FOR004 and FOR008 were analysed for zircon Lu–Hf isotopes (Table 5). The ages of oscillatory zoned zircon cores from these samples agree to within uncertainty, indicating a mean protolith crystallization age of 1611 ± 7 Ma. Zircon rims in three samples (excluding GSWA 192594) provided ages for metamorphism of 1179 ± 10 , 1153 ± 9 , and 1151 ± 6 Ma. Two zircon cores in GSWA 192594 yielded dates of c. 1724 and 1671 Ma, interpreted as the ages of inherited zircons.

Hf isotope data for c. 1611 Ma magmatic zircon cores indicate $\epsilon_{\text{Hf}(t)}$ values that range from CHUR-like to +10.0, and are bimodal, with peaks at about +2–4 and +9, corresponding to two-stage model ages of c. 1.8 Ga and 2.1–2.2 Ga (Fig. 95). Five analyses of c. 1160 Ma metamorphic zircon rims in GSWA 216276 from drillcore FOR008 yield $\epsilon_{\text{Hf}(t)}$ values that are essentially identical to those of the associated magmatic zircon cores, which is consistent with isochemical breakdown and metamorphic recrystallization in this sample.

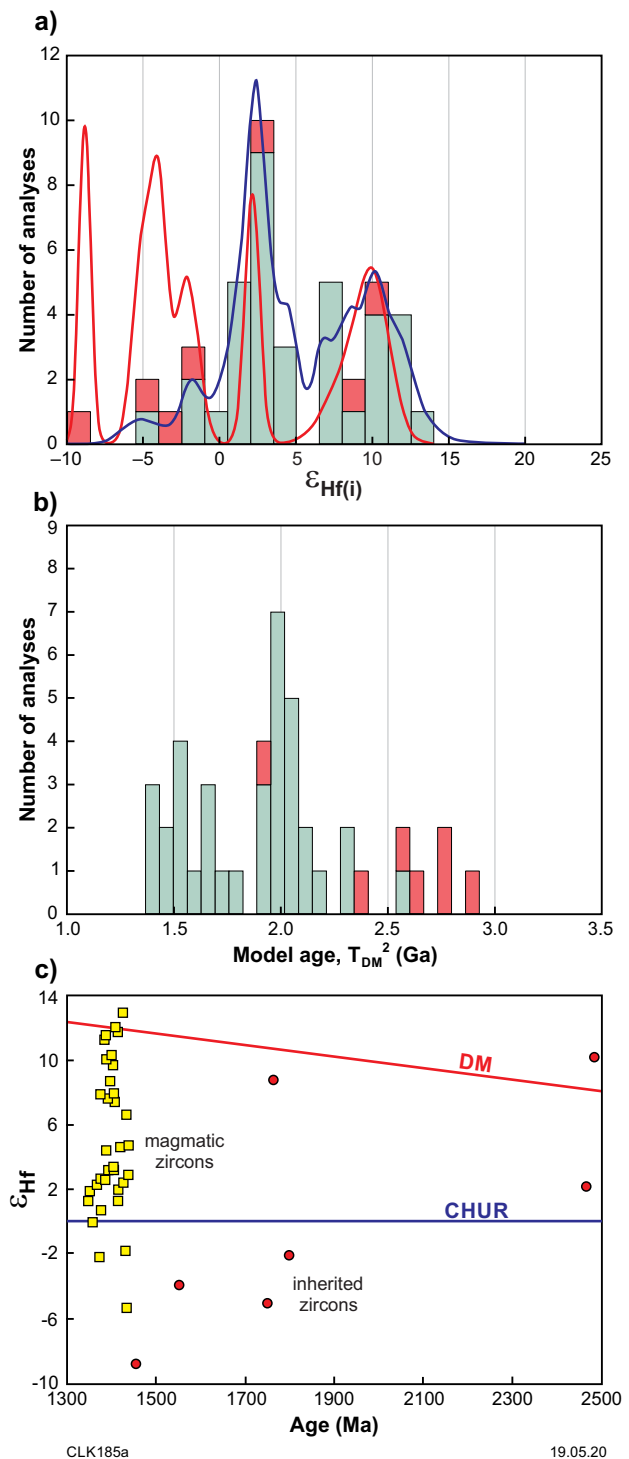


Figure 92. Hf isotope signature of zircons from the Haig Cave Supersuite: a) histogram of $\epsilon_{\text{Hf}(t)}$; b) histogram of T_{DM}^2 model ages; c) Hf evolution diagram. Green fill and blue curve in histograms indicate data for magmatic zircons whereas red fill and red line denotes data for inherited zircons (after Kirkland et al., 2017)

In contrast, six analyses of four metamorphic zircon rims in GSWA 213822 from drillcore FOR004 yield highly radiogenic compositions, with extreme ϵ_{Hf} values up to +110 (Fig. 95c), which provide strong evidence for the breakdown of garnet associated with metamorphic zircon growth. This garnet must have existed for some time prior to its breakdown to allow sufficient ingrowth of radiogenic Hf in the zircon, and indicates a metamorphic event in the Toolgana Supersuite of at least amphibolite facies with garnet growth prior to c. 1179 Ma, the age of metamorphism recorded by zircon rims in this sample. In addition, the $^{176}\text{Lu}/^{177}\text{Hf}$ (and $^{176}\text{Yb}/^{177}\text{Hf}$) ratios of the metamorphic rims in GSWA 213822 are broadly within the range of the igneous cores, which indicates that the breakdown process occurred prior to and separately from garnet growth (Fig. 96; Kirkland et al., 2017).

Undawidgi Supersuite

All five dated Undawidgi Supersuite samples were analysed for zircon Lu–Hf isotopes (Table 5). They consist of metagranites and a schistose felsic metavolcanic rock sampled in drillcores FOR010, FOR011 and FOR012. Zircons in all samples are subhedral to euhedral, concentrically zoned, and except for GSWA 206730, none of the samples exhibits zircon rims. The oldest sample is the 1499 ± 9 Ma felsic schist, interpreted to have a volcanic protolith, from the lower part of drillcore FOR012 (GSWA 206788, Wingate et al., 2016e). The five samples have bimodal $\epsilon_{\text{Hf}(i)}$ values from -6.8 to $+10.2$, with peaks at about -2 and $+4$ (Fig. 97). Two-stage depleted mantle model ages range from c. 1.7 to 2.5 Ga.

A hornblende–biotite metasyenite from drillcore FOR011 contains zircon cores that yield an igneous crystallization age of 1488 ± 7 Ma, overgrown by thin zircon rims, six analyses of which yield an age for metamorphism of 1174 ± 12 Ma (GSWA 206730, Wingate et al., 2015g). The zircon rims are slightly more radiogenic (higher $^{176}\text{Hf}/^{177}\text{Hf}_i$) than the zircon cores. This is consistent with reworking of a broadly felsic Hf isotope reservoir for which the array reflects ingrowth of radiogenic Hf from a source with crustal $^{176}\text{Lu}/^{177}\text{Hf}$ (Fig. 97; Kirkland et al., 2017). This implies that the metamorphic zircon rims grew from a crustal partial melt, rather than by isochemical zircon dissolution and reprecipitation. The Hf isotope signature therefore implies partial melting, rather than simply metamorphism, at c. 1174 Ma.

Moodini Supersuite

Six Moodini Supersuite samples from the Coompana Province analysed for zircon Lu–Hf isotopes (Table 5) comprise a variety of 1192–1140 Ma granitic rocks from drillcores FOR010, FOR011 and the Eucla No. 1 petroleum well. As with the 1182–1127 Ma Moodini Supersuite in the Madura Province, the wide range in age implies a protracted magmatic event. High-grade metamorphism and growth of zircon rims was broadly coeval with Moodini Supersuite magmatism, for example, at c. 1174 Ma in drillcore FOR011 (GSWA 206730).

Moodini Supersuite granites contain few inherited zircons (Table 5). Sample GSWA 206752 from drillcore FOR010 contains a c. 1558 Ma zircon core, and three zircon cores in GSWA 206753 from the same drillcore yield ages of

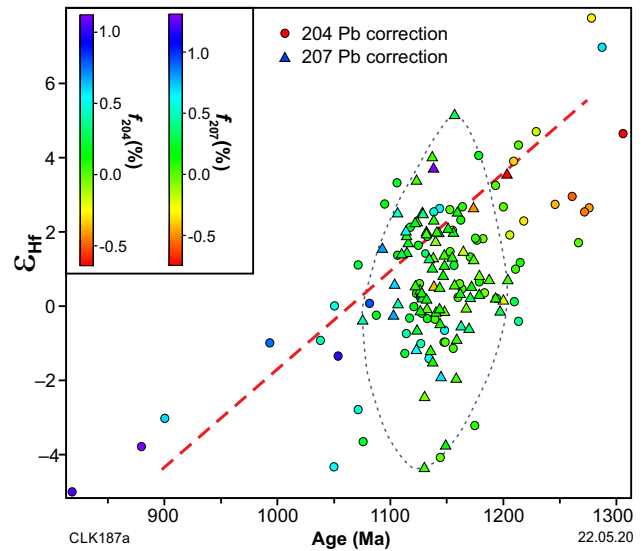


Figure 93. Hf isotope signature of zircons from the Moodini Supersuite in the Madura Province showing the correlation between 204-corrected $^{207}\text{Pb}/^{206}\text{Pb}$ age and f_{204} (the percentage of common or non-radiogenic Pb within measured ^{206}Pb) (after Kirkland et al., 2017)

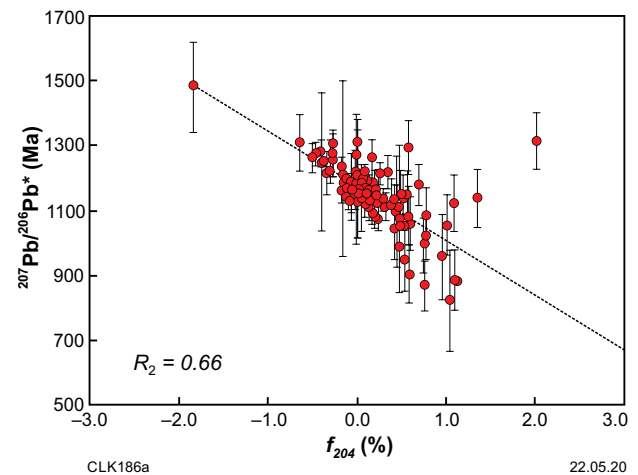


Figure 94. Hf evolution diagram for zircons of the Moodini Supersuite, Madura Province. Circles and triangles indicate 204-corrected and 207-corrected dates, respectively, used to calculate ϵ_{Hf} values. The colour scale reflects the proportion of common Pb (f_{204} , f_{207}) estimated by the two correction methods. The dashed line indicates an apparent evolution line when ϵ_{Hf} is plotted vs 204-corrected dates, whereas the dotted ellipse indicates a more coherent distribution of ϵ_{Hf} values ranging from $+5.1$ to -4.4 when calculated using 207-corrected dates (after Kirkland et al., 2017)

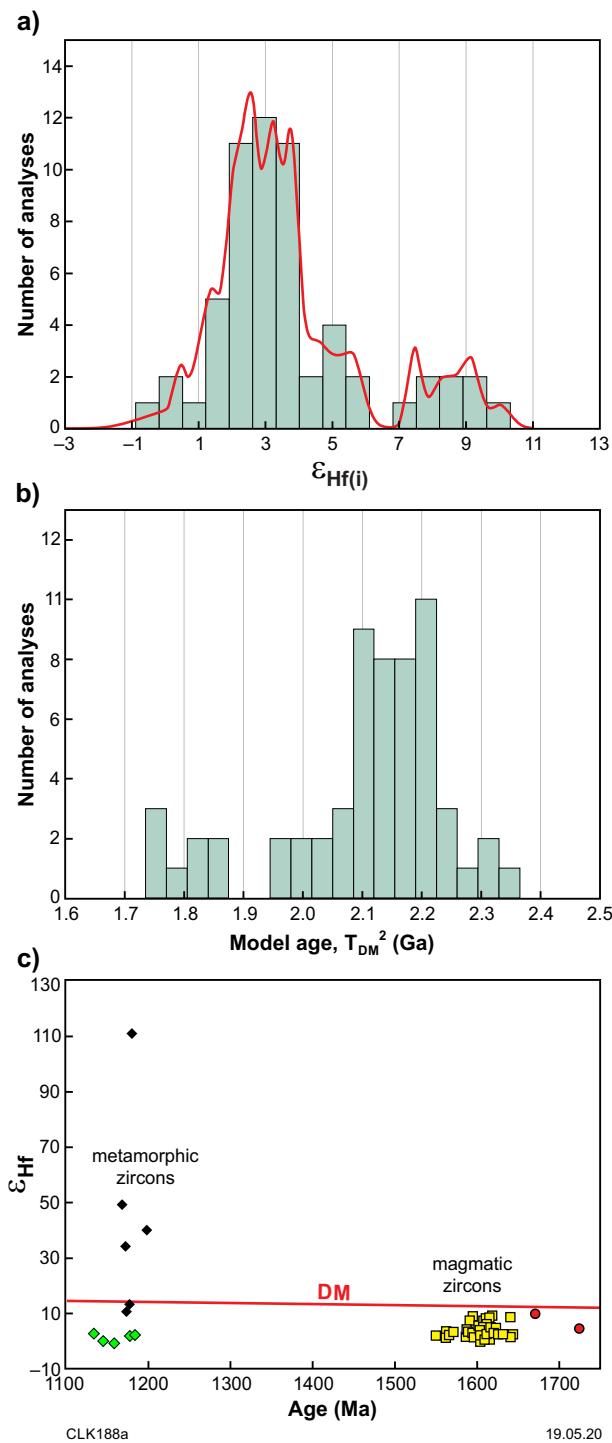


Figure 95. Hf isotope signature of zircons from the Toolgana Supersuite: a) histogram of $\epsilon_{\text{Hf}(i)}$ values for magmatic and inherited zircons (Group A); b) histogram of TD_{M}^2 model ages for magmatic and inherited zircons (Group A), note this excludes metamorphic zircon; c) Hf evolution plot for magmatic zircons and metamorphic zircons and zircon rims (Group B). Red dots denote inherited zircons. Black diamonds indicate highly radiogenic metamorphic zircons from GSWA 213822 (after Kirkland et al., 2017)

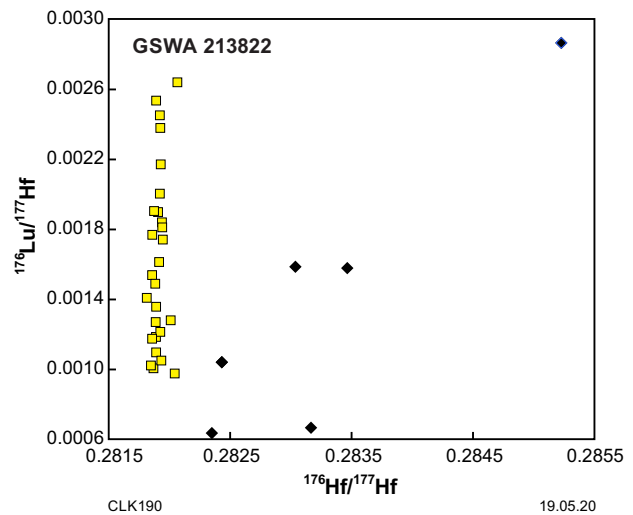


Figure 96. Plot of $^{176}\text{Lu}/^{177}\text{Hf}$ vs measured $^{176}\text{Hf}/^{177}\text{Hf}$ for Toolgana Supersuite sample GSWA 213822. Six analyses with elevated radiogenic Hf (Fig. 95) are denoted by the black diamonds and are broadly within the $^{176}\text{Lu}/^{177}\text{Hf}$ range of the other analyses

1576–1511 Ma. Sample GSWA 194773, from the Eucla No. 1 petroleum well, contains an inherited zircon dated at c. 1598 Ma (Kirkland et al., 2011c). GSWA 213838 from drillcore FOR011 contains 23 inherited zircon cores dated at 1552–1462 Ma (Wingate et al., 2015k).

Values of $\epsilon_{\text{Hf}(i)}$ for c. 1180 Ma magmatic zircons range from -6.4 to $+6.9$, with an average model age of c. 1.9 Ga. The majority of the negative (evolved) values are from the coarse, quartz-rich monzogranite vein sampled in drillcore FOR011 (GSWA 213838), whereas the other samples yield dominantly positive (more juvenile) values. In the sample from the base of the Eucla No. 1 well, one outlying analysis (194773-12.1) indicates an $\epsilon_{\text{Hf}(i)}$ value of -12.8 , which corresponds to a model age of 2.8 Ga (Fig. 98), although the Lu–Hf analysis is interpreted to represent a mixture of magmatic zircon with an inherited component sampled by the larger volume during laser analysis compared to the more restricted volume sampled by the SHRIMP U–Pb spot. The c. 1600–1500 Ma inherited material in the Moodini Supersuite samples indicates $\epsilon_{\text{Hf}(i)}$ values between -4.8 and $+9.9$, corresponding to an average model age of c. 2.3 Ga.

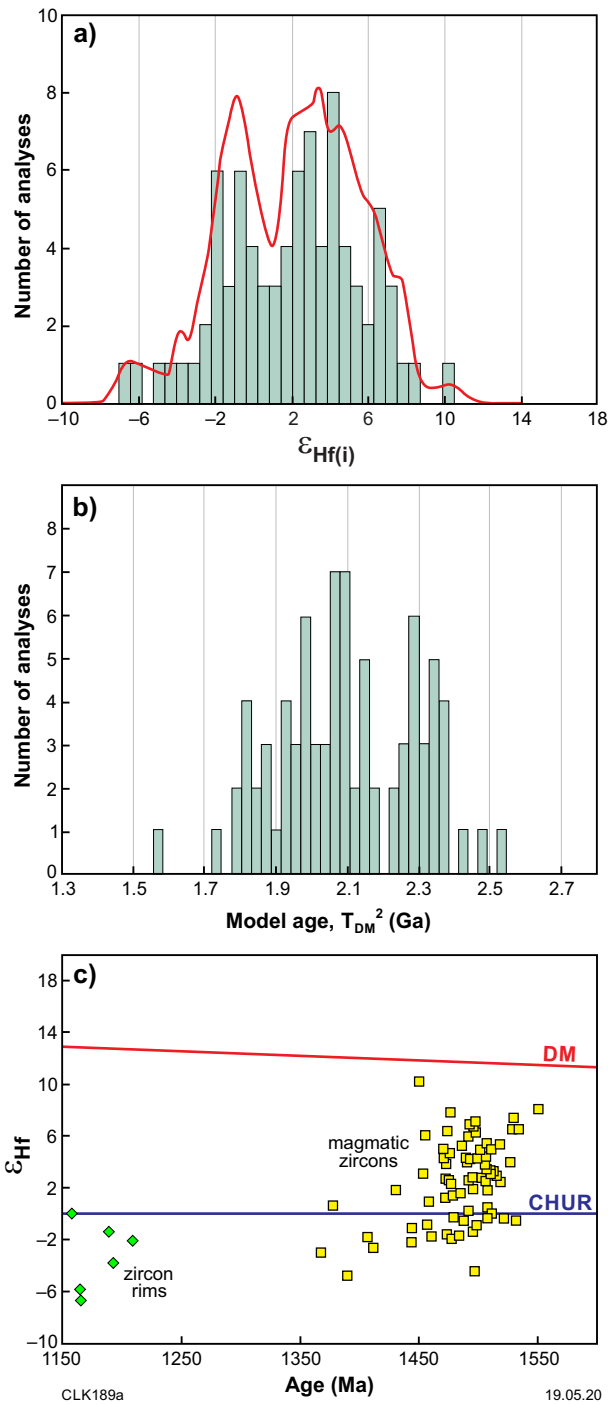


Figure 97. Hf isotope signature of zircons from the Undawldgi Supersuite: a) histogram of $\epsilon_{Hf(i)}$; b) histogram of two-stage model ages; c) Hf evolution plot. Yellow squares indicate analyses of magmatic zircons; green diamonds indicate metamorphic zircon rims

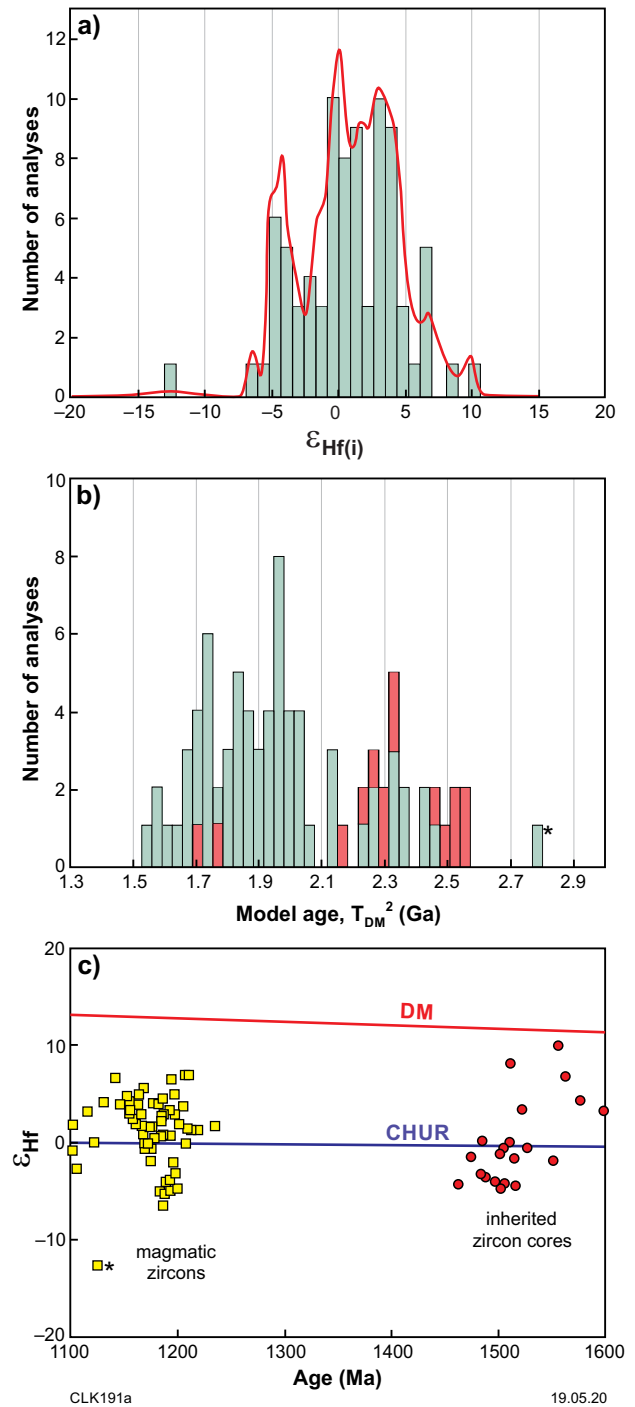


Figure 98. Hf isotopic signature of zircons from the Moodini Supersuite in the Coompana Province: a) histogram of $\epsilon_{Hf(i)}$; b) histogram of T_{DM}^2 model ages; c) Hf evolution plot. Yellow squares denote analyses of magmatic zircons, red dots denote analyses of inherited zircons, star denotes a mixture (after Kirkland et al., 2017)

Discussion

The Eucla basement drillcores and isolated outcrops at Point Malcolm provide valuable information about the covered Precambrian basement of the Madura and Coompana Provinces. However, the ability to observe rock relationships over reasonable distances, as would typically be available during field mapping, presents challenges for mapping the geology between drillhole sites. Rock relationships determined from detailed logging of individual drillcores are a vital starting point and provided fundamental information for interpreting geochronological, geochemical and isotope data, which, in turn, were used to establish the lithostratigraphic units. Geophysical data have provided a means to assist with mapping the extent of each lithostratigraphic unit and its structural setting. Below we discuss the primary formation of the lithostratigraphic units derived from the observations and data presented above. The Madura and Coompana Provinces are discussed separately due to significant differences in their tectonic histories (Fig. 8). These sections are followed by discussions on structural and crustal architecture evolution, regional implications and applicable tectonic models.

Formation of the lithological units of the Madura Province

Drillcores and limited outcrop show that protoliths in the Madura Province include basalts and mafic volcanoclastic rocks, sedimentary rocks and intrusive rocks including gabbros, ultramafic rocks, and a variety of intermediate and granitic rocks (Fig. 8). The majority of these rocks are metamorphosed and deformed. Rocks assigned to the Moodini Supersuite are discussed below in separate sections that cover both provinces.

Pinto Basalt and Haig Cave Supersuite adakite

The oldest lithological unit identified in the Madura Province drillcores is the Pinto Basalt in stratigraphic drillcore MAD002), although direct dating of this unit has not been possible as it lacks zircon. The only firm age constraint is provided by the Haig Cave Supersuite adakite, which intruded the Pinto Basalt at c. 1389 Ma (Table 5). T_{DM}^2 model ages for the adakite range from 2.21 to 1.95 Ga (Table 6), indicating a significant age gap between the oldest source component and adakite magmatism. For the Pinto Basalt, a formation age closer to c. 1950 Ma is favoured by the non-radiogenic Nd isotope composition ($\epsilon_{Nd} +1.44$ to $+2.54$) of the basalt at c. 1400 Ma, compared with values expected for uncontaminated asthenospheric melts (ϵ_{Nd} about $+6$ to 7 ; based on the value of depleted mantle at c. 1400 Ma). The non-radiogenic compositions could indicate that the basaltic magmas simply incorporated crustal material, in which case the age of the Pinto Basalt could be considered as relatively young (i.e. closer to c. 1389 Ma). However, low Th/Nb ratios in the Pinto Basalt mean that any assimilated crust cannot have been evolved (e.g. old continental material), and assimilation of old mafic crust would not significantly change compositions, except at high assimilant volumes, a process which would be difficult on thermal grounds.

The high-Ti, high-Mg group in the Pinto Basalt has Mg# (and Ni and Cr concentrations) consistent with equilibrium with mantle peridotite and might reflect near-primary mantle melts (Figs 54, 55). For both basalt types, trace element patterns and Nd isotope compositions are very similar, suggesting a cogenetic, comagmatic relationship, or at the very least, a similar source. Trace element patterns for both basalt types are transitional between E-MORB and OIB (Fig. 56) and reflect low-degree melting of a non-depleted mantle source. These patterns permit only a small degree of crustal contamination (or input), perhaps suggesting an oceanic or proto-oceanic environment. High Ti/Yb in the most primitive compositions confirms melting of a deep (>2.8 Gpa = >100 km), garnet-bearing mantle source. Hence, the basalts can be interpreted as the result of decompression melting during upwelling of relatively deep and fertile asthenospheric mantle, with only limited subsequent assimilation of evolved crustal material.

The adakite in drillcore MAD002 can be interpreted to reflect melting of lithosphere with basaltic compositions at pressures of about 1.5 Gpa (52 km depth; e.g. Martin et al., 2005; Moyen, 2009). The high K_2O (commonly >1 wt%) contents of Pinto Basalt samples indicates that these or similar rocks cannot be the basaltic source for magmas as sodic as those that formed the adakite, and hence the Pinto Basalt must be considerably older. One interpretation of these data is low-degree partial melting of subducting mafic lithosphere leaving a garnet–rutile (eclogite) or hornblende–garnet residuum. However, the Nd isotope composition of the adakite ($\epsilon_{Nd(1400\text{ Ma})} -3.79$ to -0.36) is very non-radiogenic and clearly does not reflect a melt of young oceanic lithosphere. Either the basaltic source formed close to the calculated c. 1.9 Ga T_{DM}^2 age of the adakite and was itself slightly LREE enriched, or slab melting or subsequent magma contamination incorporated a significant amount of exotic, non-radiogenic (but still primarily mafic, such as older arc-derived material) sediment, or both. Alternatively, the adakite formed through deep melting of a c. 1.9 Ga basaltic underplate.

The presence of inherited zircons in the adakite, with ages between 2487 and 1455 Ma, also clearly indicates the adakitic magmas have incorporated older crustal components at some stage — potentially sedimentary material belonging to the Arid Basin. The Haig Cave Supersuite intrusions have been interpreted to have formed within an oceanic subduction setting, and it is inviting to interpret the origins of the adakite within a similar setting.

The E-MORB – OIB geochemical signature of the Pinto Basalt distinguishes this unit from the younger Haig Cave Supersuite intrusions (Fig. 57). The basalt is interpreted to have formed within a continental margin basin — the Arid Basin — that developed during craton margin rifting in an ocean–continent transition setting (Spaggiari et al., 2015a; 2018). The distinct layered and laminated texture of the Pinto Basalt (Fig. 18) could suggest a tuffaceous protolith, perhaps part of a volcanic island or edifice. It is unknown whether the protolith was deposited subaerially or in a shallow-marine or even deep-marine setting as there are no sedimentary rocks present in the drillcore.

Haig Cave Supersuite — Loongana oceanic arc

This series of tholeiitic intrusions ranges from hornblende-bearing gabbro (Haig 2) to olivine- and pyroxene-bearing peridotites and gabbros (Haig 1 and Loongana 1 and 2). The high Mg# of the rocks from Haig 2 (up to 69) and Loongana (Loongana 1 Mg# up to 81; Loongana 2 Mg# up to 64) are indicative of source magmas in equilibrium with mantle peridotite. Haig 1 has more fractionated compositions (Mg# up to 46). Gabbros from Haig 1 are also distinct from the other intrusions in that their trace element ratios more closely approximate N-MORB values, whereas the other bodies have Th/Nb ratios consistent with either a subduction addition to their mantle source or assimilation of older crust (Fig. 57; noting the low Th and Nb concentrations). Much higher V/Ti ratios in Haig 1 gabbros (Fig. 64) are also more consistent with an unmodified, dry and reduced source similar to a MORB source, whereas lower ratios possibly indicate a more hydrated and oxidized source producing the other intrusions. It should be noted that although Haig 1 is more fractionated than the other intrusions, this would normally decrease, rather than increase, V/Ti ratios (i.e. the high ratios are meaningful and probably unrelated to fractionation).

Despite having trace element compositions approximating N-MORB, Haig 1 gabbros have Nd isotope compositions ($\epsilon_{\text{Nd}(1400 \text{ Ma})} +0.2$ to $+0.27$) similar to those of Haig 2 gabbros ($\epsilon_{\text{Nd}(1400 \text{ Ma})} -0.08$ to $+0.04$) and both have less radiogenic values than the Loongana mafic intrusions ($\epsilon_{\text{Nd}(1400 \text{ Ma})} +1.33$ to $+2.87$; Table 6). Although both the Loongana and Haig intrusions are mainly cumulate rocks, the Nd isotope variability within the Loongana mafic intrusions ($>1.5 \epsilon_{\text{Nd}}$ units) reflects an open system. Magmas forming the cumulate assemblages were extracted from a chamber itself either undergoing progressive wallrock contamination or replenished by magmas extracted from an isotopically variable mantle source. Incompatible trace element ratios show even greater variation than Nd isotope compositions but the two show no systematic variation. This tends to favour replenishment by magmas from slightly compositionally distinct mantle sources.

All the intrusions show a significant negative mantle-normalized Zr anomaly (i.e. $\text{Zr}/\text{Zr}^* < 1$; where $\text{Zr}^* = [(\text{Nd}_{(\text{PM})} + \text{Sm}_{(\text{PM})})/2]$). These are not strongly developed in the basaltic rocks of the Pinto Basalt, Sleeper Camp Formation, Malcolm Metamorphics or Connie Sue Formation, but are present in the Narilya Bore Basalt (Fig. 99). Both positive and negative Zr (and Hf) anomalies are a notable feature of arc-related magmas, often ascribed to the relative immobility of HFSE compared with REE in fluids during subduction, but may also be related to low-pressure fractionation of low-Al clinopyroxene and Ti-magnetite (e.g. Woodhead et al., 2011). The Zr anomalies in the Madura Province rocks show no correlation with Zr or Sc concentration and so are unlikely to be related to early removal of zircon or to clinopyroxene fractionation. However, they are also unlikely to result from crustal contamination because the lowest Zr/Zr^* values correlate with the isotopically most primitive magmas (Fig. 100).

MORB-normalized trace element patterns of the Loongana and Haig intrusions (Fig. 62) show negative HFSE anomalies that roughly decrease in order from Nb to Zr to Ti to Yb. These anomalies reflect a mantle source similarly or more depleted than an N-MORB source. Thus, the Madura Province gabbros show a range of features consistent with a bulk source dominated by a juvenile mantle component, but also requiring a small amount of more evolved material. These features include high Th/Yb, La/Nb ratios and variably unradiogenic Nd isotope compositions. Several lines of evidence presented above (e.g. V/Ti and Zr/Zr^* ratios) suggest that this evolved material represents a subduction addition rather than crustal contamination. Certainly, there is no systematic correlation between Nd isotope composition and MgO , Mg#, SiO_2 , K_2O , Th, etc (Fig. 101), that would implicate crustal contamination or AFC-style processes. This suggests that irrespective of how the evolved component was added to the bulk magmas, that component was compositionally and isotopically quite heterogeneous. It is possible that the evolved component was variably reworked juvenile crust (reworked older arc material).

An additional feature that favours an oceanic subduction setting for the Madura Province gabbros is the fact that they are intruded, near contemporaneously, by plagiogranites. These are typically minor components of arc stratigraphy and their sodic compositions reflect their generally basaltic parental compositions, either as basaltic parental melts or basaltic melt sources (e.g. Brophy, 2008). Their compositions vary according to the type of oceanic setting with, for example, many plagiogranites from ophiolites having distinctly higher Al_2O_3 , FeO and CaO and lower Na_2O and K_2O concentrations than plagiogranites from volcanic arcs, back-arcs and back-arc spreading centres. The plagiogranites from Loongana, in particular, resemble the low-K plagiogranites from ophiolites (Fig. 71). Oceanic leucogranites in ophiolite sequences are commonly intruded at or near the interface between the lower gabbroic sequence of the ophiolite stratigraphy and the overlying sheeted dyke complex.

In the case of the plagiogranites from the Madura Province, these typically high SiO_2 (>70 wt%) granites generally have similar to only slightly less radiogenic Nd isotope ratios to the gabbros they intrude, and their extremely low K_2O contents (mainly <1.0 wt%, but up to 1.6 wt%; see below) clearly indicates that any evolved component within the melting source of the granites itself had extremely low K_2O concentrations. Nevertheless, two plagiogranite samples with higher K_2O concentrations (~ 1.6 wt% K_2O) have clearly less radiogenic Nd isotope compositions ($\epsilon_{\text{Nd}} -1.5$ to -1.39) than their gabbro host ($\epsilon_{\text{Nd}} +1.33$) and the combined Loongana plagiogranite Nd isotope data shows a clear negative correlation with K_2O concentration (Fig. 102).

It was noted that in many cases the various plagiogranites from the Madura Province show closer compositional similarities with their gabbroic host rocks than with each other. This is also the case in terms of Nd isotope compositions, with granites and gabbros from Loongana generally being more radiogenic than granites and gabbros from Haig (Table 6). Although it is unlikely that the plagiogranites formed through melting of the gabbro body they intrude (the metamorphic grade of the gabbro clearly

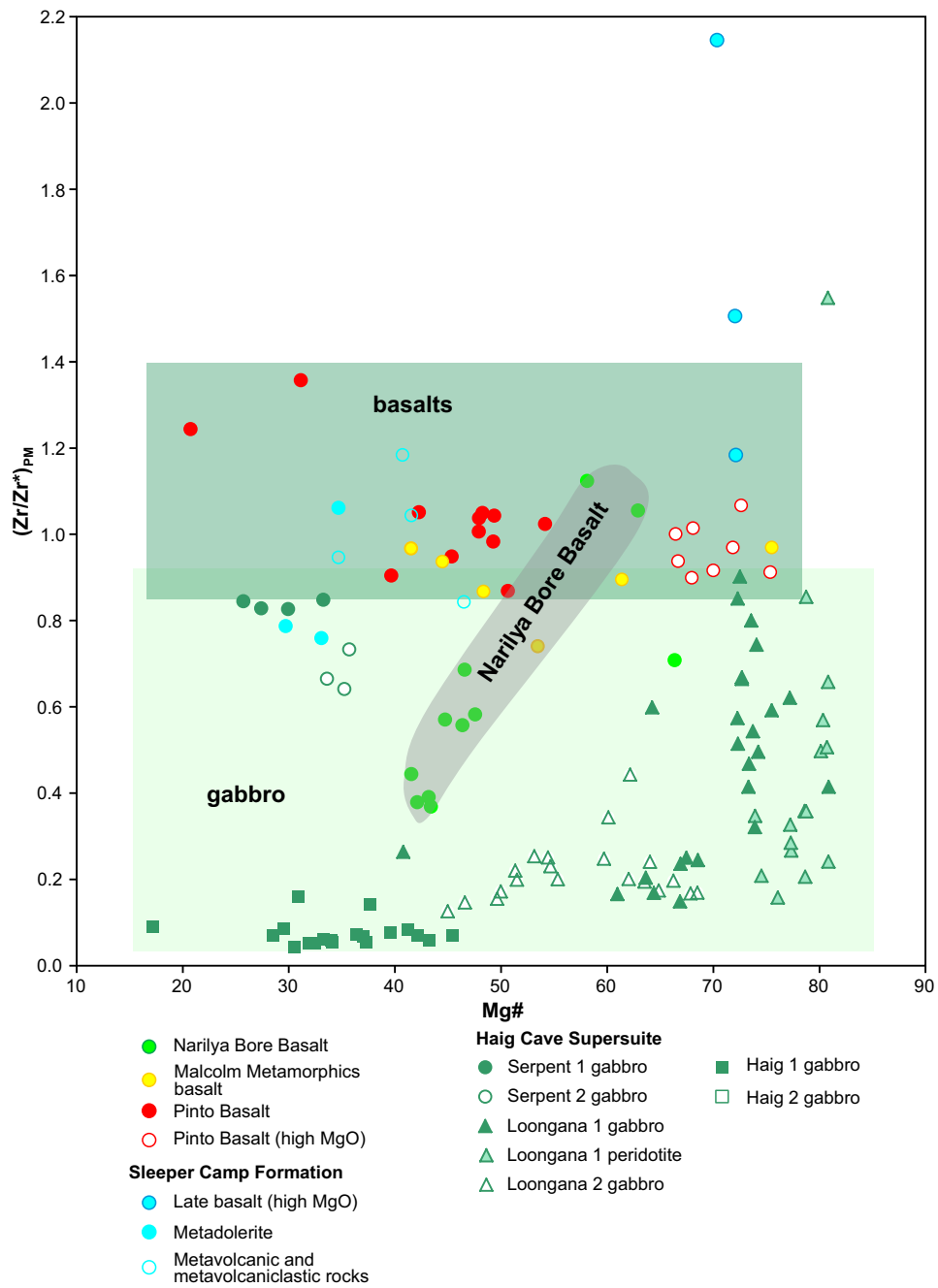


Figure 99. Variation in Zr/Zr^* (normalized to PM) with Mg# for mafic and ultramafic rocks of the Madura Province. $Zr^* = (Nd_{(PM)} + Sm_{(PM)})/2$

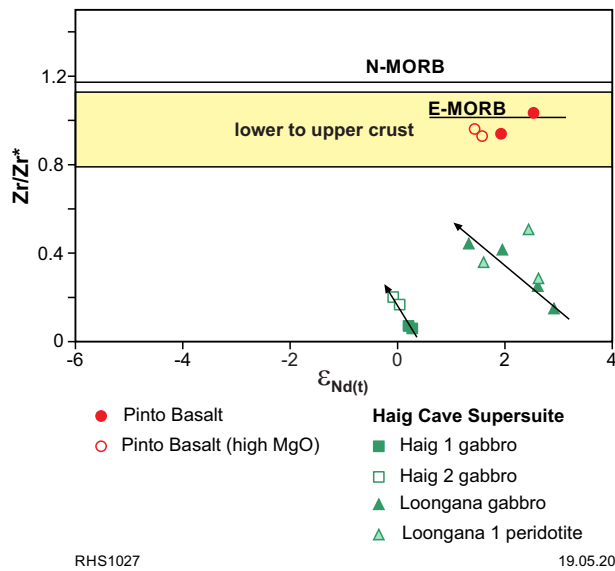


Figure 100. Variation in Zr/Zr* (normalized to PM) with $\epsilon_{Nd(t)}$ for mafic and ultramafic rocks of the Madura Province. $Zr^* = (Nd_{(PM)} + Sm_{(PM)})/2$

does not support this) it is possible that similar gabbros at depth may have partially melted or, more likely, that the gabbros are reasonably compositionally representative of the general mafic crust (i.e. melt source) of a given region. The typically very low K_2O concentrations, but accompanying trends in ϵ_{Nd} vs K_2O (Fig. 102), show that although the crustal melting source was mainly very low K_2O and mafic, it must also have included a small component of relatively K_2O -rich and relatively non-radiogenic crust (previously reworked juvenile/arc crust). It is also likely that any such component was very fusible (i.e. fertile) and so hence would be very overrepresented as a source component in the granites.

Hence, the data from the Loongana and Haig drillcores are best interpreted as indicating magma genesis within a c. 1400 Ma oceanic arc setting. This arc has been referred to as the Loongana Arc (Spaggiari et al., 2015a, 2018). The bulk source for all rocks studied here included an evolved component, most apparent within the source of the Loongana samples and particularly (or most obviously) within the source of a minor proportion of the Loongana plagiogranites, despite the interpretation that, in general, these plagiogranites closely match ophiolite plagiogranites. Much of the evolved component might simply be older arc crust. However, a ‘continental’ origin for some is also likely, particularly in view of the inherited and isotopically evolved zircon found in adakite from drillcore MAD002 to the west of the Loongana prospect. A small contribution of continental material to the bulk source of magma throughout the Madura Province is also required to satisfy Hf and Nd isotope trends (see Lu–Hf isotope geology, above). The Loongana Arc has been interpreted to have formed within a continental marginal basin, the Arid Basin, which formed through hyperextension of the Yilgarn Craton margin. Thus, in such a setting, the continental component could be explained as having been derived from the hyperextended crust, and/or from the sediments within the Arid Basin (Spaggiari et al., 2018).

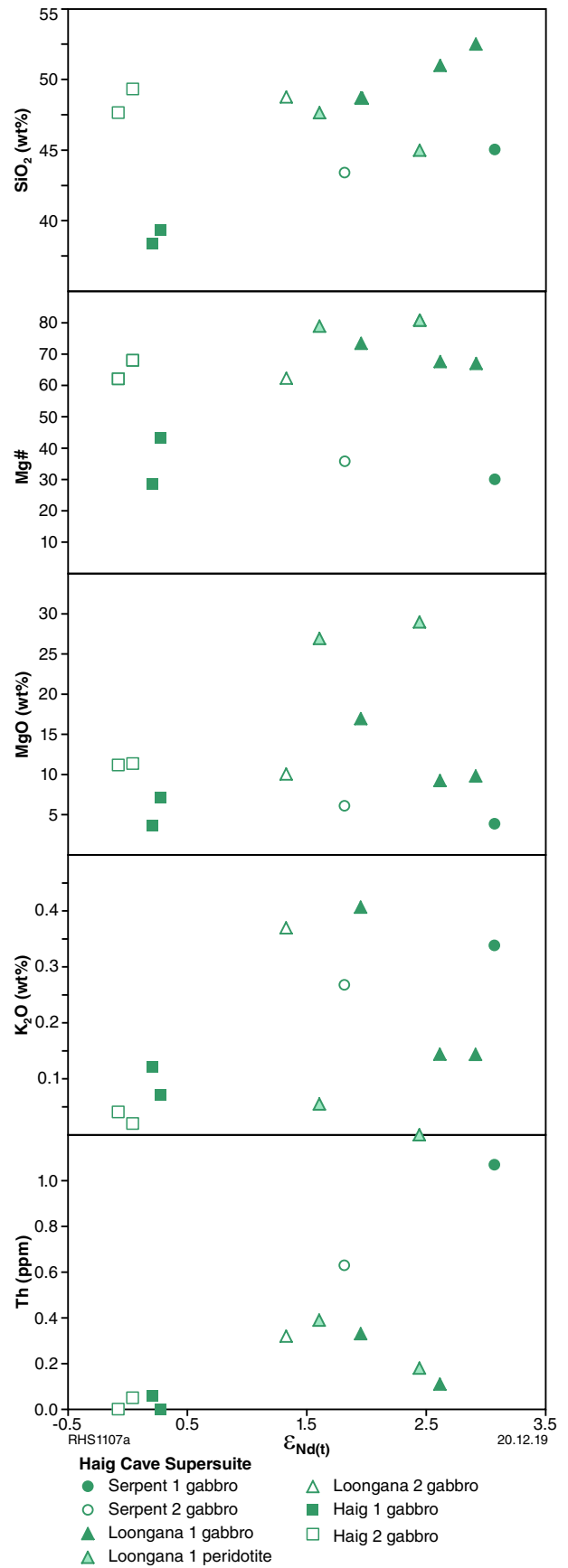


Figure 101. Variation in selected major and trace elements and Mg# with $\epsilon_{Nd(t)}$ for rocks of the Haig Cave Supersuite

Sleeper Camp Formation and the Malcolm Metamorphics

These two units have many similarities, but differ in their ages and relationships to granitic rocks (Tables 4, 5). The age of the Sleeper Camp Formation is constrained to be in the range 1536–1471 Ma (see Geochronology section), although crosscutting, highly altered, very fine-grained basalt could be younger. The mafic volcanic and volcanoclastic schist has a maximum depositional age of 1536 ± 13 Ma (GSWA 219093, Wingate et al., 2018g), providing a maximum age for mafic volcanism, and geochemically similar metadolerite is dated at 1479 ± 8 Ma (GSWA 219092, Wingate et al., 2018f). In contrast, the sedimentary component of the Malcolm Metamorphics has a maximum depositional age and dominant detrital zircon age component at c. 1470 Ma (GSWA 194867, Wingate et al., 2020a; GSWA 207001, Wingate et al., 2020c; Spaggiari et al., 2018). This dominant age component is similar to the magmatic crystallization ages for the Sleeper Camp Formation and those zircons were potentially sourced from these or similar rocks. This would suggest that the Malcolm Metamorphics are probably a bit younger than the Sleeper Camp Formation. A minimum age for the Malcolm Metamorphics is provided by metamorphism dated at 1315 ± 11 Ma (GSWA 194867, Wingate et al., 2020a), 1311 ± 4 Ma (monazite, Adams, 2012), and by Recherche Supersuite granite veins that cut folds at 1313 ± 16 Ma (Clark et al., 2000). Therefore, the age of the Malcolm Metamorphics basalt is bracketed between c. 1470 Ma, the maximum depositional age of the interlayered sediments, and 1315 Ma.

Early age constraints for the Sleeper Camp Formation were based on SHRIMP U–Pb zircon data for a sample previously interpreted as a migmatitic gneiss (GSWA 182485; Kirkland et al., 2012b). The sample yielded a weighted mean $^{207}\text{Pb}/^{206}\text{Pb}$ date of 1477 ± 4 Ma for 14 zircons, and dates of 2408–1531 Ma for seven zircon cores. Re-examination of the drillcore, further petrographic work and additional geochronology indicates that the felsic rocks are granitic veins, rather than migmatitic leucosomes, and the c. 1477 Ma date is interpreted as the age of igneous crystallization (Wingate et al., 2019). The date of 1477 ± 4 Ma is similar to the 1471 ± 5 Ma crystallization age of the granite vein sampled in GSWA 219094 (Wingate et al., 2018h). The older zircons in GSWA 182485 are similar in age to those found in the mafic volcanoclastic schist (GSWA 219093, Wingate et al., 2018g), indicating inheritance from the host rock.

Based on the rock relationships in the drillcore and similarity in geochemistry, the mafic volcanic and volcanoclastic schist and the metadolerite of the Sleeper Camp Formation are regarded as part of a single succession. The similarity in age of the granite veins that intrude these rocks suggests they are also part of the same event and are included in the same formation. The granite veins have low $\text{K}_2\text{O}/\text{Na}_2\text{O}$ ratios (<0.4), similar to the sodic plagiogranites of the Haig Cave Supersuite (Fig. 18), and in particular the adakite from drillcore MAD002, with which they also have textural similarities. In contrast, granitic veins that intrude the Malcolm Metamorphics are not part of the same succession, and are dated at

c. 1313 Ma (Clark et al., 2000). They are assigned to the Recherche Supersuite of the Albany–Fraser Orogen. Given that the Recherche Supersuite is unknown in the Madura Province (Fig. 8), this indicates that by this time, the Malcolm Metamorphics had been structurally displaced to within the vicinity of the Albany–Fraser Orogen.

The layered metasedimentary rocks of the Sleeper Camp Formation have variable compositions, including Fe-rich, BIF-like horizons and Mn-rich layers. These features are suggestive of a quiescent, below wave-base marine setting with low clastic input and associated with volcanism and exhalative hydrothermal activity. The jigsaw-fit breccia textures may indicate autobreccias formed by the deposition of mafic subvolcanic flows into the sedimentary pile. This would be consistent with the anomalous geochemistry of metasedimentary rock samples from magnetite-rich horizons with FeO from 40 to 48 wt%, MnO between 4.8 and 8.6 wt%, and >300 ppm Cu (GSWA 201271 and 201274; Appendix 7, Table A7.1).

Given the lithological and geochemical evidence that the Burkin prospect drillholes intersected subduction-modified MORB-like basaltic rocks and associated volcanoclastic units, possibly related to the early stages of development of the nearby Loongana oceanic arc, we suggest these Mn-rich ironstones are vent-distal, ocean-floor exhalative deposits. The Malcolm Metamorphics are also best interpreted as a succession of basalt and interflow sediments, and most likely include volcanoclastic rocks and pillow basalts deposited in a marine setting, although the water depth they formed in is uncertain. In summary, the basaltic successions of the Sleeper Camp Formation and Malcolm Metamorphics are interpreted as subduction-related assemblages formed in an oceanic environment.

Narilya Bore Basalt

Although considered to have formed in a similar subduction-related setting and time to the Malcolm Metamorphics and Sleeper Camp Formation, slight differences in the geochemical compositions of the Narilya Bore Basalt and its source components likely reflect its location well east of the Loongana oceanic arc, and in the vicinity of the Mundrabilla Shear Zone (Fig. 44, MAD011 drillcore). The geochemical compositions of the Narilya Bore Basalt, however, are significantly different to those of the c. 1144 Ma Kestrel Cavern Gabbro that intrudes it, supporting the view that the Narilya Bore Basalt formed much earlier, and possibly at c. 1400 Ma. This would be consistent with its metamorphic and structural character and indicates that the Narilya Bore Basalt was buried and deformed prior to intrusion of the Kestrel Cavern Gabbro.

Similar to the Malcolm Metamorphics and Sleeper Camp Formation, the Narilya Bore Basalt has HFSE ratios that suggest an N-MORB-like mantle source component, and elevated Th and LREE concentrations that require a crustal input (Fig. 56). The Narilya Bore Basalt differs, however, in showing a systematic trend to higher Th/Nb ratios with increasing Mg#, resulting in a trend on a Th/Yb vs Nb/Yb diagram consistent with progressive crustal contamination (Fig. 57). A similar trend is observed for V vs Ti, where Mg# decreases as the V/Ti ratio increases, which is suggestive of more arc-

like compositions (Fig. 103; e.g. Shervais, 1982). In the case of the Th/Yb vs Nb/Yb diagram (Fig. 57), this trend terminates at a Th/Nb ratio identical to those of the basaltic rocks of the Malcolm Metamorphics and Sleeper Camp Formation, and of the Haig Cave Supersuite gabbros. Whereas the trend indicates mixing between a mantle-derived (in this case N-MORB source) basalt and higher Th/Nb crust, that crust itself may have been slightly older oceanic arc crust. The Nd isotope compositions of the Narilya Bore Basalt ($\epsilon_{\text{Nd}(1400 \text{ Ma})} +1.02$ to $+1.14$) are within the range of the Haig Cave Supersuite gabbros ($\epsilon_{\text{Nd}(1400 \text{ Ma})} -0.1$ to $+2.9$), which is consistent with this view.

Formation of the lithological units of the Coompana Province

Protoliths in the five stratigraphic drillcores from the Coompana Province include compositionally variable but dominantly felsic to intermediate granitic rocks, some of which are now gneisses (Fig. 8). Also included are felsic metavolcanic rocks and mafic schists belonging to the Undawidgi Supersuite. Rocks assigned to the Moodini Supersuite are discussed in a separate section below — Moodini Supersuite high-KFe and high-KMg series intrusions — that covers both provinces.

Toolgana Supersuite

This supersuite is characterized by granite gneiss, and locally, diorite to amphibolite gneiss, with magmatic crystallization ages between 1613 and 1604 Ma (drillcores FOR004 and FOR008; Table 5; see Geochronology section above). Metamorphism is dated at 1179 ± 10 , 1153 ± 9 and 1151 ± 6 Ma, providing a minimum age for protolith formation.

Magmatism at c. 1610 Ma included co-genetic suites that cover an extended SiO_2 range. The mafic end-members are monzodiorite with high Mg# and high Cr and Ni concentrations reflecting compositions in equilibrium with mantle peridotite, and radiogenic Nd isotope compositions, combined with high LILE/HFSE and LREE/HFSE ratios that cannot be accounted for through contamination of known crustal components and more likely reflect a fluid-mobile, source-enrichment pattern. Thus, rocks of the Toolgana Supersuite are most likely subduction related. Rare zircon inheritance suggests the age of the crust they intruded was c. 1724 to 1671 Ma (or older if it was mafic and contained no zircon), but probably no older than c. 1950 Ma based on depleted mantle model ages. It was also isotopically juvenile. Isotope and zircon age data require that c. 1610 Ma basement occurs throughout the entire portion of the Coompana Province sampled by the stratigraphic drilling program (Fig. 3).

Geochemical and isotopic similarities with the c. 1633 to 1608 Ma St Peter Suite, situated along the southern and western edge of the Gawler Craton (Swain et al., 2008; Reid et al., 2019), permit the interpretation of a much more regionally extensive, primitive arc-related suite. Similar granite gneisses have been intersected in new drillcores from the eastern Coompana Province in

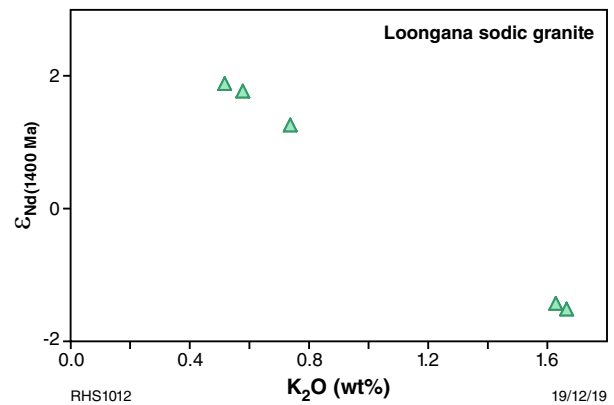


Figure 102. Variation in $\epsilon_{\text{Nd}(1400 \text{ Ma})}$ with K_2O for Loongana sodic granites

South Australia, dated at 1618 ± 6 and 1618 ± 9 Ma (Jagodzinski and Bodorkos, 2018). These rocks have been assigned to the Koomalboogurra Suite of the Toolgana Supersuite (Dutch, 2018; Wise et al., 2018b), extend the age range of the Toolgana Supersuite to 1618–1604 Ma, and confirm its significant extent. This indicates a major magmatic event at this time likely linked to subduction processes outboard of and on the margin of the Gawler Craton. The South Australian granite gneisses are slightly more evolved than the western counterparts ($\epsilon_{\text{Nd}(1620 \text{ Ma})} -2.97$ to $+1.76$ compared to $\epsilon_{\text{Nd}(1600 \text{ Ma})} -1.00$ to $+1.48$), contain similar rare inherited zircons dated at 1737–1701 Ma, and their protoliths are tentatively interpreted as formed in a back-arc setting adjacent to the continental margin of the Gawler Craton (Dutch, 2018). This magmatic event could indicate oceanic subduction directed towards the Gawler Craton margin, with the primitive arc-related intrusions preserved in the Western Australian samples, and remnants of the back-arc preserved in the South Australian samples. Alternatively, components of the magmatic arc closer to the Gawler Craton may have formed on extended continental margin basement (Reid et al., 2019). The Toolgana Supersuite has no counterpart in the Madura Province or the Albany–Fraser Orogen, forming at the end of the Biranup Orogeny (c. 1620 Ma), and as the Barren Basin was being superseded by the Arid Basin (Fig. 8).

Undawidgi Supersuite

The Undawidgi Supersuite is dominated by a variety of metagranites including metamonzogranites, metamonzodiorite and metasyenite (stratigraphic drillcores FOR010, FOR011 and FOR012). Drillcore FOR012 also contains mafic schist and a grey schist interpreted as a metarhyolite. The age range of the Undawidgi Supersuite is 1499–1479 Ma (Table 5, see Geochronology section).

Magmatic rocks of the Undawidgi Supersuite include ferroan compositions but are more typically magnesian. They all, nevertheless, show A-type, or less commonly transitional A-type, trace element characteristics. All require a significant crustal component within their bulk source, and the ferroan c. 1499 Ma felsic metavolcanic schist additionally requires a mantle component comprising upwelled asthenosphere. The Undawidgi

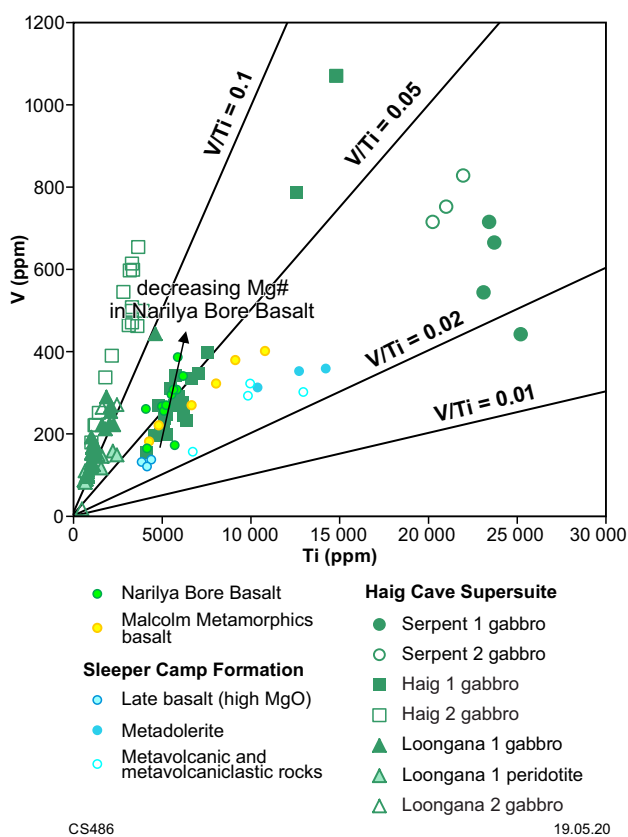


Figure 103. Comparison of V/Ti ratios for Haig Cave Supersuite mafic and ultramafic intrusions and for basaltic rocks of the Sleeper Camp Formation, Malcolm Metamorphics and Narilya Bore Basalt

Supersuite A-type magmas are interpreted to reflect extension of the 1724–1610 Ma arc-complex defined by the Toolgana Supersuite. Similar c. 1500 Ma rocks were intersected in the Mallabie 1 drillcore in the Coompana Province of South Australia (Wade et al., 2007), potentially recording the same extensional or rift-related event.

These rocks are slightly younger than the newly defined Bunburra Suite, intersected in drillhole CDP004 in South Australia, close to the border and just east of drillhole FOR008, dated at 1526 ± 5 Ma (Dutch et al., 2018). The Bunburra Suite is dominated by migmatitic, hornblende-biotite diorite gneiss with a broad SiO_2 range, and is isotopically juvenile ($\epsilon_{\text{Nd}(1520 \text{ Ma})} +1.28$ to $+3.46$; Dutch, 2018). Whole-rock geochemical data show they are magnesian, calc-alkalic to alkali-calcic, medium to high K, with enriched LILE and LREE and high LILE/HFSE ratios and are interpreted to have formed in a subduction setting (Dutch, 2018; Wise et al., 2018b). These compositions are similar in many respects to those of the mafic members of the older Toolgana Supersuite. Thus, the Bunburra Suite could indicate a continuation of the subduction event recorded by the Toolgana Supersuite, followed by extension and crustal thinning recorded by formation of the Undawidgi Supersuite. The spatial extent of drillholes FOR010, FOR011 and FOR012 suggest a large portion of the western Coompana Province was affected by this extensional event, corresponding to the northeasterly trending, significant gravity low in the hangingwall of the Tank and Mulyawara Shear Zones (Figs 10, 24, 26), and

a region of resistive crust defined in the magnetotelluric (MT) modelling along seismic line 13GA-EG1 (Fig. 104; Spaggiari et al., 2017a; Thiel et al., 2018).

Inherited zircons in Moodini Supersuite intrusions into the Undawidgi Supersuite in drillcores FOR010 and FOR011 are dated at (1σ) 1576 ± 19 , 1522 ± 16 and 1511 ± 18 Ma (GSWA 206753; Bottle Corner Shoshonite in drillcore FOR010), 1558 ± 21 Ma (GSWA 206752; syenogranite in drillcore FOR010) and between 1552 and 1462 Ma (GSWA 213838; monzogranite vein in drillcore FOR011). This record of zircon inheritance could indicate either a longer time span for Undawidgi Supersuite magmatism and related extensional events, or could suggest the c. 1526 Ma subduction-related Bunburra Suite is also present in this region, albeit including older occurrences.

Moodini Supersuite high-KFe mafic to felsic intrusions

Ferrogabbroic to granitic high-KFe rocks of the 1192–1127 Ma Moodini Supersuite are part of a regionally extensive, high-temperature event named the Maralinga Event by Spaggiari et al. (2016). Compositionally similar and broadly contemporaneous high-KFe magmas from the adjacent Musgrave Province (the 1220–1150 Ma Pitjantjatjara Supersuite; Howard et al., 2015) and Albany–Fraser Orogen (the 1200–1140 Ma Esperance Supersuite, but particularly the Booanya Suite; Smithies et al., 2015b) are considered part of the same event. This represents an extraordinarily large region of magmatism involving extremely high-temperature, lower crustal melting facilitated by crustal thinning and thermal and material input from shallow asthenosphere.

Unlike the Moodini Supersuite, the Esperance Supersuite preserves an isotopic and geochemical heritage of reworked Archean crust of the Yilgarn Craton (Kirkland et al., 2015; 2017; Smithies et al., 2015b). The eastern extent of the Maralinga Event appears to terminate at the western edge of the Gawler Craton, possibly coincident with the Jindargna Shear Zone (Fig. 10c; see also Pawley et al., 2018).

Madura Province

Based on the distinctive geophysical expressions of the high-KFe rocks, the Moodini Supersuite dominates much of the Madura Province (Figs 3, 10, 16, 17, 21). Here, the intrusions have an age range of 1182–1127 Ma, and include the c. 1144 Ma Kestrel Cavern Gabbro. The Hannah monzonite is assigned to the Booanya Suite of the Albany–Fraser Orogen, although it occurs within the Rodona Shear Zone and eastern boundary of the orogen. The youngest known Moodini Supersuite intrusion, dated at c. 1127 Ma, occurs at the eastern edge of the Madura Province within the Mundrabilla Shear Zone at the Moodini prospect (Figs 3, 21).

Apart from obvious major element differences (Fig. 75), the granitic rocks of Madura Province high-KFe series have strongly contrasting trace element compositions compared to the plagiogranites that form the other major felsic component of the province (see MORB-normalized patterns, Fig. 105). Such differences clearly reflect contrasting petrogenetic processes and possibly also slightly different source regions.

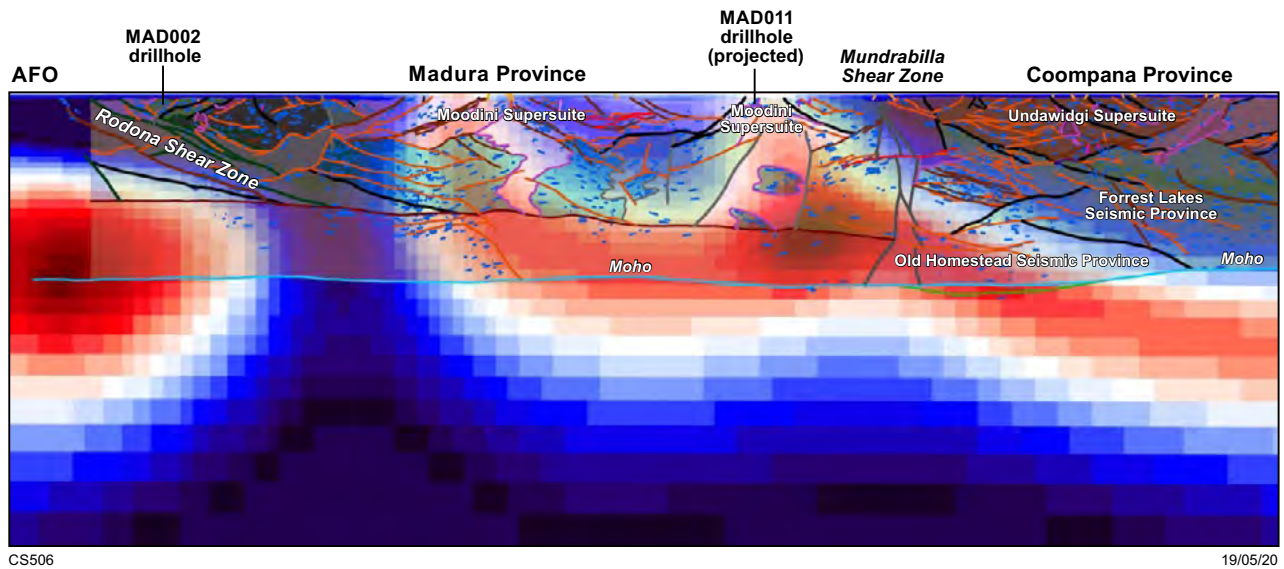


Figure 104. Section of modelled magnetotelluric data overlain with interpreted linework from merged seismic lines 12GA-AF3 and 13GA-EG1 (from Spaggiari et al., 2017a). See Figure 10 for linework details. Warm colours represent conductive features in the magnetotelluric data. Abbreviation: AFO, Albany–Fraser Orogen

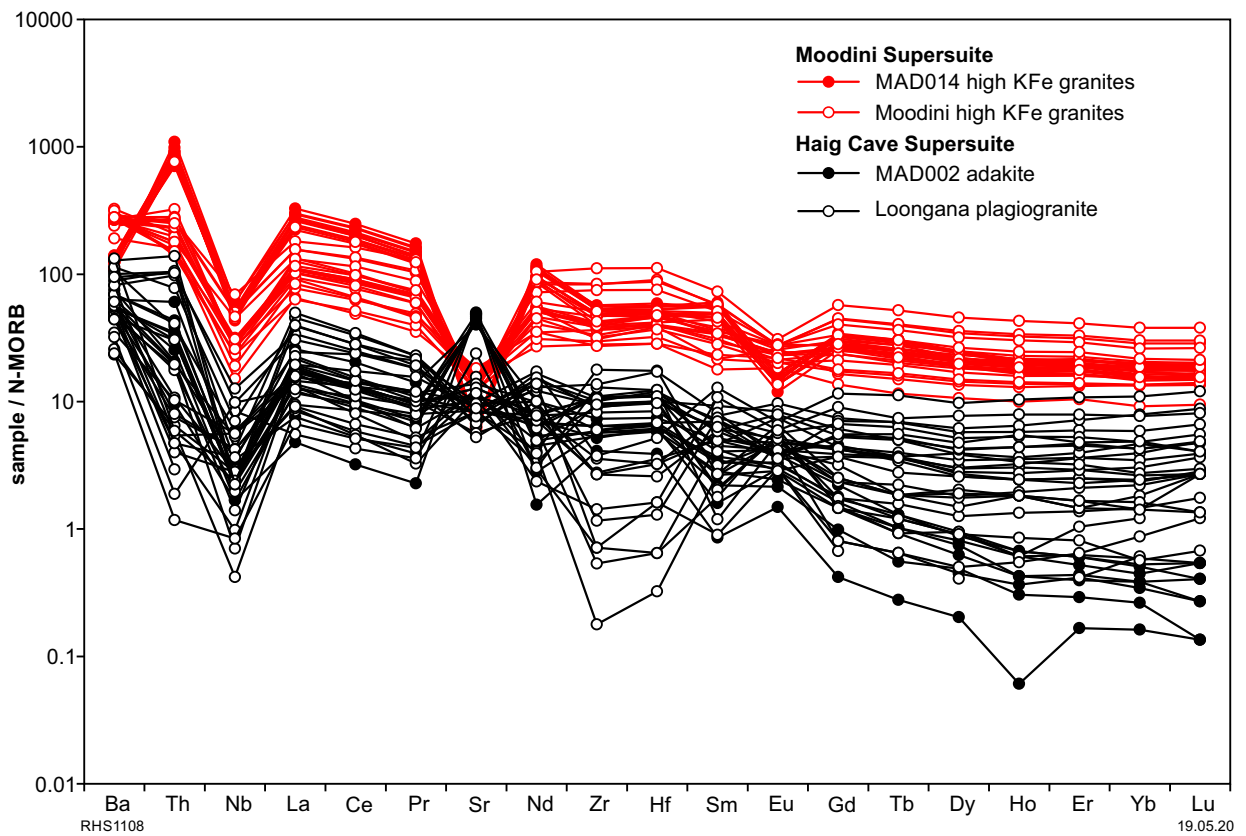


Figure 105. N-MORB normalized trace element spider diagram for the adakite and Loongana plagiogranites of the Haig Cave Supersuite and Moodini Supersuite granites from the Moodini prospect and drillcore MAD014, from the Madura Province (normalizations after Sun and McDonough, 1989)

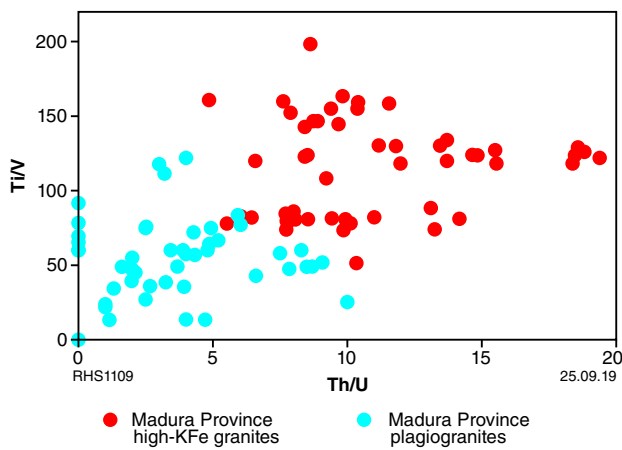


Figure 106. Variation in Ti/V vs Th/U for high-KFe granites and plagiogranites of the Madura Province

Available Hf and Nd isotope data show that the majority of the crust of the Madura Province was derived from a common, mafic source produced from c. 1950 Ma, which was variably recycled (most likely in subduction settings) and replenished through subsequent mantle additions (most likely through back-arc spreading), but was isolated from significant contributions from ‘continental’ sources. However, although the ultimate source for both the c. 1400 Ma plagiogranites and the high-KFe rocks might be similar (mainly c. 1950 Ma oceanic crust), the history of that source prior to melting might have differed. For example, the two series form distinct fields on a Th/U vs Ti/V diagram (Fig. 106). Because both U and V are more incompatible at higher oxidation states, these relationships might indicate that, at the time of melting, the source for the high-KFe group was more reduced than the source for the plagiogranites.

The high-Fe, -Ti, and -P character of the Kestrel Cavern Gabbro and Hannah monzonite (Figs 61 and 66) also contrasts with other gabbroic rocks of the province. The primary mineralogy of the Kestrel Cavern Gabbro included orthopyroxene and possibly also pigeonite. These compositions and mineralogy are characteristic of high-temperature, Fe-rich orthopyroxene–monzonite (jotunite) suites (Duchesne and Wilmart, 1997). Similar mafic high-KFe series rocks are relatively rare, except in some Grenvillian-aged Mesoproterozoic terranes, where they are intimately associated with massif-style anorthosite batholiths and with charnockitic A-type granites (the anorthosite–mangerite–charnockite [AMC] suite; e.g. Vander Auwera et al., 1998; Bogaerts et al., 2006; Duchesne et al., 2006). The Madura jotunitic rocks are associated with A-type granites (i.e. the felsic high-KFe rocks) although they lack any association with anorthosite. However, high-KFe, charnockitic A-type granites occur elsewhere with no obvious connection to either anorthosite or jotunite (e.g. west Musgrave Province; Smithies et al., 2011; Howard et al., 2015). The mineralogy (orthopyroxene–pigeonite) of the mafic end-members of the Madura high-KFe series, and zircon-saturation thermometry on the felsic rocks, point to very high melting temperatures (>900°C) under dry and relatively reducing conditions. Although very rare, high-KFe series rocks are very compositionally distinctive, and in all known occurrences, similarly high

crustal melting temperatures (e.g. >1000°C; Kilpatrick and Ellis, 1992) have been determined or inferred. In the case of high-KFe series rocks of the Musgrave Province, crustal melting was synchronous with long-lived (>80 million years) ultrahigh-temperature metamorphism involving regional lithospheric removal (Smithies et al., 2011). Volcanic equivalents to the high-KFe series granites include continental latites genetically related to flood basalts (e.g. the Mesozoic Karro latites of South Africa; Kilpatrick and Ellis, 1992) and whether related to anorthosites or not, there appears to be a potential link with continental flood basalt style magmatism (e.g. Bogaerts et al., 2006).

In the absence of any link to AMC-style suites (including massif-style anorthosites), it is most likely that the jotunite to A-type granite high-KFe series in the Madura Province involved reworking of evolved mafic crust associated with significant juvenile mantle input. As outlined above, evidence from Hf and Nd isotope trends is that the mafic crustal component was primarily the same isotopically juvenile crust (i.e. ultimately the c. 1950 Ma oceanic crust; Kirkland et al., 2017) formed during the earlier evolution of the Madura Province. However, whereas all magmatic rocks from the Madura Province fall within a common Nd isotope array, the high-KFe series lie at the lower (non-radiogenic) part of the array whereas basalts and gabbros from the Madura Province mostly lie in the upper half, more or less separated by the plagiogranites, with considerable overlap (Fig. 107). This requires an additional, small, high-K₂O component with non-radiogenic Nd in the source of the high-KFe series (cf. the basalts, gabbros and plagiogranites). This might be the same evolved component required to explain the isotope compositions of some of the Madura Province plagiogranites. It is unlikely that the plagiogranite-rich crust itself formed the evolved component because many of the plagiogranites have Sm/Nd ratios that are too low to account for the Nd isotope evolution paths of the high-KFe series (Table 6). Nevertheless, the evolved component might reflect exotic crust (e.g. Albany–Fraser Orogen continental slithers residual in the lithosphere or forming components contributing to the material being subducted) or it might reflect broadly ‘cognate’ crust (i.e. the same 1.9 – 1.6 Ga juvenile addition) that was reworked at some earlier stage to acquire high Sm/Nd ratios. Reworking of E-MORB – OIB crust similar to the Pinto Basalt is not a viable option, at least in the case of the more primitive Kestrel Cavern Gabbro, because these high-KFe samples are less enriched in (for example) K and Rb than the basalts themselves. This is reasonable on the grounds that the E-MORB – OIB crust represented by the Pinto Basalt is still preserved, and has not been subducted.

It was also noted above that rocks of the high-KFe series show regional compositional variation and this is also the case in terms of their Nd isotope compositions (Table 6). Rocks of the Boanya Suite (part of the Esperance Supersuite, e.g. Hannah prospect; Fig. 3), marginal to the Madura Province, are, at 1200 Ma, less radiogenic ($\epsilon_{Nd} -7.34$ to -4.95) than those from drillcore MAD014 ($\epsilon_{Nd} -4.8$ to -3.7), which are less radiogenic than rocks from the Moodini prospect and also the Kestrel Cavern Gabbro ($\epsilon_{Nd} -2.7$ to -1.85). This represents a systematic west-northwesterly increase in the proportion of non-radiogenic source material, a trend continued into the eastern Nornalup Zone of the Albany–Fraser Orogen

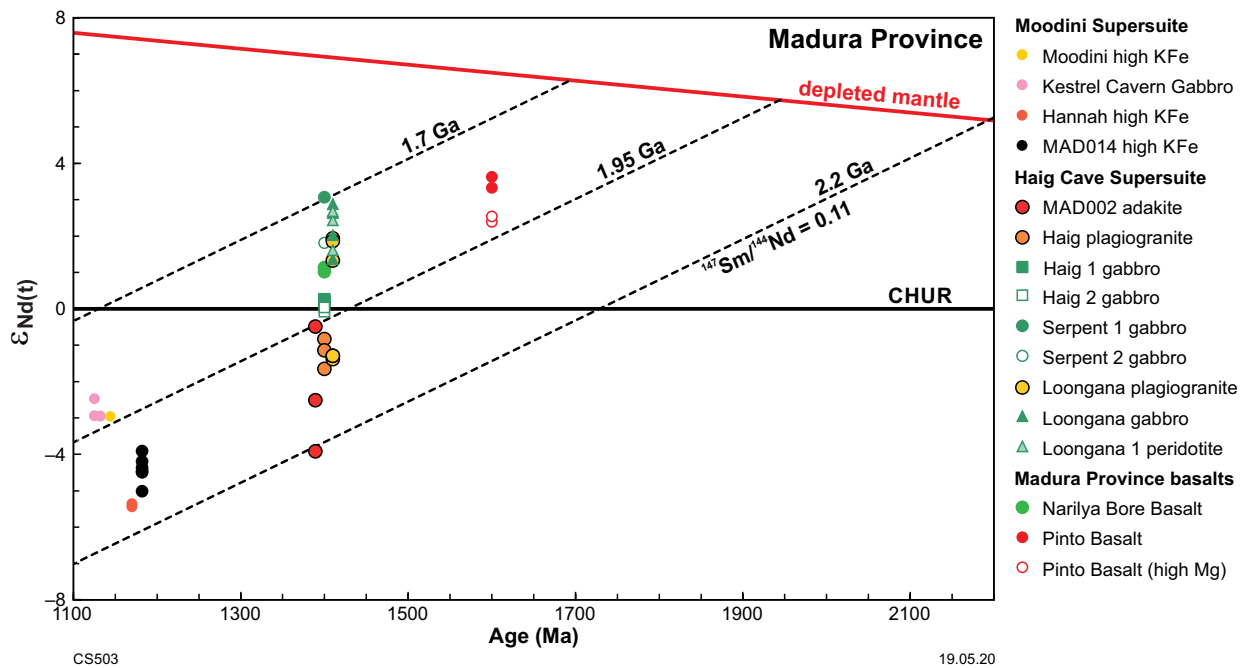


Figure 107. Nd isotope diagram for the Madura Province plotted from the data in Table 6

(Smithies et al., 2015b). These variations may also reflect a gradual east-southeastwards dilution of non-radiogenic Albany–Fraser Orogen crust by juvenile, mantle-derived material. It is also interesting to note that the more juvenile magmatism in the east-southeast of the Madura Province (Kestrel Cavern Gabbro in drillcore MAD011 and the Moodini prospect) is significantly younger (1144–1127 Ma) than magmatism to the west-northwest (drillcore MAD014 to the Booanya Suite occurrences: 1182–1170 Ma). A similar compositional trend with decreasing age was noted for the high-KFe magmas of the Musgrave Province (Smithies et al., 2011), again reflecting a greater mantle contribution with decreasing age.

Coompana Province

Moodini Supersuite intrusions in the Coompana Province have an age range of 1192–1140 Ma, slightly older than that found in the Madura Province. Magmatism during this period is diverse, ranging from in situ anatexitic melting of basement to the southeast (drillcores FOR004, FOR008) to higher degree melting and melt migration of sodic granites in the northwest (drillcores FOR010, FOR011). Also, in the northwest, extensive partial melting of lithosphere, significantly enriched during formation of the 1724–1610 Ma (or older) arc complex, resulted in voluminous mafic–felsic shoshonitic magmatism.

High-KFe rocks are found in stratigraphic drillcores FOR010 and FOR011, from the northwestern Coompana Province. However, the Moodini Supersuite has been shown to be regionally extensive within the province. In South Australia, monzogranite drill cuttings were sampled from the base of the Mulyawarra 1 petroleum well at 2682–2691 m depth, in the northern part of the Coompana Province adjacent to the Nawa Domain of the Gawler Craton. Zircons extracted from this sample record a magmatic crystallization age of 1168 ± 6 Ma, and interpreted inheritance at 1615–1530 Ma (Neumann and Korsch, 2014).

The most striking occurrence of Moodini Supersuite intrusions in the Coompana Province is the belt of northeasterly trending, high magnetic intensity plutons that occur southeast of the Border Shear Zone, extending into South Australia (Figs 3, 10, 24; Spaggiari et al., 2012). The pluton belt is truncated by the Mundrabilla Shear Zone, where the plutons are elongated with sinistral shear sense. These plutons were intersected by the Eucla No. 1 petroleum well and drill cuttings from its base were dated at 1140 ± 8 Ma (Kirkland et al., 2011c). In South Australia, recent work has confirmed similar-age rocks in new drillcores that have intersected the pluton belt to the northeast (Dutch et al., 2018; Jagodzinski and Bodorkos, 2018). Drillholes CDP003 and CDP005 intersected massive porphyritic monzogranitic to syenogranitic intrusions of the Koonalda Suite, and megacrystic monzogranite from CDP005 yielded an igneous crystallization age of 1148 ± 7 Ma (Dutch, 2018; Jagodzinski and Bodorkos, 2018). In drillhole CDP001, which lies on the southeastern edge of the pluton belt, equigranular monzogranite sheets are dated at 1141 ± 15 Ma, interpreted as coeval with metamorphism and development of the gneissic fabric in host Toolgana Supersuite granite gneiss (Dutch, 2018; Jagodzinski and Bodorkos, 2018). These new data confirm the extent of this strongly magnetic pluton belt, apparently dominated by 1150–1140 Ma intrusions.

Moodini Supersuite high-KMg series

Rocks with shoshonitic composition form a major component of drillcores FOR010 and FOR011 and are divided into mafic and felsic groups. The mafic group has compositions reflecting equilibrium with peridotitic mantle and are strongly enriched in incompatible trace elements (Figs 81, 82, 85). The felsic group shows slight enrichments in TiO_2 and P_2O_5 compared with all other

FOR-prefix granites (except those with A-type affinity) at similar SiO₂ levels, have higher Mg# (53–33) than most Coompana Province granites, are distinctly magnesian and alkali-calcic to alkali and straddle the shoshonite series high-K boundary (Figs 80–82). Compared to other Coompana Province granites at similar SiO₂ values, the felsic shoshonites are also enriched in LILE (except Rb), Zr and Hf (but not Nb and Ta) and LREE (but not HREE) and hence show the same enrichment patterns as the mafic shoshonites.

The Dy/Yb ratios for the mafic shoshonite group are high but decrease rapidly with increasing SiO₂, suggesting a strong role for hornblende fractionation, but Eu/Eu* ratios remain constant at ~1.0 – 0.8 (Fig. 85), suggesting either relatively oxidized (and possibly wet) conditions or no feldspar fractionation, or all of these. The high La/Yb, Dy/Yb, Sr/Yb ratios and low Yb support a deep melting source with residual garnet, but not plagioclase or strong metasomatic enrichment of the source in LILE and LREE. The evidence for wet and oxidized magmas favours an amphibolite or garnet amphibolite source rather than an eclogite. Scattered, but decreasing, La/Nb and Th/Nb with increasing SiO₂ or decreasing Mg# are inconsistent with a direct crustal contribution (e.g. AFC) to the mafic shoshonites.

Models for shoshonite petrogenesis typically emphasize post-orogenic extensional melting of subduction-modified lithosphere as a result of upwelling asthenosphere. The extent to which the asthenosphere supplies material (melt), or just heat, is unclear. Nd isotope data for the mafic Bottle Corner Shoshonite ($\epsilon_{Nd(1180\text{ Ma})}$ -2.39 to +0.21; Fig. 108, Table 7) appears to require a source component slightly more radiogenic than any sampled FOR-prefix material at c. 1200 Ma (Fig. 89), and slightly more radiogenic than bulk Earth — that is, likely an asthenospheric component. Nevertheless, any asthenospheric material contribution is likely to have been greatly exceeded by melting of a less radiogenic mafic lithospheric melt component, candidates for which include the source of subduction-derived c. 1610 Ma

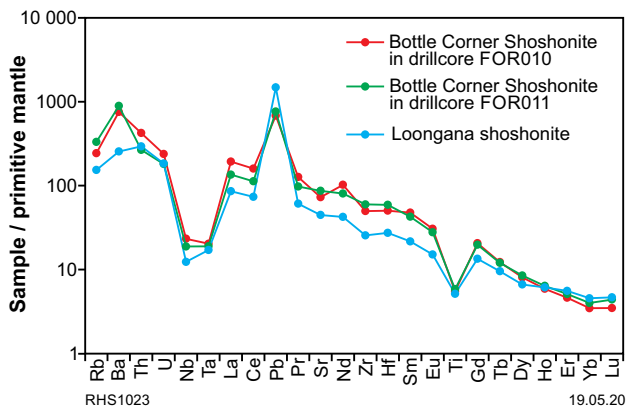


Figure 109. PM-normalized trace element spider diagrams comparing shoshonites of the Coompana Province with rare shoshonite from the Madura Province (normalizations after Sun and McDonough, 1989)

Toolgana Supersuite monzodiorite. The less radiogenic Nd isotope compositions of the felsic shoshonites are consistent with the presence of inherited zircons, but there is no clear correlation between SiO₂ and ϵ_{Nd} that would indicate significant contamination or AFC-style processes.

Mafic shoshonite also forms a minor component of the Loongana prospect drillcores in the Madura Province where it cuts the c. 1400 Ma Haig Cave Supersuite. Compared with the Bottle Corner mafic shoshonites, the Loongana prospect shoshonites are less enriched in TiO₂ and P₂O₅, and in the range of typically incompatible trace elements, except the HREE (Fig. 109). The lower La/Yb, Dy/Yb and Sr/Y (36 cf. 65) associated with the Loongana prospect shoshonites possibly indicate derivation from thinner crust and the different trace element concentrations (at equivalent MgO and Mg#) reflect a less subduction-modified source.

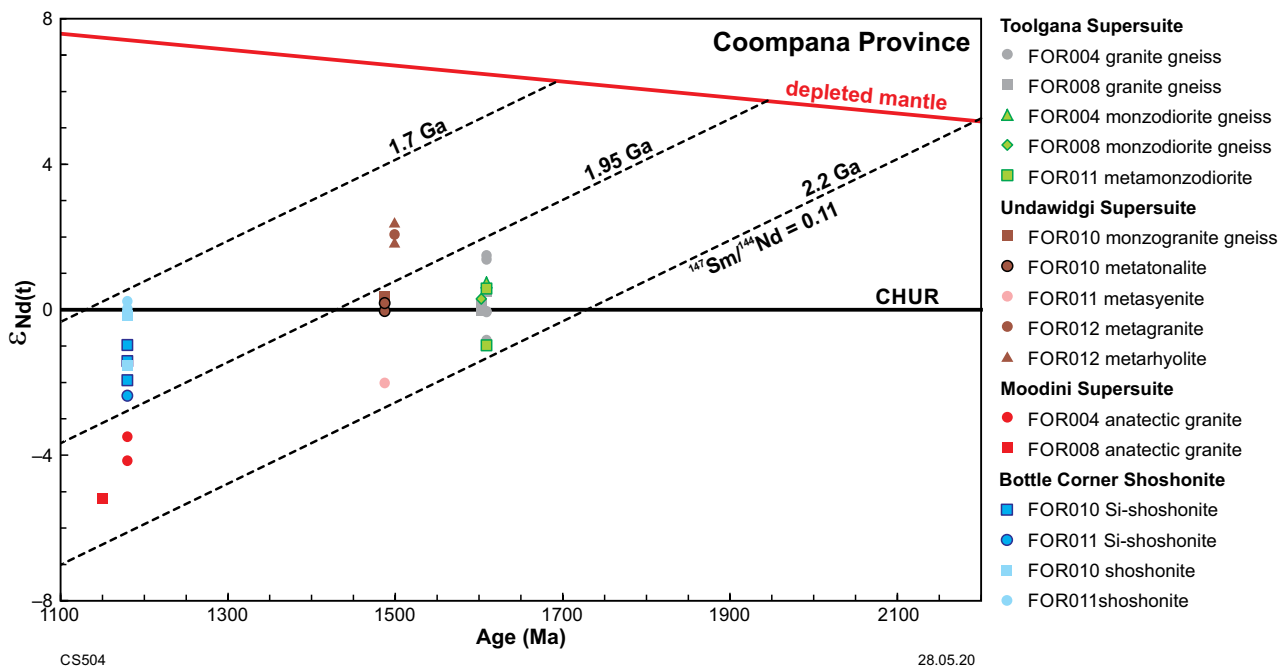


Figure 108. Nd isotope diagram for the Coompana Province plotted from the data in Table 7

As was also the case for the high-KFe Moodini Supersuite rocks, recent work has confirmed the presence of rocks of similar age and chemistry to the Moodini high-KMg rocks in South Australia (Dutch, 2018; Jagodzinski and Bodorkos, 2018). In drillcore CDP004, quartz metasyenite assigned to the Merdayerrah Shoshonite intrudes the c. 1526 Ma Bunburra Suite and yielded an igneous crystallization age of 1174 ± 9 Ma (Jagodzinski and Bodorkos, 2018). The Merdayerrah Shoshonite is geochemically very similar to the Bottle Corner Shoshonite intersected in the western Coompana Province (Dutch, 2018). However, the Merdayerrah Shoshonite is slightly more evolved ($\epsilon_{\text{Nd}(1170 \text{ Ma})} -3.14$ to -2.47 ; Dutch, 2018) than the Bottle Corner Shoshonite ($\epsilon_{\text{Nd}(1180 \text{ Ma})} -2.39$ to $+0.21$).

Comparisons of magmatic evolution between the Madura and Coompana Provinces

Both the Madura and Coompana Provinces are isotopically similar and, at c. 1.95 Ga, were essentially entirely isotopically juvenile (see below). Geochemical, and Hf and Nd isotope data indicate that juvenile, depleted mantle material was periodically added to the crust (known occurrences at c. 1610, 1490, 1400 and 1180 Ma). However, the compositional evolution does not require the addition of, or contribution from, significant volumes of older, non-radiogenic sources, and the only physical evidence for such material is in the form of rare inherited zircons, mainly in samples from areas proximal to cratonic boundaries (e.g. the Rodona Shear Zone). In all of these regards, the Madura and Coompana Provinces are indistinguishable from the Musgrave Province, to the northeast. However, although the Madura and Coompana Provinces potentially formed from the same piece of crust, they are lithologically and geochemically very different, reflecting very different histories and their separation by the Mundrabilla Shear Zone (Fig. 8).

The Coompana Province underwent early and probably multiphase subduction recycling, potentially starting at 1720 Ma (or before) and extending to at least c. 1610 Ma, synchronous with juvenile magmatism along the southwestern Gawler Craton. Although high-KFe components of the Moodini Supersuite do occur, a notable feature of a large proportion of Coompana Province magmatism, at all ages, is the dominant volumes of magnesian and very likely subduction-related (or recycled subduction-related) felsic material. No equivalents are found in the Madura Province, except perhaps in the smaller-volume plagiogranites of the Haig Cave Supersuite, and the rare shoshonites at Loongana. Hence, the Coompana Province underwent early subduction–accretion and developed a thick, enriched and hydrated lithosphere. The occurrence of high-KFe magmatism at 1190–1180 Ma indicates a regional high-temperature event, but magmatism at this time is both high-KMg and high-KFe. The high-KFe magmatism probably reflects regions where the thick lithospheric mantle was significantly thinned, or removed, whereas the high-KMg shoshonitic magmatism probably represents deep melting of the older subduction-metasomatized lithospheric mantle.

In contrast with the Coompana Province, the Madura Province appears to have recorded less magmatic activity between c. 1950 and 1500 Ma. It remained

oceanic- to oceanic arc-like in nature, and generally more ‘tholeiitic’ in character until a very late stage when, at c. 1480 Ma, oceanic subduction was initiated, as indicated by the Sleeper Camp Formation (Spaggiari et al., 2018). The lithosphere either remained thin or was removed at c. 1180 Ma, so a ‘tholeiitic’ asthenospheric component plays a much greater role in c. 1180 Ma magmatism, which is high-KFe rather than high-KMg.

Hf isotope evolution of the Madura and Coompana Provinces

The Hf isotope data from dated zircons from magmatic rocks of the Madura and Coompana Provinces are dispersed along a broad array intersecting depleted mantle at 1.7 – 2.0 Ga with occasional more juvenile components, most notably at c. 1.4 Ga (Fig. 110). Despite distinct differences in the ages of these magmatic rocks prior to the formation of the Moodini Supersuite (Fig. 8; see also Dutch et al., 2018), the broad isotopic evolution pattern in both provinces is strikingly similar, with the implication being that they shared development from the earliest crust (Fig. 110; Kirkland et al., 2017). The oldest rocks sampled in the Coompana Province (Toolgana Supersuite) lie along a similar $^{176}\text{Hf}/^{177}\text{Hf}$ age array as most of the igneous rocks of the Madura Province. This isotopic similarity is even more pronounced if only the Moodini Supersuite is considered. The $^{176}\text{Hf}/^{177}\text{Hf}$ age array defined by the Coompana and Madura Provinces is also very similar to the spread of corresponding age-equivalent data from the Musgrave Province, which projects to an apparent fractionation event at c. 1950 Ma (Kirkland et al., 2013a; 2017). In contrast, both Hf and Nd isotope evolution patterns of the Coompana and Madura Provinces are dramatically different to those of the Albany–Fraser Orogen, in which the oldest evolutionary arrays stretch well back into the Archean, consistent with a connection between the Albany–Fraser Orogen and the Yilgarn Craton (Kirkland et al., 2011b; 2015).

Based on both Nd and Hf isotope data, it can be shown that multiple phases of magmatism throughout the Musgrave Province and Madura and Coompana Provinces reflect a geographically continuous belt over a large region that to varying degrees consists of new asthenospheric melt and primordial lower crustal material (relict oceanic lithosphere) that was initially produced during a 1.9 Ga fractionation event (Kirkland et al., 2013a; 2017). Much of the melt source in the Madura and Coompana Provinces was oceanic crust, either generated at 1.9 Ga or thereafter, that was modified through partial melting and additional mantle fertilization during convergence of the WAC and SAC. A fundamental observation on the Coompana and Madura datasets is the significant absence of old evolved crust, with magmatism repeatedly driven by new depleted mantle addition, and reworking of the preceding periods of MORB-like input, commencing at c. 1.9 Ga. Only minor amounts of evolved material are present, which stands in stark contrast to the Albany–Fraser Orogen. This evolved material may reflect the influence of minor isolated crustal slivers on a hyperextended margin, or less likely, the denuded and transported erosion product of the surrounding Archean Cratons worked into the crustal melt column in the intervening ocean realm.

Magmatism within the 1950–1900 Ma time interval is globally significant in terms of juvenile magmatism. However, in an Australian context, igneous rocks of this age are very rare, and the legacy of this period is retained mainly in cryptic isotope trends of the northern Gawler Craton margin, the Musgrave Province, Rudall Province, and Madura and Coompana Provinces. Linking of the isotope signatures of these regions has been proposed to delineate an ancient ocean, named the Mirning Ocean, and its subducted and underplated equivalents (Kirkland et al., 2017). Global Nd and Hf datasets support the interpretation of widespread crust production in response to global-scale changes in plate geometry, as juvenile crustal fragments were swept into the supercontinent Nuna at this time. Kirkland et al. (2017) noted that the c. 1950 Ma Nuna-forming ocean(s) represent the first globally significant oceanic crust whose destruction remains widely recorded in the upper crustal record, and which may have ushered in the onset of ordered spreading centres and reflect the emerging dominance of crust formation through modern-style plate tectonic processes.

Structural evolution and crustal architecture

In this section, structural data from the drillcores are combined with interpretations from geophysical data to examine the structural evolution of the region. The structural and magmatic evolution of the both the Madura and Coompana Provinces and also the Albany–Fraser Orogen are considerably different from each other, supporting the view that the Mundrabilla and Rodona Shear Zones are crustal-scale features that have a history of significant displacement.

Structural interpretation of the Madura Province

The interpretation of the structural evolution of the Madura Province is based on aeromagnetic, gravity and seismic data, and drillcore analysis (see Madura Province drillcores, above, and Appendix 2). Aeromagnetic and gravity data have revealed the presence of complex structures within the Madura Province (Figs 3, 21, 44). The region is dominated by a series of northeast-trending folds, locally disrupted by intrusions of Moodini Supersuite. The folds are denoted in the aeromagnetic data by distinctive striated banding interpreted to represent dominantly metavolcanic and metasedimentary rocks related to the Pinto Basalt and Sleeper Camp Formation (Figs 17, 21). In contrast, the strong gravity response of the Haig Cave Supersuite clearly shows that this unit is discontinuous, in part disrupted by younger intrusions of the Moodini Supersuite during the Maralinga Event, but also likely due to infolding with the Pinto Basalt and Sleeper Camp Formation. The folded, striated banding visible in the aeromagnetic data is folded in a similar fashion to the steeply northeast-plunging, second-generation folds described in the MAD002 drillcore that affect both the Pinto Basalt and the Haig Cave Supersuite adakite veins (see Stratigraphic drillcore MAD002, above). Haig Cave Supersuite adakite veins that crosscut the folded layering (Fig. 19a) are mainly injections subparallel to the fold axes

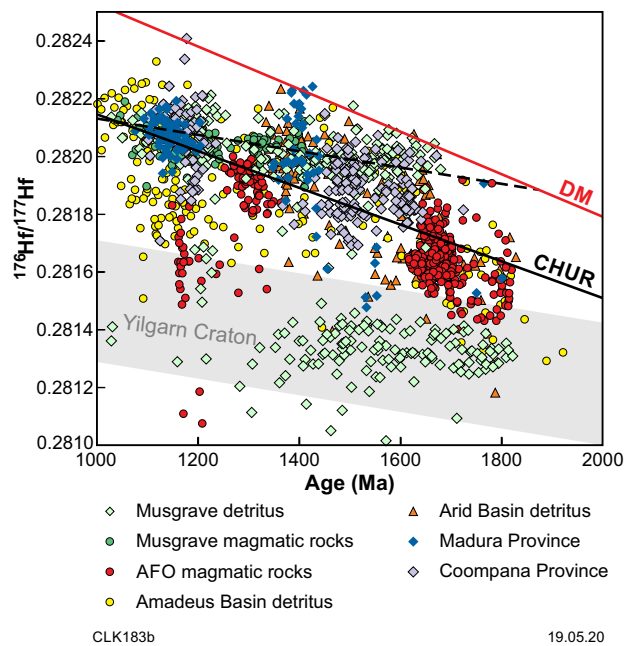


Figure 110. Hf evolution diagram for the Madura and Coompana Provinces compared to the Albany–Fraser Orogen, Musgrave Province and adjacent sedimentary basins. The Yilgarn Craton field is shown in grey (Kirkland et al., 2017). Dashed line shows the intersection of the broad array with depleted mantle (DM). Datasets included in this plot: GSWA GeoVIEW.WA (www.dmirns.wa.gov.au/geochron); Musgrave Province (Smithies et al., 2011); Albany–Fraser Orogen (Kirkland et al., 2011a,b); Arid Basin (Spaggiari et al., 2015a); Amadeus Basin (Haines et al., 2016)

or layering and could indicate stretching and boudinage as the F_2 folds formed. If this is the case, the best estimate for the timing of the northeasterly trending fold event is the age of the adakite itself, 1389 ± 7 Ma (Table 5; GSWA 206754). The axially planar, S_2 foliation is hornblende bearing and likely formed close to this time, and at the metamorphic peak.

In the aeromagnetic data, the northeast-trending folds are interpreted to be refolded into open, approximately orthogonal, west-northwesterly trending third-generation folds (F_3) forming Type-2 fold interference patterns (Ramsay, 1962) in both the Pinto Basalt and Sleeper Camp Formation. These patterns extend over the region within the hangingwall of the Rodona Shear Zone and as far east as the Serpent Shear Zone, which corresponds to the region of emplacement of the Arubiddy Ophiolite Complex above the continental margin (see Arubiddy Ophiolite Complex, below; Figs 10a, 17). In the seismic section, the apparent west-dipping reflectors in the Pinto Basalt, and structurally below as far as the Sunrise Shear Zone, are interpreted as the side view of the enveloping surface of an F_3 hinge zone. Both the Sunrise and Anniversary Shear Zones are also folded about the F_3 hinge zone (Figs 10a, 17). Smaller, upright folds are visible in this unit, and also within the mainly flat-lying reflectors of the Haig Cave Supersuite.

North of the MAD011 drillhole, which contains xenoliths of the Narilya Bore Basalt, the aeromagnetic data contains extensive areas that also display a folded, striated pattern suggestive of the presence of metavolcanic

and metasedimentary rocks. This area is dominated by northeasterly trending folds similar to the F_2 folds described above in the Pinto Basalt, and interpreted in the Sleeper Camp Formation and Haig Cave Supersuite in the vicinity of the Loongana prospect (Figs 21, 44). Therefore, it is likely that this northeasterly trending fold event was regional in scale and may have affected the entire Madura Province prior to the Maralinga Event. The geodynamic setting for this event likely relates to convergence and the initiation of accretion of the Loongana Arc onto the continental margin (Fig. 111).

In structural terms, this regional event is interpreted as an early phase of widespread, north-northeasterly trending tight folding refolded by west-northwesterly trending, upright to inclined, open folding that appears to have been more restricted to the region above the continental margin. If the F_3 orthogonal folding and Type-2 fold interference occurred at a similar time, a major reorientation of the stress field or block rotation must have occurred. However, the only constraint on the timing of the orthogonal F_3 folding is a minimum age provided by the crosscutting 1192–1125 Ma Moodini Supersuite intrusions (Fig. 17).

The region of Type-2 fold interference above the continental margin is markedly different in style to the fold structures observed within the eastern Nornalup Zone of the Albany–Fraser Orogen, and also those within the Malcolm Metamorphics. The Malcolm Metamorphics occur within a shear zone-bounded sliver linked to the Rodona Shear Zone and lack Type-2 fold interference patterns. Second-generation folds are steeply (Point Malcolm area) to moderately (Cape Pasley; Clark, 1999) plunging, and trend to the east-northeast. Given the similar orientation to the bounding shear zones and the Rodona Shear Zone, it is likely that this deformation is more directly related to large-scale shear zone movement. In addition, the timing of peak metamorphism, interpreted to relate to the formation of the folded gneissic fabric, is estimated to be much younger at c. 1315 Ma, coincident with Stage I of the Albany–Fraser Orogeny (Adams, 2012, and above). If the Malcolm Metamorphics experienced the Type-2 fold interference history observed in the Pinto Basalt and Sleeper Camp Formation, then it appears to have been erased by subsequent deformation under high-temperature conditions.

The Malcolm Metamorphics were intruded by Recherche Supersuite granite veins at 1313 ± 16 Ma (Clark et al., 2000), which demonstrates that the Malcolm Metamorphics were adjacent to, or thrust over the continental margin within the Albany–Fraser Orogen prior to this time, because the Recherche Supersuite is part of the Albany–Fraser Orogen and is not found within the Madura Province (Smithies et al., 2015b). As described above, the structural relationships suggest the granite veins, which are not folded, may have intruded during the final stages of the second folding event in the Malcolm Metamorphics, subparallel to the axial planes of the folds. Metamorphic dates of 1311 ± 4 Ma (monazite in metasedimentary rocks, Adams, 2012) and 1315 ± 11 Ma (zircon rims, GSWA 194867, Wingate et al., 2020a) likely reflects the formation of the gneissic fabric in the Malcolm Metamorphics, which was subsequently folded, as interpreted from the petrographic relationships (Adams, 2012). Thus, the folding events and

high-temperature metamorphism must be linked to Stage I of the Albany–Fraser Orogeny (cf. Clark et al., 2000) and indicate that accretion of the Arubiddy Ophiolite Complex was either well underway, or complete, by the time the Recherche Supersuite granite veins were emplaced.

The Rodona Shear Zone

First described by Clark et al. (2000), the Rodona Shear Zone is interpreted as a suture zone separating the Madura Province from reworked Archean continental crust of the Albany–Fraser Orogen (Kirkland et al., 2015; Smithies et al., 2015b; Spaggiari et al., 2015a, 2017a). To complete a seamless interpretation across this major crustal boundary, the overlapping ends of seismic lines 12GA-AF3 and 13GA-EG1 were merged (Fig. 10a; Spaggiari et al., 2017a; Holzschuh, 2019). The seismic data clearly show the easterly dip of the reflectors interpreted to relate to rocks affected by the Rodona Shear Zone. These reflectors correspond to significant north-northeasterly trending structures visible in aeromagnetic and gravity data (Figs 3, 9, 42, 44). The Rodona Shear Zone is interpreted as a complex series of west-vergent thrusts, overprinted by sinistral shear zone movement that likely steepened some of the original thrusts. Deformed Esperance Supersuite intrusions (e.g. c. 1170 Ma metamonzodiorite at the Hannah prospect) occur within and adjacent to the Rodona Shear Zone, indicating that at least some of its history post-dates emplacement of these intrusions. In the modeled MT data, there is a large gap in conductivity coinciding with the Rodona Shear Zone and surrounding rock packages, consistent with the interpretation of a major crustal boundary and its easterly dip (Fig. 104; Spaggiari et al., 2017a; Thiel et al., 2018). The Rodona Shear Zone is currently the subject of extensive exploration by BHP Global under its Seahorse Greenfields exploration project.

Geophysical expression of the Maralinga Event in the Madura Province

The geophysical data, including the deep crustal seismic and MT data, show evidence of regionally extensive 1182–1127 Ma Moodini Supersuite intrusions in the Madura Province. In the drillcores, these intrusions are mostly undeformed but in the geophysical data they appear to be associated with extensional shear zones and domal features. The region between the Serpent and Gauge Shear Zones (Figs 10a, 44) is one example dominated by complex intersections of faults and shear zones visible in the gravity and aeromagnetic data, and a large non-reflective area in the seismic data. The seismic data show interpreted extensional shear zones dipping to either side of the large domal area (Family Dam, Kybo, Gauge, Vincent and Carriage Shear Zones). The domal area includes a large non-reflective area interpreted to be dominated by c. 1192–1127 Ma Moodini Supersuite intrusions. Reflective zones appear to be truncated by non-reflective zones, consistent with this interpretation. The western side of the domal area coincides with a strongly conductive zone in the MT model, and this relationship has also been observed in the Coompana Province (Fig. 104; Spaggiari et al., 2017a; Pawley et al., 2018; Thiel et al., 2018; Wise et al., 2018a). The subvertical Serpent Shear Zone cuts the extensional shear zones and probably relates to a phase of strike-slip movement, although there are no clear shear sense indicators along this structure.

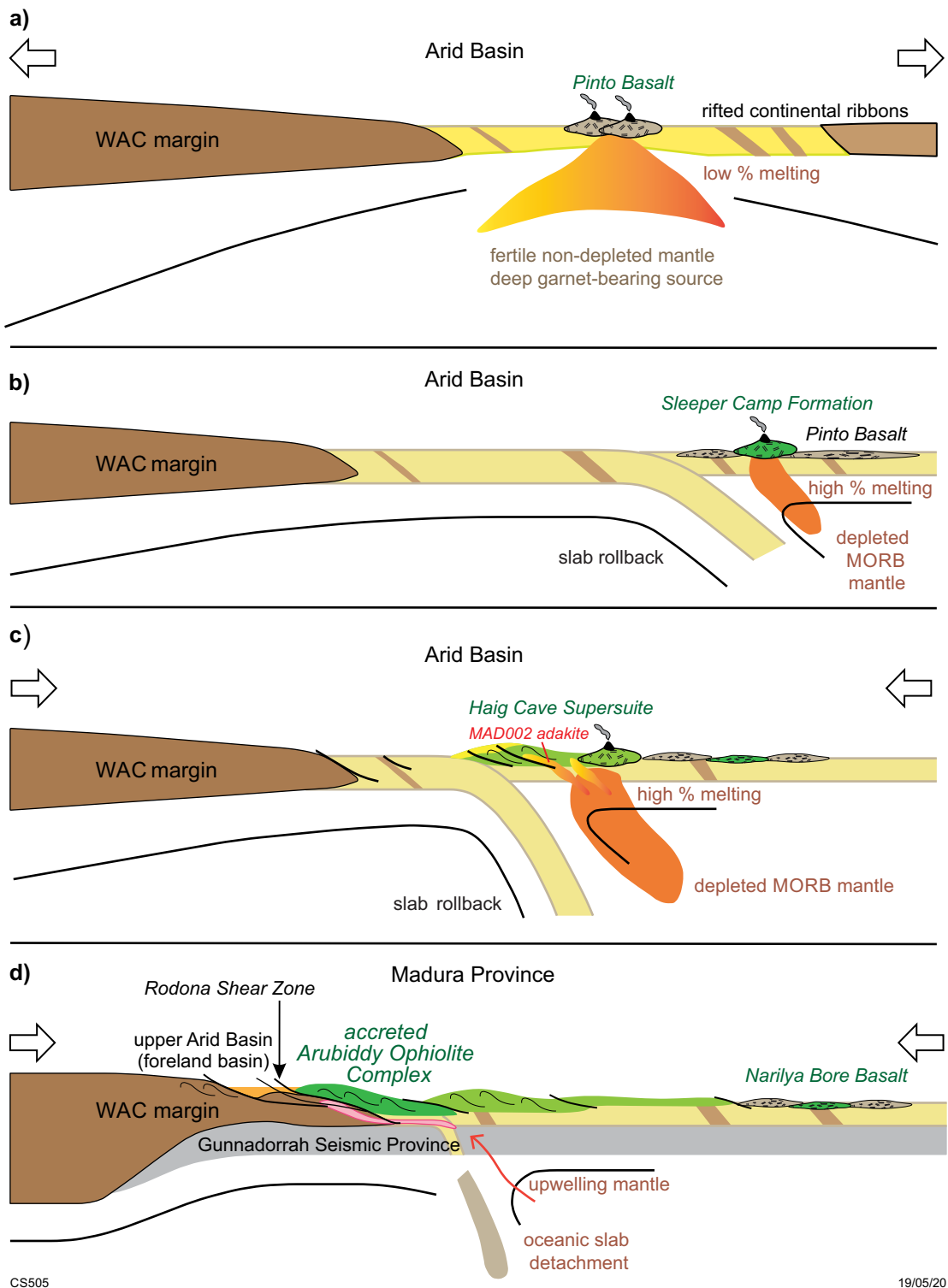


Figure 111. Schematic tectonic models showing the evolution of the oceanic crustal assemblages and accretion of the Arubiddy Ophiolite Complex onto the WAC margin (after Spaggiari et al., 2018): a) extrusion of the Pinto Basalt during formation of a continental marginal basin within an ocean–continent transition zone; b) oceanic subduction begins within the basin, initially producing the Sleeper Camp Formation at c. 1479 Ma; c) formation of the Loongana oceanic arc from c. 1415 Ma. Adakite intrudes Pinto Basalt at c. 1389 Ma, as folding and imbrication occurs during basin closure; d) accretion of the Arubiddy Ophiolite Complex above the passive continental margin between 1389 and 1330 Ma, triggering Stage 1 of the Albany–Fraser Orogeny and early Recherche Supersuite intrusions (shown in pink). Oceanic crustal assemblages remain behind those above the continental margin, including the Narilya Bore Basalt

To the east of this, and west of the Mundrabilla Shear Zone, is another domal region, similar to that described above but containing rafts of reflective crust. The domal region is flanked by the Lynch and Laundry Shear Zones, interpreted as extensional shear zones (Figs 10a, 21, 112). Stratigraphic drillhole MAD011, which occurs along strike to the southwest and is dominated by the Kestrel Cavern Gabbro of the Moodini Supersuite, penetrated the top of this domal area. This unit occurs within an elongate anomaly of strong magnetic and gravity response that is part of a large zone of similar geophysical response drawn into the Mundrabilla Shear Zone with sinistral shear sense.

Structural interpretation of the Coompana Province

As for the Madura Province, the interpretation of the structural evolution of the Coompana Province in Western Australia is based on aeromagnetic, gravity and deep crustal seismic data, coupled with drillcore analysis (see Coompana Province drillcores, above, and Appendix 2). However, unlike the Madura Province, indications of folding events are not as clear from the aeromagnetic data, potentially due to a lack of layered lithologies such as metasedimentary and metavolcanic rocks. The aeromagnetic and gravity data indicate the presence of a series of mainly northeast-trending faults or shear zones, some of which are parallel to northeast-trending gravity or magnetic anomalies (Figs 24, 26, 29, 30). The aeromagnetic data show that the northeasterly trending features are cut by numerous, north-northwesterly trending faults. Some of these offset strongly magnetic intrusions assigned to the Moodini Supersuite (Figs 24, 39), which indicates that these faults post-date the intrusions.

In Western Australia, the largest of the northeast-trending shear zones appear to be the Mulyawara and Border Shear Zones, both of which continue into South Australia (Fig. 9). The Mulyawara Shear Zone is interpreted to divide the western from the eastern Coompana Province and separates dominantly Undawidgi Supersuite to the west from dominantly Toolgana Supersuite to the east, although the two are not mutually exclusive (Figs 10b). The seismic and aeromagnetic data indicate that the Mulyawara Shear Zone dips to the northwest and extends to the top of the middle crust at a depth of about 12 km (Figs 10b, 113). At a broader scale, the Mulyawara Shear Zone has been interpreted to relate to a crustal boundary that can be traced to the northeast into the Musgrave Province (Pawley et al., 2018).

Deep crustal seismic line 13GA-EG1

Deep crustal seismic line 13GA-EG1 provided much insight into the crustal architecture of the Coompana Province. The eastern end of the line shows a series of northwest-dipping, crustal-scale shear zones and the dominant dip of reflectors is also to the west (Fig. 10c; Pawley et al., 2018). Three seismic provinces are recognized, corresponding to seismic domains in the lower crust that cannot be traced to the surface (Fig. 10b,c; Spaggiari et al., 2017a; Pawley et al., 2018).

The Jindargna Shear Zone dips moderately to the west, separating the underlying edge of the western Gawler Craton from the overlying eastern Coompana Province (Pawley et al., 2018). East of the Palinar Shear Zone (defined as the Cook Domain in South Australia) the crust is three-layered, comprising a remarkably bland, weakly to non-reflective upper crust, a strongly reflective, moderately west-dipping middle crust (Upper Jindargna Seismic Province), and a strongly reflective, subhorizontal to east-dipping lower crust (Lower Jindargna Seismic Province) (Fig. 10b,c; Spaggiari et al., 2017a; Pawley et al., 2018). The upper crust in this region is unknown, and is possibly either Toolgana Supersuite-dominated, or part of the western Gawler Craton.

West of the Palinar Shear Zone, the crust is two-layered, comprising the continuation of remarkably bland, weakly to non-reflective upper crust, and strongly reflective, subhorizontal lower crust defined as the Forrest Lakes Seismic Province. The latter continues west beneath the western Coompana Province, changing to a gentle to moderate easterly dip below the Mulyawara Shear Zone. The weakly reflective to non-reflective upper crust extends west to the Border Shear Zone, which separates it from gently west-dipping reflective crust dominated by the Toolgana Supersuite. This section of upper crust, which is between 12 and 18 km (4–6 s) thick, coincides with a distinct linear belt of northeasterly trending, magnetic intrusive rocks interpreted to be mainly granitic rocks of the Moodini Supersuite (represented by the Eucla No. 1 drillhole, Figs 3, 9, 24). Non-reflective seismic data in the lower part of the footwall of the Border Shear Zone supports this interpretation, as does a distinct west-dipping conductive zone in the MT model, although the latter also crosses into the Forrest Lakes Seismic Province (Spaggiari et al., 2017a; Thiel et al., 2018).

The Forrest Lakes Seismic Province is strongly reflective and occupies the region of thinnest crust and at its eastern end, the reflectors dip dominantly to the west (Fig. 10b,c). In contrast, at its western end, the Forrest Lakes Seismic Province has a moderate, easterly dip and lies in the middle to upper crust between the Old Homestead Seismic Province and Undawidgi Supersuite-dominated upper crust (Figs 104, 112; Spaggiari et al., 2017a; Thiel et al., 2018). Several interpreted Moodini Supersuite intrusions crosscut the Forrest Lakes Seismic Province. Both the Old Homestead Seismic Province and Forrest Lakes Seismic Province are truncated by the Mundrabilla Shear Zone.

The northerly trending, west-dipping Tank Shear Zone (Figs 10b, 24, 26, 29, 30, 39), which cuts east-dipping shear zones in its hangingwall, is interpreted to have utilized the Mulyawara Shear Zone. The hangingwall also contains strong reflectors that define an upright antiform, floored by the Approach Mast Shear Zone (Fig. 113). This is coincident with a small, but strong magnetic and gravity anomaly northeast of Forrest (Figs 29, 30). The Tank Shear Zone was likely to be extensional, and its movement may have been facilitated by Moodini Supersuite intrusions.

In the seismic section, the region between the Mundrabilla and Border Shear Zones has a bowl-shaped geometry, which appears to be mirrored in the MT model (Figs 10b, 104; Spaggiari et al., 2017a; Thiel et al., 2018). Bland, weakly reflective to non-reflective areas are interpreted to be dominated by Moodini Supersuite intrusions, some of which appear to have utilized or crosscut various shear zones, suggesting synchronous or post-deformation magmatism.

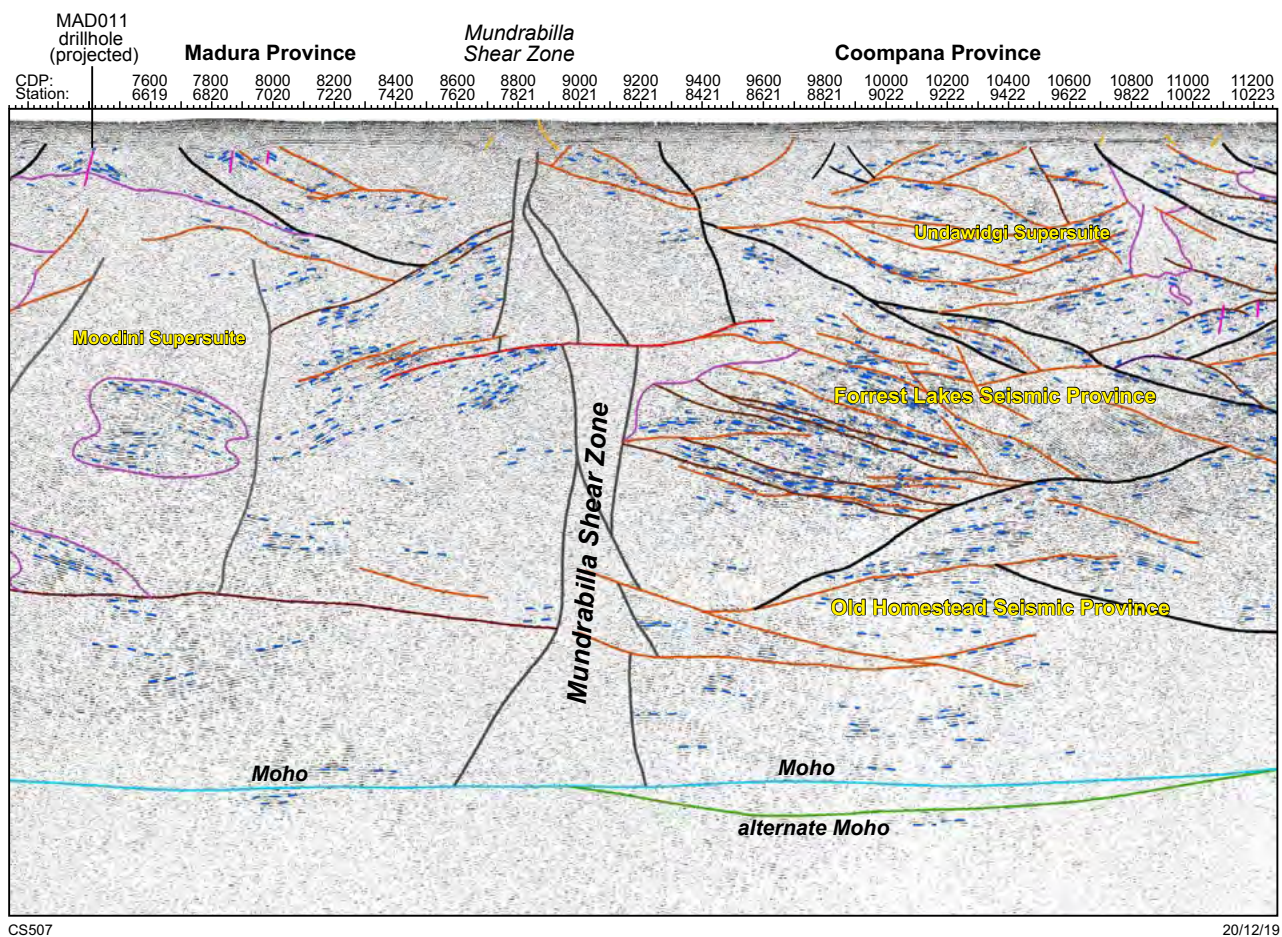


Figure 112. Interpreted migrated section of seismic line 13GA-EG1 showing the Mundrabilla Shear Zone (from Spaggiari et al., 2017a). Blue dashed lines are seismic reflectors, black, brown and orange lines are faults or shear zones, red lines indicate subhorizontal offsets (into and out of the plane) along the Mundrabilla Shear Zone, purple lines indicate Moodini Supersuite intrusions, short strong pink lines are fold axial planes, light blue line is the Moho, green line is an alternative interpretation of the Moho

Geophysical expression of the Maralinga Event in the Coompana Province

As in the Madura Province, the geophysical data, including the deep crustal seismic and magnetotelluric data, show evidence of regionally extensive 1192–1140 Ma Moodini Supersuite intrusions in the Coompana Province. One of the most striking features in aeromagnetic datasets is the northeasterly trending belt of strongly magnetic, circular to ovoid Moodini Supersuite plutons that lies southeast of the Border Shear Zone (Fig. 9; Hughes Domain in South Australia, Pawley et al., 2018). This magmatic belt coincides with a broad, strongly conductive zone in the MT model (Spaggiari et al., 2017a; Thiel et al., 2018).

In aeromagnetic data, the northeast-trending belt of plutons is very similar to a belt of northeast-trending plutons in the eastern Nornalup Zone of the Albany–Fraser Orogen. Here, they occur as 1180–1170 Ma Boonya Suite intrusions that are part of the Esperance Supersuite (Smithies et al., 2015b). It is inviting to suggest that these large, northeasterly trending magmatic belts are part of a series of structurally controlled belts that formed over time from west to east, commencing with the Fraser Zone intrusions in the Albany–Fraser Orogen at 1300–1280 Ma, followed by the Boonya Suite intrusions at 1180–1170 Ma

(including the c. 1170 Ma metamonzodiorite at the Hannah prospect within the Rodona Shear Zone), followed by the southeastern Madura Province intrusions (represented by the Kestrel Cavern Gabbro and Moodini prospect intrusions) and the Hughes Domain belt in the Coompana Province at 1150–1130 Ma. The 1180–1170 Ma Boonya Suite was emplaced at the same time as the Bottle Corner Shoshonite in the western Coompana Province. It is interesting to note that the isotope record indicates that these intrusions became increasingly juvenile with decreasing age, and likely reflect extensional processes and crustal thinning during the Maralinga Event.

Interpreted structures from the stratigraphic drillcores and links to geophysical data

The ability to link structural features observed in the drillcores with geophysical data is more ambiguous in the Coompana Province than in the Madura Province, largely because of the responses of the lithologies involved and dominance of metagranites, but also because of overprinting effects, and possibly, the effects of alteration. The northern region in the vicinity of drillholes FOR010 and FOR011 appears to show the most consistency between measured structures and the northeast-trending aeromagnetic and

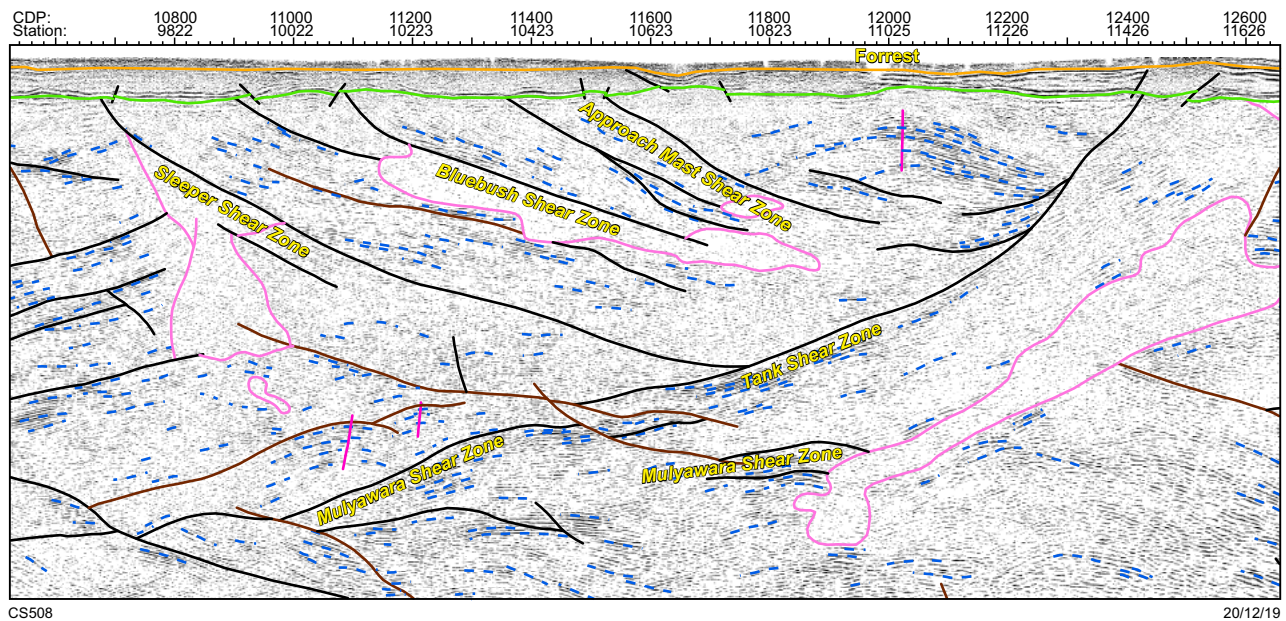


Figure 113. Interpreted migrated section of seismic line 13GA-EG1 (from Spaggiari et al., 2017a). An interpreted antiformal feature near the locality of Forrest, top right of figure, coincides with a small but strong magnetic and gravity anomaly (see Figs 24, 30). Blue dashed lines are seismic reflectors, black lines are faults or shear zones, brown lines are extensional shear zones, pink lines indicate intrusions, short strong pink lines are fold axial planes, green line indicates the base of the Bight Basin, orange line indicates the surface

gravity anomalies, although even here there are significant ambiguities (Fig. 29). In that region, shallowly northeast-plunging folds are interpreted from the drillcores (Table 9, see also the relevant sections above). These folds pre-date intrusion of the Bottle Corner Shoshonite; however, a second phase of folding is evident in the mafic components of that unit. All folds are cut by the Si-rich component of the Bottle Corner Shoshonite. Given that the magmatic crystallization ages of the two components of Bottle Corner Shoshonite are within uncertainty of each other (Table 5), the second folding event is constrained to c. 1183 Ma. This interpretation fits with the metamorphic date of 1174 ± 12 Ma recorded in Undawidgi Supersuite hornblende-bearing metasyenite from drillcore FOR011 (GSWA 206730). An alternative interpretation for this date was presented above based on the Lu–Hf data (see Crustal melting or metamorphic resetting at 1192–1150 Ma?) suggesting that new zircon grew from a partial crustal melt, rather than by isochemical zircon dissolution and reprecipitation during metamorphism. This interpretation would also fit with the similar timing of Bottle Corner Shoshonite magmatism and does not affect the structural interpretation. Regardless, it is clear that emplacement of the Bottle Corner Shoshonite brackets a period of folding, and is unlikely to be extension-related as is interpreted for the bulk of Moodini Supersuite intrusions.

The Mulyawara Shear Zone appears to separate regions of different fold styles and also metamorphic grade, with dominantly lower amphibolite facies Undawidgi Supersuite rocks to the northwest (drillcores FOR101 and FOR011) and upper amphibolite to granulite facies Toolgana Supersuite gneissic rocks to the southeast (drillcores FOR004 and FOR008). The gneissic rocks are dominated by recumbent-style folding, and drillcore FOR008 records top to the northwest shearing prior to this. Folding is cut by partial melts dated at c. 1150 Ma

and although speculative, the recumbent-style folding may have occurred at c. 1180 Ma, or at a similar time to the folding in drillcores FOR101 and FOR011. However, the transport direction of top to the northwest is not consistent with the northwest dip of the major structures such as the Mulyawara or Border Shear Zones, which suggests the recumbent folding in drillcores FOR004 and FOR008 record an older, undated event. This may relate to highly radiogenic Hf values in metamorphic zircons from metasyenogranite (GSWA 213822 from drillcore FOR004, see Lu–Hf section, above), which suggest evidence for the breakdown of garnet that existed for some time prior to its breakdown to allow sufficient ingrowth of radiogenic Hf in zircon. The highly radiogenic Hf values could therefore indicate a metamorphic event of at least amphibolite facies, with garnet growth prior to c. 1179 Ma, the age of metamorphism recorded in the sample (Table 5).

The timing of formation of the northeast-trending mylonite with its moderate northwest to southeast dip in drillcore FOR012 is unconstrained (Table 9). However, it does appear to be cut by the Tank Shear Zone, which is probably a relatively late structure (Figs 29, 39). Like most features, the Tank Shear Zone is cut by regionally extensive northwest-trending faults that typically have sinistral, or possibly reverse sense displacements.

The Mundrabilla Shear Zone

One of the most prominent features in aeromagnetic images, the north-trending Mundrabilla Shear Zone clearly separates the Madura and Coompana Provinces (Figs 3, 10). Its significant length and linearity suggest that it is a subvertical, strike-slip shear zone, and a broad zone of strong magnetic response has been drawn into the western side of the shear zone, indicating sinistral shear sense (Fig. 21). This major shear zone has been interpreted to link with the Frost Shear

Table 9. Summary of interpreted structures in the stratigraphic drillcores in the Coompana Province, in relative chronologic order

<i>FOR012</i>	<i>FOR010</i>	<i>FOR011</i>	<i>FOR008</i>	<i>FOR004</i>
5. Northwest-trending brittle faults	7. Northwest-trending brittle faults	3. Northwest-trending brittle faults	5. Northwest-trending brittle faults	4. Northwest-trending brittle faults
	6. Intrusion of youngest Si-rich component of Bottle Corner Shoshonite at c. 1180 Ma		4. Top to the northwest, thrust displacement	
	5. Localized schistose foliation in retrogressed, altered rocks; small-scale folds, shearing			
4. Wedge cut by the Tank Shear Zone	4. Weak to moderate metamorphic foliation, locally produced		4. In situ migmatization, ± felsic injections (anatectic melts) c. 1150 Ma	
3. Mylonite folded about an upright, gently northeast-plunging axis, subparallel to the mineral lineation; gentle to moderate, southeast-dipping axial plane; geometry may be indicative of the northeast-trending wedge in the aeromagnetic data	3. Intrusion of mafic component of Bottle Corner Shoshonite at c. 1180 Ma		3. Recumbent to strongly inclined, small-scale Z-folds and curvilinear folds with subhorizontal fold axes (≥c. 1179 Ma?)	3. Series of stacked, inclined to recumbent, gently west-northwesterly plunging folds (F_2) of gneissic layering with moderately southwest-dipping axial planes (Fig. 28; ≥c. 1179 Ma?)
2. Mylonitic foliation with moderate northwest or southeast dip; subhorizontal to gently northeast-plunging mineral lineation; strong flattening; intrafolial S-folds with subhorizontal fold axes and moderate southeast-dipping axial planes	2. Tightly to isoclinally folded foliation within hinges of gently northeast-plunging folds, or axially planar foliation to northwest-trending folds (Fig. 36)	2. Foliation and layering folded into a small-scale, gently northeast-plunging, tight folds	2. Top to the west or northwest shear zone	2. Small-scale (F_1) folds plunging gently to the southwest
1. Foliation	1. Moderate to strong foliation with gentle to moderate, east-northeast to northeast dip	1. Moderate intensity foliation and layering (S_1), northwest or southeast dip	1. Gneissic layering	1. Gneissic layering
		Metamorphism 1174 ± 12 Ma	Metamorphism 1153 ± 9 Ma, 1151 ± 6 Ma	Metamorphism 1179 ± 10 Ma

NOTES: See also Table 2 for drillcore FOR010. Metamorphic dates from Table 5

Zone in Antarctica, and has also been interpreted to continue northwards at least as far as the Musgrave Province, where it is defined as a fracture zone with Permian sedimentary infill (Howard et al., 2015; Aitken et al., 2016). Sinistral displacement has been estimated at up to 300 km based on matching magnetic and gravity features on either side (Aitken et al., 2016), and at least 100 km would be necessary to account for this, simply based on the length imaged in the region of the Eucla basement.

Maximum ages of 1132 ± 9 and 1127 ± 7 Ma for movement along the shear zone are provided by crystallization dates from Moodini Supersuite metamonzogranite with a subhorizontal L–S tectonite fabric from the Moodini prospect drillcores, which were drilled within the shear zone (Fig. 21). Given that the sinistral drag features clearly cut or displace northeast-trending folds interpreted in aeromagnetic data in the Madura Province, these ages also provide a minimum age for that folding event.

The Mundrabilla Shear Zone provides an opportunity to examine a large subvertical structure in the deep crustal seismic line 13GA-EG1, and to make comparisons to the MT model. In the seismic profile, the Mundrabilla Shear Zone is imaged as a stair-stepped, weakly to non-reflective zone interpreted to extend to the base of the crust and to broaden at depth (Figs 10, 112). Areas of reflective crust are truncated by the weakly reflective to non-reflective zone, and these truncations were interpreted to mark the edges of the shear zone (Spaggiari et al., 2017a). The weakly reflective to non-reflective zone is interpreted to include Moodini Supersuite intrusions that were injected within the evolving shear zone, such as those intersected at the Moodini prospect, likely facilitating its formation. Subhorizontal offsets suggest subhorizontal sliding (into and out of the plane) of portions of the shear zone during sinistral shear, likely coupled with injections of Moodini Supersuite granites.

There are distinct geophysical differences between the Madura and western Coompana Provinces across the Mundrabilla Shear Zone. The western Coompana Province shows overall higher reflectivity in the seismic data, lower densities in the gravity data, and completely different structures and features in the aeromagnetic data — none of which can be traced across as a displacement marker. In addition, the subhorizontal reflectors that define the Gunnadorrah Seismic Province in the Madura Province are lacking, and the lower crust appears as a weakly reflective, gently east-dipping wedge truncated by the Mundrabilla Shear Zone. This wedge is defined as the Old Homestead Seismic Province, and is somewhat mirrored by conductive crust in the MT model, although the conductive feature continues into the domal area west of the Mundrabilla Shear Zone in the Madura Province (Figs 104, 112; Spaggiari et al., 2017a; Thiel et al., 2018). However, a domain of very high conductivity in the lower crust is restricted to the Madura Province side of the shear zone.

Regional implications and tectonic models

In this section similarities and differences in the crustal evolution and architecture of the Madura and Coompana Provinces are compared, and the constraints their evolution provides to the broader region are discussed, with emphasis on the Albany–Fraser Orogen. We also present a model for ophiolite formation in the Madura Province (the Arubiddy Ophiolite Complex), based on Spaggiari et al. (2018).

The Madura vs Coompana Province and the role of the Mundrabilla Shear Zone

As discussed above in the section ‘The Mundrabilla Shear Zone’, it is clear that this structure separates two provinces that have distinct differences in their geophysical expression, and their magmatic, structural and tectonic history (Fig. 8). The only connections appear to be similarities in isotope data and model ages, which indicate formation of the earliest oceanic or oceanic crust at c. 1950 Ma (Kirkland et al., 2017). This interpretation extends beyond the two provinces and includes the Musgrave Province and potentially also part of the Rudall Province, suggestive of an extensive oceanic crustal realm. However, as for the Musgrave Province, the magmatic and structural history post-dating 1950 Ma for the Madura and Coompana Provinces do not appear to be closely linked, suggesting that they formed a significant distance apart. In this respect, the Mundrabilla Shear Zone may have existed as a crustal boundary prior to intrusions of the Moodini Supersuite and may have been significantly modified during the Maralinga Event to form the structure now observed.

Differences prior to the Maralinga Event and Moodini Supersuite magmatism are recorded by the magmatic products themselves, and this may also relate to some of the differences in geophysical expression. As discussed (see Comparisons of magmatic evolution between the Madura and Coompana Provinces), a notable feature of a large proportion of Coompana Province magmatism was the dominant volumes of magnesian and very likely subduction-related (or recycled subduction-related) material with felsic compositions. This led to the development of a thick, enriched and hydrated lithosphere, which can explain why Moodini Supersuite high-KMg magmatism, including the shoshonitic magmatism, was largely restricted to the Coompana Province. The high-KMg magmatism likely represents deep melting of the older subduction-metasomatized lithospheric mantle. In contrast, high-KFe magmatism that was more prevalent in the Madura Province probably reflects regions where thick lithospheric mantle was significantly thinned or removed.

These features, and the clear significance of the Mundrabilla Shear Zone, are perhaps at odds with tectonic models that suggest a series of Paleoproterozoic westward-migrating arcs culminating with the c. 1400 Ma Loongana Arc in the Madura Province (e.g. Wise et al., 2018a). In addition, the available data do not indicate a record of Paleoproterozoic arc magmatism in the Madura Province, whereas the presence of E-MORB oceanic crust represented by the Pinto Basalt supports the interpretation of a continental marginal basin pre-dating the c. 1479 Ma Sleeper Camp Formation, and Loongana Arc. If westward-migrating arcs were present, it is more likely that they were confined to the Coompana Province, represented by the St Peter Suite, Toolgana Supersuite and the c. 1526 Ma Bunburra Suite.

Previously, suggestions have been made that the Mundrabilla Shear Zone not only connects to a major shear zone in Antarctica (the Frost Shear Zone), but is also linked to a large shear zone system to the north (Aitken et al., 2016). This shear zone system has been defined as the Lasseter Shear Zone, a series of major, northwest to northeasterly trending shear zones that appear to coincide with the edges of basement terranes, including the eastern edge of the Halls Creek Orogen and the western edges of the Tanami and

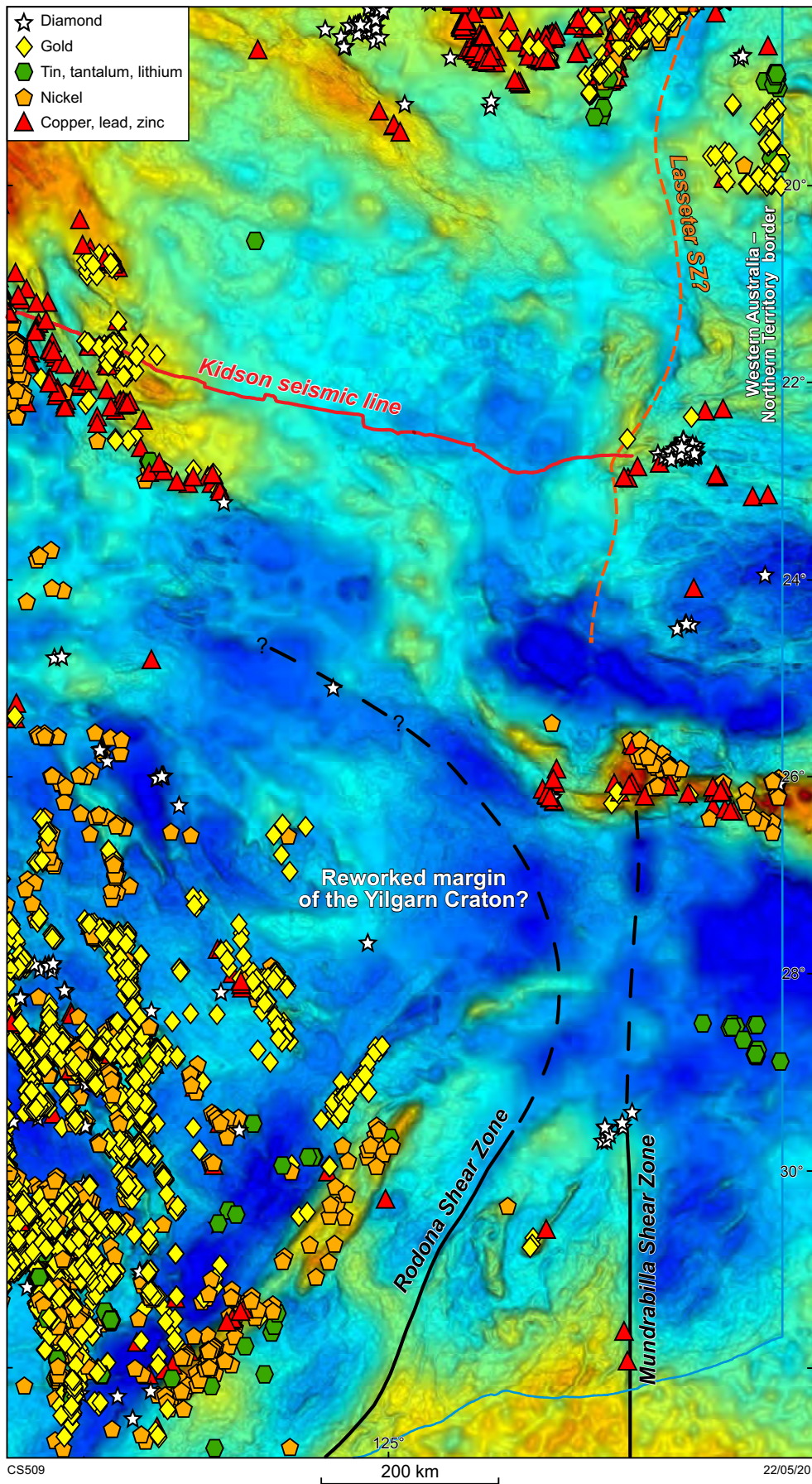


Figure 114. Gravity image showing the possible trace of the Lasseter Shear Zone as a continuation of, or related to, the Mundrabilla Shear Zone. The image also shows mineral occurrences from the GSWA mines and mineral deposits database (MINEDEX), extracted October 2019

Arunta Orogens (Fig. 114). They also define the southeastern edge of the Canning Basin, which indicates tectonic activity was not confined to the Precambrian.

Linking the Albany–Fraser Orogen

The Albany–Fraser Orogen defines the southern and southeastern margin of the Yilgarn Craton (and WAC), and abundant datasets support its Archean heritage (Kirkland et al., 2011a, 2015; Smithies et al., 2015b; Spaggiari et al., 2015a, 2018). Deep crustal seismic data highlight differences in crustal architecture within the Albany–Fraser Orogen that can be attributed to the influence of the adjacent Madura Province. Along seismic lines 12GA-AF1, 12GA-AF2 and 12GA-AF3, the western part of the orogen displays a clear (inverted) thrust-dominated architecture, whereas east of the Fraser Zone and the Coramup Shear Zone, the crustal architecture is less coherent, and less continuous structures are evident (Spaggiari et al., 2014). Apart from the portions of the upper crust, much of the Madura Province is more similar to this eastern region, corresponding to its intrusion-dominated architecture (Fig. 10).

The lower crustal Gunnadorrah Seismic Province is interpreted to be common to both, suggesting it is related to Moodini Supersuite magmatism and/or older extension related to the formation of the ocean–continent transition zone and Arid Basin (Spaggiari et al., 2015a). To the west, the Gunnadorrah Seismic Province terminates where the Yilgarn Craton crust is less reworked and more coherent. This crustal buttress also coincides with the western limit of the Mesoproterozoic Recherche and Esperance Supersuite magmatism, and a region of thickened crust (Sippl et al., 2018). This western limit has been interpreted as one of the most significant structures within the Albany–Fraser Orogen, corresponding with the Harris Lake, Fraser and Coramup Shear Zones, and has been interpreted as an inverted, originally basin-forming crustal ramp (Spaggiari et al., 2014, 2015a; Spaggiari and Smithies, 2015; Maier et al., 2016). Its position has structurally controlled deposition of upper Arid Basin units such as the Snowys Dam Formation, followed by emplacement of the 1300–1280 Ma Fraser Zone gabbros, hybrid rocks and granites (Figs 111d, 115; Smithies et al., 2013, 2015b).

Arubiddy Ophiolite complex

This section summarizes the findings presented in Spaggiari et al. (2018). Ophiolites can originate in a variety of oceanic settings, including extensional rifts in both subduction-related and subduction-unrelated settings, which, in turn, influences the emplacement mechanisms that allow their preservation within continental margins (see Coleman, 1977 and Dilek and Furnes, 2014, for reviews). The Arubiddy Ophiolite complex is interpreted as the series of Madura Province Proterozoic oceanic arc-related rocks now accreted to the eastern margin of the east Albany–Fraser Orogen. The majority of these rocks occur within the hangingwall of the Rodona Shear Zone (Fig. 10) and overlie the continental margin of the Albany–Fraser Orogen (and WAC; Spaggiari et al., 2014, 2017a). The continental margin is interpreted to extend into the middle crust at least as far east as the Serpent Shear Zone, below which the Rodona Shear Zone appears to sole onto the Gunnadorrah Seismic Province. The Gunnadorrah

Seismic Province is defined as lower crust characterized by subhorizontal seismic reflectors (Korsch et al., 2014) and extends beneath the entire Madura Province and westwards beneath part of the Albany–Fraser Orogen, where it terminates against thickened crust (Spaggiari et al., 2014, 2017a; Sippl et al., 2018). Its formation likely relates to multiple tectonic events, including the Maralinga Event.

The Arubiddy Ophiolite complex comprises rocks belonging to the Sleeper Camp Formation, Malcolm Metamorphics and Haig Cave Supersuite, all of which have N-MORB subduction-modified geochemical characteristics. The older Pinto Basalt, with its E-MORB – OIB geochemical characteristics and high Ti/Yb ratios, is interpreted to relate to mantle upwelling beneath extending crust during formation of the continental marginal basin on which the oceanic arc subsequently developed (Fig. 111). The continental marginal-basin setting is consistent with a previous model of hyperextension of Archean–Paleoproterozoic continental crust of the Yilgarn Craton (and WAC) resulting in an ocean–continent transition zone and formation of the Arid Basin (Spaggiari et al., 2015a). The Pinto Basalt was intruded by Haig Cave Supersuite adakite, potentially during a compressional event as suggested by structural relationships in the drillcore, described above. This event may have occurred at the onset of the accretion process and facilitated the incorporation of tectonic slivers of the Pinto Basalt within the ophiolite complex.

The oldest known component of the oceanic arc assemblage is the c. 1479 Ma Sleeper Camp Formation, and the V/Ti ratio trends suggest this unit could mark the initiation of oceanic subduction (Fig. 103). V–Ti plots can be used to show temporal trends in subduction-related oceanic assemblages from more MORB-like as subduction begins, to more island arc tholeiite-like as the influence of subduction processes and subducted water increases V and lowers Ti in the magma (Pearce, 2014). The progression to oceanic arc formation is recorded by the Malcolm Metamorphics basalt after c. 1470 Ma, and the Haig Cave Supersuite from 1415 to 1389 Ma.

At the Loongana prospect, both the mafic and felsic intrusions of the Haig Cave Supersuite are dated between c. 1415 and 1403 Ma, with a weighted mean age of 1409 ± 6 Ma (MSWD = 1.9) for the five samples (Table 5). The two samples of plagiogranite from the Haig prospect give a weighted mean age of 1398 ± 7 Ma (MSWD = 0.18), and the single sample of MAD002 adakite is dated at 1389 ± 7 Ma (MSWD = 1.2). These mean ages do not agree within uncertainty but indicate an apparent westward decrease in age of the mafic and felsic magmatism collectively assigned to the Haig Cave Supersuite. This could indicate westward migration of oceanic arc magmatism, excluding any structural displacement.

The Arubiddy Ophiolite complex is interpreted to have been structurally emplaced above the continental margin during convergence and marginal basin closure, leading to oceanic arc–continent collision and forming the suture zone between the east Albany–Fraser Orogen and the Madura Province. This collision triggered the initiation of Stage I of the Albany–Fraser Orogeny, at c. 1330 Ma. The interpreted subduction–accretion process is typical of arc–continent collision, in which

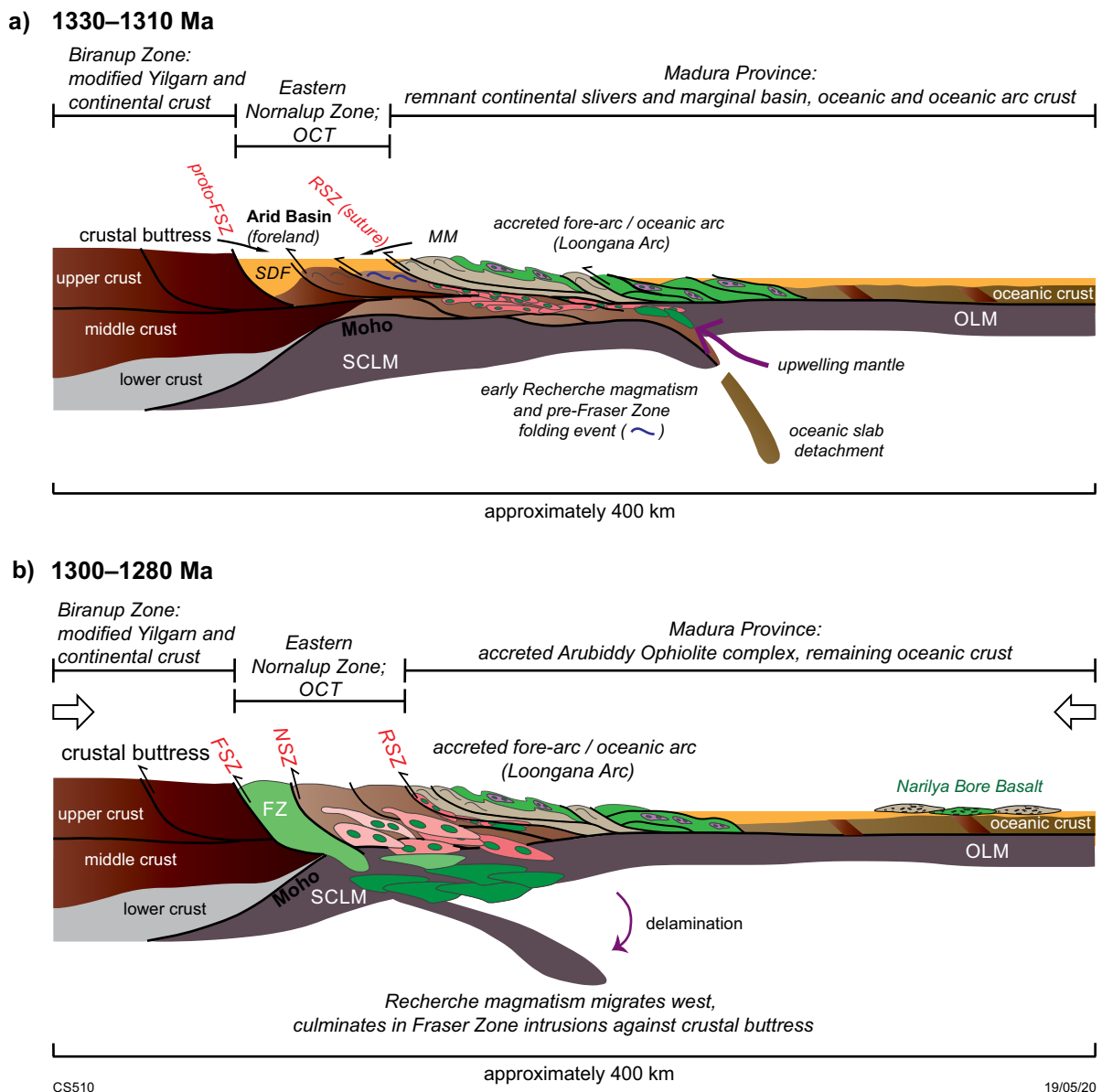


Figure 115. Schematic tectonic models showing Stage 1 of the Albany–Fraser Orogeny: a) accretion of the Arubiddy Ophiolite Complex leads to slab detachment and crustal thickening. Sediments were transferred from the accreted oceanic arc to the upper Arid Basin and a foreland deep trough, where the Snowys Dam Formation was deposited; b) instability leads to delamination, tracked by the migration of Recherche Supersuite magmatism to the northwest and culminating with mantle upwelling and intrusive magmatism into the Fraser Zone. Green indicates mafic/mantle component; pink indicates crustal melt / granitic component. Large arrows indicate approximate stress field orientation. Abbreviations: FSZ, Fraser Shear Zone; FZ, Fraser Zone; MM, Malcolm Metamorphics; NSZ, Newman Shear Zone; OCT, ocean–continent transition; OLM, oceanic lithospheric mantle; RSZ, Rodona Shear Zone; SCLM, subcontinental lithospheric mantle

subduction dips away from the continental margin and portions of the upper plate oceanic arc and its fore-arc are obducted, while sedimentation continues (Fig. 111; e.g. Brown et al., 2011, and references therein). The absence of magmatic-arc rocks and tectonic activity within the Albany–Fraser Orogen from 1620 to 1330 Ma are factors that support this model (Fig. 8). The buoyancy-driven analogue modelling of Edwards et al. (2015), which suggests that a component of continental subduction of the passive margin typically occurs before subduction termination and oceanic slab detachment, could be relevant in this case.

Structural emplacement occurred between 1389 Ma, the age of the MAD002 adakite and youngest component of the Haig Cave Supersuite, and 1330 Ma, the age of the earliest Recherche Supersuite intrusions that lie along the margin of the east Albany–Fraser Orogen and were influenced by the presence of Madura Province crust (Smithies et al., 2015b). Within the Albany–Fraser Orogen, 1330–1280 Ma Recherche Supersuite magmatism has been shown to have migrated northwestwards towards the hinterland (Smithies et al., 2015b). The early Recherche Supersuite granites have distinctly more radiogenic Nd isotope values ($\epsilon_{Nd(1300\text{ Ma})}$ about -4 , compared to -9) and

younger Nd model ages (2.18 Ga, compared to 2.56 Ga) than all other Recherche Supersuite granites, which indicates the influence of Madura Province lithosphere in the bulk source of granitic rocks intruded in the vicinity of the Rodona Shear Zone (Smithies et al., 2015b).

Although regarded as having formed in a similar setting to the Sleeper Camp Formation and Malcolm Metamorphics, the Narilya Bore Basalt is significantly distal to the continental margin, and does not overlie it. In fact, all occurrences east of the Serpent Shear Zone (Figs 10, 44) could be considered distal to the continental margin and not part of an obducted ophiolite complex. However, it is clear that the Maralinga Event has significantly disrupted and displaced the oceanic crustal assemblages. In any case, all rocks of the Madura Province that pre-date the Maralinga Event have been found to have oceanic crustal affinities, and thus indicate the preservation of a large tract of oceanic crust preserved outboard of the continental margin and suture zone. This has been interpreted to represent a unique Proterozoic setting in which the oceanic fragments related to, but outboard of those emplaced above, the continental margin have been frozen within the voluminous, isotopically juvenile, felsic and mixed mafic lower crustal and asthenospheric melts of the 1192–1125 Ma Moodini Supersuite. This is what is observed on a smaller scale in the MAD011 drillcore, in which xenoliths of Narilya Bore Basalt are preserved within the Kestrel Cavern Gabbro.

Connie Sue Formation, eastern Nornalup Zone, Albany–Fraser Orogen

The Connie Sue Formation was described in sections Exploration drillcores from the Madura Province, and in Whole-rock geochemistry of Madura Province rocks. It is only known from drillcore NDDH002 from the NSD prospect (Figs 3, 42), and its relationship to other units is therefore difficult to constrain. The whole-rock geochemical data showed that the mafic volcanic component of the Connie Sue Formation had similar E-MORB – OIB characteristics to the Pinto Basalt (drillcore MAD002), albeit with a greater degree of crustal input (Figs 56, 57). Both the high-Ti Pinto Basalt and mafic volcanic rocks of the Connie Sue Formation have compositions consistent with low-degree partial melting of a fertile mantle source at deep levels within the garnet lherzolite stability field, and are likely a result of deep asthenospheric upwelling.

The Pinto Basalt has been shown to be significantly older than c. 1389 Ma, the age of the crosscutting adakite of the Haig Cave Supersuite. Initially, based on the geochemical similarities it was thought that the Connie Sue Formation might be a similar age and also related to formation of the continental marginal basin. However, preliminary dating of zircons from a mafic schist from the Connie Sue Formation yielded a weighted mean $^{207}\text{Pb}^*/^{206}\text{Pb}^*$ date of 1172 ± 7 Ma (GSWA 219082). The mafic schist is clearly crosscut by weakly deformed, pink metamonzogranite dated at 1169 ± 6 Ma (GSWA 192562) and undeformed, strongly altered, coarse-grained leucogabbro dated at 1180 ± 8 Ma (baddeleyite from GSWA 192563; Wingate et al., 2018c–e; Figs 43b–d), providing a minimum age for the mafic schist, and also the moderate to strong foliation present in the schist. Therefore, it is unclear whether the date of 1172 ± 7 Ma for

the schist is a depositional age or is due to zircon growth in the host schist during crosscutting magmatism. If it represents a depositional age, the mafic volcanic would have to have been emplaced, buried and deformed and metamorphosed prior to intrusion of the granite and leucogabbro, and all within uncertainty of the three dates.

Based on the above, the Connie Sue Formation could have formed in a similar fashion to the Pinto Basalt but as a more inboard component or possible re-entrant of the continental marginal basin on hyperextended Yilgarn Craton crust (the Arid Basin). Alternatively, it could represent the products of a younger sub-basin of the Arid Basin that developed within the Albany–Fraser Orogen following accretion of the Arubiddy Ophiolite Complex, perhaps in similar fashion to the Snowys Dam Formation of the Fraser Zone (Spaggiari et al., 2015a). As described above, the northeastern part of the Nornalup Zone is largely unknown as it lies completely under cover, but appears to contain similar rocks to those encountered at the NSD prospect (Fig. 42). These include magnetite-bearing mafic granulite (drillhole NRAC-01) and Mn-rich and Fe-rich sedimentary gneiss (drillhole NRAC-02; Stephens, 2000), as well as occurrences of fine-grained mafic and quartz-rich amphibolite, layered Fe-rich metasedimentary rocks, and pelitic to psammitic schist (Smit, 2009). If the first scenario is correct, these successions could represent overthrust Madura Province rocks, similar to the situation for the Malcolm Metamorphics. Alternatively, they may have formed in situ within the northeastern Nornalup Zone of the Albany–Fraser Orogen and represent a younger, more extensive sub-basin than that of the Snowys Dam Formation.

Cover rocks from the slope and rise of continental margins underlying ophiolitic rocks have been described from the Uralides and Taiwan (the ‘slate belt’), where the cover is scraped off as the leading edge encounters the subduction zone during continent–arc collision (Brown et al., 2011, and references therein). As this occurs the orogen begins to imbricate and rapidly form topography, shedding sediment inboard into a foreland basin, initially in a submarine environment. A foreland basin was interpreted as the setting for the uppermost Arid Basin and deposition of the Snowys Dam Formation, which records detritus derived from both the continental margin and oceanic arc (Spaggiari et al., 2015a). A transition to subaerial sedimentation is indicated by the deposition of the Ragged Basin, which occurs as thrust sheets within the eastern Nornalup Zone and comprises metasedimentary rocks deposited within a shallow basin by a large fluvial system with a maximum depositional age of 1314 ± 19 Ma (Waddell et al., 2015). These rocks were interpreted to have been deposited during the latter part of Stage I of the Albany–Fraser Orogeny (from c. 1330 to 1260 Ma; Waddell et al., 2015). Further work is required to understand where the Connie Sue Formation and other similar successions within the northeastern Nornalup Zone might fit into the basin history of the Albany–Fraser Orogen.

Conclusions

This Report demonstrates the value of combining interpretations of regional geophysical data with detailed information from high quality diamond drillcores to map the crustal architecture and evolution of Precambrian basement geology beneath younger basin cover. No outcrop older than Eocene limestone occurs throughout the Nullarbor Plain, which covers an area of about 200 000 km². The Precambrian basement below has remained one of the significant, and to some extent forgotten regions of Proterozoic Australia, yet this region is fundamental to understanding the assembly of the WAC and SAC.

Analysis of the drillcores has shown that the Precambrian basement is dominated by Paleoproterozoic to Mesoproterozoic rocks of oceanic affinity or heritage with minimal continental influence in their sources. Based on their model ages, these rocks are no older than about 2.0 Ga, and the oldest magmatic zircon crystallization ages are c. 1611 Ma from the Toolgana Supersuite in the Coompana Province. Contrary to previously published models, the results indicate that continental collision between the WAC and SAC did not occur. Instead, these cratonic elements have remained separated by oceanic and oceanic-arc crust engulfed by Moodini Supersuite magmatism as it was structurally modified during the 1225–1125 Ma Maralinga Event. This oceanic realm likely extends northwards along the margin of the WAC.

Distinct differences in crustal evolution are evident between the Madura and Coompana Provinces, highlighting the significant displacement along the Mundrabilla Shear Zone that separates them. The Madura Province formed through hyperextension of the Archean–Paleoproterozoic continental margin of the WAC (Yilgarn Craton and Albany–Fraser Orogen) to produce the Arid Basin, which subsequently closed via subduction related to the formation of an oceanic arc. The oldest known component of the oceanic arc assemblage is the c. 1479 Ma Sleeper Camp Formation. The progression of oceanic arc formation is recorded by the Malcolm Metamorphics basalt after c. 1470 Ma, and the Haig Cave Supersuite from 1415 to 1389 Ma, forming the Loongana Arc. Accretion of the oceanic arc and slivers of marginal basin rocks (e.g. Pinto Basalt) onto the WAC continental margin between 1389 and 1330 Ma produced the Arubiddy Ophiolite complex and the suture zone marked by the Rodona Shear Zone. This event triggered the commencement of Stage I of the Albany–Fraser Orogeny (1330–1260 Ma).

In contrast, the Coompana Province underwent early and probably multiphase subduction recycling, potentially starting at 1720 Ma (or before) and extending to at least c. 1604 Ma, synchronous with juvenile magmatism along the southwestern Gawler Craton. This led to the development of a thick, enriched and hydrated lithosphere. The presence of the c. 1526 Ma Bunburra Suite could indicate a continuation of the subduction event recorded by the Toolgana Supersuite (Dutch et al., 2018), followed by extension and crustal thinning recorded by formation of the c. 1490 Ma Undawidgi Supersuite.

The Madura and Coompana Provinces share a common history from c. 1225 Ma with the commencement of the Maralinga Event, which produced widespread high-KFe Moodini Supersuite magmatism. Whereas high-KMg Moodini Supersuite magmatism occurred in the Coompana Province, its rarity in the Madura Province suggests thick lithospheric mantle was significantly thinned, or removed. The high-KMg magmatism likely represents deep melting of the older subduction-metasomatized lithospheric mantle.

Most drillcores obtained from the Eucla basement demonstrate the presence of alteration zones and sulfide minerals with anomalous values of Cu, Au, Ag and PGE from various locations. Coupled with the interpretations of the geodynamic events these occurrences indicate the potential for a variety of mineral systems. These include, but are not limited to: volcanogenic massive sulfide-style or exhalative deposit mineralization formed within the Arid Basin or in Undawidgi Supersuite and related rocks of the Coompana Province; subduction-related deposits such as porphyry Cu–Au or intrusion-hosted Ni and PGE deposits; non-subduction intrusion-related Cu–Au mineralization during emplacement of the Moodini Supersuite and in particular, the shoshonitic rocks; IOCG-type mineralization; and orogenic Au related to the large crustal-scale shear zones (see also Spaggiari et al., 2015b). The task now is to move from the regional to the camp scale, and further drilling is required to make this transition. This work has demonstrated the benefit of thorough and detailed analysis of diamond drillcores; however, such work is time-consuming and expensive. Using the background provided in this Report, cheaper drilling and analytical methods could potentially be applied to expand the exploration space in this vast greenfields region.

References

- Adams, M 2012, Structural and geochronological evolution of the Malcolm Gneiss, Nornalup Zone, Albany–Fraser Orogen, Western Australia: Geological Survey of Western Australia, Record 2012/4, 132p.
- Aitken, ARA, Betts, PG, Young, DA, Blankenship, DD, Roberts, JL and Siegert, MJ 2016, The Australo-Antarctic Columbia to Gondwana transition: Gondwana Research, v. 29, no. 1, p. 136–152.
- Alley, NF, Clarke, JDA, Macphail, M and Truswell, EM 1999, Sedimentary infillings and development of major Tertiary paleodrainage systems of south-central Australia: Special Publications of the International Association of Sedimentologists, v. 27, p. 337–366.
- Barham, M, Reynolds, S, O’Leary, MJ, Kirkland, CL, Allen, HJ, Haines, PW and Hocking, RM 2015, Stratigraphical and geochemical analysis of pre-Cenozoic sediments beneath the Nullarbor Plain and implications for basin and margin evolution, in *Eucla basement stratigraphic drilling results release workshop: extended abstracts edited by CV Spaggiari and RH Smithies*: Geological Survey of Western Australia, Record 2015/10, p. 7–8.
- Blichert-Toft, J and Albarède, F 1997, The Lu–Hf isotope geochemistry of chondrites and the evolution of the mantle–crust system: Earth and Planetary Science Letters, v. 148, p. 243–258.
- Bogaerts, M, Scaillet, B and Vander Auwera, J 2006, Phase Equilibria of the Lyngdal Granodiorite (Norway): Implications for the Origin of Metaluminous Ferroan Granitoids: Journal of Petrology, v. 47, no. 12, p. 2405–2431.
- Brophy, JG 2008, A study of rare earth element (REE)–SiO₂ variations in felsic liquids generated by basalt fractionation and amphibole melting: a potential test for discriminating between the two different processes: Contributions to Mineralogy and Petrology, v. 156, p. 337–357.
- Brown, D, Ryan, PD, Afonso, JC, Boutelier, D, Burg, JP, Byrne, T, Calvert, A, Cook, F, DeBari, S, Dewey, JF, Gerya, TV, Harris, R, Herrington, R, Konstantinovskaya, E, Reston, T and Zagorevski, A 2011, Arc–Continent Collision: The Making of an Orogen: Chapter 17, in *Arc–Continent Collision, Frontiers in Earth Sciences edited by D Brown and PD Ryan*: Springer-Verlag (Heidelberg), Berlin, Germany, p. 477–493.
- Bunting, JA and McIntyre, JR 2003, Loongana Project; Combined annual technical report C150/2001 for Exploration Licences 69/1516, 1517, 1718, 1719 and 1720 for the period 11/8/2002 to 10/8/2003: Helix Resources Limited: Geological Survey of Western Australia, Statutory mineral exploration report A67484, 29p.
- Burnett, S, Webb, JA and White, S 2013, Shallow caves and blowholes on the Nullarbor Plain, Australia — Flank margin caves on a low gradient limestone platform: Geomorphology, v. 201, p. 246–253.
- Chen, RX, Zheng, Y-F and Xie, LW 2010, Metamorphic growth and recrystallization of zircon: Distinction by simultaneous in-situ analyses of trace elements, U–Th–Pb and Lu–Hf isotopes in zircons from eclogite-facies rocks in the Sulu orogen: Lithos, v. 114, p. 132–154.
- Clark, DJ 1999, Thermo-tectonic evolution of the Albany–Fraser Orogen, Western Australia: University of New South Wales, Sydney, New South Wales, PhD thesis (unpublished).
- Clark, DJ, Hensen, BJ and Kinny, PD 2000, Geochronological constraints for a two-stage history of the Albany–Fraser Orogen, Western Australia: Precambrian Research, v. 102, no. 3, p. 155–183, doi:10.1016/S0301-9268(00)00063-2.
- Coleman, RG 1977, Ophiolites: Ancient Oceanic Lithosphere? Springer-Verlag (Heidelberg), Berlin, Germany, 228p.
- Dilek, Y and Furnes, H 2014, Ophiolites and Their Origins: Elements, v. 10, p. 93–100.
- Duchesne, JC and Charlier, B 2005, Geochemistry of cumulates from the Bjerkreim–Sokndal layered intrusion (S. Norway). Part I: Constraints from major elements on the mechanism of cumulate formation and on the jotunite liquid line of descent: Lithos, v. 83, p. 229–254.
- Duchesne, JC, Shumlyanskyy, L and Charlier, B 2006, The Fedorivka layered intrusion (Korosten Pluton, Ukraine): An example of highly differentiated ferrobasic evolution: Lithos, v. 89, p. 353–376.
- Duchesne, JC and Wilmart, E 1997, Igneous charnockites and related rocks from the Bjerkreim–Sokndal layered intrusion (southwest Norway): a jotunite (hypersthene monzodiorite)-derived A-type granitoid suite: Journal of Petrology, v. 38, p. 337–369.
- Dutch, RA 2018, Coompana Province geochemistry and petrogenesis, in *Coompana Drilling and Geochemistry Workshop 2018 extended abstracts edited by RA Dutch, TW Wise, MJ Pawley and A Petts*: Department for Energy and Mining, Adelaide, South Australia, Report Book 2018/00019, p. 76–101.
- Dutch, RA, Doublier, MP, Pawley, MJ, Wise, TW, Reid, AJ, Clark, D, Kennett, BLN, Fraser, G, Thiel, S and van der Weilen, S 2015, Geological and geodynamic implications of the western Gawler Craton section of seismic line 13GA-EG1, in *What lies beneath the Western Gawler Craton? 13GA-EG1 Seismic and Magnetotelluric Workshop 2015 edited by RA Dutch*: Department of State Development, Adelaide, South Australia, Report Book 2015/00029, p. 28–40.
- Dutch, RA, Spaggiari, CV, Doublier, MP, Pawley, MJ, Wise, TW, Kennett, BLN, Gessner, K, Thiel, S, Clark, DJ and Holzschuh, J 2016, What lies beneath the Nullarbor Plain? Insights into the geology of the Coompana Province from deep crustal seismic reflection profile 13GA-EG1, in *Geological Society of Australia Abstracts No. 118: Australian Earth Sciences Convention, 26–30 June 2016*, p. 120.
- Dutch, RA, Wise, TW, Pawley, MJ and Petts, A (editors) 2018, Coompana Drilling and Geochemistry Workshop 2018 extended abstracts: Department for Energy and Mining, Adelaide, South Australia, Report Book 2018/00019, 171p.
- Edwards, SJ, Schellart, WP and Duarte, JC 2015, Geodynamic models of continental subduction and obduction of overriding plate forearc oceanic lithosphere on top of continental crust: Tectonics, v. 34, no. 7, p. 1494–1515, doi:10.1002/2015TC003884.
- Fitzsimons, ICW 2003, Proterozoic basement provinces of southern and southwestern Australia and their correlation with Antarctica: Geological Society of London Special Publication, v. 206, p. 93–130.
- Frost, BR, Barnes, CG, Collins, WJ, Arculus, RJ, Ellis, DJ and Frost, CD 2001, A geochemical classification for granitic rocks: Journal of Petrology, v. 42, no. 11, p. 2033–2048.
- Frost, BR and Frost, CD 2008, On charnockites: Gondwana Research, v. 13, no. 1, p. 30–44.
- Frost, CD and Frost, BR 2011, On ferroan (A-type) granitoids: their compositional variability and modes of origin: Journal of Petrology, v. 52, p. 39–53.
- Griffin, WL, Pearson, N, Belousova, EA and Saeed, A 2007, Reply to ‘Comment to short-communication: Hf-isotope heterogeneity in zircon 91500’ by WL Griffin, NJ Pearson, WA Belousova, A Saeed (vol. 233 (2006) p. 358–363) by F Corfu: Chemical Geology, v. 244, p. 354–356.
- Griffin, WL, Pearson, NJ, Belousova, E, Jackson, SE, van Achterbergh, E, O’Reilly, SY and Shee, SR 2000, The Hf isotope composition of cratonic mantle: LAM-MC-ICPMS analysis of zircon megacrysts in kimberlites: Geochimica et Cosmochimica Acta, v. 64, no. 1, p. 133–147, doi:10.1016/S0016-7037(99)00343-9.
- Haines, PW, Kirkland, CL, Wingate, MTD, Allen, H, Belousova, EA and Gréau, Y 2016, Tracking sediment dispersal during orogenesis: A zircon age and Hf isotope study from the western Amadeus Basin, Australia: Gondwana Research, v. 37, p. 324–347, doi:10.1016/j.jgr.2015.08.011.
- Harley, DN 2010, Terminal Report, Burkin project, Western Australia EL 69/1972; Gunson Resource Limited: Geological Survey of Western Australia, Statutory mineral exploration report A085906.
- Hawkesworth, CJ and Kemp, AIS 2006, Using hafnium and oxygen isotopes in zircons to unravel the record of crustal evolution: Chemical Geology, v. 226, no. 3, p. 144–162.

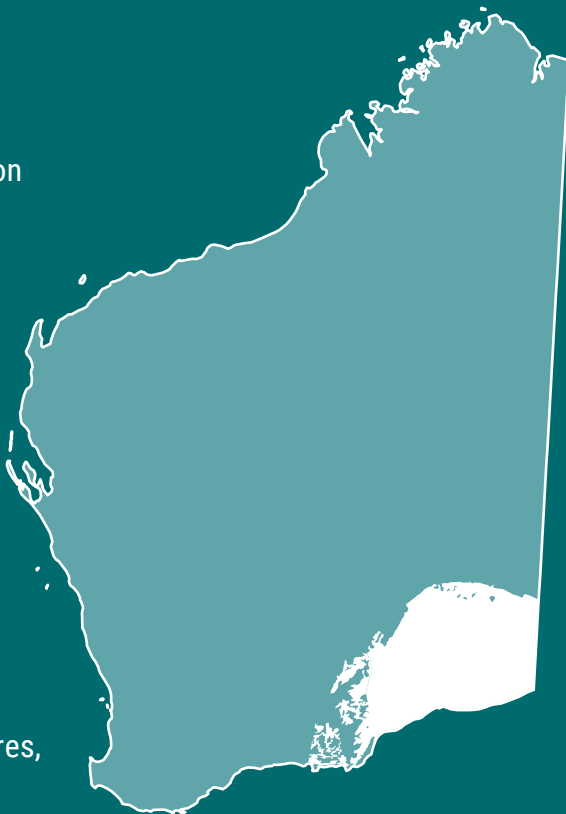
- Holcombe, RJ 2016, Mapping and structural geology in mineral exploration: where theory hits the fan: HCOV Global, Queensland, 233p.
- Holzschuh, J 2019, Eucla–Gawler Seismic Survey L203, Line 13GA–EG1: Acquisition and Processing: Geoscience Australia, Record 2019/06, 24p.
- Hoskin, PWO and Schaltegger, U 2003, The Composition of zircon and igneous and metamorphic petrogenesis: Reviews in Mineralogy and Geochemistry, v. 53, p. 27–62.
- Howard, HM, Smithies, RH, Kirkland, CL, Kelsey, DE, Aitken, A, Wingate, MTD, Quentin de Gromard, R, Spaggiari, CV and Maier, WD 2015, The burning heart – the Proterozoic geology and geological evolution of the west Musgrave Region, central Australia: Gondwana Research, v. 27, no. 1, p. 64–94.
- Jagodzinski, EA and Bodorkos, S 2018, U–Pb geochronology of the eastern Coompana Province, South Australia, in Coompana Drilling and Geochemistry Workshop 2018 extended abstracts edited by RA Dutch, TW Wise, MJ Pawley and A Petts: Department for Energy and Mining, Adelaide, South Australia, Report Book 2018/00019, p. 66–75.
- Kemp, AIS, Hawkesworth, CJ, Collins, WJ, Gray, CM, Blevin, PL and EIMF 2009, Isotopic evidence for rapid continental growth in an extensional accretionary orogen: The Tasmanides, eastern Australia: Precambrian Research, v. 284, no. 3–4, p. 455–466.
- Kilpatrick, JA and Ellis, DJ 1992, C-type magmas: Igneous charnockites and their extrusive equivalents: Transactions of the Royal Society of Edinburgh: Earth sciences, v. 83, p. 155–164.
- Kirkland, CL, Smithies, RH and Spaggiari, CV 2015, Foreign contemporaries – unravelling disparate isotopic signatures from Mesoproterozoic Central and Western Australia: Precambrian Research, v. 265, p. 218–231.
- Kirkland, CL, Smithies, RH, Spaggiari, CV, Wingate, MTD, Quentin de Gromard, R, Clark, C, Gardiner, NJ and Belousova, EA 2017, Proterozoic crustal evolution of the Eucla basement, Australia: Implications for destruction of oceanic crust during emergence of Nuna: Lithos, v. 278, p. 427–444.
- Kirkland, CL, Smithies, RH, Woodhouse, AJ, Howard, HM, Wingate, MTD, Belousova, EA, Cliff, JB, Murphy, RC and Spaggiari, CV 2013a, Constraints and deception in the isotopic record; the crustal evolution of the west Musgrave Province, central Australia: Gondwana Research, v. 23, no. 2, p. 759–781.
- Kirkland, CL, Spaggiari, CV, Pawley, MJ, Wingate, MTD, Smithies, RH, Howard, HM, Tyler, IM, Belousova, EA and Poujol, M 2011a, On the edge: U–Pb, Lu–Hf, and Sm–Nd data suggests reworking of the Yilgarn Craton margin during formation of the Albany–Fraser Orogen: Precambrian Research, v. 187, p. 223–247.
- Kirkland, CL, Spaggiari, CV, Wingate, MTD, Smithies, RH, Belousova, EA, Murphy, R and Pawley, MJ 2011b, Inferences on crust–mantle interaction from Lu–Hf isotopes: A case study from the Albany–Fraser Orogen: Geological Survey of Western Australia, Record 2011/12, 25p.
- Kirkland, CL, Wingate, MTD, Hall, CE and Spaggiari, CV 2012a, 182203: metagabbro, Hannah prospect; Geochronology Record 1049: Geological Survey of Western Australia, 5p.
- Kirkland, CL, Wingate, MTD and Spaggiari, CV 2012b, 182485: migmatitic gneiss, Burkin prospect; Geochronology Record 1054: Geological Survey of Western Australia, 4p.
- Kirkland, CL, Wingate, MTD and Spaggiari, CV 2013b, 192557, metagabbro, Haig Cave; Geochronology Record 1140: Geological Survey of Western Australia, 4p.
- Kirkland, CL, Wingate, MTD and Spaggiari, CV 2013c, 192558: granitic gneiss, Haig Cave; Geochronology Record 1089: Geological Survey of Western Australia, 4p.
- Kirkland, CL, Wingate, MTD, Spaggiari, CV and Tyler, IM 2011c, 194773: granitic rock, Eucla No. 1 drillhole; Geochronology Record 1001: Geological Survey of Western Australia, 4p.
- Korsch, RJ, Spaggiari, CV, Occhipinti, SA, Doublier, MP, Clark, DJ, Dentith, MC, Doyle, MG, Kennett, BLN, Gessner, K, Neumann, NL, Belousova, EA, Tyler, IM, Costelloe, RD, Fomin, T and Holzschuh, J 2014, Geodynamic implications of the 2012 Albany–Fraser deep seismic reflection survey: A transect from the Yilgarn Craton across the Albany–Fraser Orogen to the Madura Province, in Albany–Fraser Orogen seismic and magnetotelluric (MT) workshop 2014: Geological Survey of Western Australia, Record 2014/6, p. 142–173.
- Liew, TC and Hoffman, AW 1988, Precambrian crustal components, plutonic associations, plate environment of the Hercynian Fold Belt of central Europe: Indications from a Nd and Sr isotopic study: Contributions to Mineralogy and Petrology, v. 98, p. 129–138.
- Lowry, DC 1970, Geology of the Western Australian part of the Eucla Basin: Geological Survey of Western Australia, Bulletin 122, 201p.
- Maier, WD, Smithies, RH, Spaggiari, CV, Barnes, S-J, Kirkland, CL, Kiddie, O and Roberts, MP 2016, The evolution of mafic and ultramafic rocks of the Mesoproterozoic Fraser Zone, Albany–Fraser Orogen, and implications for Ni–Cu sulfide potential of the region: Geological Survey of Western Australia, Record 2016/8, 49p.
- Mander, P 2015, Drilling techniques – getting through complex cover to basement, in Eucla basement stratigraphic drilling results release workshop: extended abstracts edited by CV Spaggiari and RH Smithies: Geological Survey of Western Australia, Record 2015/10, p. 9.
- Martin, H, Smithies, RH, Rapp, R, Moyen, J-F and Champion, DC 2005, An overview of adakite, tonalite-trondhjemite-granodiorite (TTG), and sanukitoid: Relationships and some implications for crustal evolution: Lithos, v. 79, p. 1–24.
- McIntyre, JR and Weston, K 2015, Final Report for the Government Co-Funded Drilling Application DAG2015/0042284, Loongana Project, C50/2015: Exploration Licence 69/3104, MRG Metals Pty Ltd: Geological Survey of Western Australia, Statutory mineral exploration report A107068, 15p.
- Morrissey, LJ, Payne, JL, Hand, M, Clark, C, Taylor, R, Kirkland, CL and Kylander-Clark, A 2017, Linking the Windmill Islands, east Antarctica and the Albany–Fraser Orogen: Insights from U–Pb zircon geochronology and Hf isotopes: Precambrian Research, v. 293, p. 131–149.
- Mounsher, LC 2016, Evolution and deformation of the onshore Eucla Basin during the Cenozoic: Geological Survey of Western Australia, Record 2016/10, 70p.
- Moyen, J-F 2009, High Sr/Y and La/Yb ratios: The meaning of the “adakitic signature”: Lithos, v. 112, p. 556–574.
- Myers, JS, Shaw, RD and Tyler, IM 1996, Tectonic evolution of Proterozoic Australia: Tectonics, v. 15, p. 1431–1446.
- Nelson, DR 2005a, 178070: amphibolite, Haig Cave; Geochronology Record 596: Geological Survey of Western Australia, 4p.
- Nelson, DR 2005b, 178071: recrystallized biotite microtonalite, Haig Cave; Geochronology Record 597: Geological Survey of Western Australia, 4p.
- Neumann, NL and Korsch, RJ 2014, SHRIMP U–Pb zircon ages from Kutjara 1 and Mulyawara 1, northwestern South Australia: Geoscience Australia, Canberra, Record 2014/05, 18p.
- O’Connell, LG 2011, Sedimentology of the Miocene Nullarbor Limestone; southern Australia: Geological Survey of Western Australia, Report 111, 211p.
- O’Connell, LG, James, NP and Bone, Y 2012, The Miocene Nullarbor Limestone, southern Australia; deposition on a vast subtropical epeiric platform: Sedimentary Geology, v. 253–254, p. 1–16.
- Pawley, MJ, Wise, TW and Dutch, RA 2018, What the 13GA-EG1 Eucla–Gawler seismic survey tells us about the Coompana Province, in Coompana Drilling and Geochemistry Workshop 2018 extended abstracts edited by RA Dutch, TW Wise, MJ Pawley and A Petts: Department for Energy and Mining, Adelaide, South Australia, Report Book 2018/00019, p. 109–119.

- Payne, JL, McInerney, DJ, Barovich, KM, Kirkland, CL, Pearson, NJ and Hand, M 2016, Strengths and limitations of zircon Lu–Hf and O isotopes in modelling crustal growth: *Lithos*, v. 248–251, p. 175–192.
- Pearce, JA 2008, Geochemical fingerprinting of oceanic basalts with applications to ophiolite classification and the search for Archean oceanic crust: *Lithos*, v. 100, p. 14–48.
- Pearce, JA 2014, Immobile element fingerprinting of ophiolites: *Elements*, v. 10, p. 101–108.
- Peccerillo, A and Taylor, SR 1976, Geochemistry of the Eocene calcalkaline volcanic rocks from the Kastamonu area, northern Turkey: *Contributions to Mineralogy and Petrology*, v. 58, p. 63–81.
- Quentin de Gromard, R, Spaggiari, CV, Munro, M, Sapkota, J and de Paoli, M 2017, SGTSG 2017 Albany–Fraser Orogen pre-conference fieldtrip: Transect across an Archean craton margin to a Proterozoic ophiolite: Geological Survey of Western Australia, Record 2017/14, 100p.
- Ramsay, JG 1962, Interference patterns produced by the superposition of folds of ‘similar’ type: *Journal of Geology*, v. 70, p. 466–481.
- Reid, AJ, Pawley, MJ, Wade, C, Jagodzinski, EA, Dutch, RA and Armstrong, R 2019, Resolving tectonic settings of ancient magmatic suites using structural, geochemical and isotopic constraints: the example of the St Peter Suite, southern Australia: *Australian Journal of Earth Sciences*, v. 67, no. 1, p. 31–58, doi:10.1080/08120099.2019.1632224.
- Reynolds, S 2016, Stratigraphic evolution of the southern Australian onshore Bight Basin: A record for the breakup of Gondwana during the Cretaceous: Geological Survey of Western Australia, Record 2016/11, 64p.
- Richmond Mining Limited 2012, Combined Annual Technical Report (C102/2009) Western Australia EL 69/2444 and 69/2445 for the period 20/10/2010 to 19/10/2011: Geological Survey of Western Australia, Statutory mineral exploration report A092869, 14p.
- Sasi, R 2011, Annual geological report for the period 12/03/2010 to 12/03/2011, Exploration Licence E69/22628: Venus Metals Corporation Ltd: Geological Survey of Western Australia, Statutory mineral exploration report A093851, 23p.
- Sasi, R 2012, Annual geological report for the period 12/03/2011 to 12/03/2012, Exploration Licence E69/22628: Venus Metals Corporation Ltd: Geological Survey of Western Australia, Statutory mineral exploration report A093851, 31p.
- Scherer, E, Münker, C and Mezger, K 2001, Calibration of the lutetium–hafnium clock: *Science*, v. 293, p. 683–687, doi:10.1126/science.1061372.
- Shaw, RD, Wellman, P, Gunn, P, Whitaker, AJ, Tarlowski, C and Morse, M 1996, Guide to using the Australian Crustal Elements Map: Australian Geological Survey Organisation, Record 1996/30, 44p.
- Shervais, JW 1982, Ti–V plots and the petrogenesis of ophiolitic lavas: *Earth and Planetary Science Letters*, v. 59, p. 101–118.
- Sipl, C, Tkalčić, H, Kennett, BLN, Spaggiari, CV and Gessner, K 2018, Crustal and uppermost mantle structure of the east Albany–Fraser Orogen from passive seismic data: Geological Survey of Western Australia, Report 177, 51p.
- Smit, R 2009, 1st Annual Report and final surrender report, Kanandah Project, Eucla Basin, Western Australia, EL 28/1773: Buxton Resources Limited, Statutory mineral exploration report; Geochronology Record A081538: Geological Survey of Western Australia, 107p.
- Smithies, RH, Howard, HM, Evins, PM, Kirkland, CL, Kelsey, DE, Hand, M, Wingate, MTD, Collins, AS and Belousova, E 2011, High-temperature granite magmatism, crust–mantle interaction and the Mesoproterozoic intracontinental evolution of the Musgrave Province, Central Australia: *Journal of Petrology*, v. 52, no. 5, p. 931–958.
- Smithies, RH, Howard, HM, Evins, PM, Kirkland, CL, Kelsey, DE, Hand, M, Wingate, MTD, Collins, AS, Belousova, E and Allchurch, S 2010, Geochemistry, geochronology, and petrogenesis of Mesoproterozoic felsic rocks in the west Musgrave Province, Central Australia, and implications for the Mesoproterozoic tectonic evolution of the region: Geological Survey of Western Australia, Report 106, 73p.
- Smithies, RH, Kirkland, CL, Korhonen, FJ, Aitken, ARA, Howard, HM, Maier, WD, Wingate, MTD, Quentin de Gromard, R and Gessner, K 2015a, The Mesoproterozoic thermal evolution of the Musgrave Province in central Australia – plume vs. the geological record: *Gondwana Research*, v. 27, no. 4, p. 1419–1429, doi:10.1016/j.jgr.2013.12.014.
- Smithies, RH, Spaggiari, C, Kirkland, CL, Howard, HM and Maier, WD 2013, Petrogenesis of gabbros of the Mesoproterozoic Fraser Zone: Constraints on the tectonic evolution of the Albany–Fraser Orogen: Geological Survey of Western Australia, Record 2013/5, 29p.
- Smithies, RH, Spaggiari, CV and Kirkland, CL 2015b, Building the crust of the Albany–Fraser Orogen: constraints from granite geochemistry: Geological Survey of Western Australia, Report 150, 49p.
- Spaggiari, CV 2016, Pre-Mesozoic 1:250 000 interpreted bedrock geology of the east Albany–Fraser Orogen (digital map layer), in East Albany–Fraser Orogen, 2016: Geological Survey of Western Australia, Geological Exploration digital data package.
- Spaggiari, CV, Dutch, RA, Doublier, MP, Pawley, MJ, Thiel, S, Wise, TW, Kennett, BLN, Gessner, K, Smithies, RH, Holzschuh, J and Clark, DJ 2017a, Geological interpretation of the Madura and Coompana Provinces along the Eucla–Gawler seismic and magnetotelluric line 13GA-EG1: Geological Survey of Western Australia, non-series map.
- Spaggiari, CV, Kirkland, CL, Pawley, MJ, Smithies, RH, Wingate, MTD, Doyle, MG, Blenkinsop, TG, Clark, C, Oorschot, CW, Fox, LJ and Savage, J 2011, The geology of the east Albany–Fraser Orogen — a field guide: Geological Survey of Western Australia, Record 2011/23, 97p.
- Spaggiari, CV, Kirkland, CL and Smithies, RH 2017b, Regional geology and metallogeny of the Albany–Fraser Orogen, in *Australian Ore Deposits edited by GN Phillips*: Australasian Institute of Mining and Metallurgy, Monograph 32, p. 385–388.
- Spaggiari, CV, Kirkland, CL, Smithies, RH and Wingate, MTD 2012, What lies beneath — interpreting the Eucla basement, in GSWA 2012 Extended Abstracts: promoting the prospectivity of Western Australia: Geological Survey of Western Australia, Record 2012/2, p. 25–27.
- Spaggiari, CV, Kirkland, CL, Smithies, RH, Wingate, MTD and Belousova, EA 2015a, Transformation of an Archean craton margin during Proterozoic basin formation and magmatism: the Albany–Fraser Orogen, Western Australia: *Precambrian Research*, v. 266, p. 440–466.
- Spaggiari, CV, Occhipinti, SA, Korsch, RJ, Doublier, MP, Clark, DJ, Dentith, MC, Gessner, K, Doyle, MG, Tyler, IM, Kennett, BLN, Costelloe, RD, Fomin, T and Holzschuh, J 2014, Interpretation of Albany–Fraser seismic lines 12GA-AF1, 12GA-AF2 and 12GA-AF3: Implications for crustal architecture, in Albany–Fraser Orogen seismic and magnetotelluric (MT) workshop 2014: extended abstracts: Geological Survey of Western Australia, Record 2014/6, p. 28–51.
- Spaggiari, CV and Smithies, RH (editors) 2015, Eucla basement stratigraphic drilling results release workshop: extended abstracts: Geological Survey of Western Australia, Record 2015/10, 70p.
- Spaggiari, CV, Smithies, RH, Kirkland, CL, England, RN, Occhipinti, SA and Wingate, MTD 2015b, Eucla basement results: Implications for geodynamics and mineral prospectivity, in Eucla basement stratigraphic drilling results release workshop: extended abstracts edited by CV Spaggiari and RH Smithies: Geological Survey of Western Australia, Record 2015/10, p. 53–58.
- Spaggiari, CV, Smithies, RH, Kirkland, CL, Wingate, MTD, England, R and Lu, Y 2018, Buried but preserved: the Proterozoic Arubiddy Ophiolite, Madura Province, Western Australia: *Precambrian Research*, v. 317, p. 137–158.

- Spaggiari, CV, Smithies, RH, Wingate, MTD, Kirkland, CL and England, RN 2016, Exposing the Eucla basement — what separates the Albany–Fraser Orogen and the Gawler Craton?, *in* GSWA 2016 extended abstracts: promoting the prospectivity of Western Australia: Geological Survey of Western Australia, Record 2016/2, p. 36–41.
- Stephens, DI 2000, Final Report for the Naretha Albany–Fraser project, Western Australia, EL 28/901–905: BHP Mineral Pty Ltd, Statutory mineral exploration report; Geochronology Record A60607: Geological Survey of Western Australia, 34p.
- Sun, S-S and McDonough, W-S 1989, Chemical and isotopic systematics of oceanic basalts: implications for mantle composition and processes: Geological Society, London, Special Publications, v. 42, no. 1, p. 313–345.
- Swain, G, Barovich, K, Hand, M, Ferris, G and Schwarz, M 2008, Petrogenesis of the St Peter Suite, southern Australia: Arc magmatism and Proterozoic crustal growth of the South Australian Craton: Precambrian Research, v. 166, no. 1–4, p. 283–296.
- Thiel, S, Wise, TW and Duan, J 2018, Electrical signatures of the Coompana Province from AusLAMP and profile MT data, *in* Coompana Drilling and Geochemistry Workshop 2018 extended abstracts *edited by* RA Dutch, TW Wise, MJ Pawley and A Petts: Department for Energy and Mining, Adelaide, South Australia, Report Book 2018/00019, p. 120–130.
- Tillick, D 2010, Final Report of Co-funded Government – Industry Drilling Program at the Eucla Project, September 2010, Exploration Licences E69/2344 (Serpent) and E28/1608 (Big Red); Teck Australia Pty Ltd: Geological Survey of Western Australia, Statutory mineral exploration report A088011–A100927, 28p.
- Tillick, D 2011a, Final Report of Co-funded Government – Industry Drilling Program at the Haig Prospect, Eucla Project, August 2011, Exploration Licence E69/2343; Teck Australia Pty Ltd: Geological Survey of Western Australia, Statutory mineral exploration report A091287, 30p.
- Tillick, D 2011b, Final Report of Co-funded Government – Industry Drilling Program at the NSD Prospect, Eucla Project, August 2011, Exploration Licence E69/2341; Teck Australia Pty Ltd: Geological Survey of Western Australia, Statutory mineral exploration report A091287, 20p.
- Vander Auwera, J, Bologne, G, Roelandts, I and Duchesne, JC 1998, Inductively coupled plasma-mass spectrometry (ICP-MS) analysis of silicate rocks and minerals: *Geologica Belgica*, v. 1, p. 49–53.
- Waddell, P-JA, Timms, NE, Spaggiari, CV, Kirkland, CL and Wingate, MTD 2015, Analysis of the Ragged Basin, Western Australia: Insights into syn-orogenic basin evolution within the Albany–Fraser Orogen: *Precambrian Research*, v. 261, p. 166–187.
- Wade, BP, Payne, JL, Hand, M and Barovich, KM 2007, Petrogenesis of ca 1.50 Ga granitic gneiss of the Coompana Block: Filling the ‘magmatic gap’ of Mesoproterozoic Australia: *Australian Journal of Earth Sciences*, v. 54, p. 1089–1102.
- Watson, EB and Harrison, TM 1983, Zircon saturation revisited: Temperature and composition effects in a variety of crustal magma types: *Earth and Planetary Science Letters*, v. 64, no. 2, p. 295–304.
- Webb, J and James, J 2006, Karst evolution of the Nullarbor Plain, Australia, *in* Perspectives on karst geomorphology, hydrology, and geochemistry — a tribute to Derek C. Ford and William B. White *edited by* RS Harmon: Geological Society of America, Special Paper 404, p. 65–78.
- Wingate, MTD, Campbell, IH, Compston, W and Gibson, GM 1998, Ion microprobe U–Pb ages for Neoproterozoic basaltic magmatism in south-central Australia and implications for the breakup of Rodinia: *Precambrian Research*, v. 87, no. 3–4, p. 135–159, doi:10.1016/S0301-9268(97)00072-7.
- Wingate, MTD, Kirkland, CL, Lu, Y and Spaggiari, CV 2019, 182485: metagranitic vein, Burkin prospect; Geochronology Record 1054: Geological Survey of Western Australia, 4p.
- Wingate, MTD, Kirkland, CL, Spaggiari, CV and Smithies, RH 2015a, U–Pb geochronology of the Madura Province, *in* Eucla basement stratigraphic drilling results release workshop: extended abstracts *edited by* CV Spaggiari and RH Smithies: Geological Survey of Western Australia, Record 2015/10, p. 14–16.
- Wingate, MTD and Lu, Y 2017, Introduction to geochronology information released in 2017: Geological Survey of Western Australia, 5p.
- Wingate, MTD, Lu, Y, Kirkland, CL and Spaggiari, CV 2015b, 192565: metamonzogranite, Moodini prospect; Geochronology Record 1269: Geological Survey of Western Australia, 4p.
- Wingate, MTD, Lu, Y, Kirkland, CL and Spaggiari, CV 2015c, 192566: metamonzogranite, Moodini prospect; Geochronology Record 1270: Geological Survey of Western Australia, 4p.
- Wingate, MTD, Lu, Y, Kirkland, CL and Spaggiari, CV 2015d, 192592: monzogranite gneiss, Forrest Zone; Geochronology Record 1271: Geological Survey of Western Australia, 4p.
- Wingate, MTD, Lu, Y, Kirkland, CL and Spaggiari, CV 2015e, 192593: hornblende–biotite metagranite, Forrest Zone; Geochronology Record 1272: Geological Survey of Western Australia, 4p.
- Wingate, MTD, Lu, Y, Kirkland, CL, Spaggiari, CV and Smithies, RH 2016a, 192595: biotite–hornblende granodiorite, Madura Province; Geochronology Record 1290: Geological Survey of Western Australia, 4p.
- Wingate, MTD, Lu, Y and Spaggiari, CV 2018a, 192560: metatonalite vein, Haig prospect; Geochronology Record 1442: Geological Survey of Western Australia, 4p.
- Wingate, MTD, Lu, Y and Spaggiari, CV 2018b, 192561: metatonalite vein, Haig prospect; Geochronology Record 1443: Geological Survey of Western Australia, 5p.
- Wingate, MTD, Lu, Y and Spaggiari, CV 2018c, 192562: monzogranite, NSD prospect; Geochronology Record 1444: Geological Survey of Western Australia, 5p.
- Wingate, MTD, Lu, Y and Spaggiari, CV 2018d, 192563: altered leucogabbro, NSD prospect; Geochronology Record 1446: Geological Survey of Western Australia, 4p.
- Wingate, MTD, Lu, Y and Spaggiari, CV 2018e, 192563: altered leucogabbro, NSD prospect; Geochronology Record 1447: Geological Survey of Western Australia, 4p.
- Wingate, MTD, Lu and Spaggiari, CV 2020a, 194867: semipelitic gneiss, Point Malcolm; Geochronology Record 1660: Geological Survey of Western Australia, 5p.
- Wingate, MTD, Lu, Y and Spaggiari, CV 2020b, 194869: quartzofeldspathic gneiss, Telegraph Track; Geochronology Record 1662: Geological Survey of Western Australia, 7p.
- Wingate, MTD, Lu, Y and Spaggiari, CV 2020c, 207001: psammitic gneiss, Point Malcolm; Geochronology Record 1664: Geological Survey of Western Australia, 4p.
- Wingate, MTD, Lu, Y and Spaggiari, CV 2018f, 219092: metadolerite, Burkin prospect; Geochronology Record 1478: Geological Survey of Western Australia, 4p.
- Wingate, MTD, Lu, Y and Spaggiari, CV 2018g, 219093: mafic volcanoclastic schist, Burkin prospect; Geochronology Record 1479: Geological Survey of Western Australia, 4p.
- Wingate, MTD, Lu, Y and Spaggiari, CV 2018h, 219094: metagranite vein, Burkin prospect; Geochronology Record 1480: Geological Survey of Western Australia, 6p.
- Wingate, MTD, Lu, Y, Spaggiari, CV and Smithies, RH 2015f, 206729: biotite–hornblende diorite, Forrest Zone; Geochronology Record 1273: Geological Survey of Western Australia, 4p.
- Wingate, MTD, Lu, Y, Spaggiari, CV and Smithies, RH 2015g, 206730: hornblende–biotite metasyenite, Forrest Zone; Geochronology Record 1274: Geological Survey of Western Australia, 5p.

- Wingate, MTD, Lu, Y, Spaggiari, CV and Smithies, RH 2015h, 206751: fine-grained metatonalite, Forrest Zone; Geochronology Record 1275: Geological Survey of Western Australia, 4p.
- Wingate, MTD, Lu, Y, Spaggiari, CV and Smithies, RH 2015i, 206752: porphyritic syenogranite, Forrest Zone; Geochronology Record 1276: Geological Survey of Western Australia, 4p.
- Wingate, MTD, Lu, Y, Spaggiari, CV and Smithies, RH 2015j, 206753: equigranular syenogranite, Forrest Zone; Geochronology Record 1277: Geological Survey of Western Australia, 4p.
- Wingate, MTD, Lu, Y, Spaggiari, CV and Smithies, RH 2015k, 213838: monzogranite vein, Forrest Zone; Geochronology Record 1278: Geological Survey of Western Australia, 4p.
- Wingate, MTD, Lu, Y, Spaggiari, CV and Smithies, RH 2016b, 206754: metagranodiorite, Madura Province; Geochronology Record 1291: Geological Survey of Western Australia, 4p.
- Wingate, MTD, Lu, Y, Spaggiari, CV and Smithies, RH 2016c, 206778: coarse-grained monzogabbro, Madura Province; Geochronology Record 1292: Geological Survey of Western Australia, 4p.
- Wingate, MTD, Lu, Y, Spaggiari, CV and Smithies, RH 2016d, 206779: medium-grained monzogabbro, Madura Province; Geochronology Record 1293: Geological Survey of Western Australia, 4p.
- Wingate, MTD, Lu, Y, Spaggiari, CV and Smithies, RH 2016e, 206788: felsic schist, Forrest Zone; Geochronology Record 1294: Geological Survey of Western Australia, 4p.
- Wingate, MTD, Lu, Y, Spaggiari, CV and Smithies, RH 2016f, 213822: metasyenogranite, Forrest Zone; Geochronology Record 1295: Geological Survey of Western Australia, 5p.
- Wingate, MTD, Lu, Y, Spaggiari, CV and Smithies, RH 2016g, 216239: mylonitic metamonzogranite, Forrest Zone; Geochronology Record 1296: Geological Survey of Western Australia, 4p.
- Wise, T, Dutch, R, Pawley, MJ, Foss, C and Thiel, S, 2018a, Building the Coompana Province: MESA Journal, v. 88, no. 3, p. 25–37.
- Wise, T, Pawley, MJ and Dutch, RA 2018b, Interpreted geology map of the eastern Coompana Province, *in* Coompana Drilling and Geochemistry Workshop 2018 extended abstracts, *compiled by* RA Dutch, T Wise, MJ Pawley and A Petts: Report Book 2018/00019, Department for Energy and Mining, South Australia, Adelaide, p. 102–108.
- Woodhead, J, Hergt, J, Greig, A and Edwards, L 2011, Subduction zone Hf-anomalies: Mantle messenger, melting artefact or crustal process? *Earth and Planetary Science Letters*, v. 304, p. 231–239.
- Zhang, SB, Zheng, YF and Zhao, ZF 2010, Temperature effect over garnet effect on uptake of trace elements in zircon of TTG-like rocks: *Chemical Geology*, v. 274, p. 108–125.

This Report provides an example of mapping under cover and contains descriptions and analyses of eight Geological Survey of Western Australia stratigraphic drillcores and 14 exploration drillcores that intersect Proterozoic basement beneath the Nullarbor Plain. The stratigraphic drillsites were chosen by identifying geophysical domains in aeromagnetic and gravity data. A variety of metabasalts, felsic metavolcanic rocks and related schists, metagabbros, and dominantly metamorphosed granitic rocks including shoshonite, adakite, and granites with syenogranitic to dioritic compositions, were intersected. Combined with analysis of the Exploration Incentive Scheme co-funded and donated company drillcores, the results have provided the means to establish a stratigraphic and crustal evolution framework for the covered Proterozoic basement, and to broadly assess its prospectivity.



Further details of geoscience products are available from:

Information Centre
Department of Mines, Industry Regulation and Safety
100 Plain Street
EAST PERTH WA 6004
Phone: (08) 9222 3459

www.dmirs.wa.gov.au/GSWApublications